

Structure and Evolution of the Large Scale  
Solar and Heliospheric Magnetic Fields

by

J. Todd Hoeksema

CSSA-ASTRO-84-07

April 1984

OFFICE OF NAVAL RESEARCH  
Contract N00014-76-C-0207

NATIONAL AERONAUTICS AND SPACE ADMINISTRATION  
Grant NGR05-020-559  
Contract NAS5-24420

NATIONAL SCIENCE FOUNDATION  
Atmospheric Sciences Section  
Grant ATM77-20580

Max C. Fleischmann Foundation

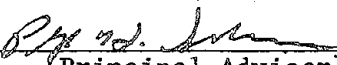


Structure and Evolution of the Large Scale  
Solar and Heliospheric Magnetic Fields

A DISSERTATION  
SUBMITTED TO THE DEPARTMENT OF APPLIED PHYSICS  
AND THE COMMITTEE ON GRADUATE STUDIES  
OF STANFORD UNIVERSITY  
IN PARTIAL FULFILLMENT OF THE REQUIREMENTS  
FOR THE DEGREE OF  
DOCTOR OF PHILOSOPHY

By  
Jon Todd Hoeksema  
April 1984

I certify that I have read this thesis and that in my opinion it is fully adequate, in scope and quality, as a dissertation for the degree of Doctor of Philosophy.

  
\_\_\_\_\_  
(Principal Adviser)

I certify that I have read this thesis and that in my opinion it is fully adequate, in scope and quality, as a dissertation for the degree of Doctor of Philosophy.

  
\_\_\_\_\_  
Arthur B. C. Walker Jr.

I certify that I have read this thesis and that in my opinion it is fully adequate, in scope and quality, as a dissertation for the degree of Doctor of Philosophy.

  
\_\_\_\_\_  
P. Ashwood

Approved for the University Committee  
on Graduate Studies:

\_\_\_\_\_  
Dean of Graduate Studies & Research

## Acknowledgments

Five years ago I knew nothing about solar physics; now I have at least begun to understand one aspect of how the sun interacts with the Earth. How does one begin to thank all those who have contributed to the completion of this work?

First of all, I thank God who made such an interesting universe and gave me the curiosity and intellect to appreciate a small part of it.

Secondly, there are those whose contributions are personal rather than technical. My wife, Carole, has supported me throughout this program with more love and understanding than anyone could have any right to expect. For living in an observatory (nice, but small), accepting interminable years of student life, baking me wonderful pies, keeping me happy, making our house a home, and a host of other things, my thanks. I am also grateful to my parents who demonstrated the meaning of love and doing one's best, sacrificed to provide me with many opportunities, taught me to 'remember who I am,' and encouraged me to aim for the stars, if that was what I wanted.

Finally, appreciation is due to those who have taught me about the sun, the Earth, being an observer, and becoming a scientist. Phil Scherrer has been a continuing inspiration and role model whose contagious enthusiasm, insight, patience with unceasing questions, and clear communication of his detailed knowledge of almost everything have made this work not only possible but fun. In spite of an increased work load, he has made time to be a fine adviser.

I also wish to thank my adviser, John M. Wilcox, whose recent sudden death saddened all those who knew him. In addition to teaching me a great deal and providing excellent resources and facilities, John did much to influence my understanding of the practice of science by his encouragement of the free flow of ideas, by the importance given to meeting colleagues at Stanford and elsewhere, by his emphasis on consistency and thoroughness, by his generosity, and by his insistence on looking at the data.

I would also like to thank the readers of this dissertation, P. H.

Scherrer, P. A. Sturrock, and A. B. C. Walker, Jr., and those others who have contributed to this work in many ways: H. Henning, Zhang Zhuwen, S. Suess, J. Knight, J. Gingerich, L. Svalgaard, K. Zaring, and D. Blaskowski. This work was supported in part by the Office of Naval Research under Contract N00014-78-C-0207, by the National Aeronautics and Space Administration under Grant NGR5-020-559 and Contract NAS5-24420, by the Atmospheric Sciences Section of the National Science Foundation under Grant ATM77-20580 and by the Max C. Fleischmann Foundation.

# Table of Contents

	Page
Acknowledgments.....	iii
Figures.....	vii
Abstract.....	ix
Chapter 1 -- Introduction.....	1
Background.....	2
Purpose.....	7
Methods.....	8
Results.....	9
Chapter 2 -- Data Collection & Analysis.....	11
The Instrument.....	11
Data Collection.....	18
Data Reduction.....	20
Coverage.....	26
Chapter 3 -- The Potential Field Model.....	31
Assumptions, Advantages, and Disadvantages.....	37
Mathematical Development of the Model.....	43
Merging Computations.....	48
Correction to the Data.....	51
Form of Results.....	52
Chapter 4 -- Setting the Parameters.....	59
Comparison of Observed and Predicted IMF.....	59
Choosing the Source Surface Radius.....	68
The Polar Field Correction.....	72
The Monopole Component.....	82
Summary.....	90
Chapter 5 -- The Heliospheric Field.....	91
Solar Minimum -- 1976 - 1977.....	92
The Rising Phase -- 1976 - 1978.....	102
Sunspot Maximum -- 1979 - 1980.....	106
Declining Phase -- 1981 - 1983.....	114
Summary & Discussion.....	116

Chapter 6 -- Comparisons & Applications.....	120
Comparison with other Potential Field Calculations.....	120
Studies of Current Sheet using other Methods.....	123
Solar Wind Velocity.....	131
Coronal Holes & the Large Scale Field.....	140
Cosmic Ray Modulation.....	150
Coronameter Data.....	153
Other Probes of the Heliosphere.....	163
 Chapter 7 -- Multipoles & Discussion.....	 169
Multipole Components.....	169
The Dipole Components.....	176
Multiple Current Sheets.....	183
The Reversal of the Polar Field.....	184
Coronal Rotation.....	186
Photospheric Sources of the IMF.....	188
 Chapter 8 -- Conclusions.....	 194
Summary of Methods.....	194
Summary of Results.....	196
Suggestions for Further Study.....	200
 Appendix -- Model Implementation.....	 202
Description of Program.....	202
Program.....	205
 Bibliography.....	 215



# Figures

Figure Title .....	Number.....	Page
Heliospheric Current Sheet .....	1-1 .....	6
Solar Observatory .....	2-1.....	13
Solar Telescope.....	2-2.....	12
Magnetogram.....	2-3.....	23
Synoptic Chart: CR 1683 .....	2-4.....	25
Data Coverage.....	2-5.....	28
Solar Eclipse .....	3-1.....	31
Potential Field Model .....	3-2.....	35
Combining Computations.....	3-3.....	50
Source Surface Field: CR 1656.....	3-4.....	53
Spherical Harmonics .....	3-5.....	55
Field Direction at $1.1 R_{\odot}$ .....	3-6.....	57
Observed IMF Polarity.....	4-1.....	62
Predicted IMF Polarity.....	4-2.....	63
IMF Correlation.....	4-3.....	65
Correlation vs Latitude .....	4-4.....	67
Correlation vs Radius: 1976-7 .....	4-5.....	69
Current Sheet vs Radius .....	4-6.....	71
North Polar Field .....	4-7.....	73
South Polar Field .....	4-8.....	75
Current Sheet vs Polar Field.....	4-9.....	77
Correlation vs Radius: 1976-82.....	4-10.....	81
Computed Monopole Component.....	4-11.....	83
Synoptic Charts: 1713 & 1714.....	4-12.....	86-87
Zero Offset Removed .....	4-13.....	89
Source Surface: CR 1648.....	5-1.....	94
Source Surface: CR 1656.....	5-2.....	96
Current Sheets: CR 1641-1649 .....	5-3.....	98
Current Sheets: CR 1650-1658 .....	5-4.....	99
Source Surface: CR 1665.....	5-5.....	103
Current Sheets: CR 1641-1669 .....	5-6.....	105
Source Surface: CR 1679.....	5-7.....	107
Source Surface: CR 1698.....	5-8.....	109
Current Sheets: CR 1670-1699 .....	5-9.....	111
Current Sheets: CR 1700-1729 .....	5-10.....	113

Source Surface: CR 1720.....	5-11.....	115
Current Sheets: CR 1730-1744.....	5-12.....	117
5-Cycles of IMF Polarity.....	6-1.....	124
Observed IMF Polarity: 1976-1982.....	6-2.....	126
Predicted IMF Polarity: 1976-1983.....	6-3.....	127
IPS, Coronameter, PF Maps.....	6-4.....	130
Solar Wind Velocity vs  B .....	6-5.....	134-5
Interplanetary Quantities.....	6-6.....	137
Source Surface Fields & CH.....	6-7.....	138
Coronal Hole During CR 1663.....	6-8.....	142
Coronal Holes During CR 1680.....	6-9.....	143
Superposed Source Surface Fields.....	6-10.....	145-8
Cosmic Ray Flux & Solid Angle.....	6-11.....	152
Coronameter & PFM Comparison.....	6-12.....	155
Synoptic Charts: 1643, 1644, 1645.....	6-13.....	157-9
Field Direction at $1.5 R_{\odot}$ : CR 1653.....	6-14.....	161
Field Direction at $2.49 R_{\odot}$ : CR 1653.....	6-15.....	162
Field Direction at $1.1 R_{\odot}$ : CR 1653.....	6-16.....	164
Current Sheet & Helios 1 and 2.....	6-17.....	166
Current Sheet & Earth.....	6-18.....	167
Monopole, Dipole, & Quadrupole.....	7-1.....	172
$l=3, 4, \& 5$ Field Components.....	7-2.....	174
$l=6, 7, 8, \& 9$ Field Components.....	7-3.....	175
Polar & Equatorial Dipoles.....	7-4.....	177
Power Spectrum of Equatorial Dipole.....	7-5.....	179
Dipole Field Direction.....	7-6.....	181
Polar Field Reversal Cartoon.....	7-7.....	185
Differential Rotation.....	7-8.....	187
Zonal Average Field.....	7-9.....	190
Superposed Synoptic Charts.....	7-10.....	192

## Tables

Table	Page
Harmonic Coefficients.....	56
Weights of Coefficients.....	170

## Abstract

The structure and evolution of the large scale photospheric and coronal magnetic fields in the interval 1976 - 1983 have been studied using observations from the Stanford Solar Observatory and a potential field model. The solar wind in the heliosphere is organized into large regions in which the magnetic field has a component either toward or away from the sun. The model predicts the location of the current sheet separating these regions. Near solar minimum, in 1976, the current sheet lay within a few degrees of the solar equator having two extensions north and south of the equator. Soon after minimum the latitudinal extent began to increase. The sheet reached to at least  $50^\circ$  from 1978 through 1983. The complex structure near maximum occasionally included multiple current sheets. Large scale structures persist for up to two years during the entire interval.

To minimize the errors in determining the structure of the heliospheric field particular attention has been paid to decreasing the distorting effects of rapid field evolution, finding the optimum source surface radius, determining the correction to the sun's polar field, and handling missing data. The predicted structure agrees with direct interplanetary field measurements taken near the ecliptic and with coronameter and interplanetary scintillation measurements which infer the three dimensional interplanetary magnetic structure.

During most of the solar cycle the heliospheric field cannot be adequately described as a dipole. For much of the cycle the quadrupole and occasionally octupole moments of the field are more important, especially for the structure in the ecliptic. The complex field configuration near maximum does not correspond to a dipole rotating from north to south as the polar fields change as has been previously suggested. The large latitudinal extent of the current sheet over much of the cycle affects the propagation of cosmic rays. The coronal field does not fully participate in differential rotation, similar to coronal holes. Locations of coronal holes coincide with strong field regions on the source surface. Correlations exist between coronal and photospheric structures but work remains to be done in relating the coronal features to photospheric and deeper lying structures.



# Chapter 1 -- Introduction

The sun piques our interest and demands our attention. As an object it inspires wonder as it rises and sets each day; as a star it provides the touchstone for stellar models; as *our* star it determines the physical environment in which the Earth moves and gives us almost all of our energy, from heat and light to weather, fossil fuels, and food; and as a laboratory it provides insight into physical phenomena not observable on Earth. For each of these reasons the sun deserves our study.

As an astronomical object the sun is the only star which can be observed in detail. Determinations of solar parameters calibrate our observations of other stars. Surface features such as granulation and sunspots can only be resolved on the sun. In situ measurements of the solar wind provide the only direct samples of stellar material. Magnetic activity cycles, observed on the sun for hundreds of years, have recently been discovered on other stars, suggesting that the study of solar features may help in understanding other stars. The study of other stars with a variety of masses, rotation rates, luminosities, etc. can in turn shed light on our understanding of the sun. For example, the relationship of rotation rate and stellar activity cycles may teach us about the solar dynamo.

The densities, temperatures, and size scales which characterize the sun greatly exceed the conditions reproducible on Earth. The observations of convection, turbulence, magnetic field organization, dynamo processes, nuclear synthesis, etc. stimulate our understanding of not only the specific solar phenomena, but the general theory of the underlying physical processes as well.

The importance of the interaction of the sun with the terrestrial environment emphasizes the significance of understanding the solar wind, the solar magnetic field, solar activity, solar radiation, and their variations as well as their influence on the Earth. The solar wind continuously interacts with the Earth's magnetosphere. Variations in the wind's velocity and magnetic field cause such things as geomagnetic activity, aurorae, and a host of

other practical effects including the disruption of communications, interference with radar, and induction of large currents in arctic pipelines and powerlines. Even small long term changes in the total luminosity of the sun would have grave consequences for the terrestrial climate. The correlation of the Maunder minimum with the "Little Ice Age" in Europe and the discovery of the 22-year drought cycle in tree ring data suggest that solar activity may affect the climate.

Apart from the practical benefits of understanding our star, studying the sun is intrinsically an interesting pursuit. The challenge of discovering Sol's secrets through careful observations and thoughtful application of mathematical models and physical laws provides a strong motivation itself. Many of the most fundamental observations of solar physics are not thoroughly understood. The dearth of solar neutrinos calls into question the most basic stellar models. The cause of differential rotation and the origin of the solar activity cycle are only incompletely modeled. Even the origins of such basic solar features as sunspots, flares, coronal heating, and the interplanetary magnetic field (IMF) are not fully understood.

All this makes the field of solar physics very interesting. Measurements of solar oscillations are just beginning to probe the solar interior. New information about the depth of the convection zone and rotation with depth have already been provided and more interesting results are sure to follow. Progress is being made on each of the problems mentioned above. This study presents results which contribute to the understanding of the evolution of the solar and heliospheric magnetic fields through the solar cycle.

### *Background*

Unlike that of the Earth, the sun's magnetic field varies fairly regularly with a 22 year period. Approximately each 11 years the senses of the solar polar fields reverse. The current solar cycle began in 1976 at the most recent minimum in solar activity. At activity minimum few, if any, sunspots are observed. The rising phase of each cycle lasts three or four years.

During this interval sunspots begin to appear in bands at mid latitudes in each hemisphere. The level of activity rapidly increases and the activity bands gradually progress toward the solar equator as the cycle continues. Simultaneously the polar fields weaken near maximum and finally reverse some time after the maximum level of sunspot activity occurs. The latest maximum occurred near the beginning of 1980 and the polar fields measured at Stanford reversed about the same time. The declining phase of the cycle lasts somewhat longer. The bands of activity continue to migrate toward the equator as the strength and complexity of the photospheric fields gradually decrease. The new polar fields quickly strengthen after reversing. We are currently in the declining phase of Solar Cycle 21.

The photosphere is the source of the magnetic field in the corona. While the surface plasma has an energy density comparable to that of the magnetic field, the rapid decrease in density in the lower corona creates a situation where the magnetic field dominates the structure of the coronal plasma. Photographs of prominences show structures over the limb of the sun which demonstrate that the plasma conforms to the configuration of the magnetic field in the low corona. Between the photosphere and about 2.5 solar radii ( $2.5 R_{\odot}$ ) the field dominates the plasma. Above that height the energy density of the accelerating solar wind plasma again exceeds that of the field. Because the plasma accelerates in the radial direction, the field, now frozen into the plasma, also becomes radial and is carried out into the heliosphere by the solar wind.

This divides the heliospheric field into two parts, that with field directed toward the sun and that with field directed away from the sun. A current sheet separates these regions in interplanetary space. At 1 AU the current sheet is characterized by low solar wind speed, high density, and rapid change in magnetic field direction. The passage of sector boundaries can greatly affect the geomagnetic field.

Wilcox & Ness (1965) first described the organization of the IMF into polarity sectors. They found that the IMF pointed either toward or away from the sun along the Parker spiral angle, switching polarity every six to eight days. This divided the interplanetary medium during a solar rotation into four

sectors in the ecliptic plane. Years of subsequent observations have shown that the IMF in the ecliptic plane near the Earth at 1 AU most commonly exhibits four sectors and less frequently two sectors per rotation. Early attempts to explain this organization by directly mapping the solar wind back to the photospheric field were only successful when large areas of the visible disk were averaged or near minimum when the surface field configuration was extremely simple. Such methods gave little insight into the three dimensional structure of the IMF.

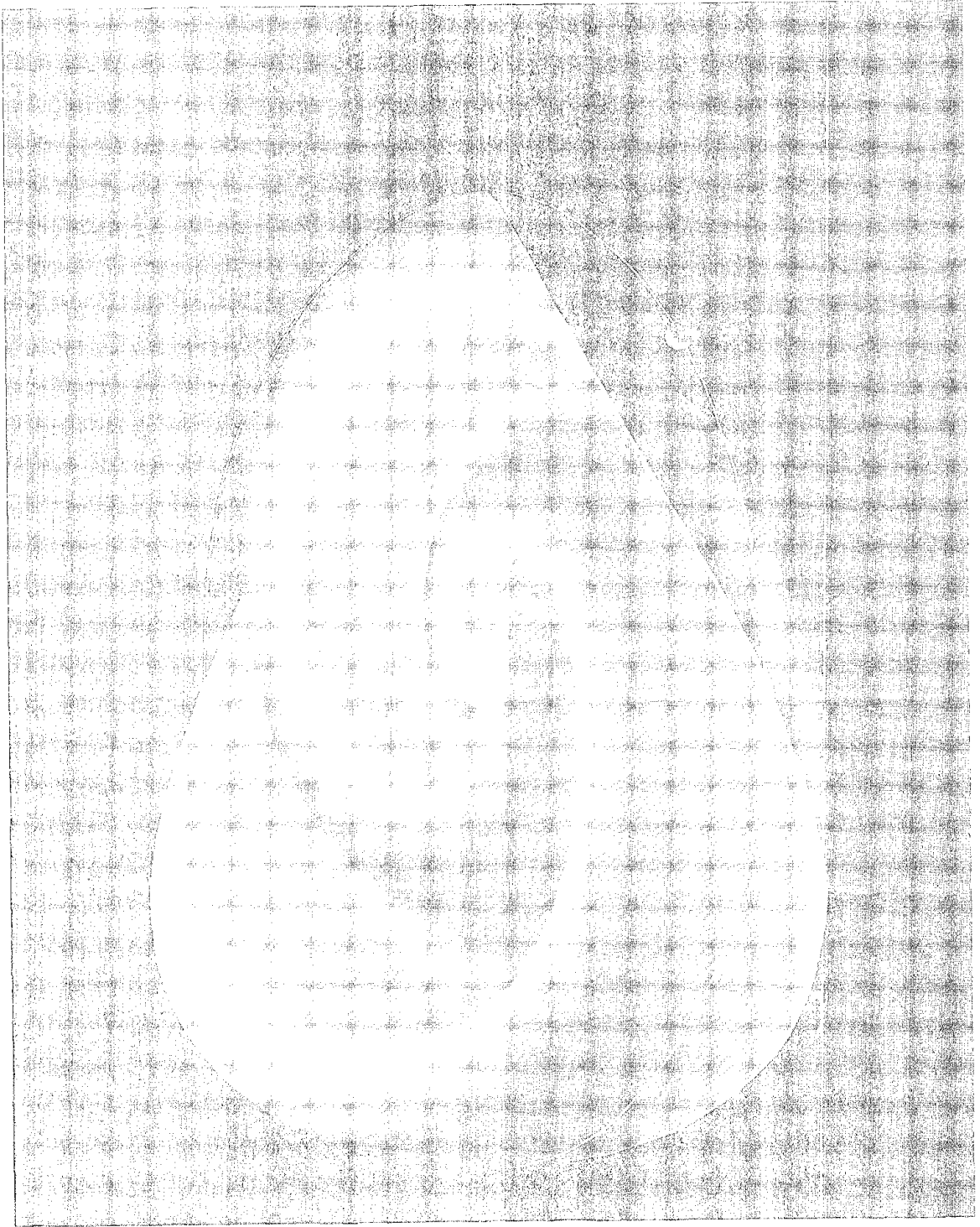
The three dimensional structure of the current sheet can be visualized with the aid of Figure 1-1. This highly idealized representation shows the configuration of the current sheet out to approximately the distance of Jupiter during an interval when four sectors would be observed in the ecliptic plane. The origin of the field pattern lies near the sun where the neutral line frequently resembles the seam on a baseball or tennis ball. This structure is then carried out by the solar wind to form the surface shown in the figure. Later observations have shown that the simpler structure near the sun is distorted beyond 1 AU by the formation of shocks due to dynamic effects in the solar wind. Nevertheless, this sketch gives a good qualitative picture of the organization of the heliospheric field out to at least 1 AU.

Schatten (1969) and Altschuler & Newkirk (1969) independently developed the potential field model to determine the configuration of the coronal and heliospheric field from the photospheric observations. This model assumes that the magnetic field near the sun can be described by a scalar potential field, i.e. that no currents flow near the sun (at least not enough to distort the field configuration). The field lines in eclipse photographs are observed to be almost completely radial above a few solar radii. To reproduce this observed distortion of the field by the plasma, a hypothetical surface is introduced at a height of 1.5 to 3 solar radii at which all the field lines are assumed to be radial. This can be accomplished by magnetic

---

Figure 1-1: Artist's impression of the heliospheric current sheet which separates regions of magnetic field directed away from the sun and toward the sun in interplanetary space. [Artist: Werner Heil]







field sources (currents) at or beyond the "source" surface.

Using measurements of the photospheric field and the radial boundary condition (i.e. equipotential) at the source surface, the field anywhere between the photosphere and the source surface can be computed. Assuming that the field configuration at the source surface is frozen into the plasma at the source surface, the solar wind carries that structure radially outward into the heliosphere. Like the seams of the baseball described above, the neutral line between inward and outward field at the source surface determines the shape of the heliospheric current sheet.

The results of such calculations using the measurements from the Stanford Solar Observatory from 1976 through 1983 are presented in this report.

### *Purpose*

As the photospheric field evolves during the solar cycle, so must the heliospheric field. This investigation seeks to determine the three dimensional structure of the heliospheric current sheet as it evolves during the solar cycle. This extends the analysis of the sector structure observed in the ecliptic plane to all heliographic latitudes. Using these results several interesting questions can be answered.

Does the structure of the IMF arise primarily in the photospheric field or is it primarily due to the dynamic effects in the solar wind on a very simple magnetic structure?

Just what is the structure of the current sheet during each phase of the solar cycle? How long do structures last? How complex is the structure in different parts of the cycle?

How does the field evolve from one configuration to another? Particularly interesting is the evolution of the polar field regions near maximum.

Can the heliospheric field be characterized as a tilted dipole as suggested by Hundhausen (1977) and others?

Can the evolution of the field be characterized as a slowly rotating dipole

as suggested by Saito et al. (1978)? I.e. does a dipole aligned along the solar rotation axis near solar minimum smoothly rotate to become an equatorial dipole near maximum and a rotation aligned dipole again (pointing the opposite direction) during the declining phase of the cycle?

How reliably can the IMF polarity at 1 AU be predicted using the potential field model through the cycle? Can other solar wind quantities, such as the solar wind velocity, be determined?

How do the locations of coronal holes relate to the field configuration at the source surface?

What is the relationship of the coronal and photospheric fields? Do both rotate differentially? Do large structures on the source surface correspond to large photospheric structures? Do interplanetary sectors arise in easily recognizable photospheric locations?

### *Methods*

To answer these questions, the potential field model has been used to calculate the configuration of the coronal field for the time period May 1976 through December 1983. Modifications have been made to the model to account for the incorrectly measured polar field which changes during the cycle, the zero offset error due to primarily to field evolution, and missing data.

The results have been compared with other methods for determining the location of the current sheet to determine the best source surface radius and to confirm the validity of the treatment of the polar field correction, the zero offset, and missing data. The measured IMF polarity provides the most complete and reliable basis for comparison. Unfortunately the Earth and most spacecraft sample only a limited range of latitudes within  $7.3^\circ$  of the solar equator. To augment the IMF data, coronameter data, interplanetary scintillation measurements, coronal hole locations, and cometary data have been used to confirm the existence of structures at higher latitudes during some parts of the solar cycle.

Finally, the magnitude of the multipole components of the field have been determined throughout the cycle and analyzed to determine the relative importance of the dipole, quadrupole, and higher order components in determining the heliospheric field structure.

### *Results*

The structure of the heliospheric field evolves smoothly during the cycle and large polarity regions have lifetimes as long as two years throughout the cycle. Near solar minimum, in 1976, the current sheet stays within about  $15^\circ$  of the equator, resembling a dipole field. Even near minimum there were four distinct warps of the current sheet, two north and two south of the equator, during each rotation. These produce a four sector structure at Earth. Soon after minimum the latitudinal extent of the current sheet began to increase. From 1978 through at least 1983 the latitudinal extent of the sheet was  $\geq 50^\circ$ .

Near solar maximum the structure was more complex, though evolutionary changes from one rotation to the next were quite small. Multiple current sheets were not uncommon during the period near maximum in 1979 - 1980. The structures during the beginning of the declining phase were very stable for long periods evolving slowly from a two sector structure during most of 1982 to a strong four sector structure during 1983.

During the entire interval the correlation of the observed IMF polarity and that predicted by the model was quite good. This suggests that throughout the cycle the photospheric field plays the dominant role in determining the large scale structure of the heliospheric field while the dynamics in the solar wind affect the detailed structure, at least within the Earth's orbit. Of course the field configuration and the solar wind conditions which cause dynamic changes in the solar wind as it propagates are not independent.

The slow evolution of the field configuration applies to the polar regions as well. The change in sign of the polar fields occurs as part of an ongoing,

ordered process. The analysis of the multipole components shows that it is incorrect to talk about a rotating dipole field. The quadrupole and higher order terms make a contribution to the total field comparable to that of the dipole near maximum. Even considering the dipole component alone suggests that the polar and equatorial dipoles are independent indicating that a rotating dipole is not the correct description.

There are occasions when a dipole or tilted dipole adequately describe the field, but these occasions occur during only a small fraction of the total interval investigated in this study. This is especially true when considering the field near the ecliptic. Even near minimum when the dipole component was by far the largest one, the Earth observed a four sector structure.

There is a relation between the solar wind velocity and the magnetic field strength at the source surface. During periods of high activity the relationship is difficult to discern. The clearest relationship holds for the correlation of minimum solar wind velocity with sector boundaries (when the field strength is a minimum). The relationship of high field and coronal holes (and therefore high solar wind speed) is not as clear. The prediction of the solar wind parameters other than polarity from calculations of the field configuration requires more work.

Except for coronal holes the relationships between photospheric features, the source surface field, and the IMF are difficult to determine. Without tracing field lines from the source surface to the photosphere it is impossible to find the source regions of the interplanetary field. Correlations between interplanetary sectors and organization of the photospheric fields exist, but there is no one-to-one correspondence. The coronal field does not even rotate at the same rate as the surface field as shown by the lack of differential rotation at the source surface. This is a puzzle that remains to be solved.

Many puzzles in fact remain to be solved, but their enumeration will be postponed until the final chapter. Now let us proceed to detailed descriptions of the data, the model, and the analysis.

## Chapter 2 -- Data Collection and Analysis

### *The Instrument*

The Stanford Solar Observatory was built in the early 1970's by John M. Wilcox and Philip H. Scherrer with support from the Office of Naval Research, the National Science Foundation, and the Fleischmann Foundation. Originally designed to measure the mean magnetic field of the sun as a star, the observatory was soon modified to make low resolution maps of the solar magnetic field and to observe low amplitude, large scale velocity fields on the sun. Built on a beautiful site in the foothills above the Stanford University campus, the observatory and adjoining observer's quarters are shown in Figure 2-1.

A sketch of the telescope observing system is shown in Figure 2-2. The telescope consists of a coelostat-second flat mirror system which directs the sunlight into the aperture of the telescope. The coelostat is clock driven to follow the daily motion of the sun across the sky. A servo guiding system controls the second flat which actively corrects the pointing of the telescope. Light from the second flat falls on two 2-inch diameter lenses. One lens forms the guiding image and the other forms the observing image.

The observing beam passes through a KDP circular analyzer, through a 100Å band pass filter, and into the spectrograph through the entrance slit. At the bottom of the pit, 75 feet down, a Littrow lens focuses the beam on the grating which forms a spectrum and reflects the light back up the pit, out through the exit slits, and to the phototubes whose output is analyzed and recorded.

---

Figure 2-1: The Stanford Solar Observatory.

Figure 2-2: A schematic diagram of the Stanford solar telescope. Note the separate light path for the guiding image and the observing image. The spectrograph head is at ground level with the Littrow lens and diffraction grating at the bottom of a 23m pit.

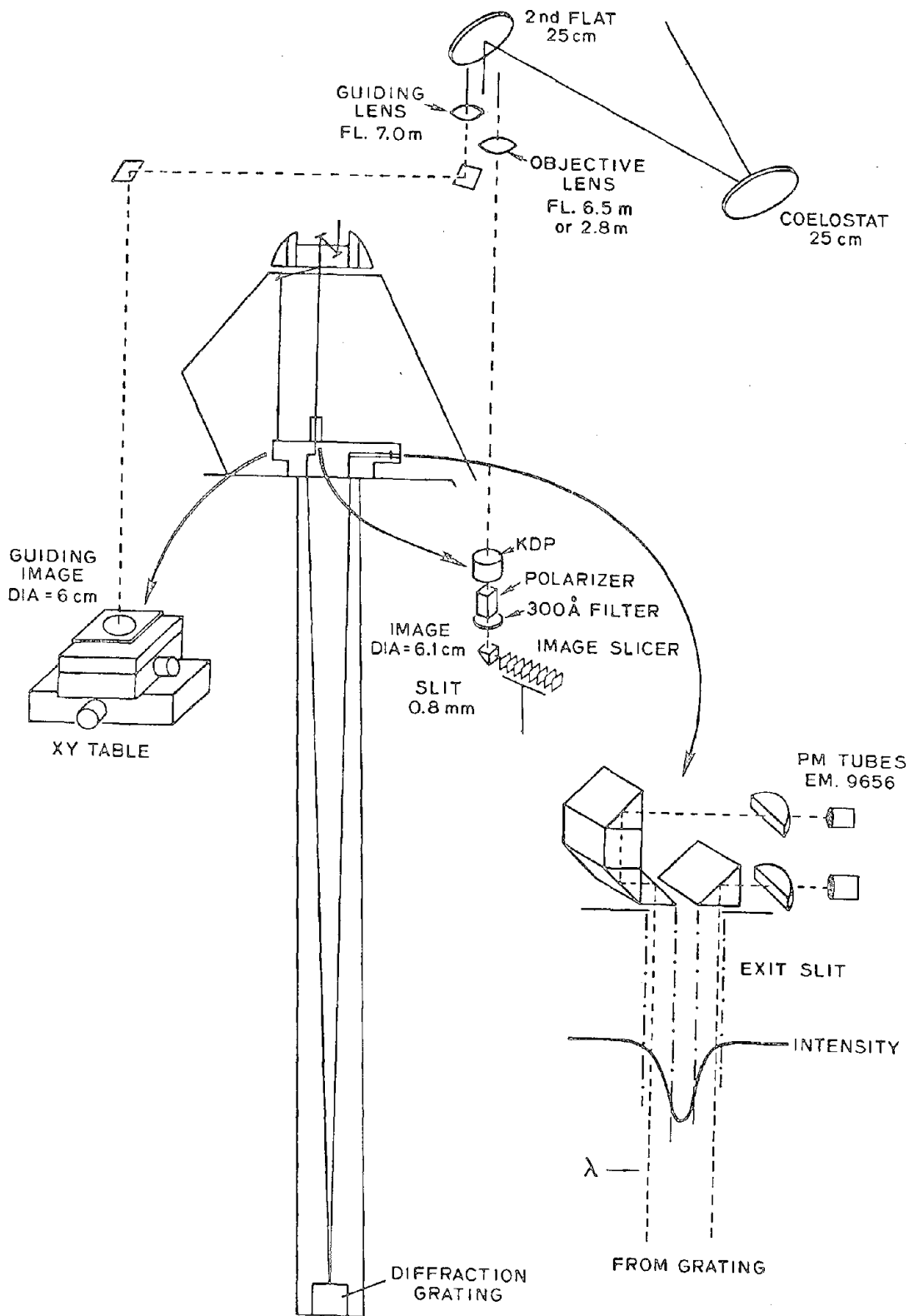
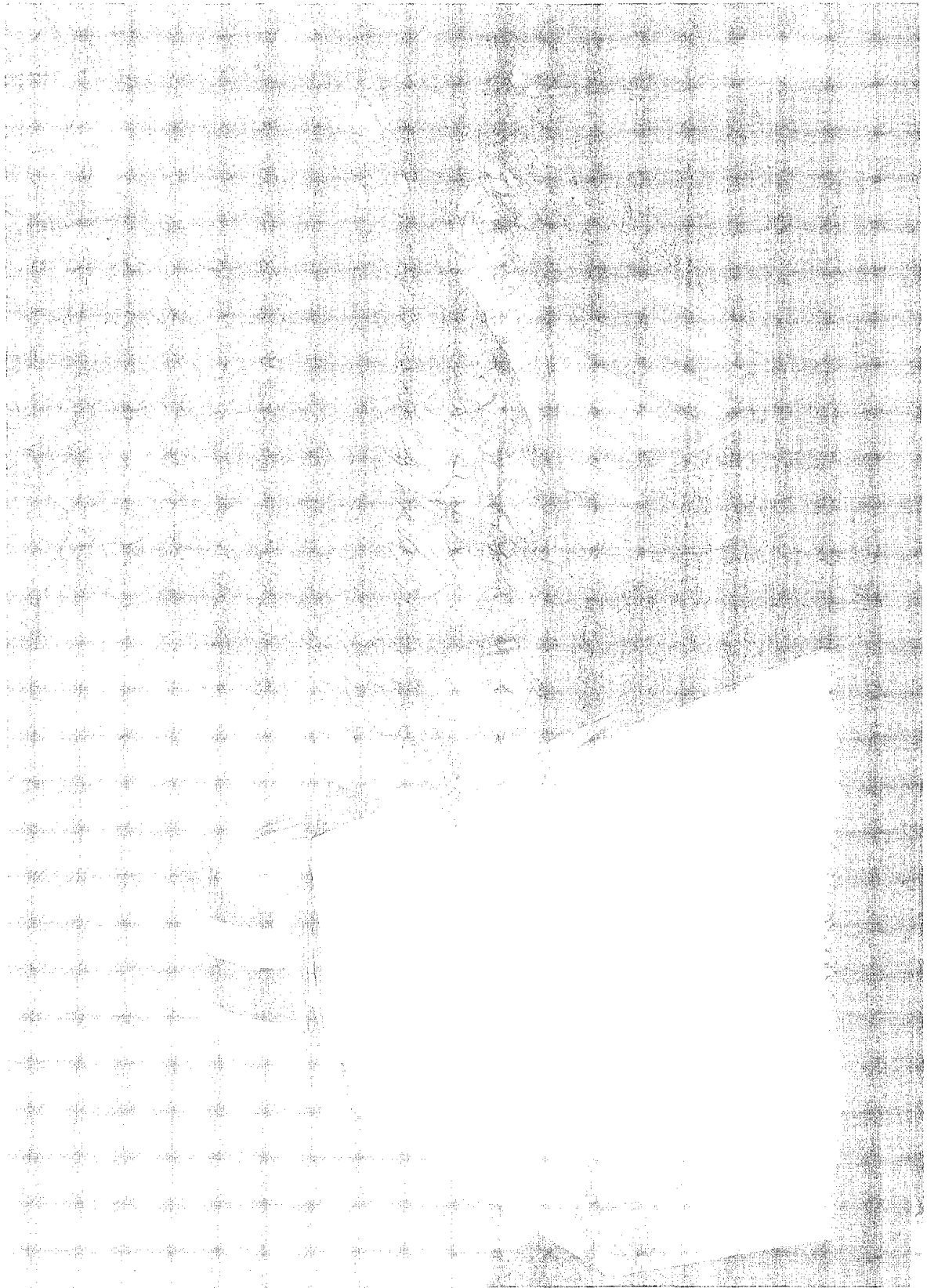
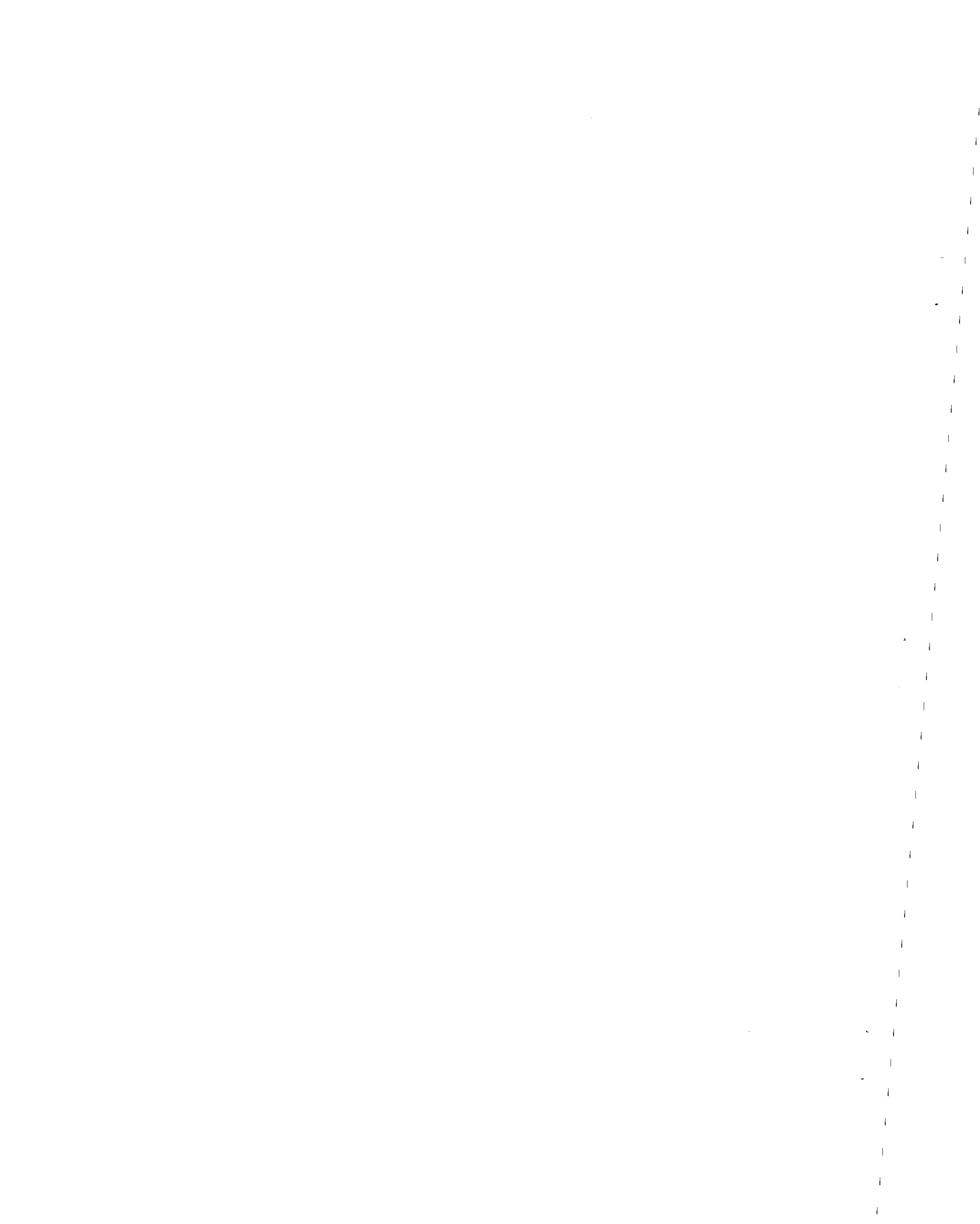


Figure 2-2







The guiding image falls on an array of 5 diodes which sense the center and limb intensities. The diodes drive the servo guiding system by balancing the light intensities at the limb. The array is mounted on a moveable stage which can be driven by two stepper motors. The computer controls the stepper motors and can position the stage to within 0.001 inches corresponding to about 1 arc second. The servo system tips the second flat to compensate for apparent motion of the sun and for the movement of the scanning table; this changes the position of both the observing and guiding images simultaneously.

A PDP 11/10 computer controlled the operation of the telescope until the fall of 1983 when a PDP 11/24 computer replaced it. With the exception of the coarse positioning of the mirrors, changing lenses, and certain calibration adjustments, the computer executes the entire observing program: everything from positioning the dome to finding the spectral lines and recording the data. A more detailed description of the magnetogram procedure can be found in the following section.

The Babcock magnetograph operates by precisely measuring the light intensities in the wings of a spectral line. By passing the entering beam through a modulated circular analyzer and synchronously detecting the final signals one can distinguish extremely small differences in the wavelengths of split spectral line components having different circular polarizations. In the case of velocity measurements polarizing filters placed in the solar image allow comparison of the velocity from one part of the sun with another, providing a differential measurement with precision on the order of 10 cm/sec.

The Zeeman splitting in certain spectral lines caused by the sun's magnetic field also has components with different polarizations. When viewed parallel to the magnetic field, the spectral line is split into two components of opposite circular polarization. The magnitude and direction of the splitting is proportional to that of the magnetic field. When the magnetic field is transverse to the line-of-sight the spectral line is split into three components which are linearly polarized, the central component along the magnetic field and the other two components perpendicular to it. Since the magnetograph is sensitive only to circularly polarized light, only the line-of-sight component

of the magnetic field can be measured. It can be measured to an accuracy of about 0.05 Gauss.

The following paragraphs describe in more detail the function of each element of the telescope and the way in which the signals are analyzed. When a large voltage is applied to the KDP crystal, it acts like a quarter wave plate, advancing or retarding the phase of one linear component of the incident beam relative to the other, depending on the sign of the voltage. This converts right circular polarization (RCP) into one linear polarization and LCP into the other. When coupled to a linear polarizer, switching the voltage polarity rapidly allows first one and then the other circular polarization to pass through to the spectrograph. Linear polarizations pass through at reduced intensities which are independent of the voltage.

Since the grating operates in the fifth order green spectrum for enhanced dispersion, a narrow band pass filter is needed to eliminate photons of wavelengths which would otherwise overlap from other orders in the spectrum. The light then passes through the image slicer which spreads the light over the 100mm by 0.8 mm entrance slit and down into the 22.8 meter spectrograph pit. The Littrow lens collimates the light for the 633 line/mm grating and focuses the spectrum on the exit slit. The computer controls the angle of the grating.

The dispersion of the spectrograph at the exit plane is approximately 13mm/Å. The exit slit consists of two 75 mA prism assemblies separated by 18 mA. The spacing and width of the slits are such that the intensity in the wings of the 5250Å line depends linearly on position. The average intensity measured in the line wings drives a servo system which keeps the line centered. The exit slit can be positioned with an accuracy of 0.6 microns by means of a long worm gear controlled and measured by the computer. Thus the resolution of the slit position corresponds to about 0.046 mA. Converting to doppler velocity in the 5250Å line this gives  $\frac{\Delta\lambda}{\lambda} \times c \approx 2.63$  m/sec (or, for comparison, converting to magnetic field using the 5250Å calibration  $3.86 \times 10^{-5}$  A/gauss this corresponds to about 1.19 Gauss.) In this manner the velocity can be measured while the magnetic field is measured as described below.

The magnetic line splitting can be more accurately measured by analyzing the line profiles of the two circularly polarized components. The intensity signals are detected synchronously with the KDP modulation by two matched phototubes giving the signals in each wing of the line for each circular polarization; red wing RCP,  $R_+$ ; blue wing RCP,  $B_+$ ; red wing LCP,  $R_-$ ; and blue wing LCP,  $B_-$ . The average intensity is  $(R_+ + R_- + B_+ + B_-)/4$ . The servo signal,  $(R_+ - B_+) + (R_- - B_-)$ , depends on the average position of the line and is used to keep the line centered. The difference in the line positions is the magnetic signal and is determined from  $(R_+ - B_+) - (R_- - B_-)$ .

The precision of the magnetic field measurement determined in this way is approximately 5 microtesla (0.002 mA) for a several second integration. Note that the equivalent line width is about 62 mA so the resolution is about  $3 \times 10^{-5}$  the line width. When the differential velocity measurements of solar oscillations are made in the same manner, the precision is about 10 cm/sec. The accuracy of the simultaneous velocity measurement depends on the integration time and on systematic errors. Since the noise is gaussian the precision is greater than the 2.6 m/sec of a single 0.1 second measurement.

A detailed description of the observatory, the hardware, and how it works can be found in Scherrer et al. (1977), Dittmer (1977), and Duvall (1977).

High resolution measurements of the solar magnetic fields and comparison of field strengths measured in spectral lines with different magnetic sensitivities indicate that most, if not all, of the photospheric field is concentrated into sub-arcsecond bundles of 1 - 2 kilogauss field rather than a large-scale weak magnetic field (Howard & Stenflo, 1972; Frazier & Stenflo, 1972, Harvey et al., 1972; Stenflo 1973). In a large aperture most of the area will contribute nothing to the magnetic signal and there will be many bundles of each polarity which will cancel. The remaining flux will essentially be averaged over the entire aperture and produce the measured fraction of circular polarization in the line wings interpreted as the large-scale magnetic field. Measurements in a single line cannot distinguish small scale strong fields from large scale weak fields.

The 5250Å line splitting due to kilogauss fields is of the order of the

separation of the exit slits. A detailed analysis by Stenflo (1973) and by Svalgaard et al. (1978) showed that there would be saturation of the magnetic field strength measured by the magnetograph and that for field element strengths of order 1.5 kG the saturation would lead to a measured field of 0.83 kG, smaller by a factor of 1.8. Since this saturation applies to all fields, since all fields occur in these high strength bundles, a correction factor of 1.8 must be made when comparing 5250 $\lambda$  magnetograph measurements with those made in other ways. Comparing field measurements made in two spectral lines with different magnetic sensitivities (Lande  $g$ -factors) would show different saturations and allow determination of the field strength in the bundles. Since such observations exist, this would be an interesting topic for further study.

Even a small distance above the photosphere the field is no longer concentrated into small bundles of radial field. It has spread into a more uniform distribution. This is supported by the change in fields strength across the disk of various features measured using spectral lines which form at different heights. As shown by Svalgaard et al. (1978), lines formed low in the photosphere, like 5250 $\lambda$ , show a cosine dependance in the line-of-sight field strength with distance from the center of the disk. However, lines formed higher in the photosphere, like 5233 $\lambda$ , show a more complex structure (Howard & Stenflo, 1972). If this occurs because the field lines are no longer radial but are rapidly diverging, the field probably does more closely resemble a large scale weak field above the chromosphere.

### *Data collection*

The global fields of the sun change slowly in time. In order to investigate the long term changes in the global solar field a long series of comparable measurements must be taken. Since the sun rotates at 13°/day measurements must be taken almost daily to insure coverage of the entire surface. Such synoptic observations began at the Stanford Solar Observatory in May 1976. Since that time magnetograms have been obtained each day, weather and equipment permitting.

Making a magnetogram consists of a set up procedure, calibration, three measurement sequences, calibration, and shutdown. During the set up procedure the observer inserts the 'image' lens which forms an image at the entrance slit, and the '3 minute' aperture which limits the light entering the spectrograph to a region 175 arc seconds square. The computer then determines the position of the sun by locating the four limbs and measures the scattered light off each limb. The observer enters the serial number, the weather quality, and the sine of the p-angle (the angle between north on the sun and north in the sky) and focuses the spectrograph by moving the Littrow lens in the pit.

Several calibrations are performed to check the equipment and to determine long term drifts. To check the phototubes and electronics, the observer balances the outputs of the phototubes in continuum light (which exposes each tube to the same intensity) and sets the outputs to zero when the tubes are darkened. The polarization modulation of the KDP analyzer is checked by measuring the contrast ratio when only one polarization is allowed to enter the crystal. Before and after the observations begin the "magnetic" signal in the magnetically insensitive  $5124\lambda$  line is measured for three minutes to determine the drift in the magnetic signal.

The computer then finds the  $5250\lambda$  line by rotating the grating to a predetermined angle and scanning the exit slits along the spectrum to search for the appropriate pattern of lines. The grating settles non-linearly for up to half an hour after moving it, producing a drift of about 0.1 mm in slit position and, therefore, of several hundred meters per second in the velocity signal. Fortunately the  $5247\lambda$  line is sufficiently close to  $5250\lambda$  that the exit slit can move to  $5247\lambda$  without repositioning the grating. So, while the grating settles, the magnetic field within 0.7 solar radii of the center is measured in the auxiliary  $5247\lambda$  line. Since the magnetic measurements do not depend on the absolute position of the line, the  $5247\lambda$  field can be compared to the  $5250\lambda$  field giving information on the field strength of the magnetic elements since the Lande g factor for  $5250\lambda$  is 3 and for  $5247\lambda$  is 2.

Moving boustrophedonically, the scan begins in a random "corner" of the disk and moves east-west on the sun. The scanning grid consists of 11 scans

lines in the north-south direction on the sun and 21 east-west positions at the equator for the full disk. Thus the image moves approximately  $1/2$  aperture east-west between each measurement and scan lines are spaced one full aperture north-south. At each position the computer records 12 parameters identifying the data, and giving the line position, time, magnetic signal, intensity, grid coordinates, scanning table coordinates, and integration time. At each grid point the image comes to rest before the (usually) 15-second integration begins.

Upon completing the auxiliary line scan, a five minute measurement of the  $5250\text{\AA}$  quantities is taken at disk center before beginning the main scan. The  $5250\text{\AA}$  magnetogram proceeds in the same way as the previous scan, but covers the entire disk, and takes about one hour. After the main scan, the telescope measures the velocity and the magnetic field along the central meridian from south to north to south. Finally, another 5-minute measurement is made at the center of the disk to fix the velocity drift for the scan and another 3 minute measurement of the magnetic zero error is made in the  $5124\text{\AA}$  line. The program also rechecks the scanning table position. The observer then refocuses the Littrow lens and removes the 3' aperture. When weather or time of day constrains the observing time, a time critical scan can be made which eliminates the  $5247\text{\AA}$  auxiliary scan.

### *Data reduction*

Substantial data reduction must be accomplished before the data recorded at the telescope is in a useful form. There are currently four levels of magnetogram reduction and a log. Level 0 contains for each magnetogram the raw data with no corrections; it is essentially a copy of the raw telescope data in a form compatible with the dataset handling programs used in the rest of the system. Level 1 holds the calibrated magnetic, velocity, and intensity data, and the position of each observed gridpoint with the drifts removed and with the heliographic positions calculated. The data in these two levels is stored in an individual file for each magnetogram. The Level 3 reduction interpolates the magnetic field data from Level 1 for each



magnetogram onto a Carrington coordinate grid. This data is then assembled into the synoptic charts published in Solar-Geophysical Data and used in the computation of the potential field model. These reductions will be described in more detail below.

The velocity data, analyzed in terms of differential rotation parameters, is stored in Level 2 along with the average intensity and magnetic field data for the central portion of the disk. The residual velocity determined by removing the standard differential rotation computed in Level 2 is stored in Level 4 both in the observed grid and in a Carrington grid. Information about each magnetogram, such as the scattered light, drifts, coelostat position, sky conditions, etc. are stored in the log. Level 0 and 1 reductions are also carried out for the auxiliary line magnetograms and for the north-south scans.

The Level 0 and 1 reductions have been described in some detail by Duvall (1977) and Scherrer et al. (1980). To summarize, the Level 0 reduction creates for each magnetogram a file containing the time of observation, grid position, scanning table location, magnetic signal, velocity signal, and intensity for each point measured at the observatory. Furthermore general information such as the observer, sky condition, etc. is stored in the log file. Essentially no processing of data is done so that there are no model dependances and there are as few chances as possible for errors in the reduction; the data is simply transferred from the telescope format to a standard format.

For each datapoint the Level 1 reduction program converts the measurements to standard units, removes the effects of the Earth's motion, removes instrumental drifts, calculates the effective position of the aperture, and corrects for limb darkening. Calculation of the effective position depends on the precise time, aperture size, and a model of limb darkening and is discussed fully in Scherrer et al. (1980). The effective position accurately reflects the intensity weighted average disk position of the aperture. The position in arc seconds and radians from the center of the disk are recorded.

Figure 2-3 shows the Level 1 results for typical observation, Magnetogram 938 taken June 30, 1979. The upper disk is a contour map of the photospheric magnetic field. Solid lines represent positive fields and negative fields are dashed; the first solid contour is the neutral line. It is easy to see the large scale organization of the magnetic field a little before solar maximum. The polar fields cover only a small area and are weakening. The mid-latitude fields are quite strong and show a variety of levels of activity. The plot at the lower left shows the velocity. The equatorial velocity is just over 2000 m/sec. A close examination shows the effect of differential rotation (the contours become more widely spaced away from the equator) and a red shift near the limbs. The intensity, shown at the lower right, has been corrected for limb darkening and shows a uniform intensity over the center of the disk. The lower intensity near the limbs is due to the aperture being partly off the disk.

The observer inspects such a plot for each magnetogram. If anything unusual appears in the data, the observer sets one or more of 14 trouble flags characterizing the nature of the anomaly. The computer also sets trouble bits if standard calibrations stray too far from the norm. Typical problems include clouds, loss of spectral line, and guiding errors. The intensity measurement is the most sensitive to clouds, the magnetic signal to loss of spectral line, and the velocity to guiding errors and turbulence in the pit. Each of the reduction levels above Level 1 tests the trouble bits to determine whether the data from a given scan should be used. Magnetic field data is not used if the relevant trouble bits are set. The observer may also change the assigned weather quality which affects the importance of the scan in constructing the synoptic chart as described below.

The third level of reduction determines from the time of observation and

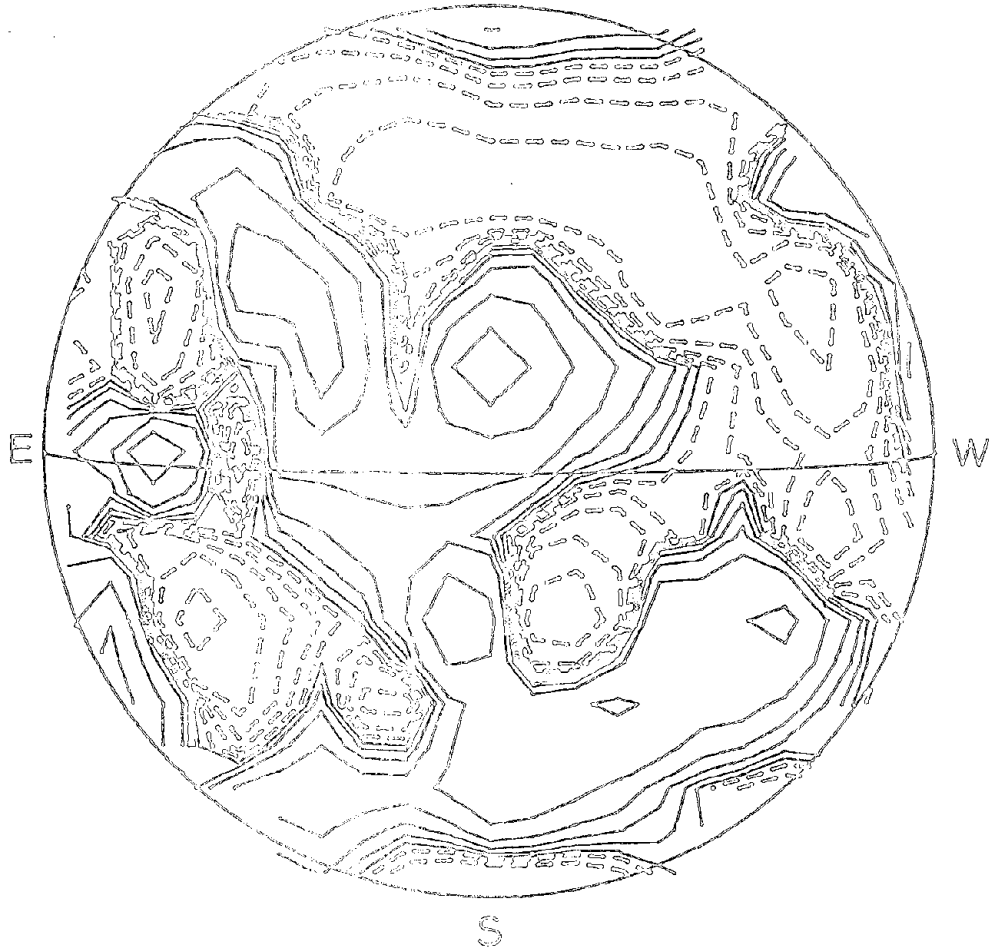
---

Figure 2-3: A typical solar magnetogram observed June 30, 1979. The top figure shows the line-of-sight magnetic field. Negative contours are dashed. The lower left figure shows the doppler measurements of velocity; negative velocities (toward the observer) are dashed. The observed intensity, corrected for limb darkening, is shown at the lower right. Intensity contours occur when the aperture is off the limb or because of clouds. The contours are at intervals of 0.1 relative intensity.

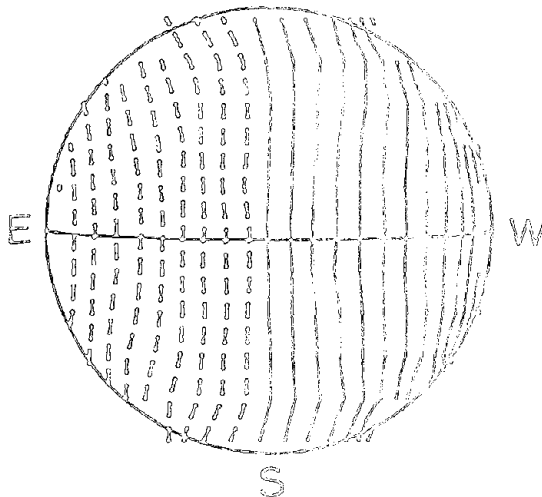
Figure 2-3

STANFORD MAGNETOGRAM # 938 30 JUNE 1979  
17:22 UT

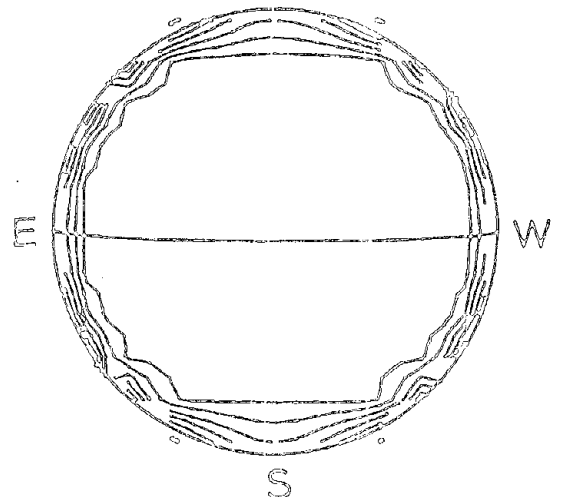
$B(\mu T)$  N 0,  $\pm 20, 50, 100 \dots$



$V(m/s)$  N 0,  $\pm 200 \dots$



I N



effective disk position computed in Level 1, the Carrington latitude and longitude of each point. A quadratic fitting routine uses these data to interpolate the field onto a regular Carrington grid. The grid is centered on the even  $5^\circ$  longitude strip nearest central meridian and extends  $55^\circ$  east and west. In the north-south direction the field is determined at 30 points evenly spaced in sine latitude (this corresponds to even steps on the disk.) The maps are stored in a list indexed by serial number and identified by the central meridian longitude of the map.

To form the synoptic charts, data for each Carrington longitude and latitude must be assembled from the various maps. Since the maps are  $115^\circ$  wide and typically separated by a minimum of  $13^\circ$ , there are usually several measurements for each point on the sun. The measurements for each longitude are averaged with the relative weight of each measurement depending on the scattered light, assigned sky quality, and central meridian distance according to the following relation:

$$Weight = ((1 + CMdist)^2 \times (1 + scattlight) \times (1 + sky))^{-1}$$

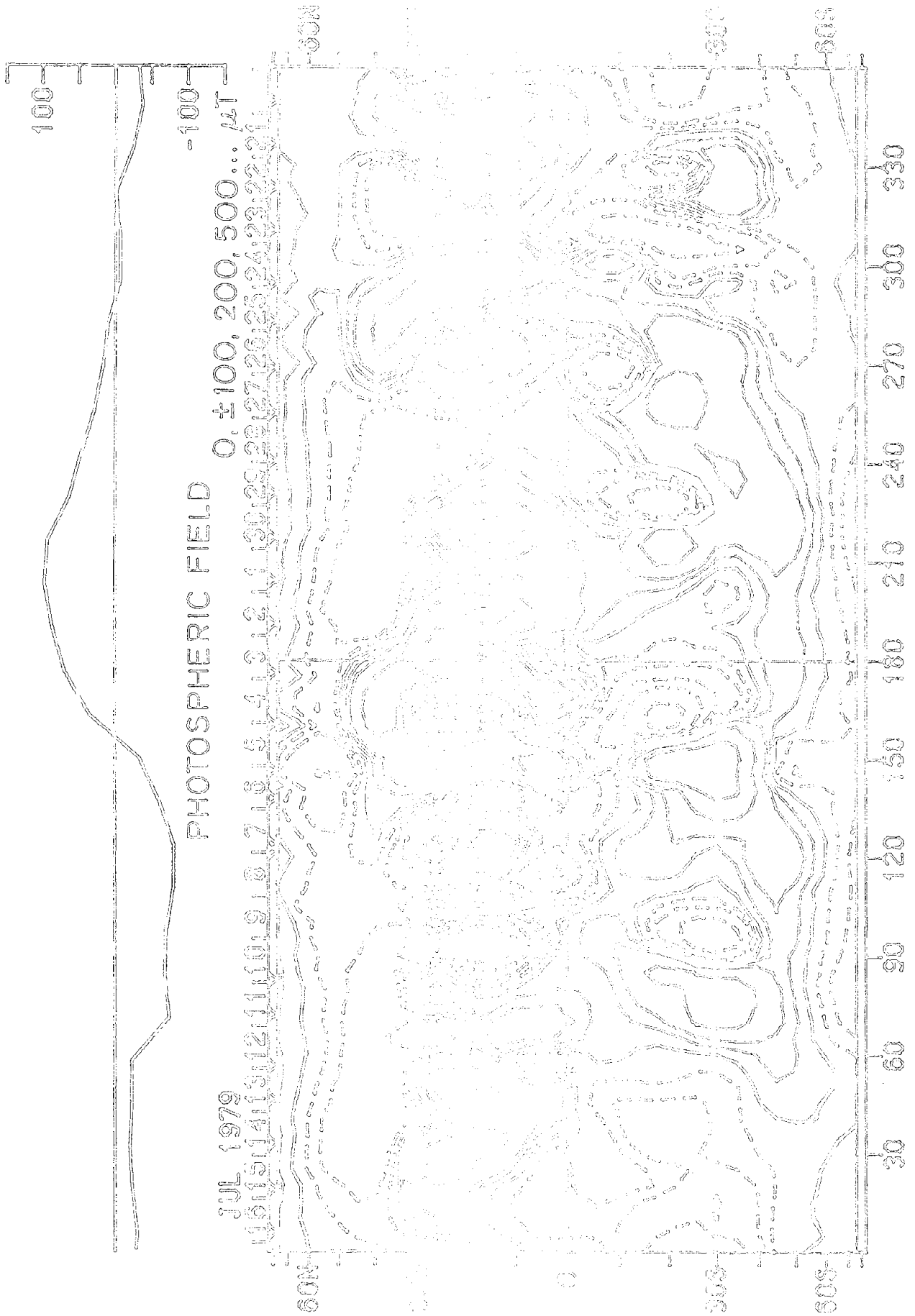
where the central meridian distance is given in units of  $5^\circ$ , the scattered light as a percent, and the sky on a scale from 0 to 5. Four to six measurements typically contribute to a given point, but the measurements taken near central meridian have by far the highest weight. To date, no projection corrections have been made to the measurements for central meridian distance.

The synoptic chart shown in Figure 2-4 is a contour map of the magnetic field over the entire surface of the sun. The data is shown in an equal area projection (equal steps in sine latitude) for easy comparison with the

---

Figure 2-4: The observed line-of-sight magnetic field at the photosphere for Carrington Rotation 1683. The upper curve shows the mean solar magnetic field. The synoptic chart is plotted in sine latitude for easy comparison with Figure 2-3. Contours are at 0,  $\pm 100$ , 200, 500, ...  $\mu T$ . The dates correspond to central meridian passage. Inverted carets show the dates of magnetograms contributing to the chart.

# STANFORD MEAN FIELD



CR 1683

Figure 2-4

magnetograms. The size of the aperture limits the resolution near the poles, so there is nothing plotted above  $75^\circ$ . The bottom axis shows the longitude within Carrington Rotation 1683, while the top axis is labelled by date. The mean magnetic field of the sun, also measured at Stanford, is displayed at the top of the figure.

The small 'V' marks along the  $75^\circ$ N line show the times of magnetograms which contribute to the synoptic chart. Data from Magnetogram 938 is centered near  $210^\circ$  longitude and contributes to the synoptic chart in the range from  $265^\circ$  to  $155^\circ$ . Comparing Figure 2-3 with this region of the synoptic chart, one can see that near  $210^\circ$  they are almost identical, while farther from central meridian the differences are greater.

### *Coverage*

In order to provide as complete a record as possible, magnetograms should be taken each day that the weather is good enough. Because measurements as far as  $55^\circ$  from central meridian can be used in making up the synoptic chart, a gap of almost  $110^\circ$  can be tolerated without creating an interval of missing data. Since the sun rotates at about  $13^\circ$  per day, this corresponds to a maximum observing gap of approximately 8 days. Fortunately the weather at the observing site is such that during most years there are typically only a few relatively small gaps in the synoptic charts.

The magnetic fields low in the photosphere where the  $5250\lambda$  line is formed are almost radial (Svalgaard et al. 1978). Since the magnetograph observes only the line-of-sight component of the magnetic field, fields measured away from the center of the solar disk will be diminished because of the projection into the line-of-sight. This means that field measurements near the limb will not be as accurate. The north-south projection is unavoidable and the potential field model program compensates for it. However, the measurements which comprise the synoptic chart are not corrected for the various central meridian distances at which they are observed. This affects the data most severely near gaps where the only available data is measured

far from central meridian. At large distance from disk center errors due to decreased resolution and field evolution are also important.

For this reason the observing program at the Stanford Solar Observatory places a high priority on obtaining daily magnetograms. Each day's observations begin with one or two measurements of the mean magnetic field of the sun which take approximately one hour. Under good weather conditions, this is followed by a magnetogram which takes about 2.5 hours. If the weather is questionable a time critical magnetogram which takes approximately 1.5 hours can be done. The observing program then continues with doppler observations or more mean field measurements. Because of the morning fog in the summer in the San Francisco Bay area, there are typically only a handful of intervals of about five days duration during the summer when consecutive sunrise to sunset doppler observations are possible. During these intervals the priority of magnetogram observations is lower, though gaps of no more than five to six days between observations is allowed.

This is perhaps a good time to recognize and thank the observers who, over the years, have done an excellent job of operating the observatory and keeping it running. Through their efforts we have been able to compile the excellent string of data analyzed in this paper. The observers have been: Eric Gustavson, 1976-77, Steve Bryan, 1977-78; Todd Hoeksema, 1978-79, 1981-83; Phil Duffy, 1979-80; John Foster, 1980-81; and Harald Henning, 1983-84.

In the 2740 days from May 16, 1976 to November 15, 1983, there have been 2049 magnetograms of which 1806 on 1727 days have been used in constructing the synoptic charts. There are magnetograms on 63% of the days.

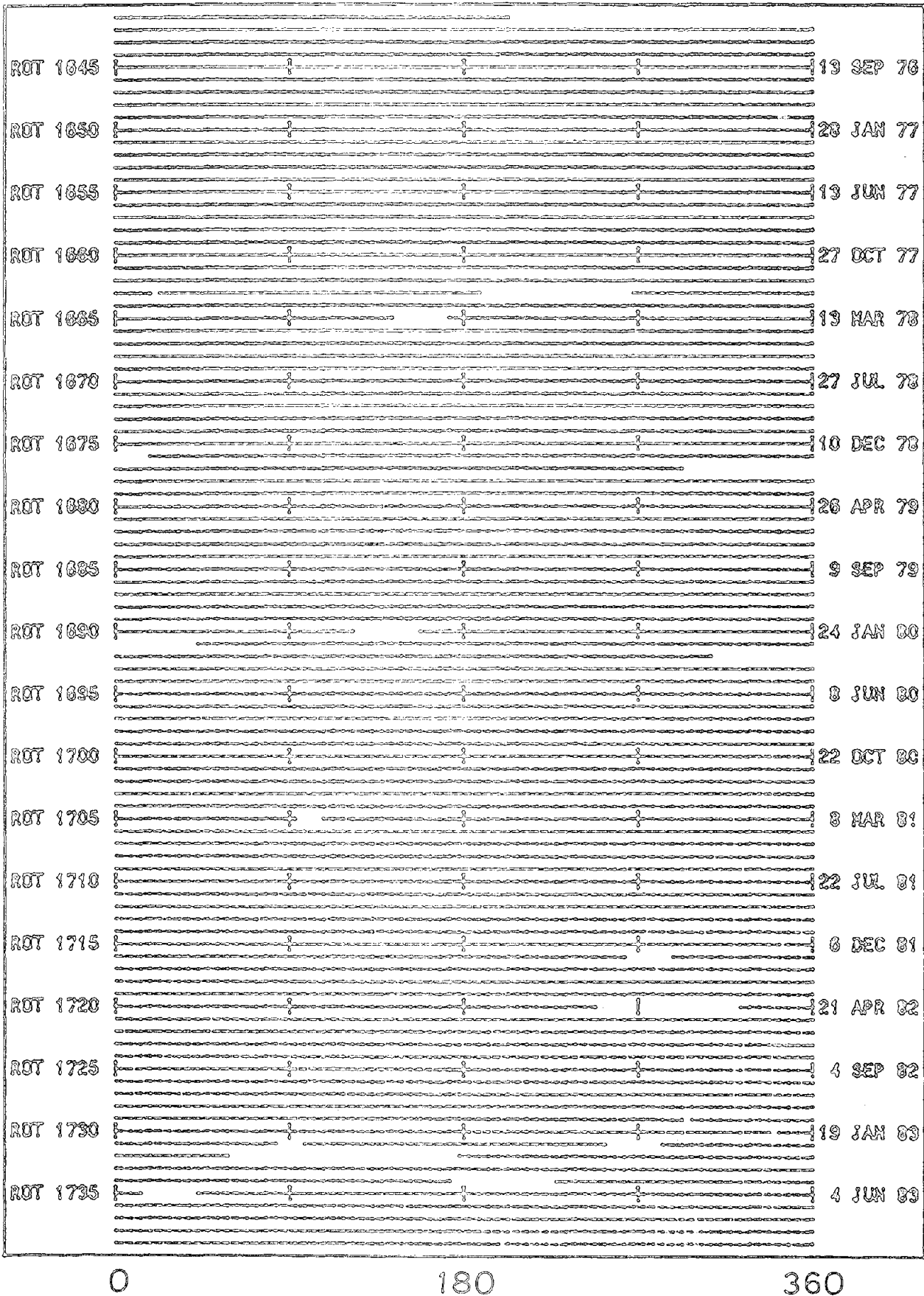
Figure 2-5 shows the synoptic chart data coverage since May of 1976 when the first magnetogram was taken at the Stanford Solar Observatory. Each line represents one Carrington Rotation. Caps in the bars represent gaps in the data. Most of the gaps occur during the winter months. The good

---

Figure 2-5: Each line represents the data coverage for one Carrington Rotation. A solid line is plotted wherever synoptic chart data is available. Gaps occur when there was missing data because of weather or equipment problems.

Figure 2-5

# DATA CONTINUITY





coverage in the first two years reflects the drought conditions experienced during 1976 and 1977. The number of gaps in the last two years are indicative of the wet winters experienced in northern California which were attributed to El Nino. Very few gaps are due to equipment or procedural failures.

One of the steps in the potential field model requires decomposing the surface fields into its multipole components using the orthogonality of the Legendre polynomials. The coefficients can be determined accurately only when the field is known over the entire surface of the sun. Most data gaps are too wide to allow a simple interpolation to fill in the data gaps in such a way as to provide a reasonable approximation to the actual field values. Since most changes in the photospheric fields from one rotation to the next are relatively minor, missing data has been replaced by the average of the field measured one rotation earlier and one rotation later at the same Carrington latitude and longitude. This has the advantage of retaining the same general characteristics as the actual field.

Of course no method accurately reconstructs the actual data. This method is susceptible to errors due to evolution of the magnetic structures and to differential rotation. The multipole components most seriously affected by missing data will be those with the same spatial structure as the data gap. As will be discussed in more detail in following chapters, the components with the largest spatial scales have the greatest influence on the computed structure of the heliospheric field structure. Since the photospheric magnetic features of corresponding size evolve relatively slowly, the above method of filling in the gaps will provide for an accurate determination of the lower order multipole coefficients.

## Chapter 3 -- The Potential Field Model

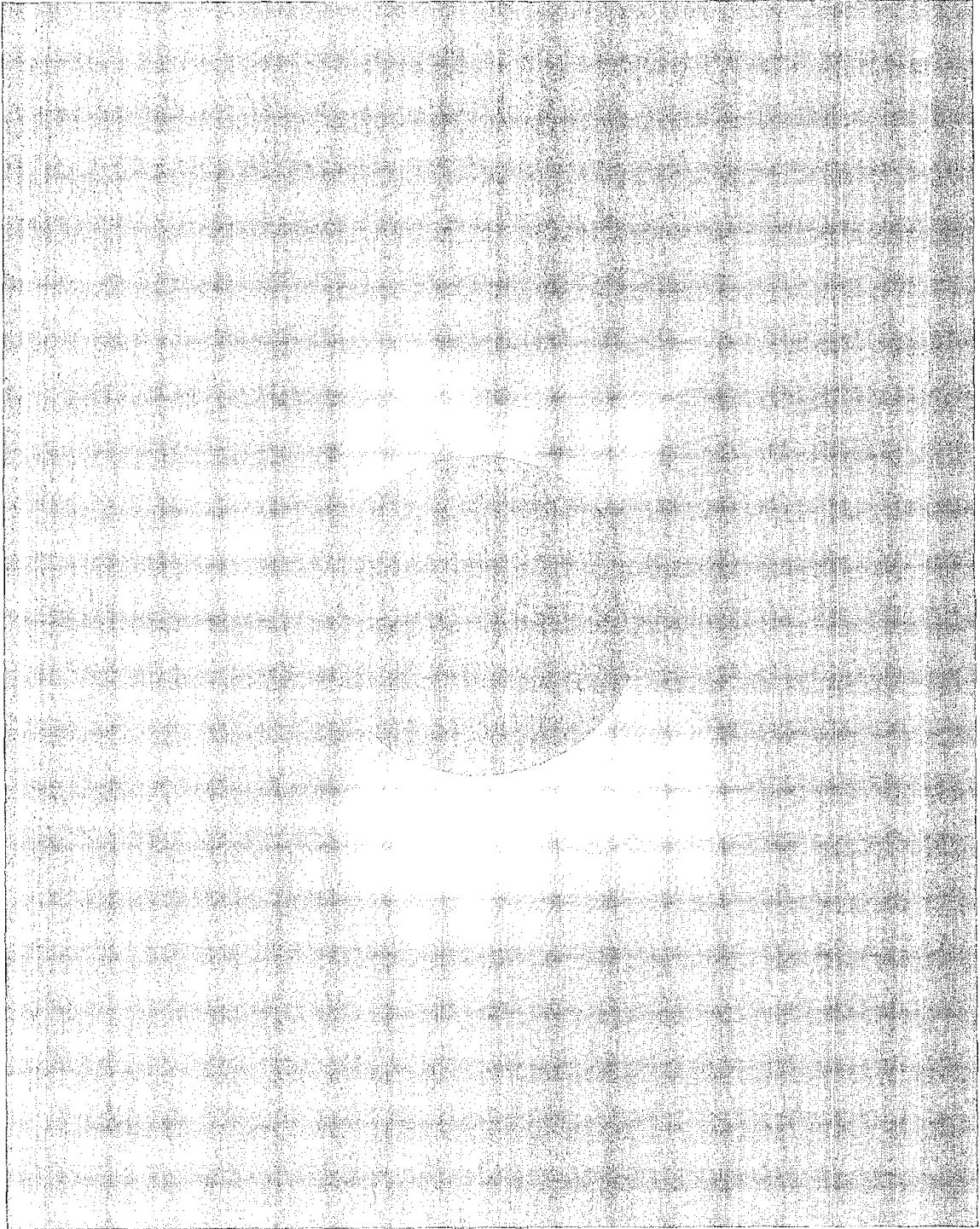
The field structure at the photosphere varies greatly through the solar cycle both in complexity and strength (Howard & Labonte, 1981). The interplanetary field, on the other hand, shows much smaller changes in field strength (Slavin & Smith, 1983) and the structure in the ecliptic remains rather simple throughout the cycle (Svalgaard & Wilcox, 1975). Near minimum the photospheric field has few active regions and the northern and southern hemispheres have large scale weak magnetic fields of opposite polarity. The polarity of the interplanetary field seen at Earth is typically divided into four or two sectors per solar rotation.

During the rising phase of the cycle the photosphere becomes more and more active with sunspot groups developing at relatively high latitudes, near  $40^\circ$ , just after minimum. Active regions occur closer to the equator as the cycle progresses. The total photospheric flux increases by a factor of three from minimum to maximum (Howard & Labonte, 1981). Near Earth the field in the solar wind shows much smaller variation in strength, less than 20% during the last solar cycle and no more than 40% during the current cycle (Slavin & Smith, 1983). The polarity structure at Earth continues to show simple two or four sector patterns through maximum and the declining phase of the cycle. During the previous declining phase in the early 1970's, the photosphere was divided into a few large unipolar field regions which developed into low latitude coronal holes and sometimes connected to the polar coronal holes. These immense regions dominated the structure of the solar wind during the Skylab period in 1973 and 1974 (Hundhausen, 1977.)

Clearly the lower corona acts much like a coarse filter within which most of the field lines close and through which only the largest scale magnetic

---

Figure 3-1: The total solar eclipse of 31 July, 1981 photographed at Tarma, Siberia. The instrument developed by G. Newkirk, Jr. photographs the corona in red light through a radially graded filter that suppresses the bright inner corona to show the much fainter streamers of the outer corona in the same photograph. (Courtesy: High Altitude Observatory).





structures pass. This chapter describes the potential field model with which the magnetic structure above the photosphere can be calculated using the measurements of the surface field and some simple assumptions about the field in the lower corona.

Photographs of the corona taken during eclipses, such as Figure 3-1, show the density of coronal material. These structures trace out the pattern of the magnetic field. Closed field regions and regions of low field strength or field reversal have the highest density. This photograph was taken with a filter having a large radial density gradient. Taken after maximum at the eclipse in Russia on July 31, 1981, the polar field strength is growing and there is little structure right over the poles. Many structures extend to fairly high latitudes including several helmet streamers over large closed field regions. Near the sun the structures seem to be confined by the magnetic field, but at higher altitudes the structures become primarily radial. Near minimum most of the coronal structure occurs nearer the equator and the low density polar caps are much larger. Through the entire cycle most of the structure is largely radial above a couple of solar radii.

Schatten et al. (1969) and Altschuler & Newkirk (1969) independently introduced the concept of a potential field model with a spherical source surface surrounding and concentric with the Sun. Schatten et al. (1969) compared the energy densities of the total magnetic field and the transverse magnetic field, the thermal energy of the plasma, and the flow energy of the plasma near the sun. They found that below about 2 solar radii,  $2 R_{\odot}$ , the transverse magnetic energy dominates both the thermal and bulk flow energy of the plasma. At  $2 R_{\odot}$  the thermal energy is comparable to the transverse magnetic energy, but the total magnetic energy is larger still. Beyond that point the relative energy in the plasma grows until at  $20 R_{\odot}$  the flow energy of the plasma dominates completely. This suggests that below about  $2 R_{\odot}$  the magnetic field can be successfully approximated by a potential field, since it dominates the motion of the plasma.

Figure 3-2 shows a diagram of the fields near the sun from Schatten (1971a). Most of the field lines above active regions close. Above large unipolar regions the field tends to diverge and becomes open to the heliosphere.

Between opposite polarity regions a neutral line develops. The energy density of the plasma in the low corona is very low compared with the transverse magnetic field energy density, therefore the magnetic field will determine the motion of the plasma and therefore the structure of the corona. Above a certain height coronal structures seem to proceed radially from the sun. If the plasma accelerates throughout the low corona and the field strength gradually declines with height above the photosphere, at some point the plasma energy density begins to dominate. At this radius the field lines will be stretched by the plasma radially outward.

For convenience we choose a sphere of radius  $R_s$  at which the field becomes purely radial. This surface is called the source surface. Assuming that the currents carried by the plasma are relatively small in the region between the source surface and the photosphere, the field can be described purely in terms of a scalar potential. Using the boundary conditions of radial field at the source surface and the measured photospheric field the magnetic field in the region can be calculated. The mathematical details of the solution will be developed later in this chapter.

The structures in Figure 3-2 which are like those computed with the potential field model clearly resemble those shown in Figure 3-1 from an eclipse. Many authors have compared the results of the model to individual eclipse photographs, e.g. Schatten (1968 a, b, 1969), Stelzried et al., (1970), Smith & Schatten (1970) and found that there is generally a fairly good agreement between structures predicted by the model and the structures observed in the corona, though certain systematic discrepancies do exist.

Several criteria were used to set the radius of the source surface. Schatten (1969) used the field strength at the source surface extrapolated to 1 AU, the average size of magnetic polarity sectors predicted by the model, observations of the highest closed magnetic structures seen in eclipse

---

Figure 3-2: Schematic representation of the potential field model. Photospheric fields are measured at the Stanford Solar Observatory. Beneath the source surface the field is calculated using a potential field model. The radial field at the source surface is carried outward by the solar wind where it can be measured by spacecraft. (Schatten, 1971a).

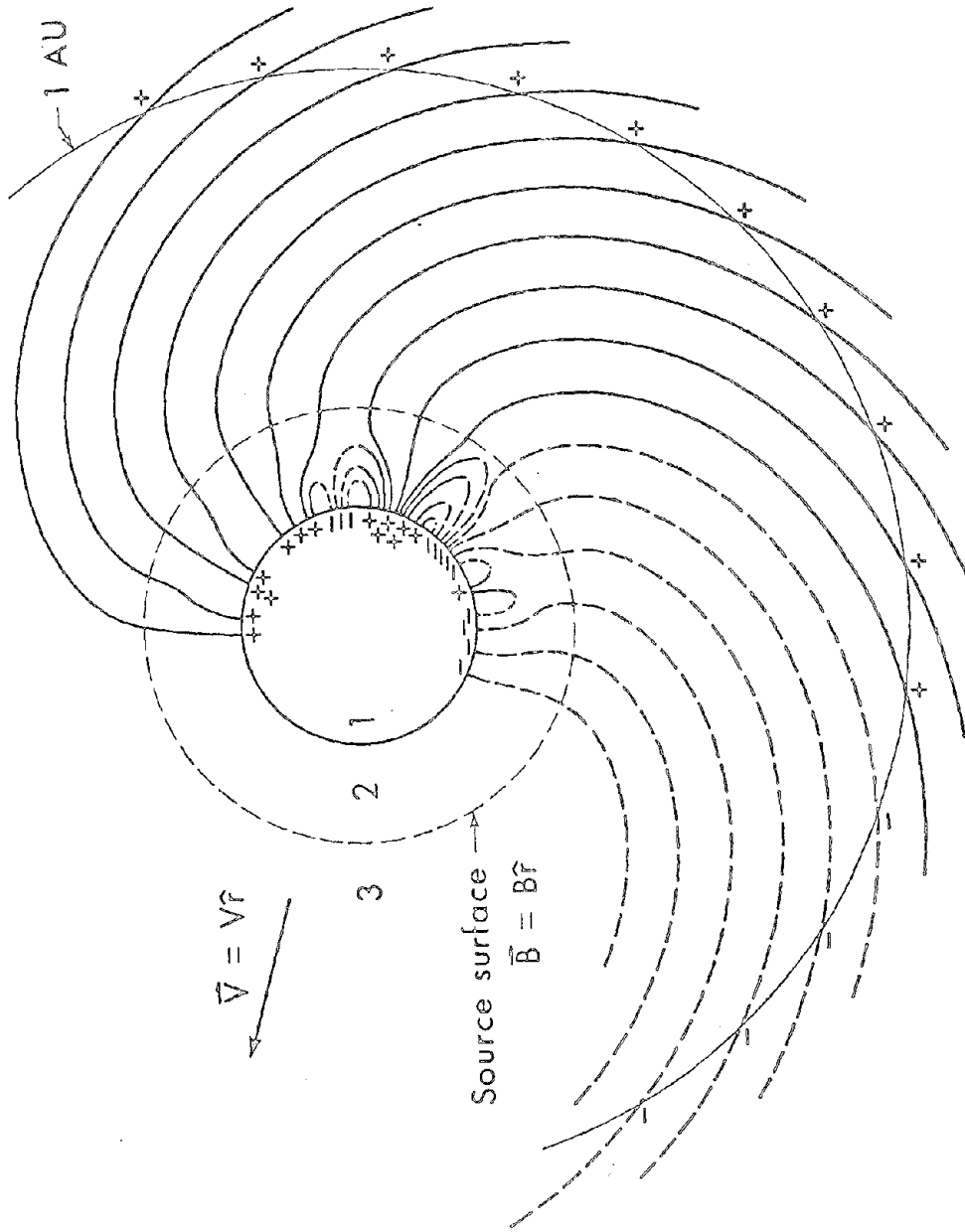


Figure 3-2

photographs, and the magnitude of the variation in the radial magnetic field magnitude to place the source surface at  $1.6 R_{\odot}$ . Altschuler & Newkirk (1969) considered the shape of the computed structures over active regions compared with eclipse photographs to place the source surface radius at  $2.5 R_{\odot}$ .

In 1973 Newkirk et al. published their first microfilm atlas of the coronal magnetic field and the spherical harmonic coefficients computed with the Mt. Wilson data which eventually spanned the interval 1959 - 1974. In their report the fields were computed each half Carrington Rotation and the harmonic expansion extended to order nine. Recently Marubashi & Watanabe (1983) have republished this data in a technical report including the source surface magnetic fields, the footpoints of open field lines, and a map of the field line divergence for each half rotation for the interval 1959 - 1974. Inspection of those maps often reveals large changes in zero level, total flux, and general configuration of the field from one half rotation to the next. The results presented in the later chapters of this report show only small changes from rotation to rotation in any of the above quantities and many of the corrections described below were not made in those calculations.

Adams & Pneuman (1976) used Mt. Wilson data and a different mathematical method from Altschuler et al. (1977) who used Kitt Peak data, but both extended the potential field computation to very high spatial resolution. At the height of the source surface these methods showed little difference from earlier, coarser computations. At lower altitudes the use of higher resolution magnetograph data to include more of the flux and the increased resolution of the computations themselves gave a much better agreement with the observed extent of the sources of open field regions. This also made it easier to study the detailed field in small regions of the sun. Because of the resolution of the Stanford magnetograph and the focus of our interest on the large scale field at and beyond the source surface, we have not increased the resolution of these calculations past order nine. Svalgaard & Wilcox (1978) and Riesebieter & Neubauer (1979) developed the method used in this study to determine the field in terms of the harmonic coefficients of the associated Legendre polynomials. This document contains the first detailed description of the Stanford work in this area.



### *Assumptions, Advantages, and Disadvantages*

As suggested by the foregoing discussion, the potential field model has both advantages and disadvantages. The advantages are that it is simple to understand, it is simple and practical to compute, and it is apparently quite successful. Its disadvantages are that it is insensitive to rapid evolution, it assumes a potential field near the sun, it coarsely approximates the effects of the plasma on the field, it uses a spherical source surface, and it accounts for no changes outside the source surface. Several modifications of the model have been made to improve the accuracy and to minimize these disadvantages while retaining the advantages. In this section the model assumptions will be critically examined. The advantages, disadvantages and possible improvements of the model will be discussed with respect to the problems I wish to address in this document, viz., the large scale heliospheric field and its evolution over the solar cycle.

The primary assumptions of the model are that 1) the field can be approximated by a potential field, 2) the field at the photosphere is known, and 3) an equipotential source surface exists at some location and has a spherical shape. This last condition implies that at the source surface all field lines are open and extend radially out into the heliosphere.

Whether the field can be adequately approximated by a potential field has been investigated by several authors. Levine & Altschuler (1974) computed the field configuration using the potential field approximation and then included a) curl free electric currents and b) force-free currents. They found that unless the currents contributed a large fraction of the total field in the corona, the field configuration did not change. This means that the potential field approximation *works* on the large scale whether there are currents or not. This also means that the success of the potential field model says little about the presence of currents in the corona.

Poletto et al. (1975) studied the smaller scale of active regions. They found that the potential field calculated from magnetograms was consistent with the field orientations observed with images of X-ray active regions. It seems that this approximation succeeds even when large currents would not

be unexpected.

The method of determining the photospheric field was discussed in Chapter 2. There are many uncertainties in the measurement of the field by magnetographs and its interpretation. Major uncertainties arise because of the measurement of only the line-of-sight component of the magnetic field, projection effects, magnetograph saturation because of the concentration of the field into 2 kG bundles in the photosphere, correlation of magnetic field and brightness variations, and line weakening in field regions. Several studies (Stenflo, 1971; Howard 1977; Suess et al. 1977; Pneumann et al. 1978; Svalgaard et al. 1978) indicate that the polar fields are much stronger than that measured by the magnetographs. Other uncertainties arise because of the evolution of the field during the time of observation of the whole solar surface and the mapping of the field onto a coordinate system which does not differentially rotate. Missing data further complicates the situation.

In evaluating the dependance of the potential field model on these uncertainties, it is found that most of the effects can be understood or compensated for. By using central meridian measurements the effects of projection in the east-west direction are minimized. Line-of-sight projection in the north-south direction is explicitly assumed in the model calculations. Investigation of the variation of the field strength across the solar disk shows that the field is radial in the level of the photosphere where the 5250Å measurements are taken. Large strong field regions are often dark, thus the flux from such regions will be underestimated. Magnetograph saturation and line weakening affect all of the field measurements in the same way when the field is concentrated into high strength bundles, requiring an increase of all the field measurements by a factor of 1.8. This changes the overall level of field strength, but not the configuration.

The additional polar field can be added to the data when the potential field calculation takes place. The procedure for determining this is outlined in Chapter 4. The effects of evolution and differential rotation can be minimized by using the results of the potential field model only near the center of a data window; in this way all the nearby measurements were recorded at about the same time. This minimizes the effects of differential rotation

mapping as well. Clearly missing data cannot be replaced, but by carefully filling in with other related data the effects of missing data can be minimized. These corrections are described later in this chapter.

Transient events may rearrange the coronal fields but most have only a temporary effect on the large scale field. It must be realized that these measurements do not provide a complete description of the heliospheric magnetic field, but only the background onto which perturbations due to active events are superimposed. Our level of confidence in the photospheric data is quite high. Furthermore any other method which relies on the same or similar data shares the same sorts of problems.

The postulation of a simple source surface is probably the weakest assumption in the model. If there is a potential field, there must be a surface of constant potential, but that surface is probably quite complex. At the source surface it is assumed that the field becomes radial because the plasma begins to influence the shape of the magnetic field and draw it in the radial direction. Clearly this violates the assumption of a purely potential field configuration since the distortion must begin below the source surface.

A second problem arises in the location of the source surface at a constant radius over the surface and in time. A spherical source surface is clearly a simplifying assumption for convenience of computation. Since the field strength and solar wind speed vary with location and time, the source surface can not be a simple sphere. This simplification contributes to two consistent failings of the potential field model: 1) the magnetic field magnitude predicted at 1 AU is smaller by about a factor of five than the measured field, even after correcting for magnetograph saturation; and 2) often structures beyond the source surface radius are observed to have a non-radial component.

A third deficiency occurs because the model does not address what happens above the source surface. The simplest assumption is that no more evolution takes place and that the magnetic field at the source surface is simply convected radially outward into the heliosphere by the solar wind with few changes in structure and configuration. Eclipse photographs and spacecraft coronagraphs show that while this is a reasonable generalization, there are

many cases where it is not true. During most of the solar cycle the structures over the polar coronal holes bend toward the equator. Many eclipse photographs show non-radial streamers to at least  $10 R_0$ .

These problems have been addressed in part by Schulz et al. (1978) and Levine et al. (1982) who introduced a non-spherical source surface into the computation. Instead they used a surface of constant magnetic field strength to which the magnetic field must be perpendicular. Their results showed that the detailed agreement with the location of open field regions, such as coronal holes improved. They also found that the magnitude of the field at 1 AU is larger, and that non-radial structures appeared in the appropriate places. Comparison with MHD calculations for simple field configurations (Pneuman & Kopp, 1971) also improved. While prediction of the detailed structure of the corona improved, the large scale structure did not change greatly. In a later study of the photospheric sources of open magnetic field regions, Levine (1982) used a spherical source surface to investigate the sources of open field regions even after having developed the non-spherical source surface. For some investigations the non-spherical source surface is clearly necessary and desirable, but for studying the large scale field and the current sheet in the interplanetary medium a spherical source surface seems sufficient.

The minimum magnitude of the field on the source surface occurs at the current sheet and increases smoothly away from the sheet to some maximum. At Earth the interplanetary field shows a maximum field strength near the sector boundary and a minimum in field strength near the center of large sectors. During most of the sector the field strength remains relatively constant.

These facts suggest that substantial changes occur in the field configuration outside the source surface and that all the field lines are not radial at a spherical source surface. Suess et al. (1977) simulated the north polar coronal hole of the 1973 Skylab era as studied by Munro & Jackson (1977). They found that at the base of the coronal hole at  $2 R_0$ , a substantial gradient in the magnetic field would exist, but that by  $5 R_0$  the field strength would be uniform across the hole. Their results suggest that while the field

configuration does not change, the distribution of the field lines within a given polarity region may change substantially.

Relatively early Schatten (1971b) extended the model by considering the effects of current sheets above the source surface to include the effects of transverse pressure stresses. This provided for non-radial structures and for evolution of the field above the source surface. Agreement with the coronal structures observed during eclipses improved. For a simple dipole field configuration this also gave better agreement with an MHD calculation of the field (Pneuman & Kopp, 1971) than the potential field model alone.

Clearly for predicting the magnetic field strength at 1 AU or anywhere else the evolution of the field above the source surface must be considered. It would be interesting to investigate the field structure by modifying the method using the procedure of Schatten (1971b) or the non-spherical source surface (Schulz et al. 1978). Computing the full MHD solution would be even more desirable, but each of these improvements substantially increases the computation time, particularly the MHD calculations for realistic field configurations (if in fact it can be done at all). Since this study concerns the large scale configuration of the field which improves only slightly using these considerations, the simplest assumption of radial propagation of the source surface field will be used to compare with polarity measurements made at the Earth.

To summarize, some of the disadvantages of the model are clear. Rapid evolution of the field is not handled well by the model because the observations are taken for a given solar location are dispersed in time over nearly a month. Furthermore the resolution of the Stanford magnetograph is rather coarse and does not include all the fine scale field. Of course for calculation of the large-scale organization of the structure this is not important, but in studying the photospheric origin of open field regions and the field very near the photosphere, data with a higher resolution should be used.

The model as used does not accurately predict the strength of the radial magnetic field at 1 AU. Nor does it accurately predict the form of the variation of the field strength during magnetic sectors. As discussed above, the problem of the form of the variation of the field magnitude probably occurs

because changes in the field above the source surface have not been considered. The problem with the field magnitude may be improved by changing the shape of the source surface, but in general remains an unsolved problem.

The problems of the potential field assumption and the spherical source surface were discussed above. Each of these disadvantages is important and much can be learned from attempting to minimize the problems by modifying the assumptions and improving the calculations. However each of these problems affects the details of the field strength and makes small changes in the field configuration. In looking at the "big picture" of the general field configuration and its evolution over the solar cycle these problems are not critically important. For detailed calculations and predictions for the environment of the Earth improvements should be implemented, but to see the basic structure of the heliospheric field the simple method is well suited. It is likely that during periods of high activity when the model is most uncertain in predicting this background structure, the interplanetary medium is greatly affected by the occurrence of transient events such as flares and erupting filaments. Nevertheless, the IMF polarity predictions of the model seem to be just as good near maximum as near minimum so a great deal can be learned throughout the cycle.

The advantages of using this model are also clear. The mathematics are relatively simple and the assumptions are straightforward. The computational procedure is quite simple and will be outlined in the remainder of this chapter. The time required to compute the model is very small. Another advantage of the model is that it seems to work quite well. Comparisons of the results of the model with other observed data show remarkably good agreement considering the crude assumptions and simplicity of the method. These comparisons will be discussed in the following chapter. Using this method the structure of the heliospheric magnetic field can be determined at all heliographic latitudes independent of spacecraft measurements with little missing data. The evolution of large scale structures near the sun can be traced out into the heliosphere. We can also follow the evolution of these structures through the solar cycle and come to a better understanding of the general magnetic field of the sun. Discussion of these results will occupy the following chapters.

*Mathematical Development of the Potential Field Model*

We now turn to a more detailed description of the method of calculating the field using the potential approximation. As described in the preceding sections, the configuration of the large scale heliospheric magnetic field can be determined if the line-of-sight photospheric magnetic field is known and if it is assumed that 1) there are no currents in the region between the Sun's surface and a larger concentric sphere called the source surface and 2) that at the source surface the magnetic field is purely radial.

Under these assumptions  $\mathbb{B} = -\nabla\Psi$  where  $\Psi$  is the scalar potential between the photosphere and the source surface. The potential satisfies Laplace's equation,  $\nabla^2\Psi = 0$ . Solutions of Laplace's equation in spherical coordinates can be expressed in terms of the spherical harmonic functions.

The total potential arises from sources inside the inner sphere,  $\Psi_I$ , and from sources outside the source surface,  $\Psi_O$ .

$$\Psi = \Psi_I + \Psi_O$$

$$\Psi_I = \sum_{l=0}^{\infty} r^{-(l+1)} \sum_{m=-l}^l Y_{lm}(\vartheta, \varphi) A_{I_{lm}}$$

$$\Psi_O = \sum_{l=0}^{\infty} r^l \sum_{m=-l}^l Y_{lm}(\vartheta, \varphi) A_{O_{lm}}$$

Scaling  $r$  in terms of  $R_o$ , the radius of the sun, for  $\Psi_I$  and in terms of  $R_s$ , the radius of the source surface, for  $\Psi_O$  and writing  $Y_{lm}(\vartheta, \varphi) = P_l^m(\cos \vartheta) [a_{lm} \cos m \varphi + b_{lm} \sin m \varphi]$  it is found that

$$\Psi = R_o \sum_{lm} P_l^m(\cos \vartheta) \left[ g_{lm} \cos m \varphi \left[ \left( \frac{R_o}{r} \right)^{l+1} + \frac{R_s}{R_o} \left( \frac{r}{R_s} \right)^l \right] c_{lm} \right]$$

$$+ h_{lm} \sin m \varphi \left[ \left( \frac{R_o}{r} \right)^{l+1} + \frac{R_s}{R_o} \left( \frac{r}{R_s} \right)^l a_{lm} \right]$$

Assuming that at the source surface  $\mathbb{B}$  is radial, then  $B_\varphi \sim \frac{\partial \Psi}{\partial \varphi} = 0$  and  $B_\vartheta \sim \frac{\partial \Psi}{\partial \vartheta} = 0$ ; hence  $\Psi$  is constant on the surface  $r = R_s$ . Setting  $\Psi_{R_s} = 0$  we find

$$c_{lm} = a_{lm} = - \left( \frac{R_o}{R_s} \right)^{l+2} = c_l.$$

Since  $-\nabla \Psi = \mathbb{B}$  we can write: (Equation 3-1)

$$B_r = - \frac{\partial \Psi}{\partial r} = \sum_{lm} P_l^m(\cos \vartheta) (g_{lm} \cos m \varphi + h_{lm} \sin m \varphi) \left[ (l+1) \left( \frac{R_o}{r} \right)^{l+2} - l \left( \frac{r}{R_s} \right)^{l-1} c_l \right]$$

and (Equation 3-2)

$$B_\vartheta = - \frac{1}{r} \frac{\partial \Psi}{\partial \vartheta} = \sum_{lm} \left[ \left( \frac{R_o}{r} \right)^{l+2} + c_l \left( \frac{r}{R_s} \right)^{l+1} \right] (g_{lm} \cos m \varphi + h_{lm} \sin m \varphi) \frac{\partial P_l^m(\cos \vartheta)}{\partial \vartheta}$$

and (Equation 3-3)

$$B_\varphi = - \frac{1}{r \sin \vartheta} \frac{\partial \Psi}{\partial \varphi} = \sum_{lm} \left[ \left( \frac{R_o}{r} \right)^{l+2} + c_l \left( \frac{r}{R_s} \right)^{l-1} \right] m \cdot P_l^m(\cos \vartheta) \cdot (g_{lm} \sin m \varphi - h_{lm} \cos m \varphi).$$

The Stanford Solar Observatory measures the line-of-sight component of the photospheric field,  $B_{ls}(R_o, \vartheta, \varphi) = B_r \sin \vartheta + B_\vartheta \cos \varphi$  for fields near central meridian. Defining



$$F_{lm}(\varphi) = (g_{lm} \cos m\varphi + h_{lm} \sin m\varphi), \quad u_l = l+1+l \left( \frac{R_o}{R_s} \right)^{2l+1}, \quad \text{and} \quad v_l = 1 - \left( \frac{R_o}{R_s} \right)^{2l+1},$$

and doing some algebra with the above expressions for  $B_r$  and  $B_\vartheta$ , we can write

$$B_{ls} \sin \vartheta = \sum_{lm} F_{lm}(\vartheta) [u_l P_l^m(\cos \vartheta) - u_l \cos^2 \vartheta P_l^m(\cos \vartheta) - v_l \cos \vartheta \sin \vartheta \frac{\partial}{\partial \vartheta} P_l^m(\cos \vartheta)].$$

Using the recursion relations

$$\cos \vartheta P_l^m = \frac{1}{2l+1} \left\{ \left[ (l+1)^2 - m^2 \right]^{\frac{1}{2}} P_{l+1}^m + (l^2 - m^2)^{\frac{1}{2}} P_{l-1}^m \right\}$$

$$\sin \vartheta \frac{\partial P_l^m}{\partial \vartheta} = \frac{1}{2l+1} \left\{ l \left[ (l+1)^2 - m^2 \right]^{\frac{1}{2}} P_{l+1}^m - (l+1) (l^2 - m^2)^{\frac{1}{2}} P_{l-1}^m \right\}$$

and defining  $Q_l^m = \left[ l^2 - m^2 \right]^{\frac{1}{2}}$ , we can express the line-of-sight field as:

$$B_{ls} \sin \vartheta = \sum_{l=0}^{\infty} \sum_{m=-l}^l F_{lm}(\vartheta) \left\{ u_l P_l^m(\cos \vartheta) - \frac{Q_{l+1}^m}{2l+3} \left[ Q_{l+2}^m P_{l+2}^m(\cos \vartheta) + Q_{l+1}^m P_l^m(\cos \vartheta) \right] \right. \\ \left. - \frac{Q_l^m \left( \frac{R_o}{R_s} \right)^{2l+1}}{2l-1} \left[ Q_l^m P_l^m(\cos \vartheta) + Q_{l-1}^m P_{l-2}^m(\cos \vartheta) \right] \right\}$$

These sums can be reorganized by defining  $B^m$  such that  $B_{ls} \sin \vartheta = \sum_m B^m$  where

$$B^m = \sum_{l=m}^{\infty} F_{lm}(\vartheta) \left\{ \alpha_l^m P_l^m(\cos \vartheta) + \beta^m P_{l+2}^m(\cos \vartheta) + \gamma^m P_{l-2}^m(\cos \vartheta) \right\} \\ = \sum_{l=m}^{\infty} F_{lm}(\vartheta) \alpha_l^m P_l^m(\cos \vartheta) + \sum_{l=m+2}^{\infty} F_{l-2,m}(\vartheta) \beta_{l-2}^m P_{l-2}^m(\cos \vartheta)$$

$$+ \sum_{l=m-2}^{\infty} F_{l+2,m}(\varphi) \gamma_l^m P_l^m(\cos \vartheta)$$

where

$$\alpha_l^m = u_l - \frac{(Q_{l+1}^m)^2}{2l+3} - \frac{(Q_l^m)^2 (R_o / R_s)^{2l+1}}{2l-1}$$

$$\beta_l^m = \frac{Q_{l-1}^m Q_l^m}{2l-1} \quad \text{note } \beta_m^m = \beta_{m+1}^m \equiv 0$$

$$\gamma_l^m = \frac{Q_{l+1}^m Q_{l+2}^m \left( \frac{R_o}{R_s} \right)^{2l+5}}{2l+3} \quad \text{note } \gamma_{m-1}^m = \gamma_{m-2}^m \equiv 0$$

Taking advantage of cases where  $\beta$  and  $\gamma$  are 0 we can write:

$$B^m = \sum_{l=m}^{\infty} P_l^m(\cos \vartheta) \left\{ \alpha_l^m F_{lm}(\varphi) + \beta_l^m F_{l-2,m}(\varphi) + \gamma_l^m F_{l+2,m}(\varphi) \right\} \quad (3-4)$$

We can also independantly write an expression for the photospheric field in terms of the Legendre polynomials without referring to the potential solution developed above:

$$B_{ls} \sin \vartheta = \sum_{lm} P_l^m(\cos \vartheta) (a_{lm} \cos m \varphi + b_{lm} \sin m \varphi)$$

where the associated Legendre Polynomials are a complete, orthogonal basis set,

$$\int_0^{\pi} \int_0^{2\pi} \sin \vartheta \, d\vartheta \, P_l^m(\cos \vartheta) \frac{\cos m \varphi}{\sin m \varphi} P_{l'}^{m'}(\cos \vartheta) \frac{\cos m' \varphi}{\sin m' \varphi} = \frac{4\pi}{2l+1} \delta_{ll'} \delta_{mm'}$$

Therefore

$$\begin{pmatrix} a_{lm} \\ b_{lm} \end{pmatrix} = \frac{2l+1}{NM} \sum_{i=1}^N \sum_{j=1}^M B_{ls}(\psi_i, \varphi_j) \sin\psi_i P_l^m(\cos\psi) \frac{\cos^m \varphi_j}{\sin^m \varphi_j}$$

where the integrals over the sphere have been converted to sums over the N x M map grid which can be implemented on the computer.

These coefficients,  $a_{lm}$  and  $b_{lm}$  can be determined from the measured line-of-sight field. Equating the above expression with the earlier expression for the field in terms of the Legendre polynomials in Equation 3-4 a system of equations is found:

$$a_{lm} = \alpha_l^m g_l^m + \beta_l^m g_{l-2}^m + \gamma_l^m g_{l+2}^m$$

$$b_{lm} = \alpha_l^m h_l^m + \beta_l^m h_{l-2}^m + \gamma_l^m h_{l+2}^m$$

which can easily be solved for  $g_l^m$  and  $h_l^m$ . If the series is truncated at a maximum index, T, then

$$\bar{a}_m = \bar{K}^m \bar{g}^m$$

$$\bar{b}_m = \bar{K}^m \bar{h}^m$$

where

$$\bar{K} = \begin{pmatrix} \alpha_m^m & 0 & \gamma_m^m & \cdot & \cdot & \cdot \\ 0 & \alpha_{m+1}^m & 0 & \cdot & \cdot & \cdot \\ \beta_{m+2}^m & 0 & \alpha_{m+2}^m & \cdot & \cdot & \cdot \\ \cdot & \cdot & \cdot & \cdot & \cdot & \cdot \\ \cdot & \cdot & \cdot & \cdot & \gamma_{T-2}^m & \cdot \\ 0 & 0 & 0 & \beta_T^m & \alpha_{T-1}^m & 0 \\ 0 & 0 & 0 & \beta_T^m & 0 & \alpha_T^m \end{pmatrix}$$

This matrix can easily be inverted and solved for  $\bar{g}^m$  and  $\bar{h}^m$ . Now having the  $g_{lm}$  and  $h_{lm}$  coefficients, the magnetic field can be calculated at any point in

the region between the photosphere and the source surface using Equations 3-1, 2, 3. The details of the implementation of this procedure on the computer can be found in Appendix I.

### *Merging of Computations*

Our method of computing the potential field requires that the solution be determined over the whole surface of the sun whenever the fields are calculated. Since less than half of the solar surface can be observed at any given time, the observations which determine the inner boundary conditions must be taken over an extended period of time. The photospheric fields used are taken from the synoptic charts constructed from the daily magnetograms taken at Stanford as described in Chapter 2. For a given  $360^\circ$  of Carrington longitude the observations are obtained over a period of  $\sim 27$  days. Thus "rapid" evolution of the larger scale features of the solar magnetic field is not handled well by this model since the model must assume that the observed boundary conditions are those which apply over the whole surface of the globe at the time of calculation.

It is important to realize that Carrington coordinates refer both to time and to position on the sun. The Carrington coordinate system is a fixed, rigid grid which rotates with a mean synodic period of 27.2753 days. The Carrington time is determined from the longitude of the point at central meridian and the number of times that location has crossed central meridian since Lord Carrington first started counting solar rotations on November 9, 1853. During each rotation the longitude at central meridian decreases from  $360^\circ$  to  $0^\circ$ . Thus Carrington Rotation 1642 :  $5^\circ$  and 1642 :  $355^\circ$  are separated in time by about 26 days, though they refer to physical locations on the sun separated by only  $10^\circ$ .

In addition to the time evolution of the magnetic field, a further complication arises because of the differential rotation of the sun. The equatorial regions have a synodic rotation period close to 27 days while the polar regions rotate only every 32 days. Because the Carrington grid does not

rotate differentially, the data from 360 Carrington degrees will not include data from the entire solar surface; at higher latitudes every longitude will not pass central meridian during the 27.28 day Carrington interval. Fortunately this effect is greatest far from the equator where the structure is usually simple. However, this may account for part of the zero offset or "monopole" component of the magnetic field discussed briefly below.

In most previous work the magnetic field on the source surface was computed only once or twice for each Carrington Rotation, i.e. at intervals of  $180^\circ$  or  $360^\circ$  in longitude. This forces the beginning (near  $360^\circ$ ) and the end (near  $0^\circ$ ) of the Carrington Rotation to have the same structure, even though they are separated in time by 27 days. To avoid this difficulty we have computed the field on the source surface many times for each rotation, beginning successive calculations at  $10^\circ$  intervals. From each such calculation only the central  $30^\circ$  were retained. This means that for each strip in longitude there were three determinations of the field, as is shown in Figure 3-3 below. We combined the results from each of the calculations for a given longitude by weighting the three values in the ratio 1:2:1. In this way the field was determined from the observations which most nearly corresponded to the actual field configuration for that time and place.

For example, in calculating the source surface field for Carrington Rotation 1642 we placed a window on the data in the interval from  $355^\circ$  to  $0^\circ$  longitude. The observations of the photospheric fields at  $355^\circ$  were taken on May 27, 1976, while the observations at  $0^\circ$  were taken on June 23, some 27 days later. On the sun's surface these points are physically adjacent. The fields must be continuous on the sun's surface at a given time, but the photospheric fields observed 27 days apart are not constrained in this way since the fields may evolve in the intervening month. The photospheric data near the edges of the window, i.e.  $355^\circ$  and  $0^\circ$ , were observed nearly 27 days apart and any secular field evolution would be more likely to affect the results there. However, near the center of the data window the nearby longitudes would have been observed at times as close to that of the longitude under consideration as possible. Retaining only the central  $30^\circ$  of each calculation minimizes the affect of this problem.



strong, sharply peaked polar field of the form  $11.5 \cos^6\theta$  G best represented the usually omitted polar field. A correction of this form has been added to the line-of-sight magnetic field when performing these computations. The precise nature and form of this correction and its change through the solar cycle will be discussed in more detail in Chapter 4.

The method as described above is the same as that used in Hoeksema et al. (1982). One further correction has been added to account for the zero offset in the field. Using the composite dataset described above, for each longitude,  $L0$ , we compute the average field strength of the  $360^\circ$  region in the final dataset (one complete rotation) centered on  $L0$  and record the result. To the extent that we accurately measure the total solar magnetic flux this would represent the monopole component of the field. Our final dataset consists of 30 field values equally spaced in sine latitude from North to South for each  $5^\circ$  in Carrington longitude and the zero offset term. Because we believe that the zero offset is largely due to isolated regions of unbalanced measured flux and to effects of local field evolution which "contaminate" the global field, the "monopole correction" is subtracted whenever the data is retrieved. This form is the same as that used in Hoeksema et al. (1983). The meaning and significance of the zero offset will be considered in more detail in Chapter 4.

#### *Form of Results -- Fields & Multipole Components*

There are three forms of data which result from the potential field model calculation: the radial magnetic field at the source surface, the harmonic coefficients, and the 3-component vector field between the photosphere and the source surface. This section very briefly summarizes the meaning of each type of data and describes the presentation of each form. A detailed discussion of the results will be deferred to later chapters.

The model requires that the field at the source surface be radial; therefore, there is only one component of the field on that surface. The assumption is that the energy of the accelerating solar wind overcomes the energy

of the magnetic field and carries the field lines radially outward into the heliosphere. Thus the pattern of the magnetic field at the source surface extends into the heliosphere along Archimedian spiral lines. Therefore the source surface field forms a crude map of the magnetic fields throughout the inner heliosphere. Of course the configuration is subject to change due to the dynamic interactions of the solar wind plasma as it travels outward and to any further field interactions which may occur beyond the radius of the source surface (e.g. Schatten, 1971b; Suess et al. 1977.)

To represent the source surface fields we use a contour map of the magnetic field strength as shown in Figure 3-4 for Carrington Rotation 1656 in June 1977. This particular rotation shows a structure typical of the rising phase of the solar cycle. The format is the same as the synoptic charts shown in the previous chapter. Carrington longitude is on the x-axis and latitude on the y-axis. In this and subsequent plots the latitude scale will be shown in equal steps of latitude, though the data and the computations are done with a grid spaced in equal steps of sine latitude. This is done for ease of comparison with other solar data published in similar form.

Because of the resolution of the Stanford magnetograph and the conversion to equal steps in latitude, there is no data above  $70^\circ$ . The Carrington rotation and longitude are shown below. The date of central meridian passage of  $180^\circ$  is given at the upper right. The contour levels are at 0,  $\pm 1$ , 5, 10, 20, and 50 microtesla. This may be compared with the contour levels of 0,  $\pm 100$ , 200, 500, ... microtesla on the photospheric plots. Negative contour lines are dashed, the first thickened solid contour is the neutral line, and

---

Figure 3-4: Computed magnetic field contours on a spherical source surface concentric with the Sun at a radius of  $2.35 R_\odot$  for Carrington Rotation 1656, beginning 13 June 1977. The solid contour lines represent field directed away from the Sun with observed field strengths 1, 5 and 10 microtesla; the dashed contours represent field directed toward the Sun. The observed field strengths should be multiplied by a factor of 1.8 to account for magnetograph saturation (Svalgaard et al, 1978). The heavier line shows where the direction of the computed field changes from away to towards, and is assumed to be the source of the heliospheric current sheet. The + and - symbols represent daily values of the polarity of the interplanetary magnetic field observed at Earth, adjusted for the five day transit time of solar wind from Sun to Earth.



SOLAR SOURCE SURFACE

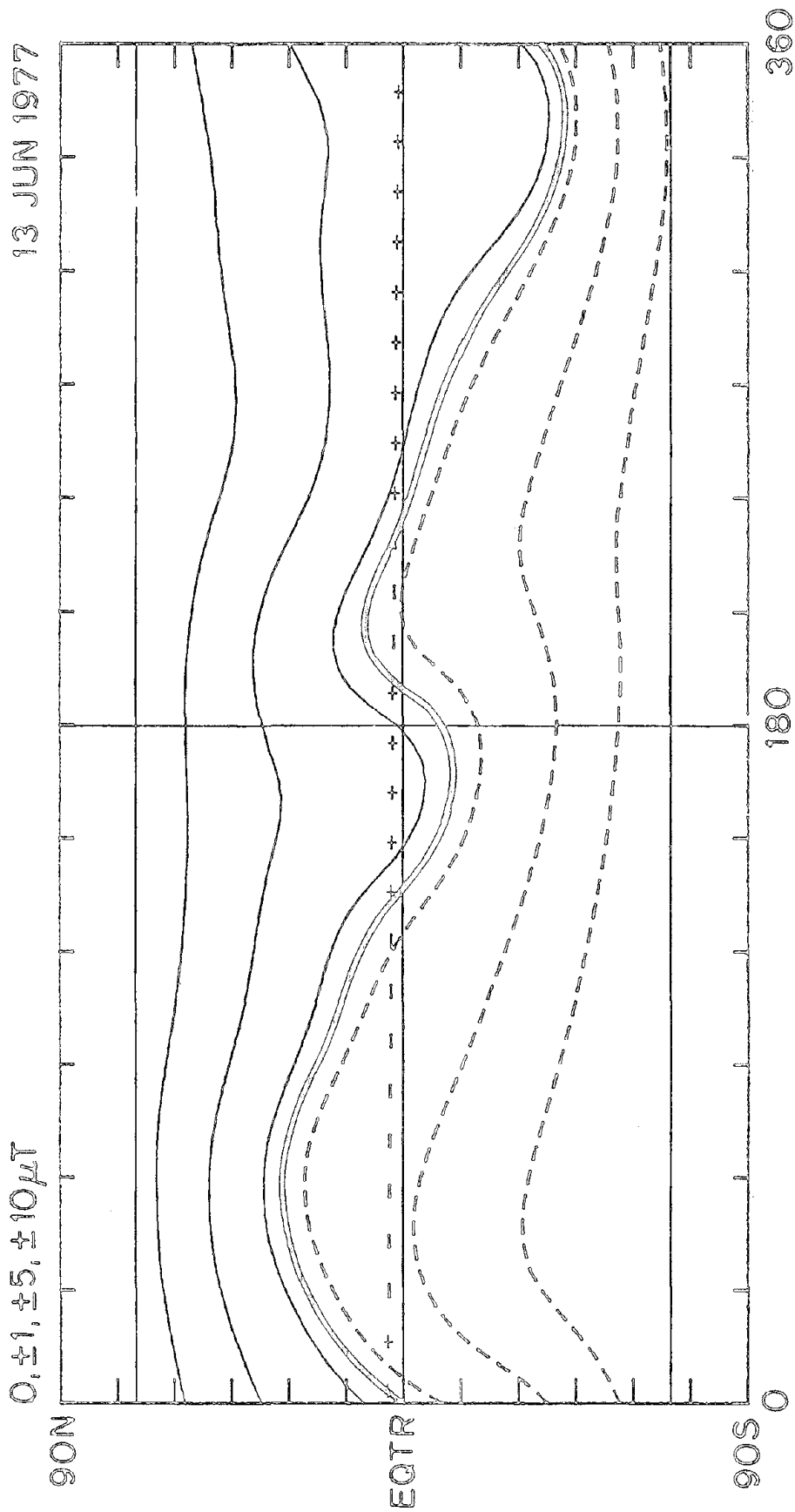


Figure 3-4

subsequent solid contours represent positive flux regions. As discussed in the following chapter, the plus and minus signs represent the interplanetary magnetic field polarity measured at Earth and corotated back to the sun. In this plot the source surface radius was placed at 2.35 solar radii and the standard polar field correction was made. The zero offset was very small and has not been removed.

Full page contour plots of the source surface magnetic field for Carrington Rotations 1641 through 1739, May 1976 through September 1983, can be found in Hoeksema (1984). In that report the source surface radius was fixed at 2.5 solar radii, the standard polar field correction was made, and the zero offset was removed. Reasons for these choices will be discussed in later chapters.

The harmonic coefficients can be used to calculate the field in the region between the photosphere and the source surface. For investigation of the heliospheric fields, expansion of the fields out to order 9 of the spherical harmonics seems to be more than sufficient. Calculations including higher orders show negligible differences in the field at the source surface. For investigation of regions near the photosphere one should really use more terms. The resolution of the Stanford data limits the calculation to approximately order 23.

In the normalization used here for the associated legendre functions, the  $g_{lm}$  and  $h_{lm}$  coefficients refer to the magnitudes of the multipole components of the magnetic field multiplied by  $(2l+1)^{\frac{1}{2}}$ . Thus the  $g_{00}$  term is the monopole term, the  $g_{10}$  term is the standard polar dipole, the  $g_{11}$  term is the equatorial dipole, and the  $h_{11}$  is the equatorial dipole oriented  $90^\circ$  out of phase with  $g_{11}$ . To compare the magnitudes of the dipole components with the monopole term, each coefficient must be divided by  $\sqrt{3}$ . Higher terms refer to the quadrupole, octupole, and higher moments. The principle index,  $l$ , is the total number of circles-of-nodes on the sphere for that multipole and the second index,  $m$ , is the number of those nodal circles passing through the pole. As shown in Figure 3-5,  $g_{70}$  is the harmonic with seven circles of nodes in the horizontal direction, i.e. zonal structure;  $g_{77}$  refers to the harmonic with seven circles of nodes passing through the pole forming sectoral

## SPHERICAL HARMONICS

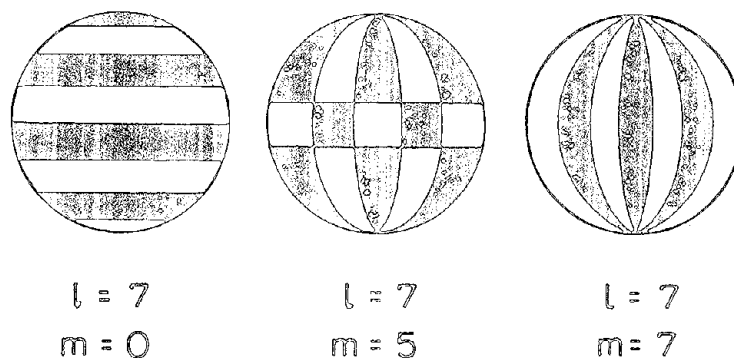


Figure 3-5: The form of the spherical harmonic functions: the zonal harmonic,  $P_7^0$ ; the tesseral harmonic,  $P_7^5$ ; and the sectoral harmonic,  $P_7^7$ .

(i.e. meridional) structures; and  $g_{75}$  would have two lines of nodes parallel to the equator and five passing through the poles. The  $h$  coefficients are displaced  $90^\circ$  in the longitudinal direction.

The following table contains the harmonic coefficients for Carrington Rotation 1656. The coefficients for each Carrington Rotation can be found in the same format in Hoeksema (1984). The row number is the primary index,  $l$ , of the harmonic, the column is the secondary index,  $m$ . Substituting these into equations 3-1,2,3 allows computation of the potential field. These were calculated including the polar field correction with the source surface at 2.5 solar radii.

Between the source surface and the photosphere all three components of the field can be computed from the  $g$ 's and  $h$ 's. The presentation and interpretation of the data becomes more complex. As the radius approaches the photosphere, the higher order terms which depend on  $\left(\frac{R_0}{r}\right)^l$  become more prominent and the structure begins to resemble the complex

$g's$	0	1	2	3	4	5	6	7	8	9
0	-4.285									
1	24.543	-3.035								
2	-1.123	-1.427	3.206							
3	18.878	-1.843	-10.537	2.685						
4	-0.482	-3.357	-0.537	5.436	10.844					
5	13.824	0.659	-5.192	7.644	-4.606	-1.658				
6	-0.431	0.758	0.619	4.639	10.020	-9.175	6.140			
7	5.292	-0.079	2.058	2.844	3.156	-5.063	-6.175	1.463		
8	0.018	0.870	-0.066	0.368	1.639	-0.459	2.165	-5.605	0.428	
9	1.667	-0.957	-2.517	-2.781	3.797	1.310	-1.997	1.863	-0.465	7.725

Carrington Rotation 1656

$h's$	0	1	2	3	4	5	6	7	8	9
0	0.000									
1	0.000	-12.277								
2	0.000	-0.188	-13.740							
3	0.000	-8.355	5.194	-0.729						
4	0.000	2.534	-10.594	12.047	-9.680					
5	0.000	5.871	-5.917	-4.707	-1.320	3.013				
6	0.000	-3.127	0.017	-0.717	2.749	14.853	-9.662			
7	0.000	-0.070	0.146	-0.055	7.055	-1.936	-12.668	3.313		
8	0.000	-0.398	-1.542	-0.464	7.972	2.884	-8.165	14.853	-0.727	
9	0.000	0.642	2.981	-0.385	0.513	1.437	2.462	-1.760	-7.068	-2.519

photospheric structure rather than the relatively simple structure in the interplanetary medium. Because the calculations have been completed only to order 9, the structure near the photosphere is also much simpler than the measured field. Comparison of the fields calculated for a variety of maximum orders of the expansion will be discussed in a later chapter.

Figure 3-6 shows the field direction at  $1.1 R_0$  for a source surface radius of  $2.5 R_0$  at a height of  $1.1 R_0$  for Carrington Rotation 1656. At each grid point, marked by plus symbols, an arrow is drawn to show the direction of the field computed from the  $\vartheta$  and  $\varphi$  components. The zero contour of radial field is drawn and the arrows corresponding to a negative radial field component are dashed. The y-axis is scaled in sine latitude. This plot gives no

Figure 3-6: The direction of the magnetic field at  $1.1 R_0$  for Carrington Rotation 1656. The arrows show the direction of the field at each grid point but not the magnitude. The contour line separates regions of positive and negative radial field. The arrows in negative field regions are dashed. The latitude is scaled in sine latitude.

DIRECTION OF  $\vec{B}$  AT  $R = 1.1 R_0$

27 JUN 1977

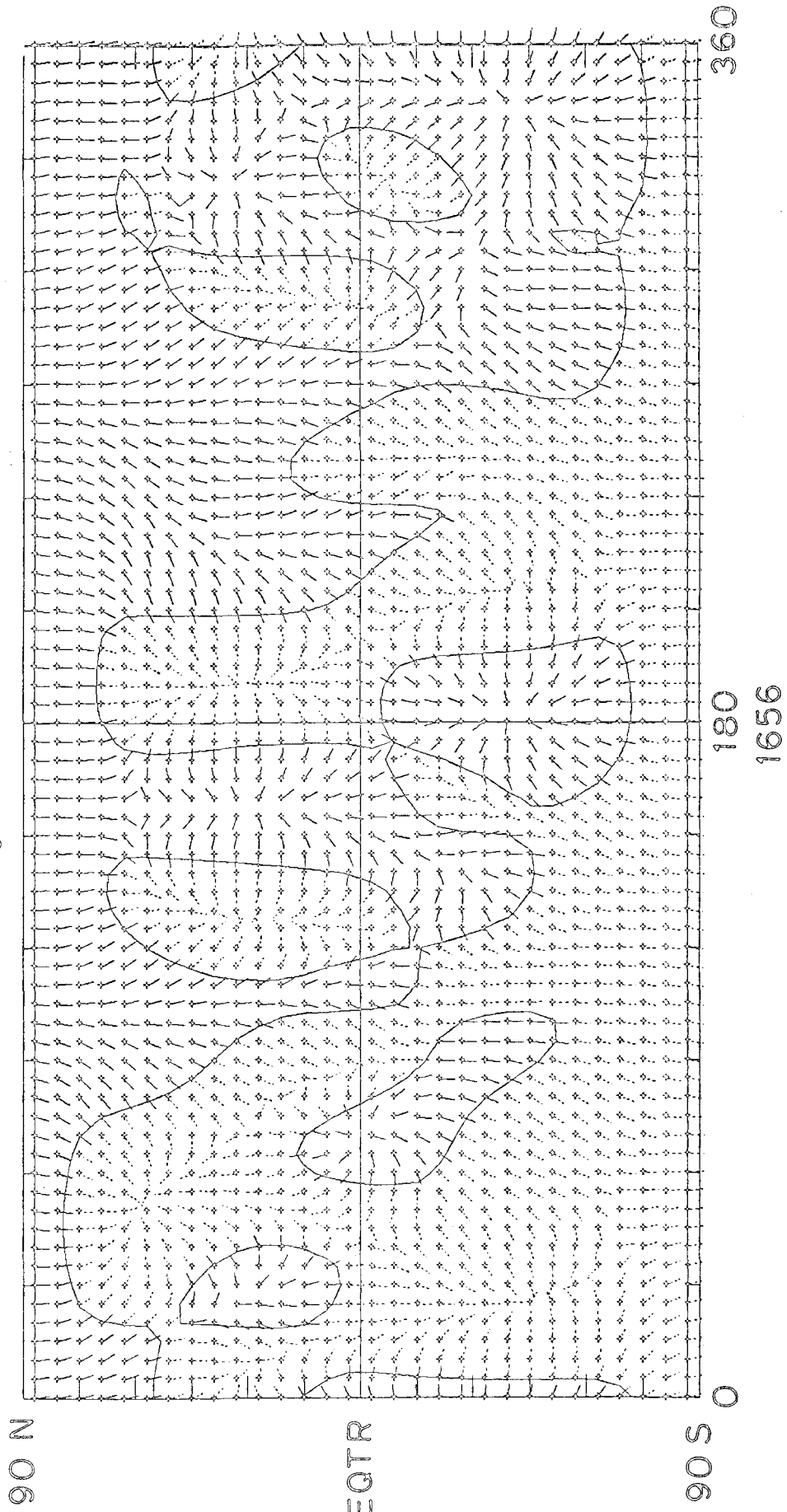


Figure 3-6

information about the magnitude of the field. It should be noted that the results shown are from a single computation of the field for the entire Carrington Rotation and that the zero offset has not been removed. The polar field correction has been made to the data. Near the surface the zero offset has even less effect than at higher altitudes because its relative importance decreases with decreasing altitude. It is interesting to note both the similarities and differences from the plot of the source surface field and the photospheric fields for this rotation.

We now turn to a more extensive discussion of the comparison of the source surface fields and the interplanetary field polarity. Using this comparison the best source surface radius can be determined and the strength of the polar field correction can be verified. The zero offset correction will also be discussed.

## Chapter 4 -- Setting the Parameters

The previous chapter described the potential field model. Before proceeding to an investigation of the evolution of the heliospheric magnetic field structure, the source surface radius must be determined, the polar field correction must be investigated, and the handling of the monopole component must be discussed. To determine the best alternative in each case, the polarity of the interplanetary magnetic field (IMF) predicted by the model and that measured at the Earth are compared. Thus the method used should give the most accurate prediction of the large scale polarity structure at Earth. It should be emphasized that the Earth is not a very sensitive probe of the heliosphere, since it never travels more than  $7.3^\circ$  from the solar equator.

After explaining how the IMF polarity is determined near the Earth and predicted by the model, we discuss the correlation of the two for a given source surface radius and polar field strength. Then the factors influencing the selection of the source surface radius and the effect of varying the radius on the large scale configuration of the source surface field will be discussed. The polar field correction of Svalgaard et al. (1978) has been extrapolated through the polar field reversal at maximum and the effect of the polar field strength and the source surface radius on the correlation with the observed IMF polarity is shown. Finally the origin and handling of the zero offset or "monopole" component will be explained.

### *Comparison of Predicted and Observed IMF Polarity*

Spacecraft provide the most reliable determination of the interplanetary field, but when spacecraft data are unavailable the daily polarity can be quite accurately inferred from geomagnetic data using the method described by Svalgaard (1975). The IMF polarity dataset is constructed using a three-step process.

From the high resolution spacecraft data, hourly averages of the field direction are computed. For each 24-hour interval no more than half of the data may be missing. For a polarity to be assigned, at least 7/12 of the hourly averages must be of the same polarity, otherwise the day is designated mixed.

After the computer makes the original assignment, an observer familiar with the interplanetary data, in this case Leif Svalgaard, Grazia Borinni, or John Wilcox, checks the value for each day. The IMF polarity is usually organized into a few strong sectors per solar rotation with some short periods of opposite polarity imbedded within them. Using plots of the data for an entire rotation, the observer judges the character of each day with respect to the large scale sector structure and verifies each day's polarity assignment.

Finally, the inferred polarity data is included for those days for which no spacecraft polarity can be assigned. Thus for each day there is a value corresponding to field directed predominantly away from the sun along the spiral field direction (+1), toward the sun (-1), or mixed (0).

For comparison with the IMF polarity measured at Earth the model must predict one polarity value per day; +1, corresponding to days when the average field direction points away from the sun, -1, corresponding to field toward the sun, or 0, when the field is changing or indeterminate. The following paragraphs give a detailed description of the method for making a dataset of predicted IMF polarity.

Under the assumption of purely radial flow from the source surface to Earth, the relevant field comes from the subterrestrial point. Using a quadratic fit to the source surface field maps, the computer interpolates the magnetic field value at the heliographic coordinates of the Earth for each 3-hour time interval (about every 2 degrees of longitude). Positive three-hour intervals are assigned a positive polarity and a corresponding assignment is made for negative regions. Field values less than 0.001 microtesla (a value small at any relevant source surface radius) receive a zero. Using a typical source surface radius of  $2.35 R_{\odot}$ , this results in about five 3-hour intervals of indeterminate polarity in the interval 1976 - 1982. One might argue that a zero polarity should be assigned for some larger range of field values since



there are uncertainties in the current sheet location. However, considering the variation of field strength with source surface radius and solar cycle, it would be difficult to choose a meaningful cutoff value. Uncertainty in the neutral line location is accounted for as described below.

To find the daily polarity eight of the 3-hour values described above are averaged. If at least six of the eight values have the same sign, that day is assigned a polarity. Otherwise the day receives a zero. This corresponds to an uncertainty in longitude of about  $3^\circ$ . Uncertainty in latitude is not considered. About 100 days from May 1976 to December 1982 are undetermined. This is roughly equivalent to the number of mixed polarity days in the measured IMF polarity dataset and corresponds to about one day per rotation.

In order to compare the measured and predicted polarities the propagation time of the signal from the sun's surface to 1 AU must be accounted for. In simply using the measured solar wind speed to map the measured IMF back to the source surface two severe problems are encountered: 1) velocity data coverage is much less complete than the polarity data and 2) when the velocity increases significantly with time, several days of interplanetary field may appear to come from a single longitude since the propagation time may vary from  $2\frac{1}{2}$  to 5 days.

Another alternative is to map the values on the source surface outward using to some rule relating velocity and field strength (or distance from current sheet, or the latitude difference of the current sheet and Earth, or  $|B^2|$ , or ...) Besides the difficulty in deciding which quantity to use in what way, this would require computation of the solar wind interactions in transit which is far beyond the scope of this investigation.

---

Figure 4-1: The IMF polarity observed at Earth is presented in the the Bartels chart format. Each row has 27 boxes with the polarity for each day indicated in a box. A filled box indicates toward polarity; a hatched box indicates indeterminate polarity; an empty box indicates away polarity. This format emphasizes the 27-day recurrence pattern in the polarity and the large-scale structure over many rotations.

Figure 4-2: The IMF polarity computed at the source surface by the model is presented in the same format as Figure 4-1. The plot is displaced by five days to account for the solar wind transit time from Sun to Earth.

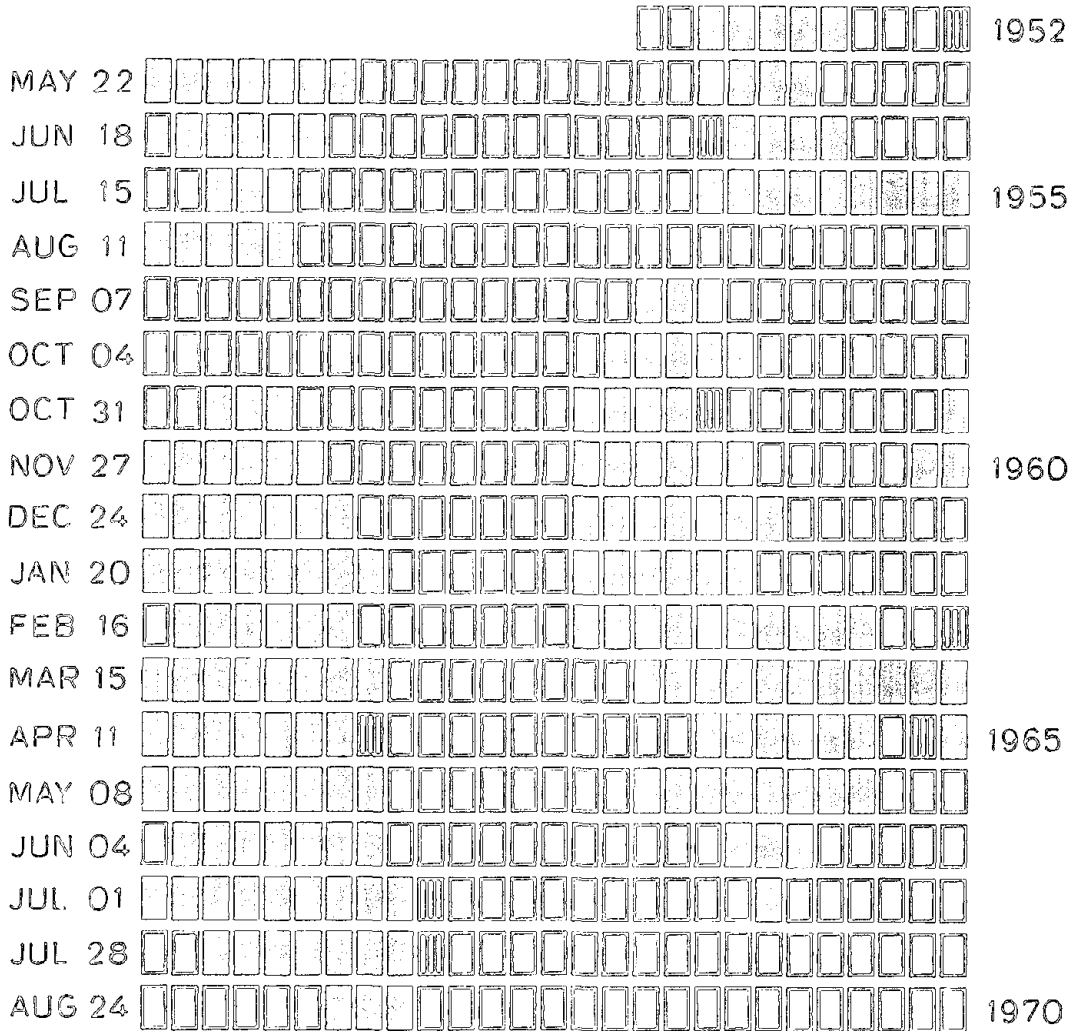


# PREDICTED IMF POLARITY

= AWAY  
 = TOWARD

1976

BARTELS  
ROTATION



The field is organized into large single polarity sectors both on the source surface and as measured in the IMF. A comparison of the predicted structure and that observed at Earth as shown in Figures 4-1 and 4-2 for the interval May 1976 through September 1977 demonstrates this. In this case a source surface radius of  $2.35 R_{\odot}$  and the standard solar polar field correction of  $11.5 \cos^2 \lambda$  G were used. (The choice of interval and how these values were determined are discussed in the next two sections.) These figures show the data plotted in Bartels rotations as is customary for geomagnetic observations which typically have a recurrence period of 27 days. Filled boxes correspond to negative polarity days and open boxes to positive polarity. The predicted data has been displaced five days to compensate for the transit time. Comparison of the two figures shows that the model predicts the large-scale structure quite well and that most of the disagreements occur near sector boundary crossings or as isolated events likely due to transient events. A portion of the disagreement near boundary crossings is caused by our use of a constant five-day solar wind transit time from sun to Earth, since in fact there are some variations in the actual transit times. On the one day scale used in plotting Figures 4-1 and 4-2, however, these variations in transit time would not make a large effect.

Since most of the disagreements between the two do occur in the location of sector boundaries, this means that the comparison is sensitive to the propagation time only near the edges of sectors. Near sector boundaries the solar wind velocity is typically relatively low (Wilcox and Ness, 1965). This explains the long five-day lag which is greater than the average solar wind transit time. Solar wind velocities near sector boundaries also show relatively little scatter, suggesting that the approximation of boundary speed by a single value is not unreasonable.

Using this approximation a reasonable comparison of the two quantities

---

Figure 4-3: The cross correlation between the IMF polarity predicted from the adopted computation of the heliospheric current sheet and the polarity observed at Earth. The lag of the first peak is five days, which represents the transit time from Sun to Earth of the solar wind near the sector boundaries.

CORRELATION OF PREDICTED AND OBSERVED IMF POLARITY

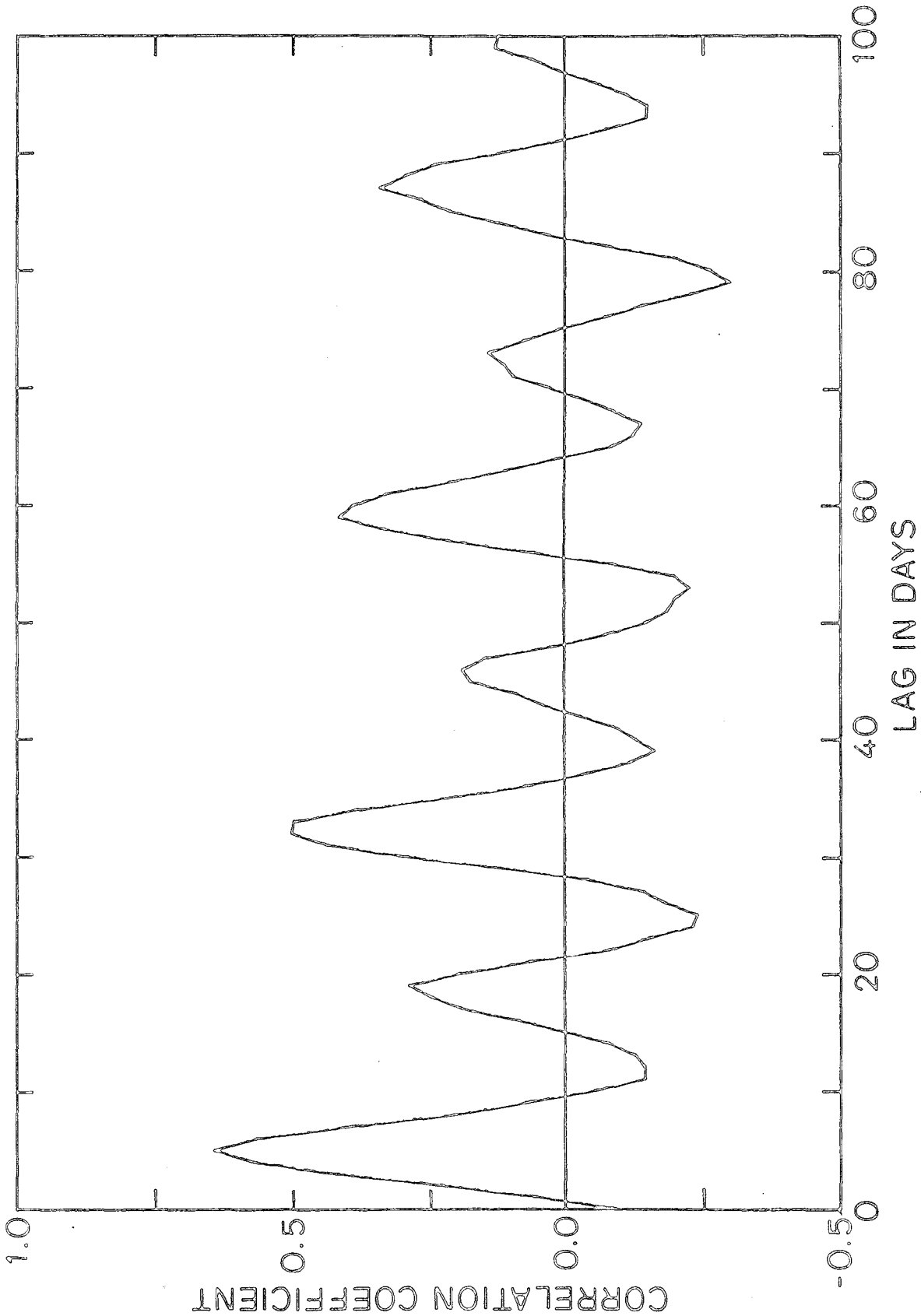


Figure 4-3

using a constant lag time can be made. Computation of the correlation between the predicted field polarity at the sub-terrestrial point on the source surface and the IMF polarity observed at Earth for a variety of lags is shown in Figure 4-3 for the interval May 1976 to September 1977. The first peak at  $5.0 \pm 0.3$  days represents the transit time for the solar wind plasma to transport the magnetic field from sun to Earth near a boundary. The five day lag corresponds to a solar wind velocity of 350 km/s. The relatively slow decline in amplitude of the peaks near 32 days, 59 days and 86 days shows that the large-scale IMF structure is quasi-stationary. The intermediate peaks are caused by the four-sector nature of the IMF structure at this time. The 27 day difference in time between the peaks at 32 days and 5 days shows that the recurrence time of the IMF is close to 27 days.

In the discussion so far the IMF polarity observed at Earth has been compared with the source surface field polarity at the heliographic latitude of the Earth. What happens if instead we compare the observed IMF polarity at Earth with the polarity on the source surface 5 degrees north of the sub-terrestrial latitude? Figure 4-4 shows that the maximum cross correlation decreases from 0.64 to 0.54. These results refer to the same 1976 - 1977 interval with the same parameter values. Figure 4-4 demonstrates that the sub-terrestrial latitude on the source surface has the most similar magnetic polarity structure to that observed at Earth, and that even a few degrees north or south of the sub-terrestrial latitude the correlation with the observed field is smaller.

---

Figure 4-4: The maximum cross correlation between the IMF polarity predicted from a computed current sheet on a source surface at  $2.35 R_{\odot}$  with  $11.5 \cos^{\theta} \text{ G}$  added polar field and the IMF observed at Earth as a function of the latitude on the source surface at which the field polarity was predicted. In the abscissa, zero represents the heliographic latitude of the Earth.

CORRELATION vs. LATITUDE OFFSET

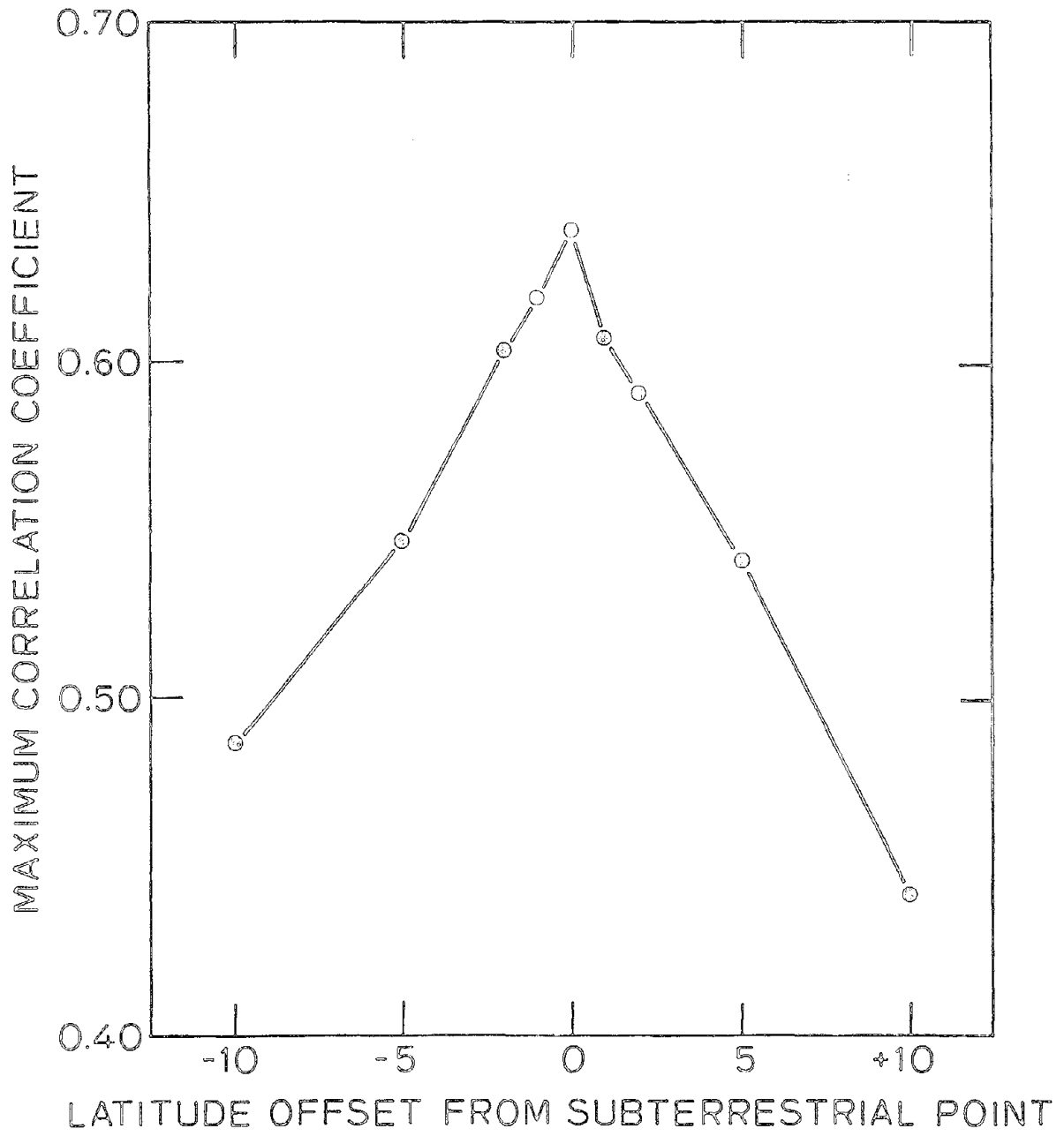


Figure 4-4

### *Choosing the Source Surface Radius*

Different authors have used various criteria for choosing the source surface radius. Schatten et al. (1969) used energy considerations, eclipse pictures, field strength extrapolated to 1 AU, and complexity of the sector structure to set the source surface radius,  $R_s = 1.6 R_o$ . This referred primarily to the areas over large weak field regions. Altschuler & Newkirk (1969) used the shape of structures over active regions observed during eclipses to set  $R_s = 2.5 R_o$ . The difference lies in the type of region over which the potential field is being calculated. Several studies suggest that open field lines occur lower over quiet regions than they do over active regions (Zirker, 1977; Schulz et al., 1978; Burlaga et al., 1978; Levine et al., 1982.) For example Levine (1977a,b), and Pneuman et al. (1978), use a source surface radius of  $1.6 R_o$  to study the large scale open field regions while Jackson & Levine (1981) use  $2.6 R_o$  to study the area above active regions. Levine (1982) extended this relation and used  $1.6 R_o$  near sunspot minimum and  $2.6 R_o$  near maximum.

In this study the optimum source surface radius is empirically determined for each of three intervals by computing the source surface field over a range of radii and comparing the resulting IMF predictions with the IMF measurements. This optimizes the agreement of the model with the large scale IMF polarity structure. In order to first investigate an interval during which the polar field did not change and the level of solar activity remained relatively constant, the time period May 1976 through September 1977 was chosen. The results for this interval are shown in Figure 4-5. The correlation, labelled on the vertical axis, is shown for various source surface radii ranging from  $1.6$  to  $3.1 R_o$ . Each line corresponds to a different magnitude of

---

Figure 4-5: Maximum correlation between the IMF polarity predicted from the computed heliospheric current sheet and the IMF polarity observed at Earth as a function of the source surface radius on which the current sheet was computed. Source surfaces were computed with an added solar polar field strength of  $11.5 \cos^{\theta} G$  as computed by Svalgaard et al. (1978), and for other values of the added solar polar field as shown.



MAXIMUM CORRELATION vs. SOURCE SURFACE RADII'S

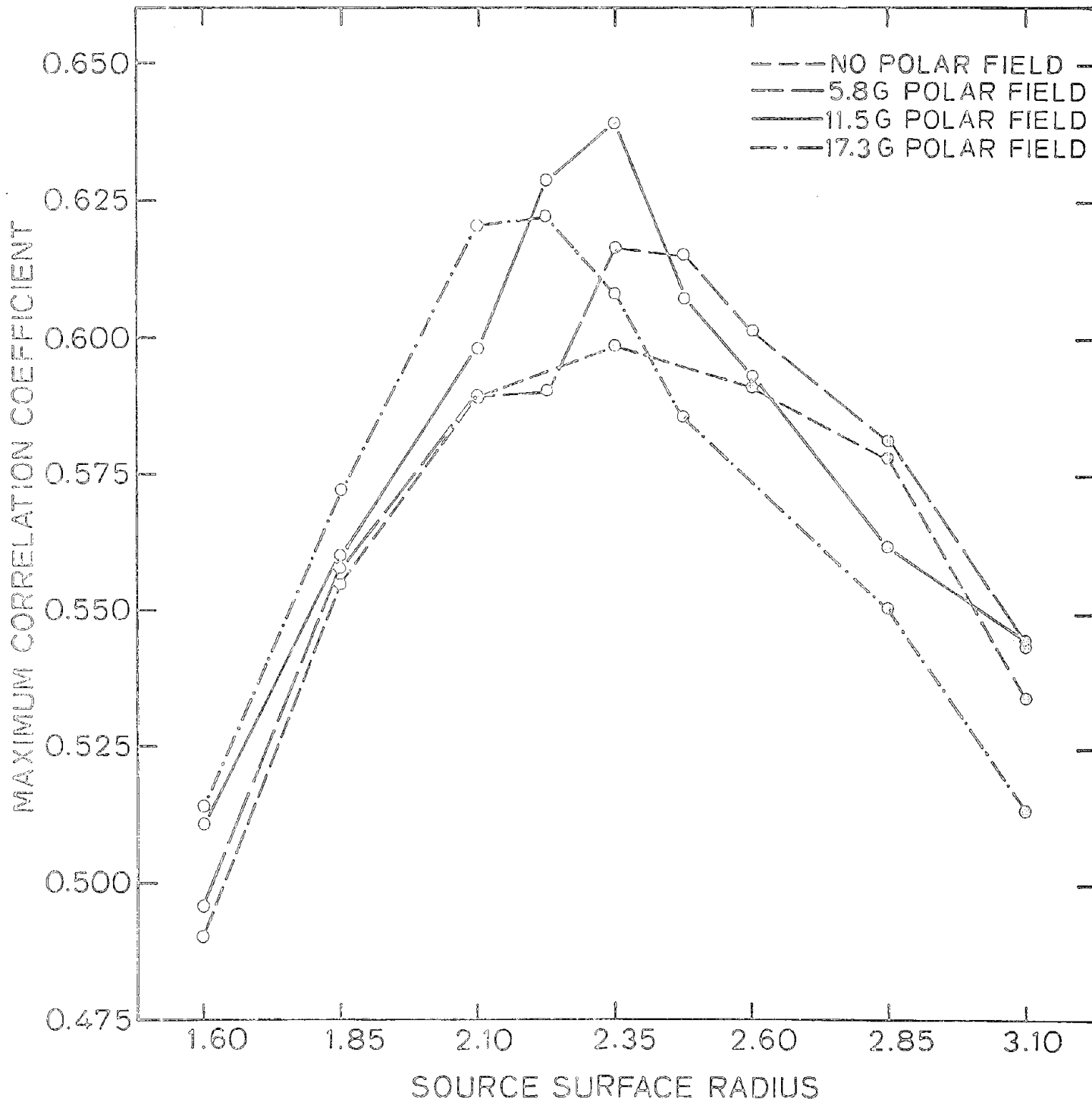


Figure 4-5

the polar field correction. The polar field correction will be explained in more detail in the next section. The solid line represents the results using the standard polar field correction of Svalgaard et al. (1978) discussed below.

At each radius the maximum correlation occurred with a lag of five days between the source surface and 1 AU. The largest correlation occurs for a source surface of radius  $2.35 R_o$  (with the expected polar field correction) and corresponds to correct prediction of the IMF polarity on 82% of the days. For this reason most of the results for this time period refer to calculations with this source surface radius and polar field correction. For comparison, the polarity inferred from geomagnetic data agrees with spacecraft measured polarity 85 - 90% of the time (Svalgaard, 1975). Considering that this is a *prediction* using photospheric data and that most of the discrepancies occur in the day or two near boundary crossings, this is a good success rate. The figure suggests that differences of up to a quarter solar radius have little effect on the correlation. The correlations for  $R_s = 1.6 R_o$  and  $R_s = 3.1 R_o$  are noticeably poorer. Correlations for other intervals are presented in the next section after discussing the polar field correction.

It is also interesting to see how varying  $R_s$  changes the computed field. Figure 4-6 shows the configuration of the current sheet for Carrington Rotation 1656 calculated with several different source surface radii. Each calculation included the standard polar field correction. Since the higher order multipole components fall off with increasing dependence on radius,  $r^{-(l+1)}$ , increasing the source surface radius essentially filters out the higher order contributions. For a given set of coefficients this will emphasize the dipole term. Of course the harmonic coefficients do change as  $R_s$  varies, though since the photospheric boundary condition is the same they do not change a great deal. The neutral lines in Figure 4-6 demonstrate this effect quite graphically. With  $R_s = 1.6 R_o$ , the neutral line shows quite a bit of structure

---

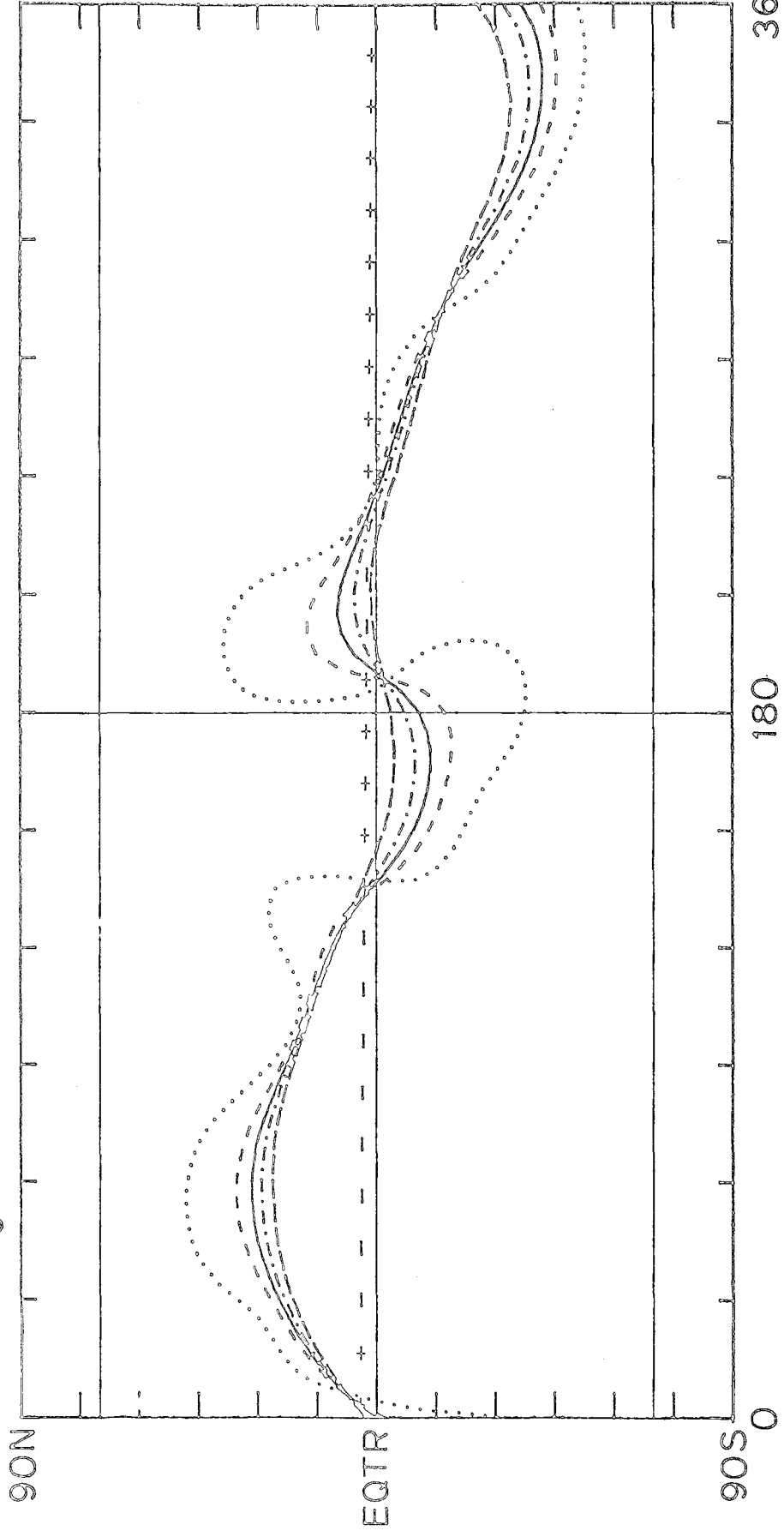
Figure 4-6: Computed current sheets for Carrington Rotation 1656 beginning 13 June 1977 for source surfaces at several different radii, as indicated. As the radius of the source surface is increased the computed current sheet approaches the solar equator.

VARIATION OF CURRENT SHEET WITH SOURCE SURFACE RADIUS

- .....  $1.6R_{\odot}$
- - - -  $2.1R_{\odot}$
- — —  $2.35R_{\odot}$
- · - ·  $2.6R_{\odot}$
- - - -  $3.1R_{\odot}$

Figure 4-6

13 JUN 1977



and extends to relatively high latitude. As the radius increases the amount of structure due to the higher order terms decreases and the polar dipole is emphasized, pushing the current sheet closer to the equator.

Interestingly, all of the computed current sheets in Figure 4-6 agree almost equally well with the observed IMF polarity. Thus a comparison of the IMF polarity predicted from a computed current sheet with the IMF polarity observed at Earth is only a *weak* test of the extent in latitude of the computed current sheet. A spacecraft observing at large heliographic latitudes would give the definitive answer to the problem of the extent in latitude of the heliographic current sheet.

#### *The Polar Field Correction*

Stenflo (1971), Howard (1977), and Svalgaard et al. (1978), have pointed out that conventional line-of-sight field observations made by solar magnetographs do not directly measure all of the solar polar magnetic field. Pnevman et al. (1978), Burlaga et al. (1981), Hoeksema et al. (1982, 1983), and Levine et al., (1982) have shown the importance of the sun's polar field strength for the potential field model results. This is especially true near sunspot minimum when the polar fields are strong and the lower latitude fields are relatively weak. Wilcox et al. (1980) computed the heliospheric current sheet configuration for early 1976 using solar magnetograph observations from Mt. Wilson Observatory which did not include the solar polar magnetic field only partially observed in daily solar magnetograms. As a result the computed extent in latitude of the heliospheric current sheet was

---

Figure 4-7: The diagram shows the approximate location and size of the northernmost aperture on the Sun during the observations for a magnetogram. The aperture is 3 arc minutes square. Ten-day averages of the field strength measured in this aperture from May 1976 through December 1982 are plotted. The annual variation due to the inclination of the solar pole to the ecliptic can be clearly seen. Before polar field reversal the average field strength was about 95 microtesla. After reversal it was about 45 microtesla. The straight lines show the scaling factor used to determine the polar field correction throughout this interval with  $11.5 \cos^{\theta}(\vartheta)$  G being the canonical value in 1976-77.

FIELD STRENGTH IN NORTHERNMOST APERTURE

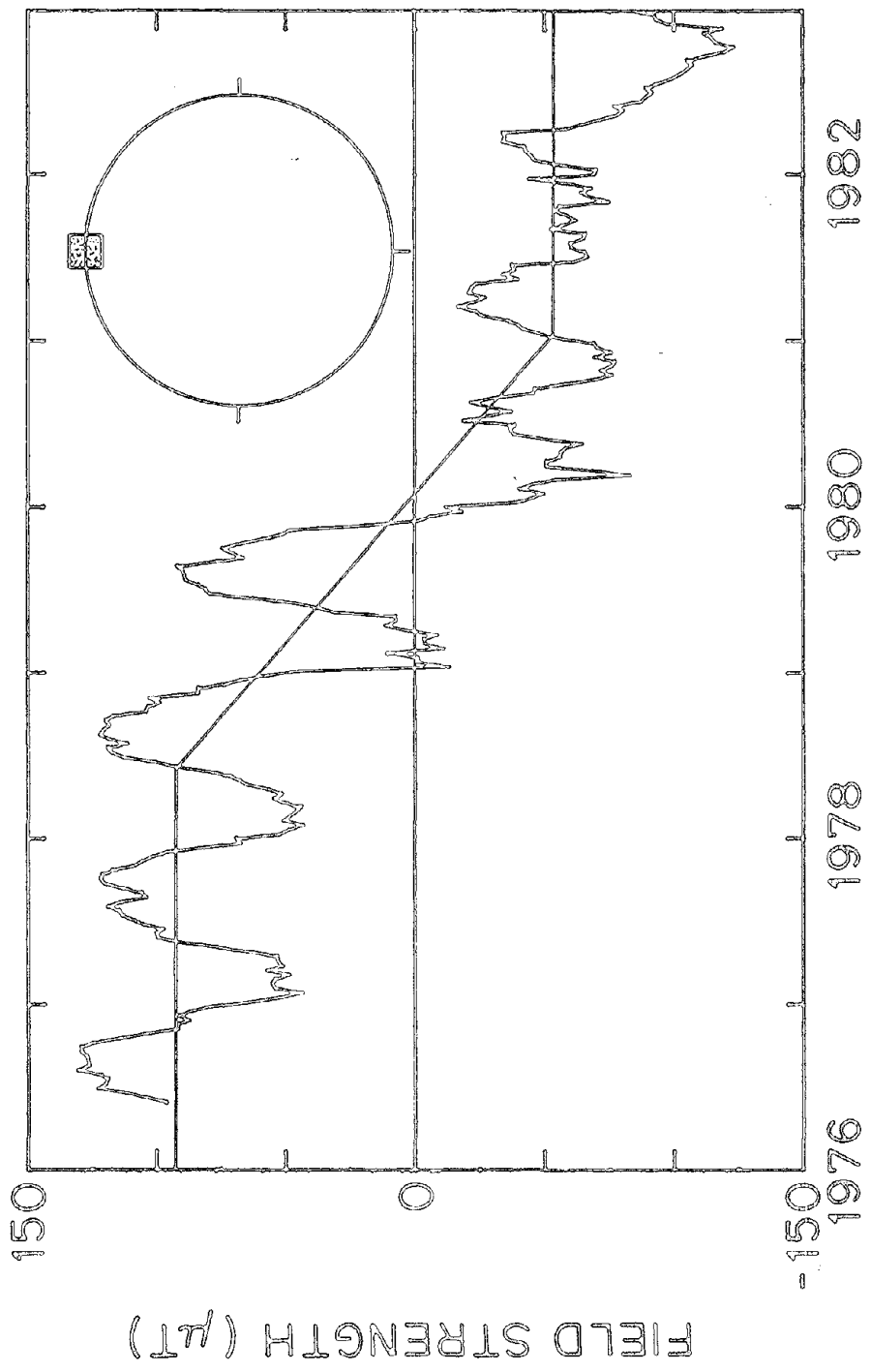


Figure 4-7

probably too large, as was pointed out by Burlaga et al. (1981).

That some of the polar flux escapes detection can be seen in the Stanford measurements by considering the field measurements obtained in the apertures nearest the poles. Figure 4-7 shows a diagram of the northernmost aperture of a Stanford magnetogram relative to the solar disk. The aperture is 3 arc-minutes square. Ten-day averages of the field strength measured in this aperture are shown for May 1976 through December 1982. Svalgaard et al. (1978) studied the interval May 1976 through September 1977, a time when the solar polar field was not changing. By considering the annual variation in measured field strength due to the  $7^\circ$  inclination of the solar rotation axis to the ecliptic plane they determined the strength of the field in the northern and southern polar regions. Their study discovered that an additional sharply peaked radial field of the form  $11.5 \cos^3 \vartheta$  G was required to reproduce the observed annual variation in the polar apertures. (This is the value corrected for magnetograph saturation.)  $\vartheta$  is the colatitude. This annual variation can be clearly seen in Figure 4-7, as can the reversal of the field polarity which occurred near the end of 1979. The corresponding plot for the south pole, shown in Figure 4-8, is very similar.

Pneuman et al. (1978) computed the field on a source surface located at  $2.5 R_\odot$  during the Skylab period in 1973 and found that their computed neutral lines were systematically poleward of the brightness maxima observed at  $1.8 R_\odot$  with the K-coronameter at Mauna Loa, Hawaii. If the fields above  $70^\circ$  latitude measured with the full disk magnetograph at Kitt Peak National Observatory were increased to about 30 gauss this effect was removed. This is a much larger correction for the solar polar field than that determined for the Stanford data. The reason for the difference from this work is not clear. Pneuman et al. (1978) suggested other possible causes for their systematic poleward displacement of the neutral line; to the extent that these operated

---

Figure 4-8: The corresponding curve for the southernmost aperture shows that the polar field in this hemisphere evolved much like the northern field. From these curves the polar field in each hemisphere appears to have reversed at the same time. The magnitudes of the fields were also very similar.

FIELD STRENGTH IN SOUTHERNMOST APERTURE

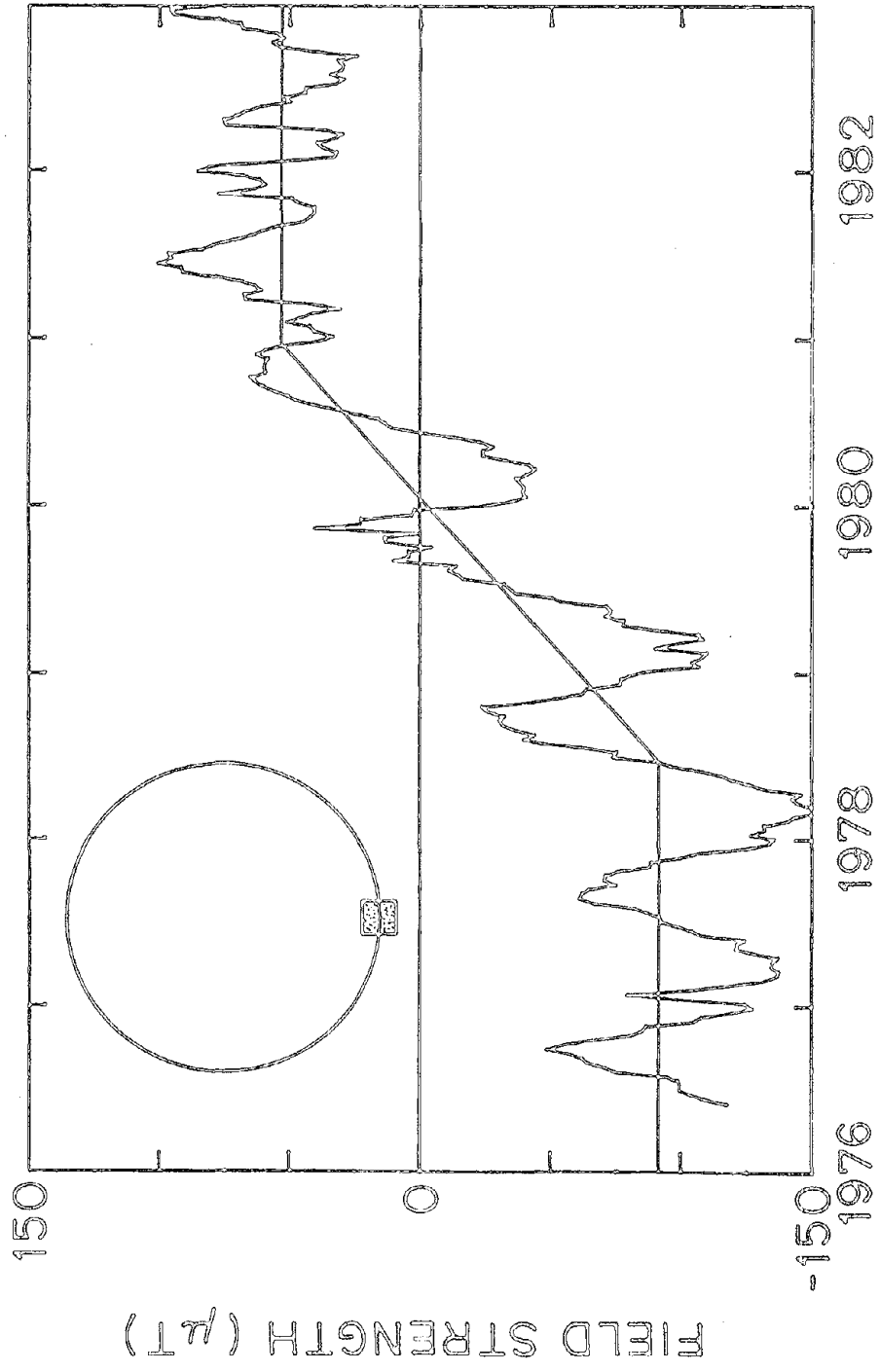


Figure 4-8

the solar polar field correction would be reduced. A difference in solar magnetograph calibrations between Kitt Peak and Stanford may contribute to the different corrections, furthermore the solar polar field strength may have been different in 1973 and 1976.

We can now finish the discussion of Figure 4-5 which shows the maximum correlation of the predicted and observed IMF polarities for the interval studied by Svalgaard et al. (1978). Each curve refers to the results computed for a single value of the polar field correction at several source surface radii. The solid curve represents the standard correction described above,  $11.5 \cos^{\theta} \vartheta$  G. The best correlation occurs when the standard correction is applied to the data. This occurs with  $R_s = 2.35 R_o$ .

For comparison the potential field model has been calculated using polar field corrections of different magnitudes. The short-dashed line shows the correlations with no polar field added. The other lines refer to corrections of  $\frac{1}{2}$  and  $1\frac{1}{2}$  times the standard correction. Apparently any polar correction is better than none. During this interval the correlation for a given  $R_s$  is relatively sensitive to the polar field correction, though by varying  $R_s$  good agreement can be found for any polar correction. While the polar field of  $11.5 \cos^{\theta} \vartheta$  of Svalgaard et al. (1978) does give the best agreement, the differences are not large.

Figure 4-9 shows computed current sheets on a typical Carrington rotation (Rotation 1656 again) for the four values of added solar polar magnetic field. The source surface radius is held constant at  $2.35 R_o$ . The current sheet for the selected value of 11.5 gauss is shown with a solid line. The current sheet shown with short dashes was computed with no added solar polar field, and has the largest extent in latitude in Figure 4-9. The dash-dot line is the current sheet computed with 17.3 gauss added solar polar field (i.e. one and one half times the preferred value), and has the smallest extent

---

Figure 4-9: Computed heliospheric current sheets on Carrington Rotation 1656 beginning 13 June 1977 for several values of added solar polar magnetic field. As the strength of the polar field is increased the computed current sheet approaches the plane of the solar equator.



VARIATION OF CURRENT SHEET WITH POLAR FIELD STRENGTH

13 JUN 1977

- NO POLAR FIELD
- - - - 5.8G POLAR FIELD
- 11.5G POLAR FIELD
- · - · 17.3G POLAR FIELD

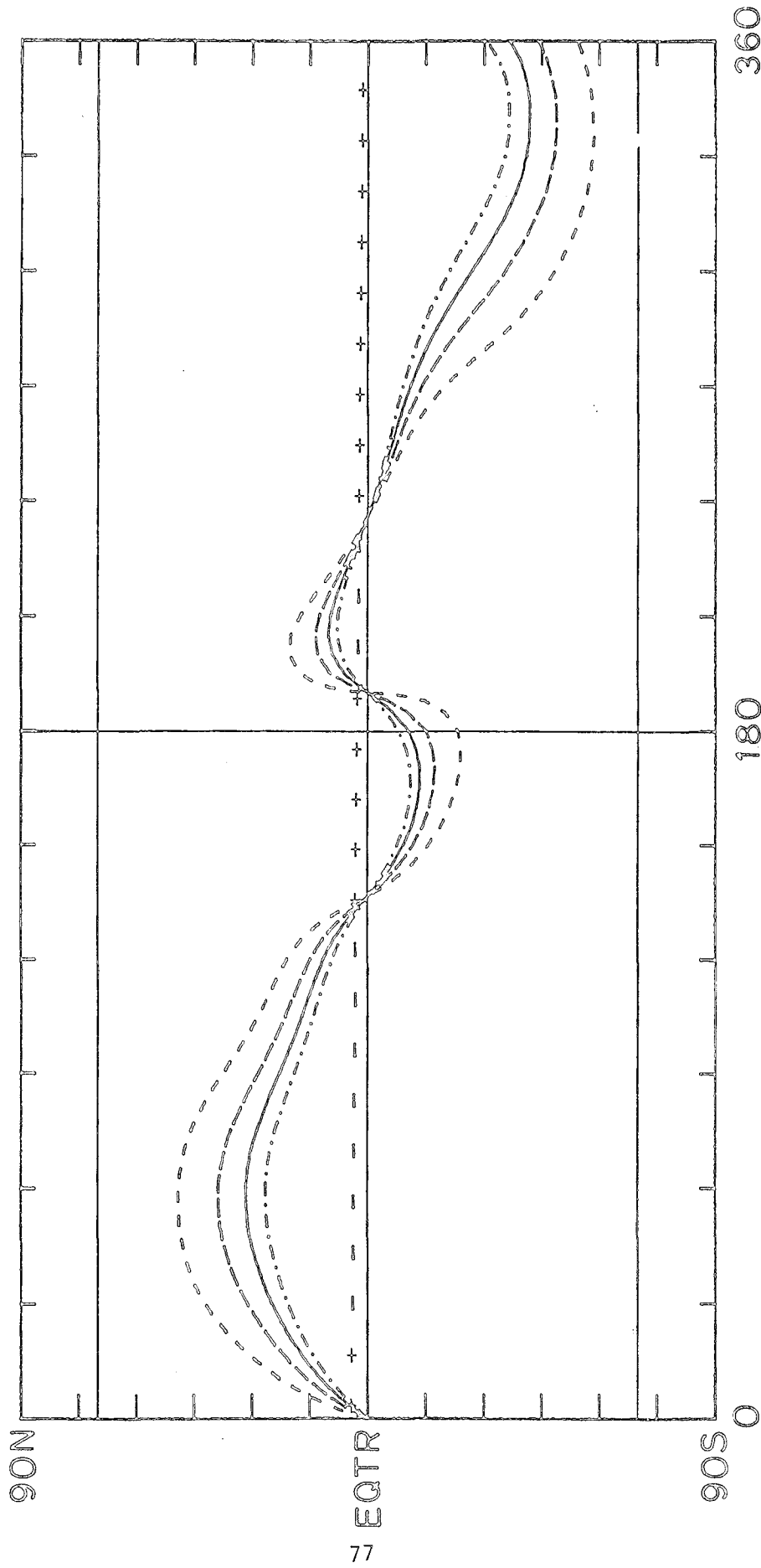


Figure 4-9

in heliographic latitude.

Near  $340^\circ$  longitude the maximum latitude of the current sheet decreases from 58 degrees with no added solar polar field to 37 degrees for 17.3 gauss added field. All of the computed current sheets in Figure 4-9 cross the solar equator at the same longitudes and all of the computed current sheets agree almost equally well with the IMF polarity observed at Earth. The maximum correlation coefficients shown in Figure 4-5 for this interval are nearly the same for all the values of added solar polar magnetic field.

It is interesting that when a larger [smaller] polar field is added, the optimum source surface radius moves lower [higher]. This is because during this interval increasing the polar field and the source surface radius have a similar effect. The polar field correction is anti-symmetric about the equator and therefore reinforces the dipole field. This has the effect of pushing the current sheet toward the equator as shown in Figure 4-9. Increasing the source surface radius tends to emphasize the lower order harmonics, specifically the dipole term. This also tends to push the current sheet toward the equator as shown in Figure 4-6.

Another method of verifying the location of the current sheet is to compare the structure calculated with the potential field model with that inferred from synoptic maps of the observed coronal polarization brightness. Using the neutral line inferred from the Mauna Loa coronameter data at  $1.75 R_\odot$  and the potential field calculated with  $R_s = 2.35 R_\odot$  and the standard polar correction, Wilcox & Hundhausen (1983) made such a comparison for the interval May 1976 through September 1977 near sunspot minimum. On most of the rotations compared, the two methods give essentially the same results; the basic shape of the current sheet and the amplitude in solar latitude of the displacement of the current sheet from the solar equator are similar.

In early 1976 Pioneer 11 reached a heliographic latitude of  $16^\circ\text{N}$  and observed a single polarity in the interplanetary medium for several rotations (Smith et al., 1978). This occurred just a few months before the interval discussed here. Since the field changes slowly near minimum, it is significant

that this is consistent with the extent in latitude of the current sheet calculated for this interval only when the polar field correction is made.

Wilcox et al. (1980) used this model with Mt. Wilson photospheric data in early 1976 to compare with Helios I & II measurements of the interplanetary field reported by Villante et al. (1979). They found good agreement with both Earth and spacecraft measurements from various latitudes within  $7\frac{1}{2}^{\circ}$  of the equator. Unfortunately they neglected the polar field correction as later pointed out by Burlaga et al. (1981). As a result the current sheet extended to higher latitudes than the Pioneer data could allow. This is a further indication of the importance of higher latitude measurements for testing the applicability and accuracy of the model.

During the rising phase of the solar cycle the polar fields weaken and near maximum ultimately reverse polarity. Meanwhile the lower latitude fields become much stronger. The Svalgaard et al. (1978) method requires that the polar field remain relatively constant during the year so that the annual variation can be used to determine the high latitude field. The same method can not be used to calculate the polar correction near maximum, since the polar field strength changes substantially in a year. The strength of the solar polar field correction through December 1982 has been determined by extrapolating the method of Svalgaard et al. (1978).

The straight lines in Figure 4-7 show an estimate of the average polar field strength. This value is used to scale the strength of the polar field correction. Thus the standard field of  $11.5 \cos^{\theta} \delta$  G is added in 1976 - 1977, 0 G near the end of 1979, and a field of about half the original magnitude with the opposite sign following 1981. This indicates that the relative importance of the polar fields in determining the magnetic structure in the equatorial region is probably much smaller near maximum than near minimum. At higher heliographic latitudes the effects may still be important (Levine, 1982). Comparison with coronagraph measurements might be a good way to test this.

The predicted IMF polarity computed with  $R_s$  ranging from 1.6 to 3.1  $R_s$  for each value of the polar field correction has been determined. As before the effects of varying  $R_s$  and the polar field correction on the correlation of

IMF polarity predicted by the model and that observed near Earth have been investigated. Figure 4-10 shows the correlation coefficient at a lag of 5 days to account for the transit time from Sun to Earth vs. source surface radius. The data from 1976 through 1982 divided rather naturally into three equal parts coinciding roughly with intervals when (I) the polar field was constant, (II) the polar field was changing rapidly, or (III) after the field had changed polarity.

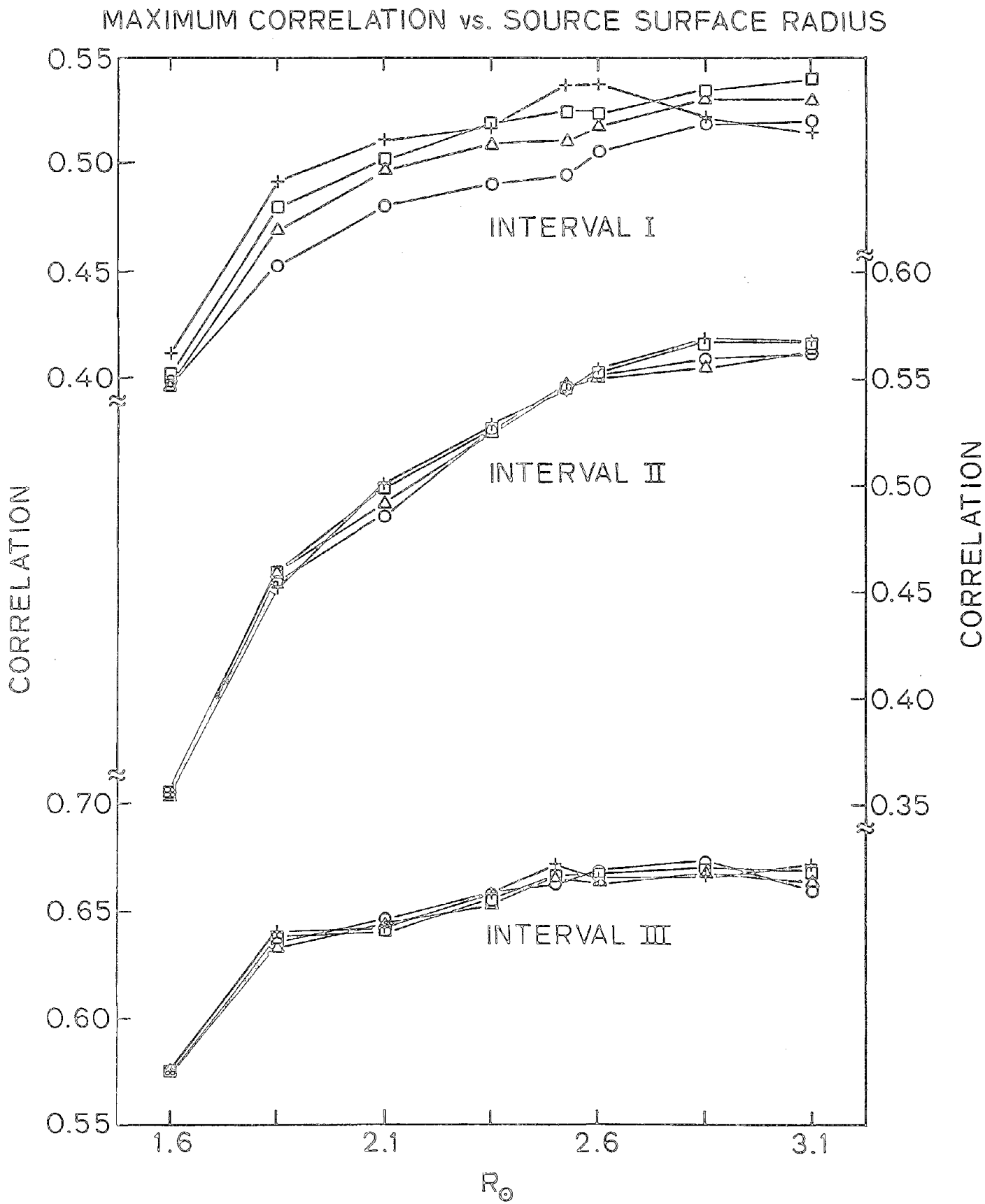
Interval I includes May 1976 through June 1978, the rising phase of the sunspot cycle which includes the time period discussed above. The four curves correspond to different values of the polar field correction. Circles show the result for no polar field addition; triangles for half the standard field; squares for the standard correction of  $11.5 \cos^2 \vartheta$  G; and plusses for 1.5 times the standard strength. The correlations are somewhat lower than those shown in Figure 4-5 because the year beginning September 1977 was a year of large changes in field configuration and the correlation was worse.

Similar curves for the period around maximum, July 1978 to August 1980, are labelled Interval II. Almost no differences exist between the curves for this interval, which demonstrates the unimportance of the polar field in determining the equatorial structure. Interval III, September 1980 through December 1982, shows the results for the beginning of the declining phase. The maximum correlation is substantially higher, due primarily to the structure's simplicity during most of 1982. Again the correlation is rather insensitive to polar field strength.

---

Figure 4-10: Correlation of the measured IMF polarity with that predicted by the model vs. source surface radius. The maximum correlation coefficient for the time period May 1976 - June 1978 (Interval I), indicates an optimum source surface radius of about  $2.5 R_0$ . Circles show the result computed with no polar field correction; triangles for half the standard field; squares for the standard polar field correction of  $11.5 \cos^2 \vartheta$  G; and plusses for 1.5 times that strength. Interval II shows the results for the period around maximum, July 1978 - August 1980, and Interval III for the period September 1980 to December 1982. The correlation is somewhat higher for this last period. The magnitude of the polar field correction does not affect the predictions at the latitude of the Earth during the later intervals. The later curves show little variation with  $R_s$ , so that with an uncertainty of  $0.3 R_0$ ,  $2.5 R_0$  still seems to be about the best source surface radius.

Figure 4-10



In no interval is there a sharp peak suggesting that one source surface radius or polar field strength is clearly the best. There is, therefore, substantial uncertainty in the selection of source surface radius and polar field. Good choices are a source surface radius of  $2.5 R_o$  and the standard polar field correction. There is no significant change with time in the distance at which the source surface should be located. In light of the insensitivity of the determination of the optimum source surface radius, a radius of  $2.5 R_o$  will be used for the entire span of the data unless otherwise indicated. This reflects the uncertainty of about  $0.25 R_o$  in  $R_s$ . Interestingly, for no interval does the correlation for  $R_s = 1.5 R_o$  approach the accuracy of  $2.5 R_o$ . It should again be emphasized that Earth is not a good probe of the heliosphere being limited to solar latitudes less than  $7.3^\circ$ . When the latitudinal extent of the current sheet substantially exceeds this limit, the best source surface radius or polar field correction cannot be conclusively determined using this method.

#### *The Monopole Component*

Discussion of the monopole component, or zero offset, is more a consideration of the errors that contribute to the calculation of the potential field model than the determination of some parameter of the model. While there has been speculation that the sun may have a small monopole field (Wilcox, 1972), the zero offset determined in this study varies in both magnitude and sign on relatively short time scales, suggesting another source for this signal. Figure 4-11 shows the monopole component computed at each  $10^\circ$  interval from May 1976 through December 1983. Scaled in microtesla, this figure shows that during most of the interval the zero offset was rather small and fluctuated slowly about zero.

---

Figure 4-11: The monopole component of the field computed each  $10^\circ$ . The magnitude of the component varies with the general field strength of the photospheric field and has an average value very close to zero (about  $0.2 \mu T$  at the source surface). This component comes mostly from evolving active regions and differential rotation.

CALCULATED MONOPOLE AT SOURCE SURFACE

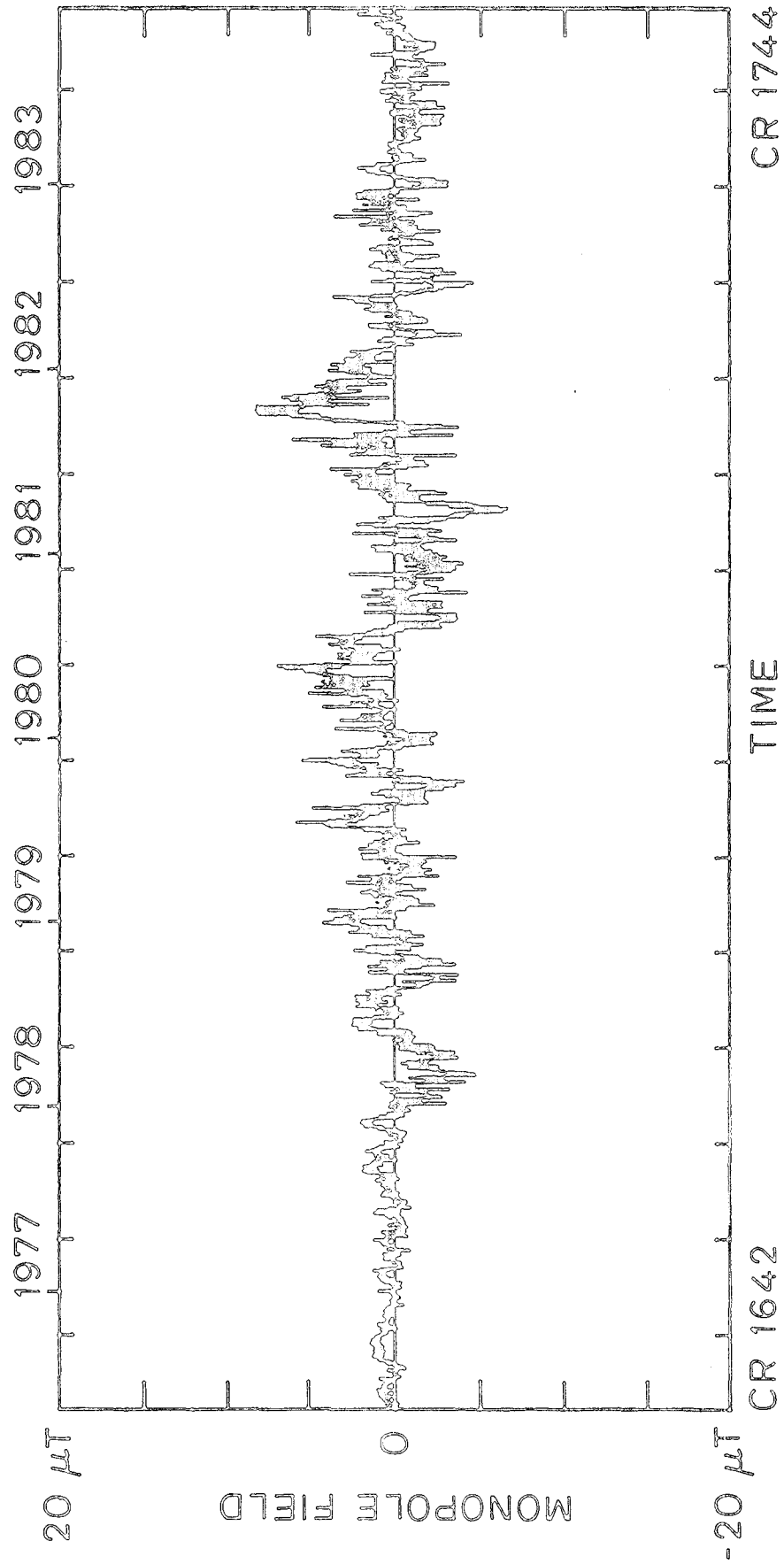


Figure 4-11

During only three intervals near Carrington times (CT) 1695:220, 1706:060, and 1713:030, in May 1980, and April and October of 1981, does the zero offset become very large. In the first two cases the extremely high values persisted for only a single rotation; the trend following Rotation 1713 lasts somewhat longer. Examination of the photospheric data for each of these intervals shows that in no case is there any missing data which could contribute to the signal. However comparison of the photospheric field near the edges of the data shows that rapidly evolving active regions probably produce this signal.

Figure 4-12 shows the photospheric field for Carrington Rotations (CR) 1713 and 1714. Compare the positive region at  $40^\circ$  longitude just south of the equator on the two rotations. The peak field during CR 1713 is about  $600 \mu T$  whereas the maximum strength is well over  $2000 \mu T$  in the following rotation. The region is also located farther to the east in the second rotation which adds to the imbalance when computing the potential field using a  $360^\circ$  interval. Similar strengthening has occurred in the neighboring positive regions but not in the negative regions. This suggests that there is an excess of measured positive polarity near this longitude. The mean field of the sun measured as a star, also determined at the Stanford observatory using an independent set of measurements and plotted above the synoptic charts, also shows an excess of positive flux for CR 1714.

Each of the other large excursions in zero offset can be explained in a similar manner. This suggests that most of the "monopole" component arises because of rapid evolution of strong field regions and because of the slower than Carrington rotation rate of the mid-latitude strong fields. This explains why this component varies only slightly near minimum: there are few strong field regions. This also explains why the variations are strongest near maximum: there is more flux everywhere on the sun, more rapid evolution of the field configuration, and the active regions occur at higher latitudes where differential rotation effects are more pronounced. After maximum, as the latitude of the active regions decreases, the variations in the monopole component become smaller as well.

Other conditions which may produce a zero offset are zero level errors



in the magnetograph signal, magnetograph saturation effects, luminosity weighting of strong field regions, measurement of only the line-of-sight component of the field, and the tilt of the polar regions (Pneuman et al., 1978).

As discussed in Chapter 2, the Stanford instrument was built to measure the large scale, weak field of the sun. As such zero level errors have been largely eliminated and are tested for in conjunction with each measurement. Saturation effects in the large aperture are understood and have the effect of scaling all the measurements by a constant factor (Svalgaard et al., 1978). Luminosity weighting is a problem, especially for the largest active regions, and probably contributes the most to the unbalanced flux measured near some active regions.

The effect of measuring only one component of the field is uncertain. Svalgaard et al. (1978) showed that the  $5250\text{\AA}$  measurements varied with disk longitude as if they were radial fields for both strong and weak field regions. This suggests that except near the poles, the field will be measured quite accurately. One would expect that the annual variation in the tilt of the poles would influence the zero offset, especially near minimum since the polar field is so strong. However the line-of-sight component of the field is very small and, since the Stanford instrument measures the field accurately only to  $75^\circ$ , contributes little to the offset. This can be shown from analysis of the power spectrum of the monopole component which shows very little power contribution from frequencies near a 1/year.

Typical field values near maximum at the photosphere are several hundred to several thousand microtesla. The zero offset is usually less than  $20 \mu T$ , being only a few per cent of typical field values at the photosphere. As discussed in Chapter 5, the power in the zero offset is almost always negligible compared with the power in the other components.

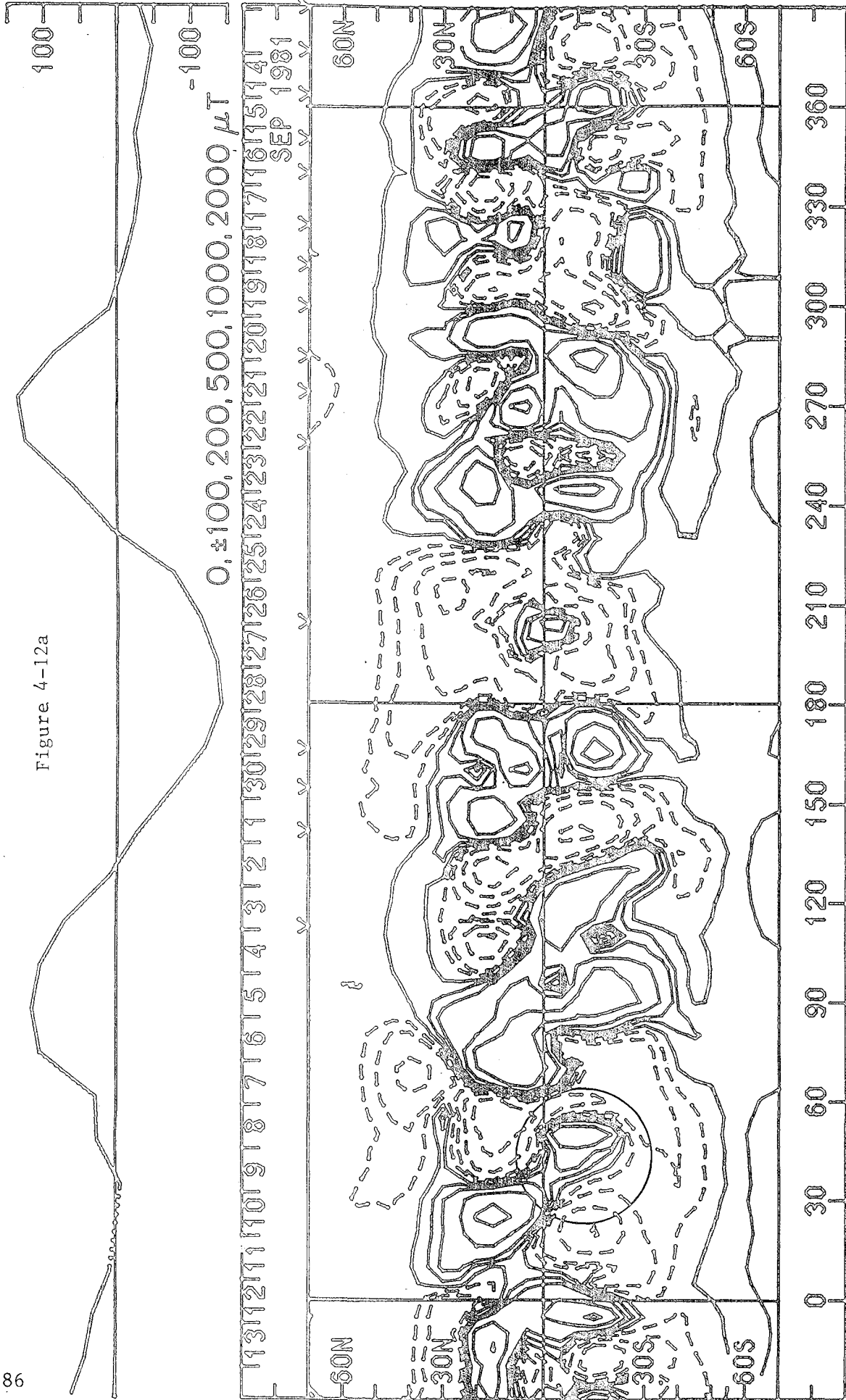
Having described the zero offset, the question of what to do with it remains. Since it arises from errors in the magnetograph measurements and

---

Figure 4-12: a) Synoptic chart for CR 1713. b) Synoptic chart for CR 1714. Note the changes in the circled field regions which produce a large monopole component in the computed field.

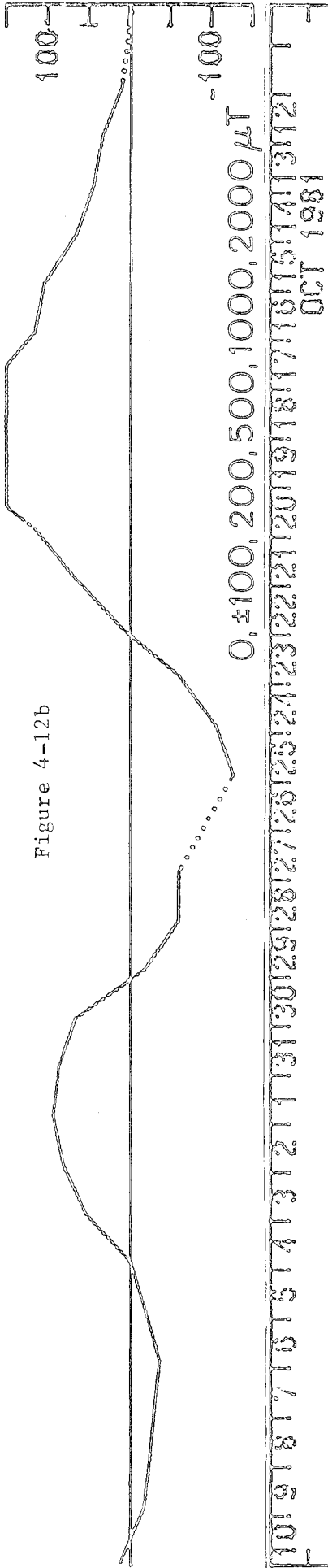
STANFORD MEAN FIELD

Figure 4-12a



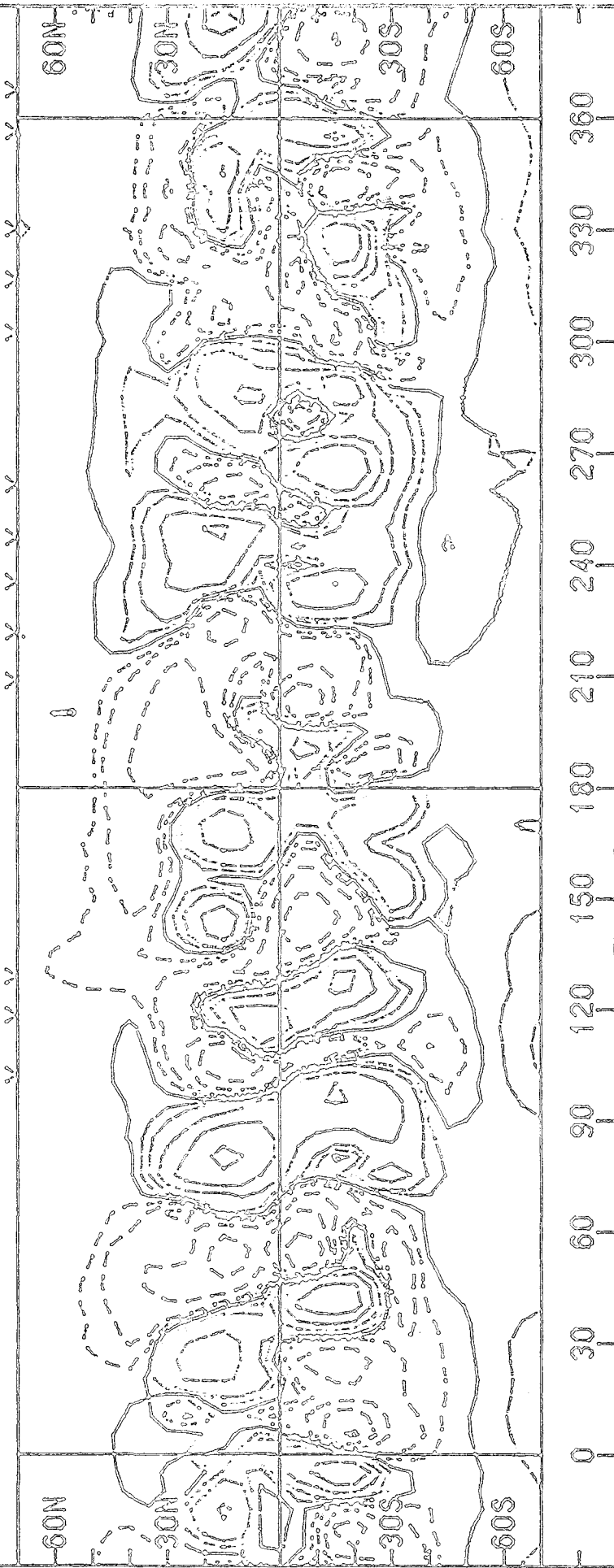
# STANFORD MEAN FIELD

Figure 4-12b



0, ±100, 200, 500, 1000, 2000 μT

OCT 1981



# PHOTOSPHERIC FIELD

1714

problems with the observation of an evolving field over an extended period of time, it should be removed. Justification for removing the monopole component comes from a consideration of where it arises relative to the data kept in this analysis. Most of the offset comes from rapid evolutionary changes in the field strength near the edges of a data window. The data kept when constructing the final dataset comes only from the center of the data window. The monopole term changes the zero level over the whole surface, far from the edges where the signal arises. For this reason it is best to remove the "monopole" signal to get the best representation of the field.

The question remains of how to do this. Simply excluding the calculated monopole from the field constructed from the g's and h's makes the combination of consecutive calculations difficult because the variations in the zero offset create large jumps between successive  $10^\circ$  calculations of the field. This is apparent from the noisy character of Figure 4-11. A second alternative would be to subtract the  $360^\circ$  running mean of the monopole components. But these components no longer really represent the final dataset which is composed of only the central strips of many computations, the monopole components of which arise from data far from the central strips of the calculations.

It was finally decided that the best way to determine the zero offset was for each  $5^\circ$  strip of source surface data to compute the average field (zero offset) for the surrounding  $360^\circ$ . This is the smooth curve shown in Figure 4-13 and represents the best estimate of the zero offset error. This zero offset is subtracted from the computed field. The curve has been normalized to be directly comparable with the magnitude of the zero offsets plotted in Figure 4-11 which refer to the photospheric field.

---

Figure 4-13: The zero offset removed from the final field computation. Because the final dataset is a composite of many computations, the zero offset finally removed is calculated for each longitude from the surrounding  $360^\circ$ . As in Figure 4-11, the magnitude refers to the source surface value.

ZERO OFFSET ACTUALLY REMOVED AT SOURCE SURFACE

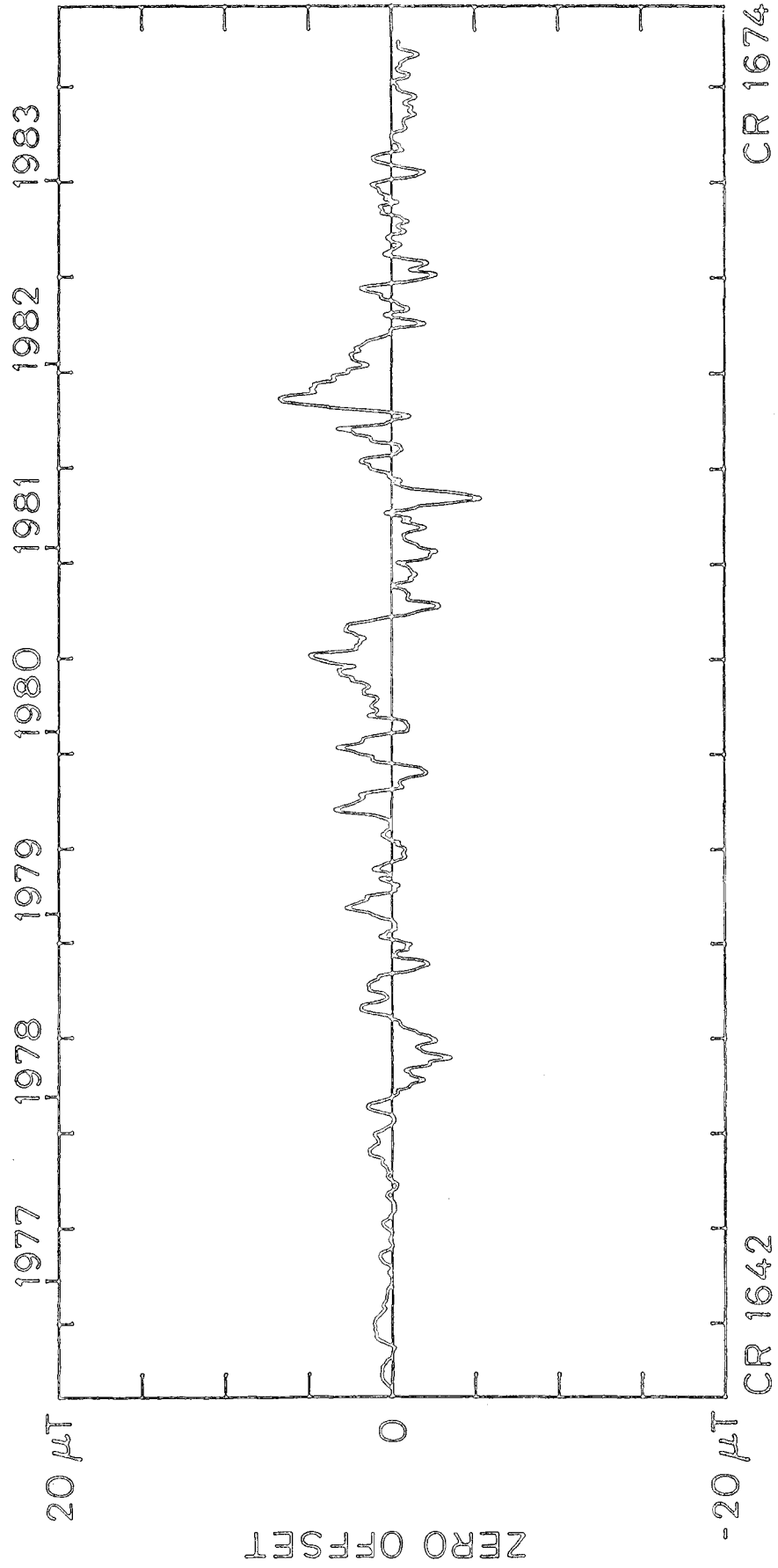


Figure 4-13

### *Summary*

In this chapter the model introduced in Chapter 3 has been developed to a point where it can provide useful information about the heliospheric field. Comparison of the IMF polarity measured by spacecraft near Earth with that predicted by the model shows that the model predicts the large scale structure quite accurately. Unfortunately this is only a weak test of the model's validity; however, it is the only test available during the entire interval. Using this comparison to investigate the source surface radius, the only real parameter of the model, it is found that a source surface radius of about  $2.5 R_{\odot}$  gives a good prediction of the IMF polarity throughout the entire interval.

The polar field, not completely measured by the magnetograph, has been inferred from the annual variation in the polar field strength (Svalgaard et al., 1978). This and the fact that the latitudinal extent of the current sheet is incorrect when the polar field is ignored (e.g. Burlaga et al., 1981 in reference to Wilcox et al., 1980) indicates that additional polar field must be added to the photospheric data. In order to test the inferred polar field strength, several values of the correction were added to the data. Comparison of the measured and predicted IMF indicates that the inferred field value near minimum of  $11.5 \cos^2 \theta$  G (corrected for magnetograph saturation) should be added to the data. The polar field correction was modified through the cycle as the polar field weakened and reversed sign. Around maximum when the low latitude fields were strong and the polar field weak, the form of the added field had little effect on either the field configuration at the source surface or the correlation with the measured IMF polarity.

Finally, the nature and significance of the zero offset in the calculated field was discussed. Most of the zero offset arises from the relatively rapid evolution of strong field regions. In any case the zero offset is almost always very small compared to the rest of the field. Comparison of the predicted and observed IMF polarity shows a slight (0.01 - 0.03) improvement in the correlation during most intervals when the "monopole" computed for each longitude is removed.

Having set up the model calculation, the results are discussed in the following chapter.

## Chapter 5 -- The Heliospheric Field

At last the investigation of the heliospheric field can begin. The magnetograph data have been described, the model has been developed, the source surface radius, polar field correction, and zero offset have been determined and incorporated into the model. Even the form in which the results are presented has been described. Finally we proceed to learn about the sun!

In this chapter the configuration of the heliospheric magnetic field is described as it evolves from a simple, equatorial structure near minimum in 1976; to a convoluted structure near maximum in 1980 which extends to high latitudes; to a simpler, stable high latitude structure in 1982 - 1983. To do this we follow the development of the field at the source surface by discussing typical Carrington rotations from each time interval and by presenting the computed current sheets in such a way that the long term evolution can be easily seen. This incorporates the analysis of two papers published using this data by Hoeksema et al. (1982, 1983). The first interval includes the quiet time around minimum from May 1976 to September 1977. During this interval the polar field changed very little, the current sheet evolved relatively slowly, and the latitudinal extent of the current sheet conformed with the prevailing opinion that the extent in latitude must be rather small. As in Hoeksema et al. (1982), for this interval a source surface radius of  $2.35 R_{\odot}$  will be used since it gave the best correlation with the IMF polarity. During this period the zero offset was extremely small and so has been ignored for the field values computed at  $2.35 R_{\odot}$ .

The following section deals with Interval I which encompasses the expanded interval CR 1641 - CR 1669, May 1976 through June 1978. This overlaps the original interval but includes what is typically considered the rising phase of the solar cycle. As in Hoeksema et al. (1983), for this and subsequent intervals  $R_s = 2.5 R_{\odot}$  and the zero offset has been removed. The latitudinal extent of the current sheet increases markedly near the end of the interval, but the structure is a simple deformation of the configuration observed in 1976. The polar field correction remained constant throughout

this interval.

During the next interval which includes solar maximum, CR 1670 - CR 1699, June 1978 to September 1980, the polar field reverses. For much of this interval the current sheet extends to the poles. The structure is quite complex and even includes multiple current sheets at times. In spite of the more rapid evolution of the field, the large scale structures continue to show lifetimes of several years.

Interval III includes the beginning of the declining phase of the cycle from September 1980 - December 1982, CR 1700 - CR 1729. During this time the field structure is extremely stable and exhibits both 2 and 4 sector structure in the ecliptic plane. The polar field remains constant but is opposite in sign to that during Interval I with about half the magnitude. Because of the stability and simplicity of the ecliptic structure, the accuracy of the predicted IMF polarity increases for this interval.

The computations for 1983 show that the latitudinal extent of the current sheet remains fairly high and that the structure keeps about the same level of complexity for the entire year. The strong field regions are extremely stable. The IMF data has not yet become available to us for 1983 for comparison with the predicted polarity.

#### *Solar Minimum - 1976 - 1977*

The first interval investigated includes only the time nearest solar minimum when the structure was simple and the polar field remained constant. The structure of the heliospheric current sheet on a spherical source surface of radius  $2.35 R_{\odot}$  has been computed using the potential field model during the first year and a half after the last sunspot minimum, CR 1641 - CR 1658. The solar polar magnetic field not fully observed in conventional magnetograms has been included. Being very small, the zero offset has been ignored in the analysis of this interval.

During this time interval there was an electric current sheet that was warped northward and southward of the plane of the solar equator (Schulz,



1973). North of the current sheet the interplanetary magnetic field (IMF) was directed away from the sun and south of the current sheet the IMF was directed toward the sun. The magnetic field polarity (toward or away from the sun) at the sub-terrestrial latitude on the source surface agreed with the interplanetary magnetic field polarity observed or inferred at Earth on 82% of the days. The interplanetary field structure observed at Earth at this time is finely tuned to the structure of low-latitude fields on the source surface.

The minimum between sunspot cycles 20 and 21 occurred in June 1976. During the 18 Carrington Solar Rotations beginning in May 1976 the computed current sheet was quasi-stationary, having in each solar rotation two northward extensions and two southward extensions. This usually produced the characteristic four sector structure in the IMF observed at Earth (Svalgaard and Wilcox, 1975). Occasionally during a rotation one or even both of the northward extensions of the current sheet "missed" the Earth resulting in a two sector or even a "zero" sector structure being observed at Earth. Around sunspot minimum the maximum extent in latitude of the computed current sheet was about  $15^\circ$ , while by the end of the 18 solar rotations discussed here the maximum latitude had increased to about  $45^\circ$ . Just after the time interval discussed here the maximum latitude of the current sheet increased further and the quasi-stationary structure of the current sheet began to change, so September 1977 seems a natural point to end the first interval. Furthermore the original Svalgaard et al. (1978) analysis of the polar field covered this same time period. The structure of the computed heliospheric current sheet in later portions of sunspot cycle 21 will be discussed in later sections.

The radial magnetic field computed on a spherical source surface at  $2.35 R_\odot$  for CR 1648 beginning 7 November 1976 is shown in Figure 5-1. The neutral line, corresponding to the zero contour, appears as a thick solid line

---

Figure 5-1: A contour map of the radial magnetic field in the same format as Figure 3-4, but for Carrington Rotation 1648 beginning 7 November 1976. Note that the computed heliospheric current sheet extends only a few degrees in latitude from the solar equator.

SOLAR SOURCE SURFACE

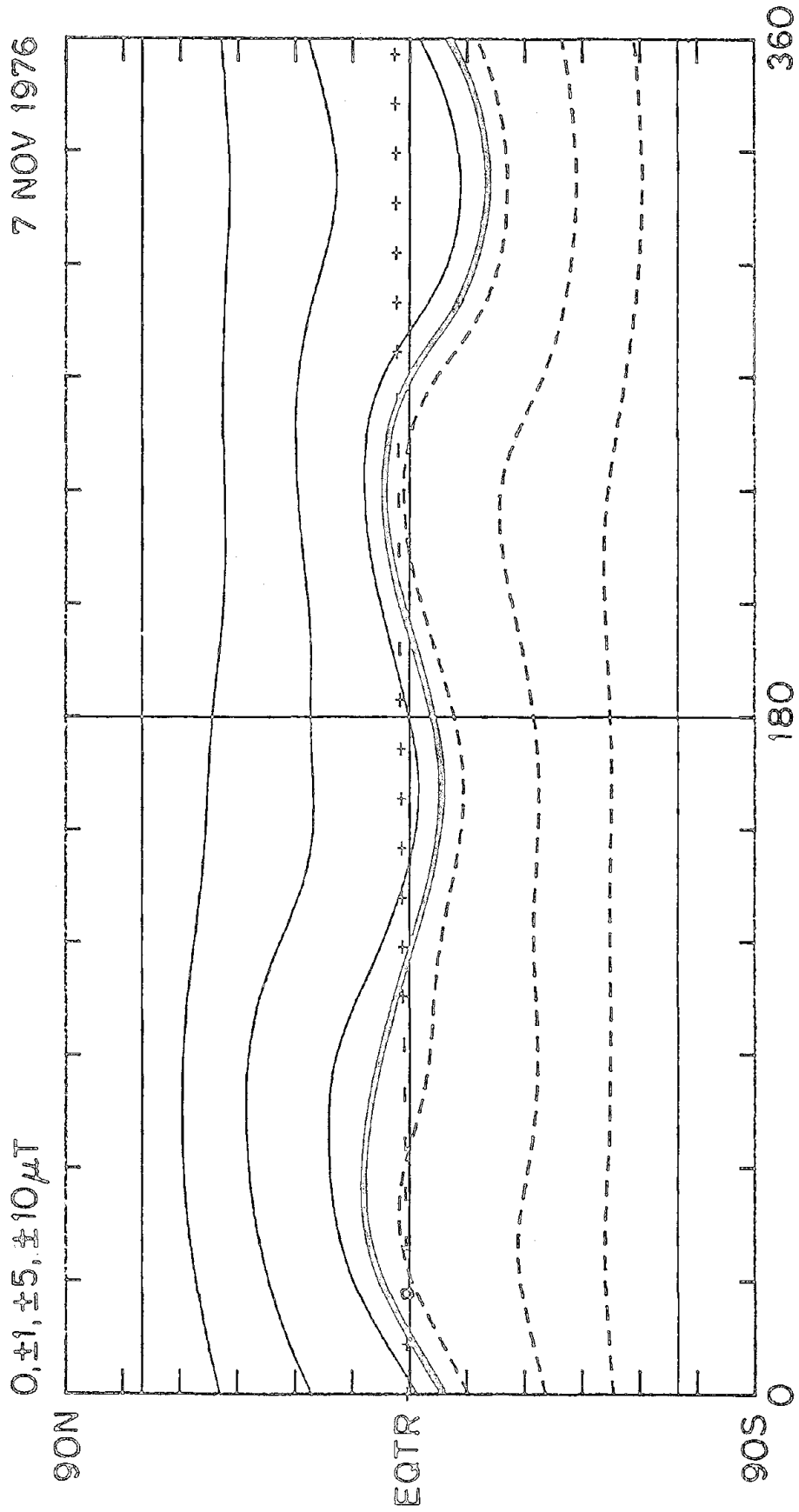


Figure 5-1

near the equator. Extension of the neutral line radially outward by the solar wind defines the current sheet in the heliosphere. This line will henceforth be referred to as the current sheet. The solid contours above the current sheet represent field directed away from the sun with magnitudes  $\pm 1$ , 5, and 10 microtesla, while the dashed contours represent field directed toward the sun with the same magnitudes. The predominance of away polarity magnetic field in most of the northern region of the heliosphere and of toward field in most of the southern heliosphere is apparent in Figure 5-1. In all cases, contours of the magnetic field refer to values which are *not* corrected for magnetograph saturation. These values should be increased by a factor of 1.8. The magnitude of the polar field correction is always quoted in units which *are* corrected for saturation.

The + (away from the sun) and - (toward the sun) symbols in Figure 5-1 represent daily polarities of the interplanetary magnetic field at Earth as observed by spacecraft (King, 1979a) or, when spacecraft observations were not available, inferred from polar geomagnetic observations (Svalgaard, 1973). The IMF polarities at Earth shown in Figure 5-1 have been displaced by five days corresponding to the average transit time of solar wind from sun to Earth near the times when the large-scale magnetic polarity changes (sector boundaries) as determined by the correlation analysis described in the previous chapter. Since the velocity of the solar wind near sector boundaries is almost always a local minimum (Wilcox and Ness, 1965), this transit time is longer than the average solar wind transit time.

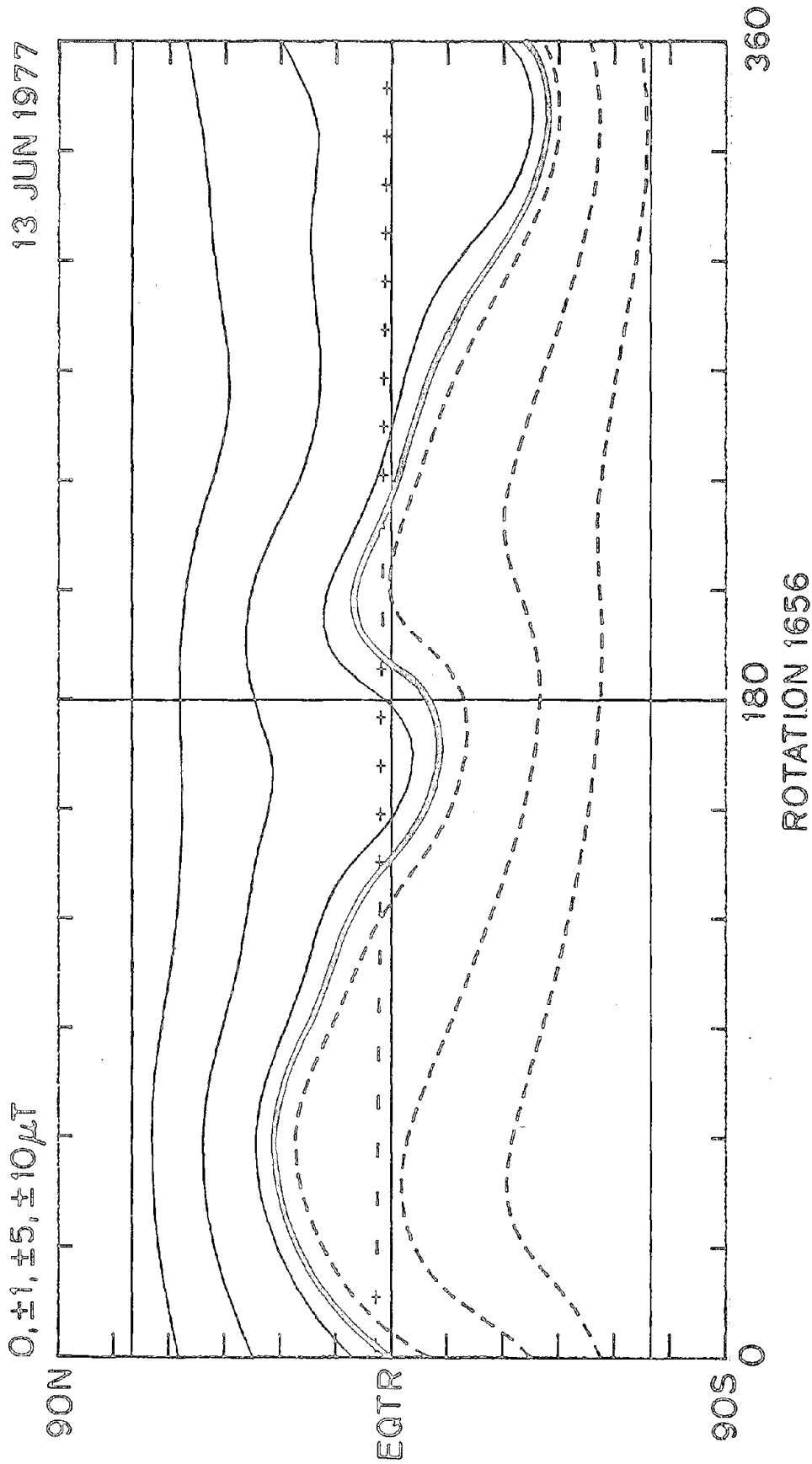
The structure exhibited in CR 1648 is typical of the structure near minimum -- largely equatorial with warps in the current sheet producing 4 sectors near the Earth. CR 1656 beginning 13 June 1977, presented in Figure 5-2, exemplifies the computed field at the source surface later in this interval. The extent in latitude of the computed current sheet had increased to about  $40^\circ$ , but the same property of two northward excursions and two southward

---

Figure 5-2: The same format as Figure 5-1, but for a later Carrington Rotation 1656 beginning 13 June 1977. Note that the extent in latitude of the computed heliospheric current sheet extends to higher latitudes than in Figure 5-1.

Figure 5-2

SOLAR SOURCE SURFACE



excursions in the current sheet (a four sector structure) was still evident. At latitudes slightly greater than that of the Earth, only two sectors would have been observed in either the northern or southern hemispheres.

Figures 5-3 and 5-4 show the computed current sheets and IMF polarities observed at Earth during the 18 solar rotations in this interval. In every rotation except CR 1644 there were two northern and two southern extensions of the current sheet, corresponding to a basic four sector structure. In CR 1645 the computed current sheet was everywhere southward of the heliographic latitude of the Earth, and the IMF polarity observed at Earth was almost entirely away from the sun. This presumably is an example of the situation discussed by Wilcox (1972) in which near the last five (now six) sunspot minima the observed or inferred IMF polarity has been largely away from the sun during a few consecutive rotations. If the current sheet simply "misses" the Earth near the time of a sunspot minimum the resulting predominant IMF polarity could be either away from or toward the sun according to the considerations discussed in this paper. A predominance in *away* polarity in the observed photospheric field also discussed by Wilcox (1972) would not necessarily be directly related to the situation shown here in CR 1645.

Hundhausen (1977) noted that a "monopolar" sector structure as seen in CR 1645 of Figure 5-3 might appear at the beginning of a new solar cycle. However, the suggestions that at this time "The prominent recurrent sectors, streams and geomagnetic activity sequences should end abruptly" and that

---

Figure 5-3: The heliospheric current sheet computed on a source surface at  $2.35 R_{\odot}$  on nine successive Carrington Rotations, 1641-1649, beginning on 30 April 1976 to 4 December 1977. Compare for example the current sheet shown here for Carrington Rotation 1646 with that shown in Figure 5-2. Each succeeding base line (solar equator) is displaced by 45 degrees heliographic latitude. The + and - symbols represent daily values of the IMF polarity observed at Earth allowing for the five day transit time of solar wind from Sun to Earth. Significant disagreements between the predicted and observed IMF polarities are indicated with a thicker neutral line. (The first rotation shown in Figure 5-3 is near sunspot minimum.)

Figure 5-4: The same as Figure 5-3, but for the next nine Carrington Rotations, 1650-1658, beginning 1 January 1977 to 7 August 1977. Note that the extent in latitude of the computed current sheet increases in the later rotations.

Figure 5-3

# HELIOSPHERIC CURRENT SHEETS

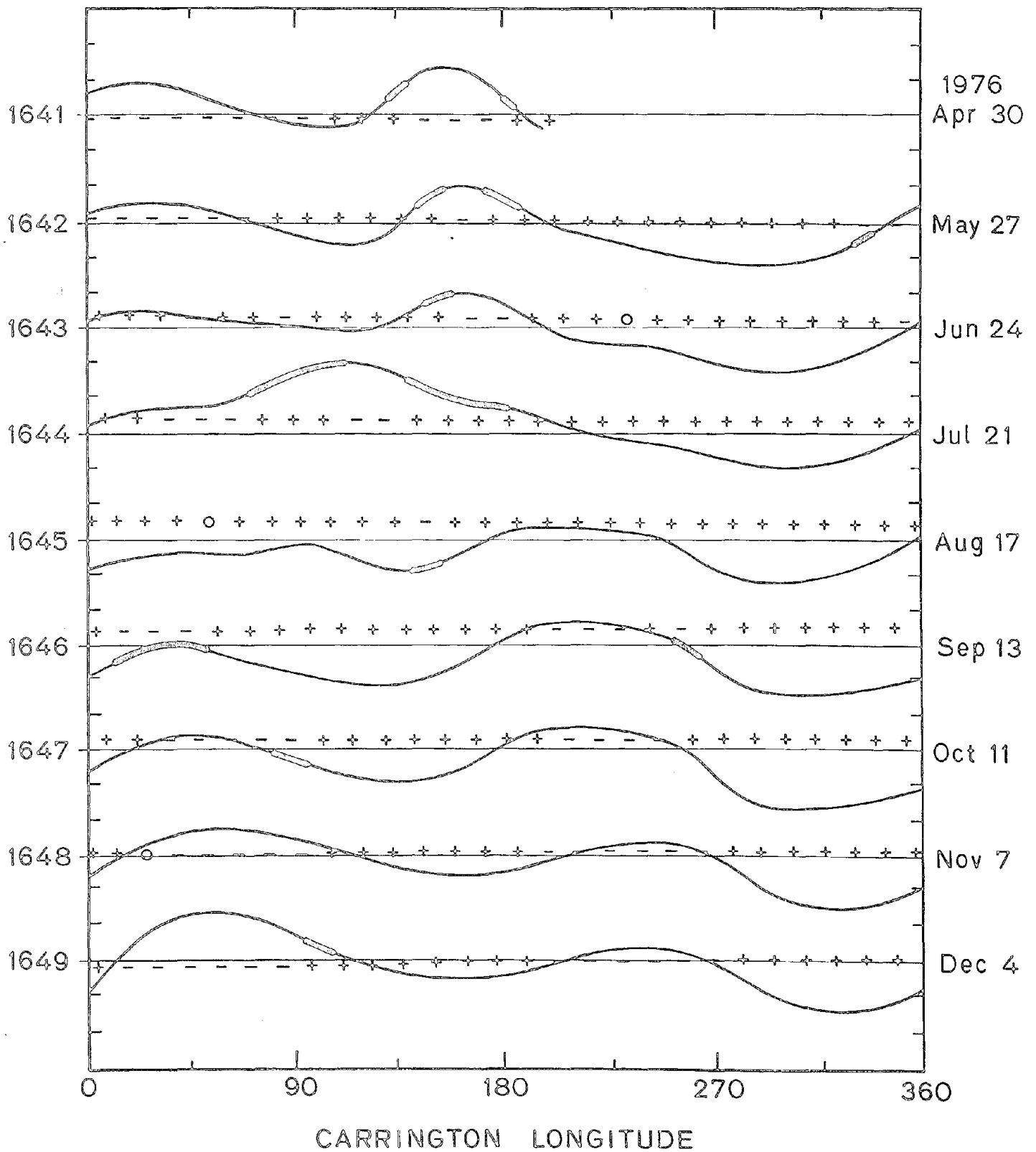
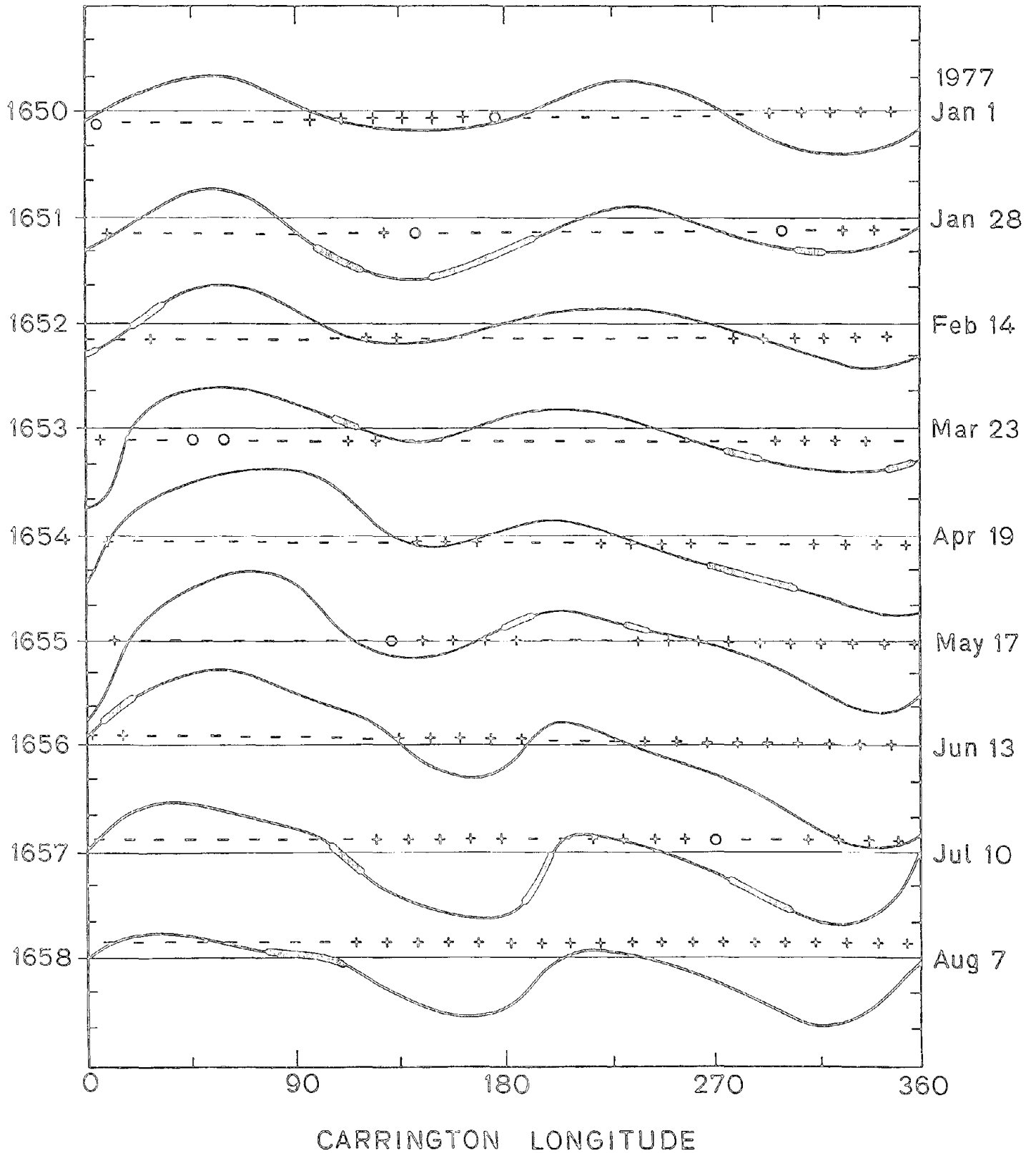


Figure 5-4

# HELIOSPHERIC CURRENT SHEETS



"Recurrence with the 27-day solar rotation period should become rare" are not consistent with either the observed IMF structure or the computed current sheets in Figures 5-3 and 5-4.

In CR 1658 the computed current sheet had a clear "four sector" structure, but was sufficiently far south of the heliographic latitude of the Earth that only two sectors were observed. This appears to be the same geometry but the opposite sense from the situation in early 1976 described by Scherrer et al. (1977).

From the start of Figure 5-3 near the minimum of the eleven year sunspot cycle to the end of Figure 5-4, 1.5 years later, the maximum extent in latitude of the computed current sheet increased from about  $15^\circ$  to about  $45^\circ$ . This increase is qualitatively similar to but larger than the average variation computed by Svalgaard and Wilcox (1976) through the previous four sunspot cycles.

Burlaga et al. (1981) noted that for CR 1639 and CR 1640, just before the start of the interval shown in Figure 5-3, a solar dipole magnetic axis tilted about  $20^\circ$  to  $15^\circ$  with respect to the solar rotation axis cannot explain the sector pattern observed by Helios. The sector patterns shown in Figure 5-3 and 5-4 during 1.5 years after the rotations discussed by Burlaga et al. (1981) also cannot be explained with a tilted dipole, as was proposed by Smith et al. (1978), Villante et al. (1979), Smith and Wolfe (1979), Zhao and Hundhausen (1981), and Hakamada and Akasofu (1981).

On most of the rotations during 1976 shown in Figure 5-3 the current sheet extended more into the southern heliosphere (the case of CR 1644 is discussed below), which is consistent with the results of Wilcox et al. (1980), Burlaga et al. (1981) and Villante et al. (1982). The conjecture of Villante et al. (1982) that the current sheet during the first half of 1977 was confined to a narrower latitude region is not consistent with the current sheets shown in Figure 5-4.

In Figures 5-3 and 5-4 intervals of significant disagreement between the IMF polarity predicted by the computed current sheet and that actually observed are indicated by a bar attached to the current sheet. We note that for the most part the daily polarity of the IMF observed at Earth is quite well



predicted by the computed current sheet; in fact there is agreement on 82% of the days.

A conspicuous disagreement is associated with the rapid change in the computed current sheet from one rotation to the next at CR 1644. This change in the computed current sheet was caused by the appearance of a particularly large bipolar magnetic region in the photosphere. The corresponding IMF polarity observed at Earth was away on several days during which the computed current sheet would lead to a prediction of toward field. It seems possible that there may have been a region of toward magnetic field polarity in the heliosphere corresponding to this bipolar magnetic region, but at a latitude sufficiently far north so as not to intersect the Earth, but we have no direct evidence for this. This discrepancy is investigated in more detail in a later chapter in conjunction with discussion of the Mauna Loa coronameter determination of the current sheet. That analysis suggests that the potential field configuration for CR 1644 is incorrect. The zero offset increases during this rotation. Comparison of the current sheet calculated here with that shown in the following section with the zero offset removed shows some moderation of the effects of this unbalanced flux region, though the change is not great. A similar event occurred near 140° longitude in the southern hemisphere in CR 1651.

The rather rapid change in the computed current sheet near longitude zero from CR 1652 to CR 1653 was also caused by the appearance of a large bipolar magnetic region in the photosphere, but in this case the region remained in the photosphere for several rotations, and the corresponding effects on the computed current sheet also continued for several rotations.

In many of the rotations shown in Figures 5-3 and 5-4, the latitude of the current sheet at the end of the rotation differs significantly from the latitude at the start of the rotation. This illustrates the advantage gained from computing the field structure on the source surface at steps of 10 degrees in the starting longitude, since if only one computation were made for each rotation the latitude of the current sheet at the beginning and the end of the rotation would be forced to be the same.

### *The Rising Phase - 1976 - 1978*

In order to extend the analysis described above, the polar field correction of Svalgaard et al. (1978) had to be extended, as described in the previous chapter. The extension naturally divided the available data into three roughly equal segments characterized by (I) constant polar field strength, (II) changing polar field strength, and (III) constant polar field of polarity opposite to that in Interval I. The correlation analysis described in Chapter 4 indicated that a source surface radius of  $2.5 R_{\odot}$  adequately represented the optimum choice for the entire period. The zero offset has been removed from the data for the entire period as well.

In order to compare with the calculations described in the last section and to put the results for later in the rising phase of the cycle in perspective with those nearest minimum, all of the current sheets from CR 1641 through CR 1669 computed with these parameters are presented and discussed. Comparison of the results shown below with the earlier results presented above show only very small differences. This indicates that the uncertainty in  $R_s$  of about a quarter solar radius is reasonable. This also shows that except for CR 1644 the zero offset had little effect during this period. After presenting the results for a representative rotation, as in the previous section, the evolution of the large scale structure for the interval as a whole will be discussed.

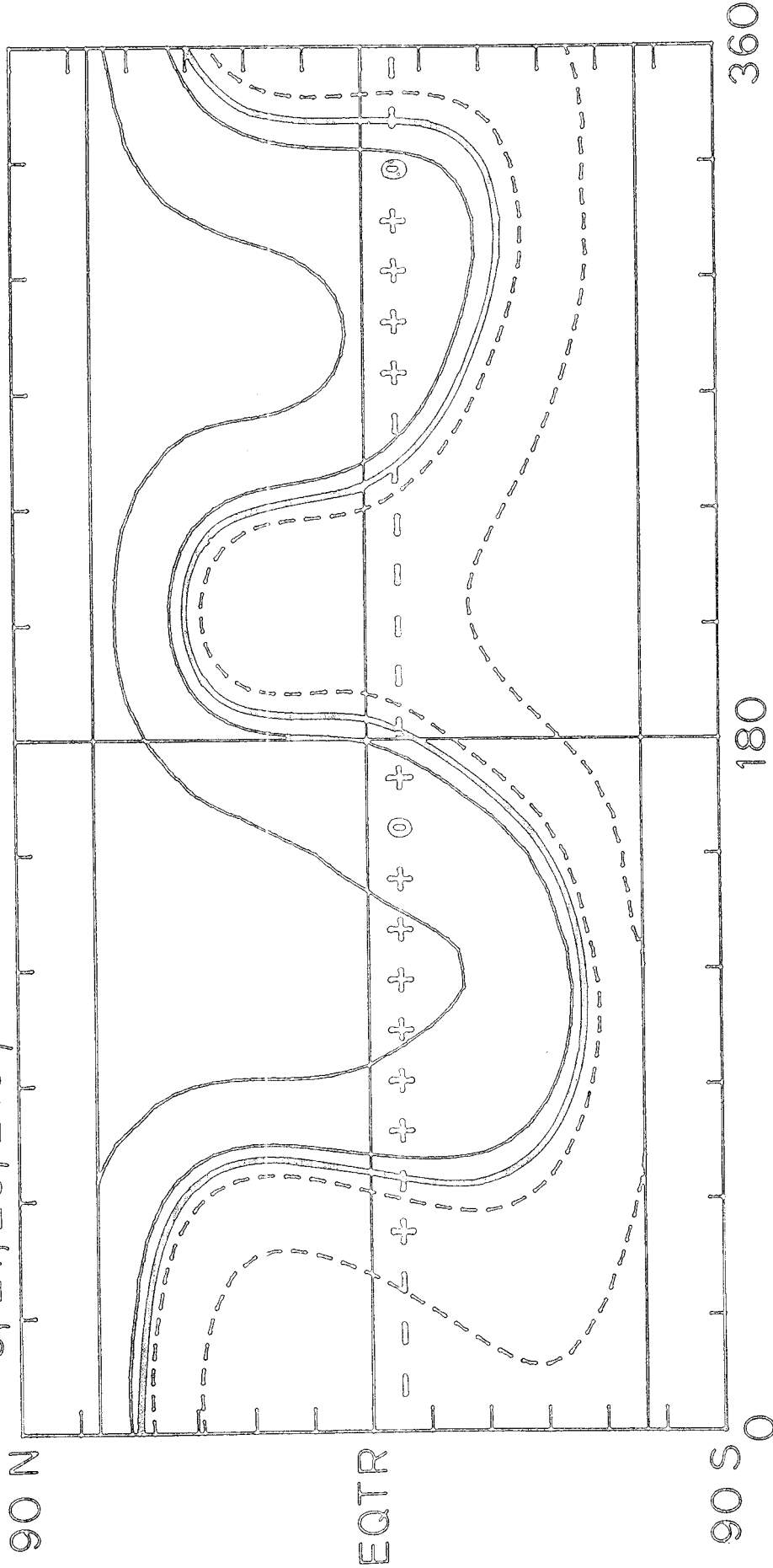
The contour plot in Figure 5-5 depicts the radial field strength at the source surface for CR 1665. This magnetic configuration is characteristic of the heliospheric structure throughout 1978. Once again the daily averages of IMF polarity measurements made near Earth have been corotated back to the source surface at the heliographic latitude of the Earth assuming a propagation time from sun to Earth of five days.

---

Figure 5-5: The radial field computed at the source surface for Carrington Rotation 1665 is typical of the interval 1978 - 1979. The sector structure at Earth is much the same as it was near minimum though the current sheet extends to almost  $60^{\circ}$  latitude.

SOURCE SURFACE AT  $2.5 R_{\odot}$   
27 FEB 1978

$0, \pm 1, \pm 5, \pm 10 \mu T$



ROTATION 1665

Figure 5-5

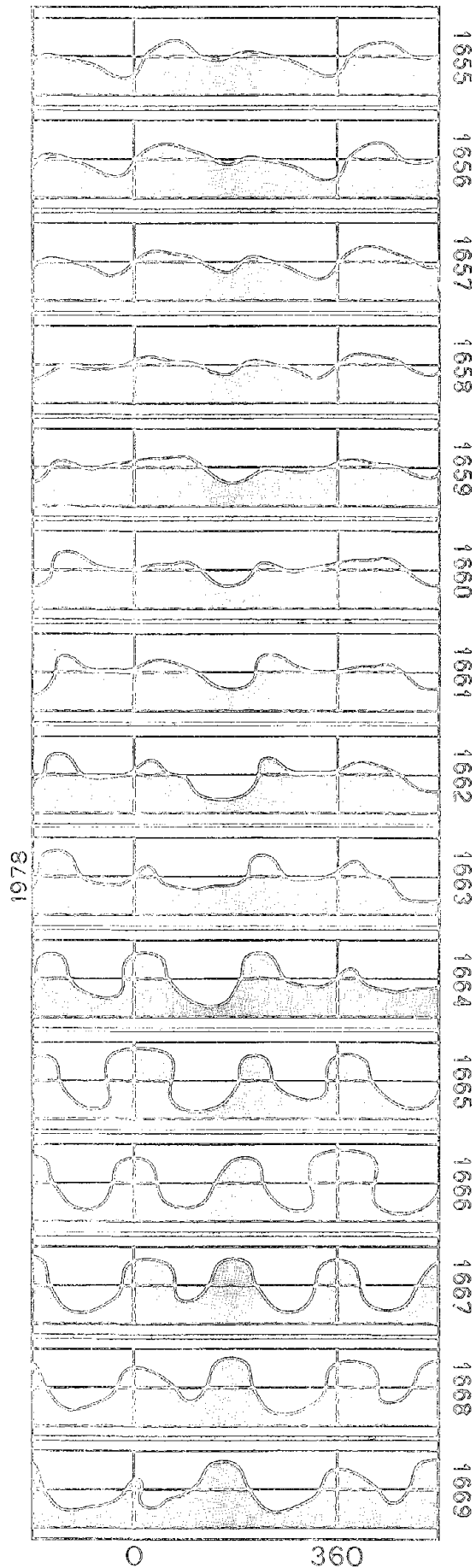
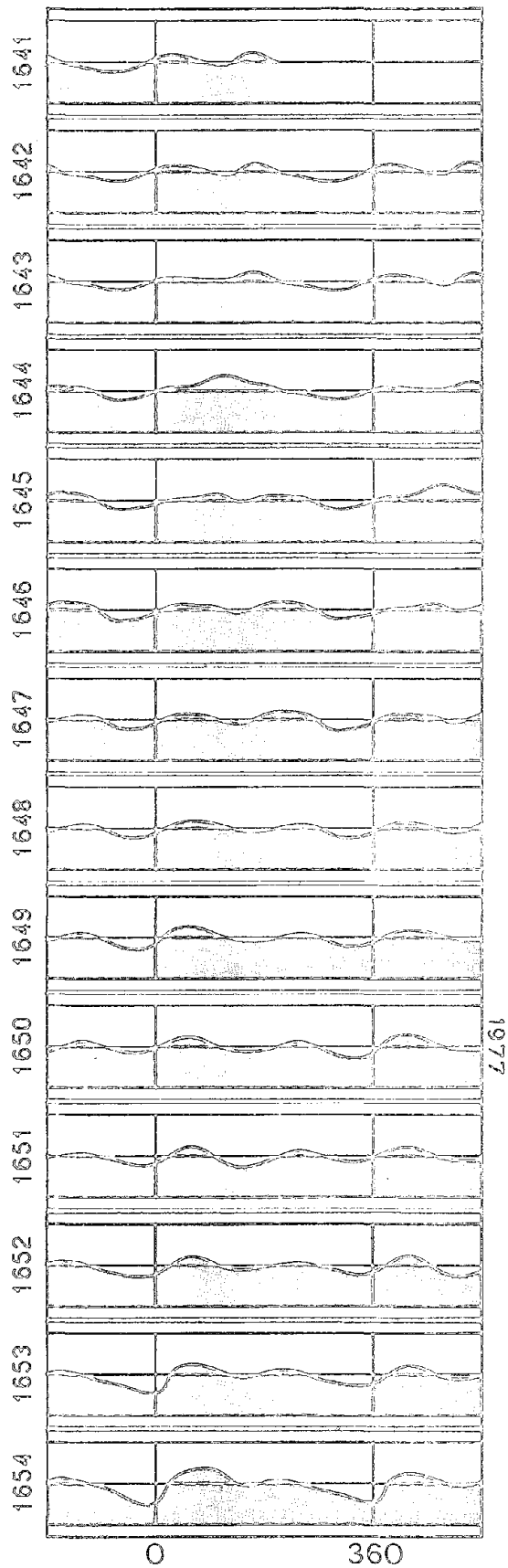
There are two extensions of the current sheet north of the equator and two extensions south of the equator, predicting a four-sector structure at Earth, similar to the structure shown for the earlier part of this interval. The magnetic field polarity on the source surface agrees well with that observed at Earth five days later. The current sheet extends to a latitude of about  $60^\circ$  in each hemisphere so one would expect that a spacecraft anywhere within  $60^\circ$  of the equator would have observed a four-sector structure similar to that at Earth. This contrasts with the period near solar minimum in 1976 when the current sheet extended to only about  $15^\circ$  N latitude and Pioneer 11, at a latitude of  $16^\circ$  N, observed only a single polarity (Smith et al., 1978).

Let us now consider the evolution of the field structure. Figure 5-6 shows the current sheets at the source surface for CR 1641 through CR 1669, May 1976 through June 1978. The format for each rotation is the same as in the previous figure except that only the zero contour is plotted (i.e. the locus of the current sheet) and regions of negative polarity (toward the sun) are shaded. The frames for each rotation include an additional half rotation from the previous and following synoptic maps at the ends so that structures near rotation boundaries can be seen more easily. Most evolution in the large scale structure occurs slowly, with a time scale of several months. The basic pattern of two northward and two southward extensions of the current sheet persists throughout this interval. The locations of maximum latitudinal extent shift only a little in longitude. For example, the northward bulge of the current sheet near  $30^\circ$  longitude, already apparent in rotation 1641, is present through at least rotation 1670. This corresponds to a persistent toward polarity structure in the observed interplanetary field. Other features show much the same longevity with only small, slow drifts in

---

Figure 5-6: The heliospheric current sheets for Carrington Rotations 1641 - 1669 are shown. Regions of negative polarity are shaded. Each box shows the labelled rotation plus an additional half rotation appended to each side; each box is two rotations wide so that structures near the ends of a rotation can be traced more easily. Vertical lines show rotation boundaries. Horizontal lines denote  $\pm 70^\circ$  and the equator. Rotations which include January 1 are labelled in the center with the year. The latitudinal extent of the current sheet increases greatly from 1976 to 1978, though the underlying 4-sector pattern in the ecliptic plane persists. Most features can be traced for at least 10 rotations and show little distortion by differential rotation.

HELIOSPHERIC CURRENT SHEET STRUCTURE: 1976-1978



longitude. A permanent marked increase in latitudinal extent and size of the warps in the current sheet occurs in early 1978 (rotations 1663 - 1665) and the pattern begins to drift slowly eastward (left).

Each Carrington rotation is 27.28 days long. Features on the sun which rotate with a synodic period of 27 days will arrive a little earlier on each successive rotation. This will be observed as a drift to the right of about 3.5 degrees per rotation or about  $55^\circ$  in 15 rotations. For comparison, some structures in the IMF recur with a period near 28.5 days (Svalgaard & Wilcox, 1975) which would be observed as a rather rapid drift to the left of about  $20^\circ$  per rotation.

Generally this interval can be characterized by slow changes in the heliospheric magnetic field. The major change is in the latitudinal extent of the current sheet. The large scale structure does not in general participate in differential rotation. Structures spanning wide ranges in latitude persist much longer than expected in light of differential rotation. This has been noticed before for large scale photospheric magnetic structures (Wilcox et al., 1970), for the green line corona (Antonucci & Svalgaard, 1974) and for coronal holes (Timothy et al., 1975).

#### *Sunspot Maximum - 1979 - 1980*

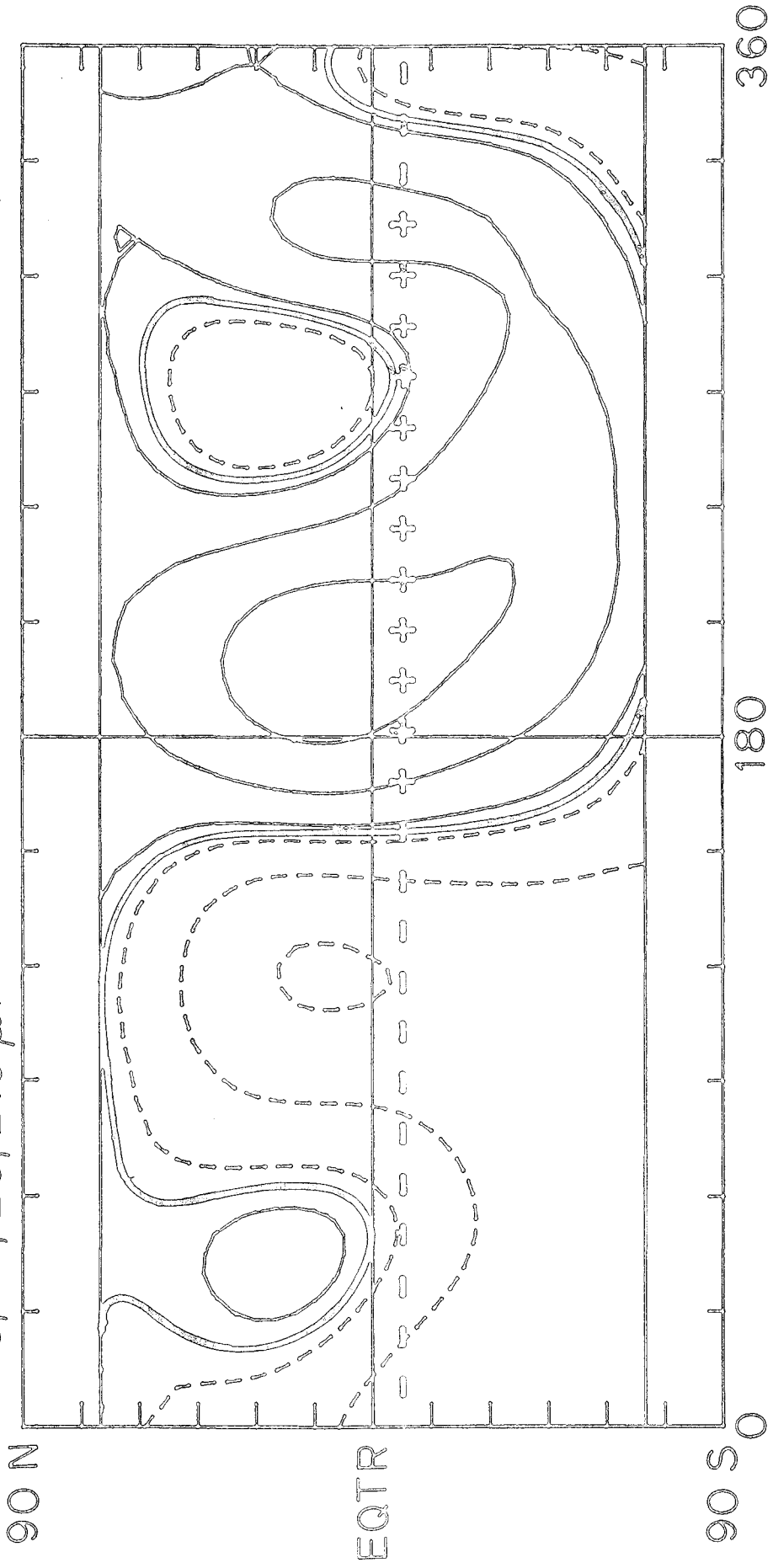
Near maximum, 1979 - 1980, the field structure was more complex. The dominance of the polar fields gradually disappeared and the current sheet commonly extended to the poles. Figure 5-7, in the usual format, shows the structure for CR 1679 which is fairly typical of the structure near maximum. There were two large unipolar regions on the source surface with a smaller region of the opposite polarity in each. At Earth only two sectors were

---

Figure 5-7: Carrington Rotation 1679 is shown in the same format as Figure 3-4. There is a disconnected current sheet near  $270^\circ$  longitude in the northern hemisphere which does not intersect the latitude of the Earth. A two-sector pattern is observed at Earth. Such complex configurations of the current sheet are common during the period near sunspot maximum.

SOURCE SURFACE AT  $2.5 R_{\odot}$   
16 MAR 1979

$0, \pm 1, \pm 5, \pm 10 \mu T$



ROTATION 1679

Figure 5-7

observed. The smaller positive region near  $45^\circ$  longitude was connected to the positive northern polar region, but did not extend far enough south to intersect the latitude of the Earth. The main current sheet extended almost from pole to pole in an approximately north-south direction at  $150^\circ$  and  $330^\circ$  longitude; spacecraft at any latitude would have seen a change in IMF polarity. The small negative polarity region at  $270^\circ$  was completely disconnected from the large negative region thus forming a second closed current sheet. The second current sheet lay in the Sun's northern hemisphere and would therefore have been detected only by an observer there. The Earth at that time was several degrees south of the solar equator and so did not see the effect of this region.

CR 1698, shown in Figure 5-8, is another typical example. Notice that the polar regions have changed sign by this time in mid 1980. Near longitude  $90^\circ$  a positive region connected to the now positive south pole intersected the latitude of the Earth and there was a single day of away polarity. A second current sheet enclosing a positive polarity region, somewhat larger than the one enclosed by the isolated current sheet in CR 1679, intersected the latitude of Earth. There was an away sector corresponding to it in the IMF.

The detailed agreement with the measured IMF polarity is not as good during this rotation, though clearly the model predicts the large scale structure quite well. The alternating polarities for the days corresponding to longitudes  $300^\circ$  to  $210^\circ$  suggest that the southern boundary of the positive region did not extend quite so far southward. Consideration of each rotation shows that most of the errors are similar in nature to these.

During the interval near maximum, changes in magnetic configuration occurred somewhat more rapidly, yet individual features last for a long time.

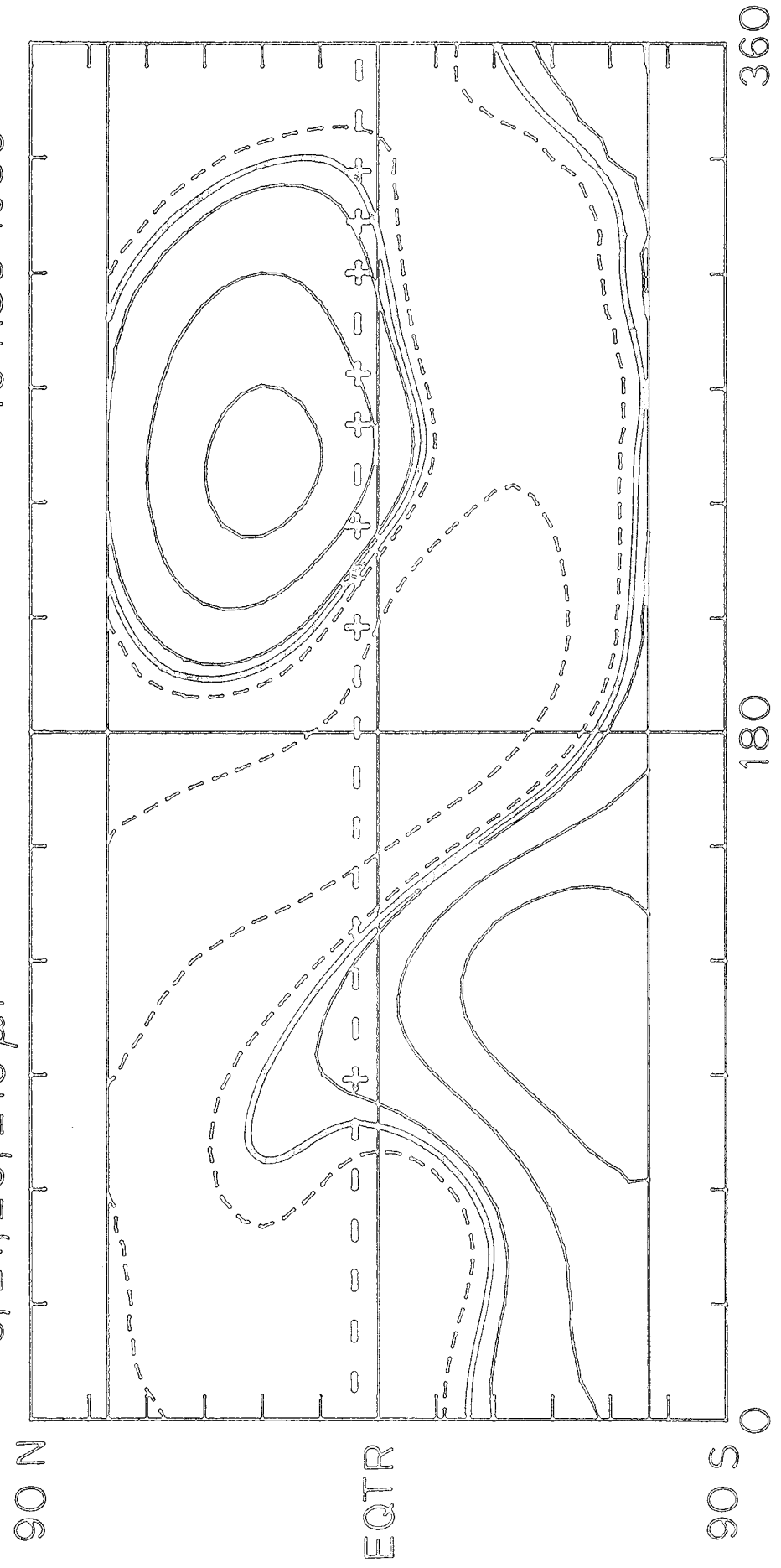
---

Figure 5-8: After solar polar field reversal the northern hemisphere is predominantly negative polarity. Carrington Rotation 1698 shows a large disconnected positive field region in the northern hemisphere around  $270^\circ$  longitude. The south polar region has become positive. The southern current sheet reaches the equator near  $90^\circ$  longitude and we observe a single day of away polarity at Earth. The sector structure is essentially two-sector with a predominance of toward polarity.



SOURCE SURFACE AT  $2.5 R_{\odot}$   
15 AUG 1980

$0, \pm 1, \pm 5, \pm 10 \mu T$



ROTATION 1698

Figure 5-8

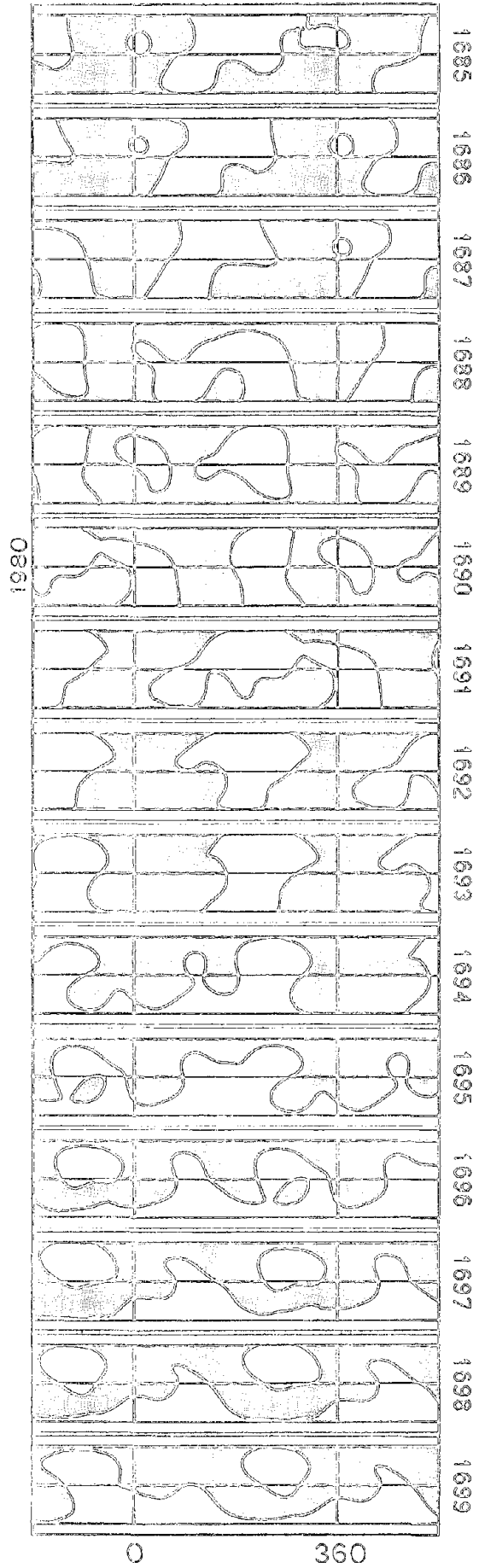
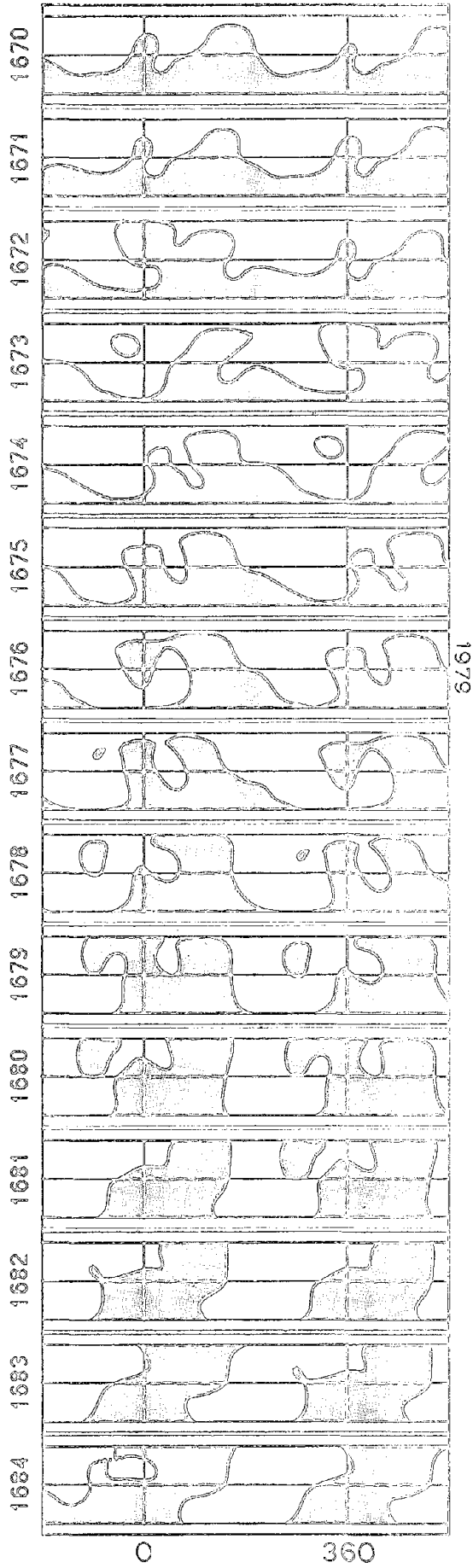
Figure 5-9 shows the current sheets for CR 1670 - CR 1699, July 1978 through September 1980, in the same format as Figure 5-6. The polarity of the solar polar fields reversed near the beginning of 1980 -- about CR 1690. Many rotations exhibit multiple current sheets and often there are two sheets at the same longitude. From one rotation to the next the changes are usually small: a region of magnetic flux may grow a little, shrink a little, drift a little in longitude or latitude, or connect in a different way with the surrounding regions of flux. The transition of the polar fields from one polarity to the other occurs smoothly. Catastrophic changes in field alignments or structure occur neither near the poles nor at the latitude of the Earth.

Most features can be observed for many rotations and their evolution can be traced. For example the large positive region clearly visible in CR 1689 centered near  $200^\circ$  longitude can be traced through CR 1717. The small positive feature that appears near  $120^\circ$  on CR 1694 does not disappear until at least CR 1712 (see Figure 5-10 below). The extension of negative polarity into the northern hemisphere that first expands in CR 1660 at longitude  $230^\circ$  drifts slowly eastward until it connects to the northern polar region in CR 1682 or CR 1683. The eastern boundary of this region can be traced to CR 1687. The small negative feature clearly visible in the northern hemisphere of CR 1678 near  $300^\circ$  longitude can be followed from rotation to rotation in all but CR 1684 until it merges with a larger negative region in CR 1685. The small region of positive polarity lying across the equator on CR 1674 near  $60^\circ$  longitude drifts slowly eastward from rotation to rotation. During CR 1681 through CR 1683 it is evident only as a warp in the current sheet, but reappears in CR 1685 through CR 1687 at  $360^\circ$  longitude. During the course of 15 rotations it shifts a total of about  $60^\circ$  eastward in longitude, corresponding to a rotation rate very close to 27.5 days.

---

Figure 5-9: The evolution of the current sheet near sunspot maximum is shown for rotations 1670 - 1699 in the same format as Figure 5-6. The polar fields reverse near Carrington Rotation 1690. The structure is complex throughout this interval, extending to the poles through most of the period and often having multiple current sheets. Many features can be traced for long periods of time. Most structures show less distortion than would be expected from differential rotation. In spite of the complexity, Earth experiences slowly varying two and four sector structures.

# HELIOSPHERIC CURRENT SHEET STRUCTURE: 1978-1980



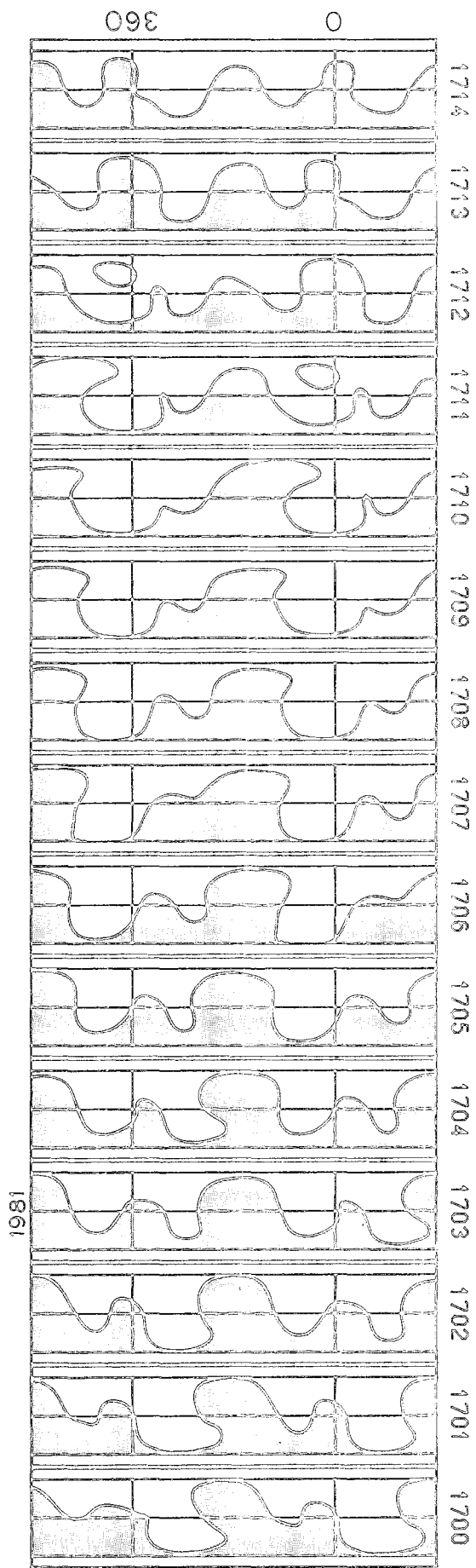
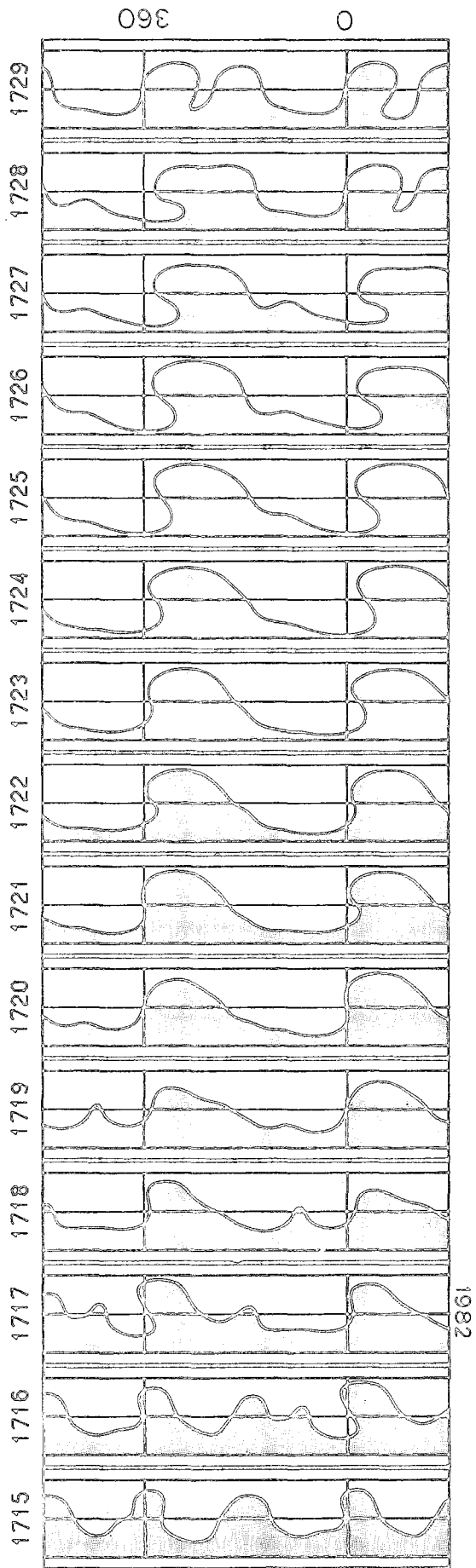
The greatest changes occur during CR 1688 through CR 1692, just at the time of solar polar field reversal determined from the magnetograph polar region measurements. The solar field added to our computation at this time is very small and so has little effect on the overall configuration of the fields. During these few rotations the positive flux region becomes disconnected from the poles and seems gradually to move southward, enveloping the southern polar region completely by CR 1695. This is independent of the inclusion of additional polar flux; graphs of the solutions with no polar field correction show essentially the same result. Throughout this interval the changes near the equatorial plane are small. There are few sudden changes in the IMF sector structure observed at Earth which often has only two sectors. After maximum the pattern returns to the four-sector structure commonly observed before maximum.

The shape of the current sheet changes more rapidly than the pattern of the large field regions because of its sensitivity to relatively small changes in regions where the field is weak. An example of this comes in the changes from CR 1693 - CR 1697. These rotations look very dissimilar, yet the differences occur because of the slight strengthening of the polar fields, the development of the positive region near  $100^\circ$ , and the growth of the negative channel in the southern hemisphere near  $270^\circ$ . The positive northern structure near  $270^\circ$  and many of the other strong features persist through this short interval.

---

Figure 5-10: This shows the evolution of the current sheet after sunspot maximum during Carrington Rotations 1700 - 1729. The current sheet becomes much simpler and the extent in latitude decreases a little. Earth experiences both two and four sector structures during this period. Changes in structure occur slowly and many features again persist for more than a year. Some features experience differential rotation, while others do not. The structure is simple and almost stationary through most of 1982.

HELIOSPHERIC CURRENT SHEET STRUCTURE: 1980-1982



### *Declining Phase - 1981 - 1982*

As the new polar fields strengthen during the beginning of the declining phase from late 1980 through 1982, the large scale heliospheric magnetic structure simplifies and becomes more ordered. Figure 5-10 shows the computed current sheets for CR 1700 - CR 1729, October 1980 through December 1982. Through most of 1981 the structure resembles the structure observed in 1978 except that the sign of polar field is reversed. Again there are two extensions of the current sheet into each hemisphere, but now the south pole is positive polarity and the north pole negative.

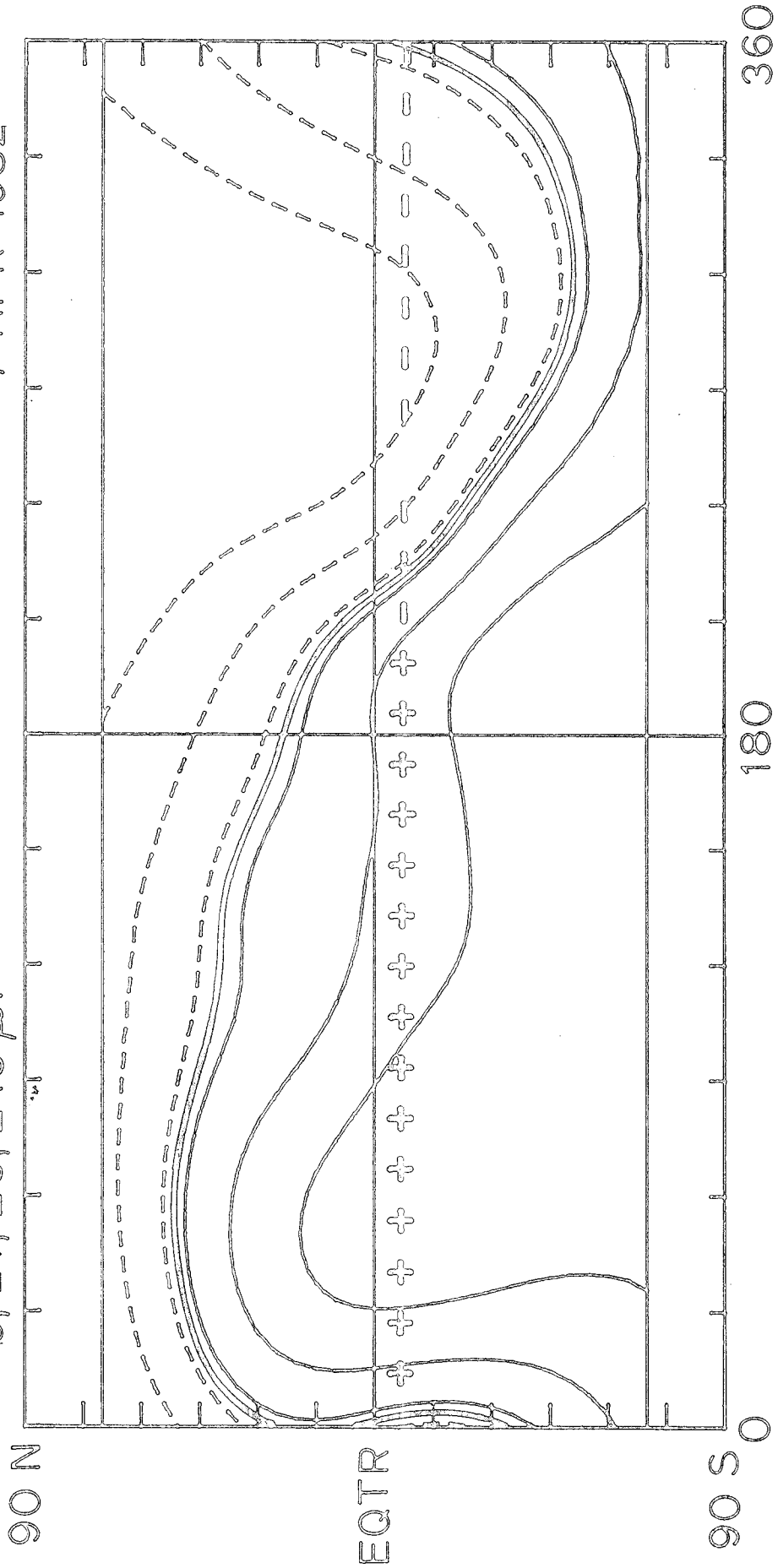
The large positive polarity region near  $270^\circ$  longitude in CR 1698 connects to the positive south polar region in CR 1700 and moves southward in succeeding rotations, disappearing by CR 1719. The large negative flux region extending from the north pole at  $180^\circ$  remains strong through CR 1710. This region is apparently undergoing differential rotation and splits in CR 1711. The flux region which remains connected to the north pole begins to die away and by CR 1718 has disappeared. The differentially rotating negative polarity region in the southern hemisphere merges with another small extension of negative flux in CR 1712 near  $0^\circ$ . This new region grows and continues to move eastward at a slower rate, broadening considerably until by CR 1718 there is only one sector of each polarity. The structure remains essentially unchanged through most of 1982 (through CR 1726), exhibiting almost no signs of differential rotation. A four-sector structure seems to be emerging again in the last few rotations. Throughout this interval the latitudinal extent of the current sheet is very great, extending almost to the poles. This is very different from the structure near minimum.

Figure 5-11 shows CR 1720 which is characteristic of the simple two-sector structure during most of 1982. A predominantly two-sector structure in the IMF has been observed after solar maximum in most of the five

---

Figure 5-11: In the same format as Figure 3-4, CR 1720 typifies the configuration during most of 1982, exhibiting a two-sector structure at Earth and changing very slowly in time.

SOURCE SURFACE AT 2.5 R<sub>o</sub>  
0, ±1, ±5, ±10 μT  
7 APR 1982



ROTATION 1720

Figure 5-11

previous sunspot cycles according to Svalgaard and Wilcox (1975). The field regions are very strong, simple, and stable which accounts for the improved agreement between the predicted and observed IMF polarity.

The four-sector structure which began to appear in CR 1729 strengthens in 1983. Figure 5-12 shows the continued evolution of the structure through CR 1744. The configuration of the field changes only a little during the entire year. The maximum latitude of the current sheet reaches at least  $50^\circ$  for the entire interval. The negative sectors near  $180^\circ$  and  $0^\circ$  retreat from the south polar region a little during the year, but remain strong and drift only slightly in longitude. The positive sector near  $90^\circ$  remains strong through the year too. The positive sector near  $270^\circ$  appears to grow in strength during the year. None of these regions seem to be affected greatly by differential rotation even though they extend from  $50^\circ$ N to  $50^\circ$ S. The IMF data for this interval has not become available to us yet, so there is no way to compare the predicted and observed polarities. One would expect that the correlation should be high because of the stability of the structures and the large inclination of the current sheets to the ecliptic.

### *Summary & Discussion*

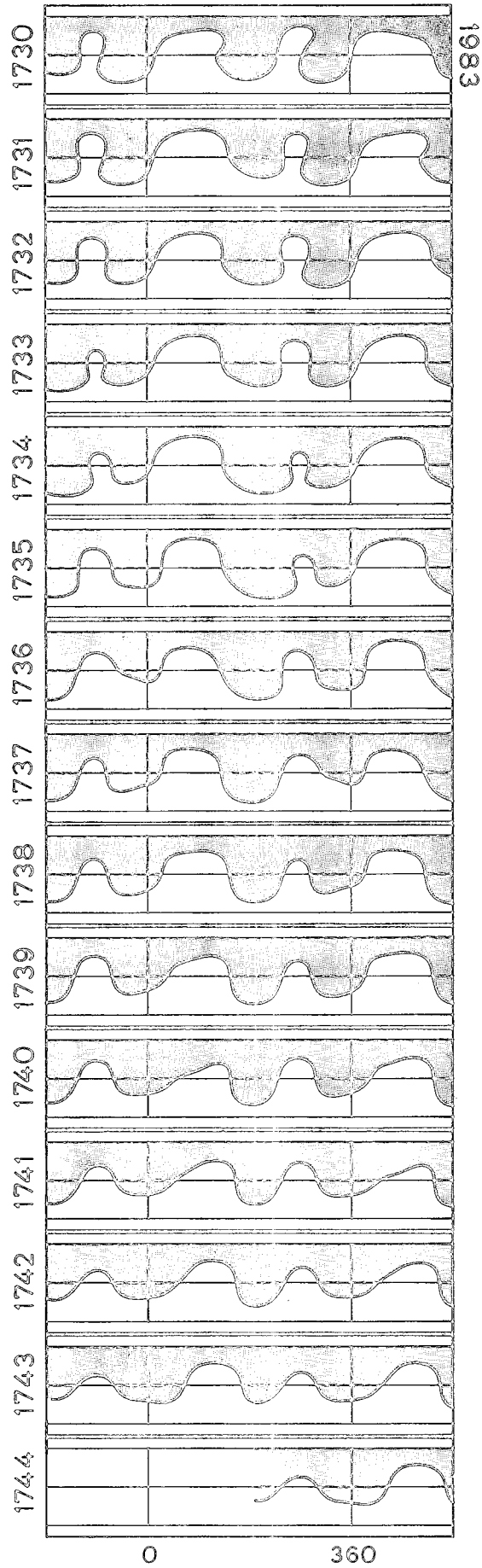
The heliospheric current sheet reaches high latitudes for much of the solar cycle. From 1978 through at least 1983 the extent was greater than  $50^\circ$ . The large scale structure of the heliosphere changes slowly during most of this period. Even near maximum there is continuity for many rotations in the structure, in spite of the complexity of the photospheric fields. The IMF polarity predicted by the model agrees fairly well with that observed near Earth by spacecraft such as ISEE-3 in every interval. This suggests that the

---

Figure 5-12: During 1983 the field structure evolved slowly. The current sheet produced four sectors in the ecliptic. The latitudinal extent of the sheet began to decrease, but reached more than  $50^\circ$  throughout the year. The large structures continue from the previous interval (Figure 5-10) through at least the end of 1983.



HELIOSPHERIC CURRENT  
SHEET STRUCTURE: 1983



potential field model, which does not treat rapidly evolving fields accurately, approximates the heliospheric magnetic structure for this period quite adequately.

The structure of the IMF observed at Earth remains fairly simple, consisting of either four or two polarity sectors. The three dimensional configuration of the heliosphere is more complex near maximum. These calculations show that multiple current sheets probably exist in the two or three years near maximum. The current sheets shown in Figure 5-9 show that the time of polar field reversal is not one of cataclysmic realignment of the heliospheric magnetic structure, but rather marks the moment when an ongoing process reaches a certain stage.

Near sunspot minimum in 1976 the computed heliospheric current sheet usually stays within  $15^\circ$  latitude of the solar equator. In Figures 5-6, 5-9, 5-10, and 5-12 one can see the maximum latitude of the current sheet increasing with time and reaching the solar polar regions near sunspot maximum. After solar maximum the maximum latitude begins to decrease with time. Presumably the continuation of this process in the current sunspot cycle 21, ending with a near-equatorial current sheet, will be similar to that reported in the last years of cycle 20 by Hundhausen et al. (1981) and by Hundhausen (1977).

That the current sheet extends to such high latitudes over such a large fraction of the solar cycle suggests that cosmic ray propagation models may need to take this into account. Jokipii and Thomas (1981) considered the effect of a simple two-sector current sheet on the solar modulation of galactic cosmic rays by varying the latitudinal extent of the current sheet from  $10^\circ$  to  $30^\circ$  degrees. This study shows that not only is the structure much more complex, but the extent in latitude is greater than  $50^\circ$  from 1978 through 1983. Comparison of IMF observations taken in the last few years with inferred measurements of five previous sunspot cycles (Svalgaard & Wilcox, 1975) suggests that the structures observed during this cycle are not very different from those observed in past epochs. One would expect that similar configurations of heliospheric magnetic field occur in each cycle.

While a few of the large scale structures shown here exhibit differential

rotation effects, many of them do not, even though they stretch over great ranges in latitude. This is similar to the rotation of coronal holes. This suggests that a more fundamental magnetic structure far beneath the photosphere may be rotating rigidly. Discussion of the relationship between the structures found in this chapter and other measurements of the solar corona will be conducted in the next chapter.

## Chapter 6 -- Comparisons & Applications

The shape and complexity of the heliospheric magnetic field vary considerably through the solar cycle. Previous investigations have considered different parts of the cycle and have used other data. This study provides the first complete study of the heliospheric field for this time interval. Comparison with the results from earlier time periods and with the field configurations determined using other methods will be made in this chapter. Further discussions will address the relationship of the computed field to other quantities such as coronal holes, solar wind velocity and cosmic ray intensity.

### *Comparison with other Potential Field Calculations*

Most studies have considered only a few Carrington rotations of data. The exception is the atlas of potential fields calculated from Mt. Wilson data published by Newkirk et al. (1973) and Altschuler et al. (1975) and later by Marubashi & Watunabe (1983) of the interval 1959 - 1974. Covering more than a solar cycle these computations give an impression of the heliospheric field similar to the results presented in the previous chapter in the sense that the field is simpler near minimum and extends to high latitudes for much of the cycle. However those computations did not account for the stronger polar field and appear to suffer from zero level errors which have not been corrected. Often from one half-rotation to the next large changes occur both in the field configuration and the general level of the magnetic field strength. This makes it very difficult to trace the evolution of the field from rotation to rotation. Wilcox et al. (1980) in studying the period near minimum of the following cycle also used Mt. Wilson data but averaged the data from six Carrington rotations to get an accurate stable picture of the field configuration. Unfortunately they too neglected the polar field correction. These facts suggest that one can be confident in the conclusions drawn from that data only if the feature manifests itself over a period of several rotations.

Many authors (see the references in Chapter 3) have studied the heliospheric field using the potential field model. Probably the most complete studies have been those by Levine (1977, 1978) in which a model of the coronal field was calculated for several consecutive rotations during each of three intervals: the Skylab period during the declining phase of solar cycle 21, CR 1601 - CR 1611, the interval near solar minimum, CR 1626 - CR 1634, and near solar maximum, CR 1668 - 1678. In these studies the emphasis was on the changing nature of the photospheric source regions of open magnetic field in the corona rather than on the large scale structure itself. These studies used high resolution Kitt Peak data and higher order harmonic expansion to determine the photospheric origins of the open field lines on the source surface. Because Levine's studies provide the greatest number of rotations with which to compare, the following discussion deals primarily with his results.

What comparison can be made between Levine's results and the results of this study for corresponding times of the solar cycle? The Skylab period occurred during the later declining phase of the previous activity cycle, a period which we are just entering in the current cycle. The coronal structure and the solar wind were dominated by the presence of large coronal holes which rotated rigidly and evolved slowly. Levine's study showed that open structures in the corona were almost always associated with coronal holes or active regions. The results from the present study show that during the comparable interval, 1982 - 1983, the large scale structure evolved in the same way; there was little differential rotation and the structure was dominated by a few very strong field regions. As will be shown later in this chapter, the locations of coronal holes correspond to the highest field strength regions on the source surface.

Near solar minimum the structures calculated by Levine (1982), CR 1626 - CR 1634, occurred about a year before the beginning of the present study. Because a source surface radius of  $1.6 R_{\odot}$  was used, the structures extend to higher latitudes and show a more complex structure than would be calculated using a higher source surface radius. Nevertheless, the structures are relatively simple during this period and extend to latitudes between  $30^{\circ}$  and  $60^{\circ}$  degrees. Hundhausen (1977) used coronameter data from CR 1616 and CR 1627 to infer that the structure resembled a tilted dipole during some of

the rotations during that interval. Levine's results show that this is a fair approximation to the field configuration during some of the rotations, but that most of the rotations require a more complex structure including higher order moments of the field to adequately represent them.

A year later, in 1976, when the present investigation began the field resembled an equatorial dipole with a significant quadrupole contribution. Bruno et al. (1982) used coronameter data for this same interval to determine that the sectoral quadrupole contribution was 17% of the polar dipole for this interval. This corresponds roughly to the relative magnitudes at the source surface of the components computed using harmonic analysis. This may seem a small contribution, but since the Earth remains within  $7.25^\circ$  of the solar equator this greatly affects the observed IMF structure. Because of the lack of coronal hole data it is hard to relate open field structures to coronal holes, but it appears that open regions are not always necessarily related to active regions or coronal holes during this period (Levine, 1982).

During the rotations near solar maximum where direct comparison between the calculations can be made, the two methods predict essentially the same large scale structure. Discrepancies appear to arise between the two primarily because of the granularity of Levine's computations (once per rotation). Near the center of each rotation where each model uses the same data the agreement is extremely good. Levine also used a polar field correction during this time interval which was probably too large. The structures computed by both analyses show the same sort of complexity; the current sheet extends to high latitudes and there are occasionally multiple current sheets. Levine's study of the photospheric sources of open field regions found much the same relation near maximum as for the Skylab period during the declining phase: coronal holes and active regions account for almost all of the open flux, although the relation is not quite as strong because of the smaller, shorter-lived nature of coronal holes near maximum.

Other studies which analyze only a few rotations show much the same sorts of patterns, although the long term structure and evolution of the field can only be seen when analyzing many rotations simultaneously.

### *Studies of the Current Sheet using other Methods*

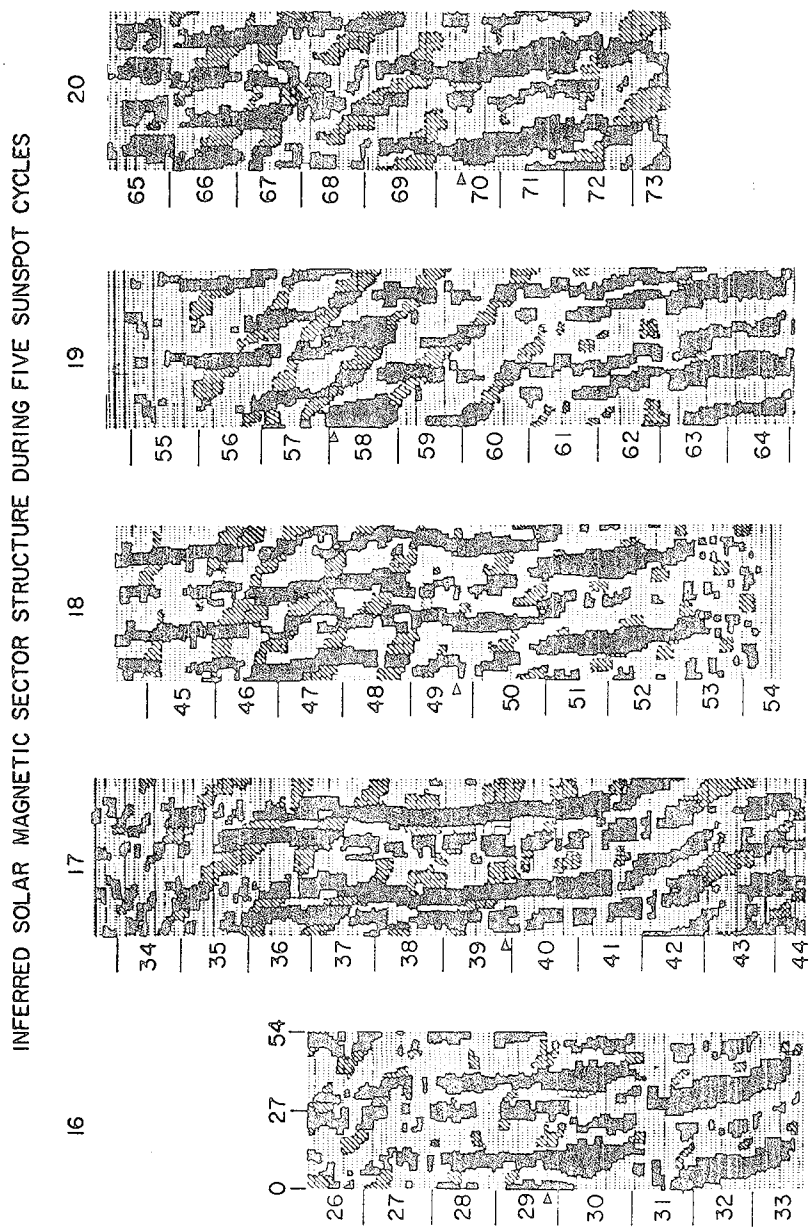
Measuring the coronal density provides an alternative method of determining the coronal structure. Hansen et al. (1974) showed a relation between coronal streamer patterns observed with the Mauna Loa coronameter and sector boundaries. Howard & Koomen (1974), using OSO-7 coronagraph measurements from 1972 and 1973, demonstrated a strong correlation between the density structures observed in the corona and the IMF pattern observed at Earth. The assumption is that the density near the current sheet will be higher since the field in that region is not open to the solar wind. Therefore when the current sheet lies parallel to the equator at some latitude a streamer will be seen at the corresponding location in the corona. Current sheets perpendicular to the equator will produce a fan.

During this period a couple of years past maximum, a four-sector pattern was observed in the IMF. Coronal images in 1972 showed the presence of two northern streamers spaced  $180^\circ$  apart and two southern streamers also spaced  $180^\circ$  apart,  $90^\circ$  out of phase with the northern streamers. These occurred at latitudes of approximately  $40^\circ$ . If the streamers correspond to the location of the current sheet, this would result from a structure much like that observed throughout 1983 as shown in Figure 5-12, a current sheet extending to high latitudes with two warps north and two warps south of the equator. Similar structures should be observed during 1977 - 1978 as well. (See Figure 5-6). Through 1972 and 1973 the coronagraph data predicted either two or four sectors according to the number and location of the streamers in agreement with the measured IMF polarity. This is very similar to the evolution of the field in 1982 and 1983 where the field evolved slowly from a two sector structure in 1982 to a four sector structure during most of 1983.

---

Figure 6-1: A plot of the inferred solar magnetic structure during sunspot cycles 16 - 20. A 26.84 day calendar system starting February 19, 1926 is used. Two successive rotations are displayed horizontally to aid in pattern recognition. Sectors with field polarity toward the sun are shaded black if they are judged to be part of the four-sector pattern, and have a dashed shading if they are judged to be part of the 28.5 day structure. A visual impression of the large-scale solar magnetic features can be obtained from this figure (Svalgaard & Wilcox, 1975).

Figure 6-1





The inferred IMF polarity record extends back to 1926 (Svalgaard & Wilcox, 1975). As shown in Figure 6-1, the structure for each of that last 6 sunspot cycles shows a similar recurrence period of about 27 during most of the cycle (this pattern is highlighted in black). Sometimes a superposed pattern with a recurrence period of  $28\frac{1}{2}$  days (highlighted in gray) appears. Note that each column is two rotations wide to show the evolution of the structure more clearly.

Figures 6-2 show the measured IMF polarity for the current solar cycle beginning in 1976 and extending through 1982. This is presented in the same format as the previous figure with a recurrence time of 27 days. The various recurrence patterns are not highlighted and the columns are only a single rotation wide. Most of these measurements come from spacecraft, yet comparison with earlier cycles shows no significant differences. For comparison Figures 6-3 show the predicted IMF polarity from the model. Obviously the general structure is duplicated quite well. The predicted polarity seems smoother because transient events and evolution of the field structure near boundaries affect the observed IMF. The similarity of these structures (representative of the solar equatorial regions) to those of earlier cycles (derived from the IMF) suggests that the types of structures computed for this cycle are typical of the structures present in other cycles.

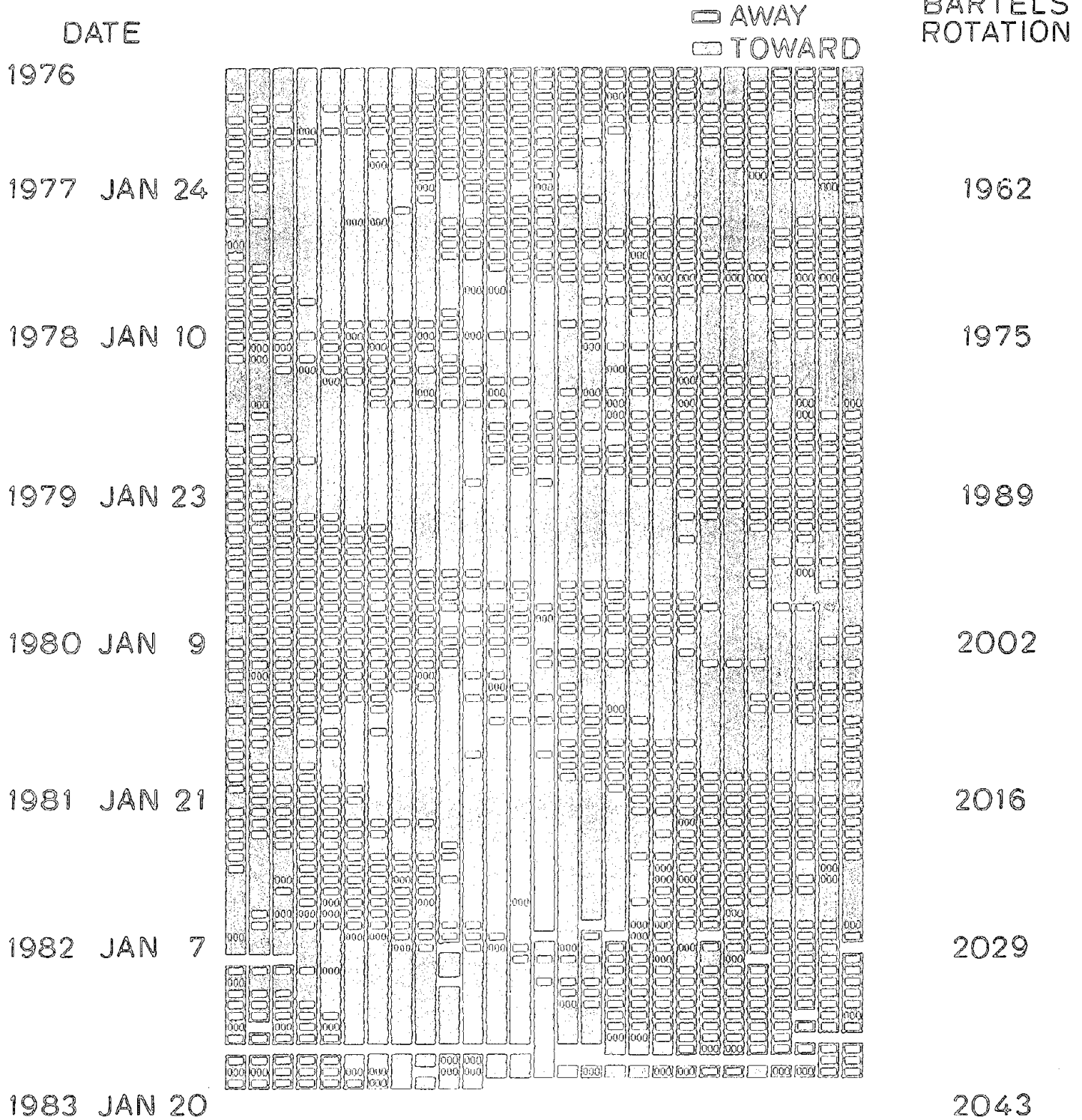
Rosenberg & Coleman (1969) found that the number of days with a given IMF polarity during a solar rotation depended on the heliographic latitude of the spacecraft. When the Earth or spacecraft was away from the sun's equator, an excess of the polarity corresponding to the nearest solar pole was observed. Svalgaard & Wilcox (1976) used the magnitude of this effect during several solar cycles to infer the latitudinal extent of the current sheet during the eight years around the solar minimum. Considering the current sheets

---

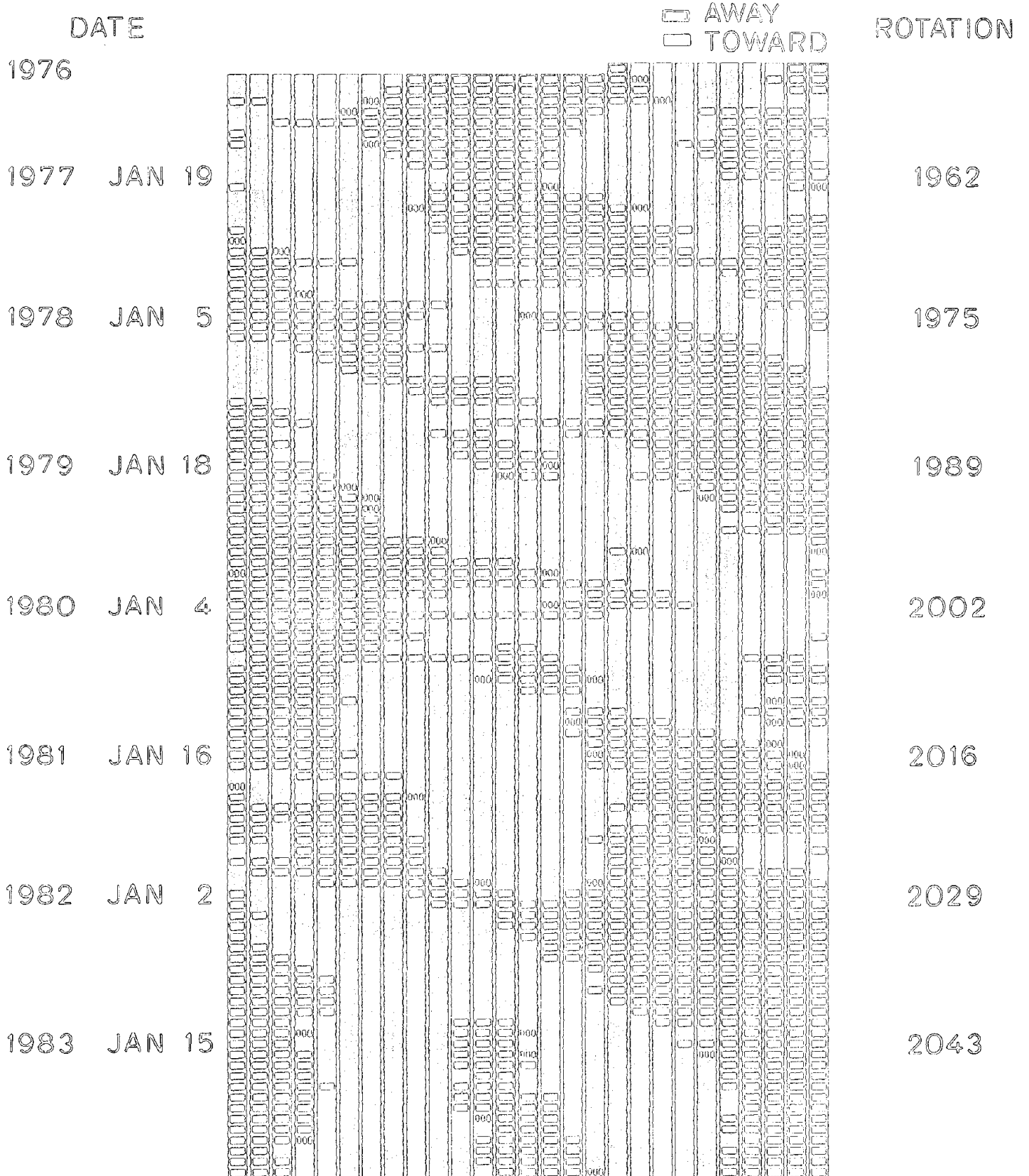
Figure 6-2: The observed IMF polarity from 1976 - 1982. In this figure a 27 day calendar is used and the plot is only one rotation wide. The structures in the current cycle are similar to those observed in previous cycles.

Figure 6-3: The IMF polarity predicted by the potential field model for 1976 - 1982 plotted to the same scale as Figure 6-2. Note the striking similarity of the general structure. Most discrepancies occur near sector boundaries and on isolated days.

# OBSERVED IMF POLARITY



# PREDICTED IMF POLARITY



shown in the previous chapter, it is easy to see how this works near minimum when the neutral line has a relatively small inclination to the equator. Even the small latitudinal excursion of the Earth will affect the number of days of a given polarity during a rotation. During the several years around maximum the current sheet often has a large inclination with respect to the equator and does not resemble a simple sine wave which could be used to predict the maximum extent in latitude of the sheet. In fact the complex current sheets near maximum often show both highly inclined neutral lines and neutral lines almost parallel to the equator in the ecliptic during a single rotation (see Figure 5-9). Recent measurements of the inclination of IMF boundaries using multiple spacecraft determinations of the minimum variance direction of the IMF show the same effect (Behannon et al., 1983).

A method for determining the solar wind velocity from measurements of interplanetary scintillation (IPS) of distant radio sources was developed by Armstrong & Coles (1972). The advantage of this technique is that it is not confined to the ecliptic plane since the radio sources lie in various directions. The disadvantage is that given the number of sources and their distribution it takes about six months to build up a map of the heliospheric velocity distribution and the coverage is complete during only about half the year, from March through July. This implies that rapidly changing structures will add noise to the data. During intervals of relatively rapid evolution the method will determine results only for the average configuration.

The relation of velocity to field strength on the source surface will be discussed in more detail in the following sections. Suffice it to say, for now, that a strong correlation exists between field strength and velocity. This is intuitively obvious from the fact that the current sheet, which has a field strength of zero on the source surface, always lies in a region of relatively low solar wind velocity. Coronal holes, on the other hand, tend to occur in regions where the field strength is a local maximum and are the sources of high speed solar wind streams.

Sime & Rickett (1978) investigated the solar wind velocity determined from IPS measurements for the years 1974 through 1977 and found a good correlation between the regions of low [high] coronal density observed by the

Mauna Loa coronameter and the regions of high [low] solar wind velocity. Both methods found that from 1973 - 1975 that the high speed regions were aligned about  $30^\circ$  from the rotation axis. During 1976 and 1977 the equatorial region corresponded to both high coronal density and low solar wind speed. The high speed regions over the poles were aligned with the rotation axis. This is confirmed by the potential field model computations and by the Mauna Loa determination of the current sheet.

Rickett & Coles (1983) have extended these results through 1982, again comparing the solar wind velocity with the Mauna Loa current sheet. During 1976, 1978, and 1980 they also compare with the structure found using our potential field model. These results have been reproduced in Figure 6-4. During 1976 there is a good relation among the methods. Mauna Loa and the potential field model find a current sheet near the equator. IPS data showed a minimum in solar wind velocity near the equator and higher velocity far from the equator. In 1978 both methods for determining the current sheet showed a lot of structure extending to much higher latitudes. Since the method averages over six months no comparison in longitude is really possible during this interval of more rapid evolution. The velocity data does show that within the range of latitudes where there is structure, the solar wind velocity stays rather low. There appear to be no really large streams in 1978.

During 1980 there is really very little structure common to the three methods. This suggests that the field was evolving rapidly near maximum and the extent in latitude of the current sheet was relatively large. The only exception is near  $270^\circ$  longitude where the potential field model predicts a complex configuration including a tube in the current sheet and the solar wind at that longitude is relatively low. The structure in 1982 seems to be much more established because the IPS and Mauna Loa data show much

---

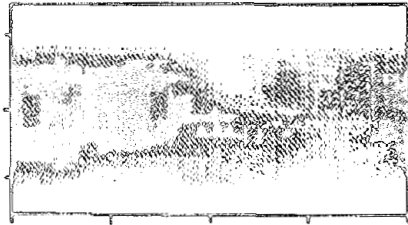
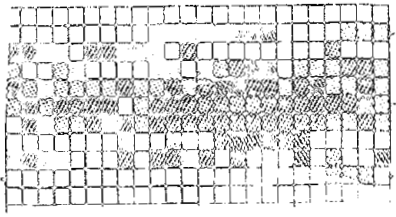
Figure 6-4: Left panels show solar wind speed from IPS observations as synoptic maps averaged over 6 rotations. Heavier shading denotes higher wind speed; missing data is blank. The center column shows coronal electron density. Areas of high density are dark. The right panels show the coronal field computed with the potential field model for a representative rotation. Strong field regions are dark. Also compare the 1982 structure with that shown in Figure 5-10.

IPS VELOCITY

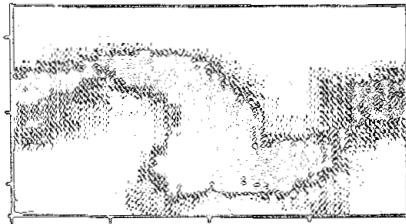
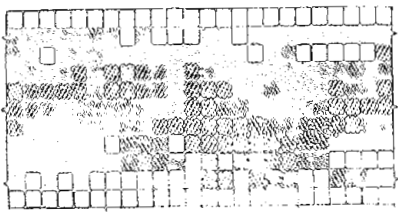
K CORONAMETER  
BRIGHTNESS

POTENTIAL FIELD  
MODEL

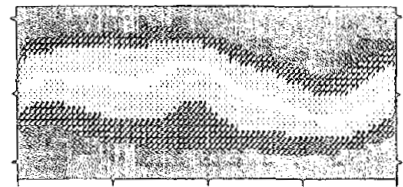
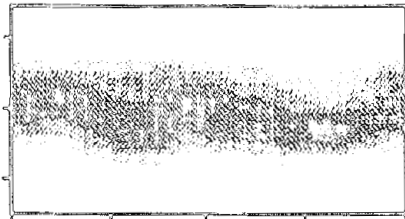
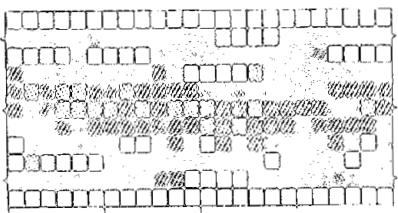
1972



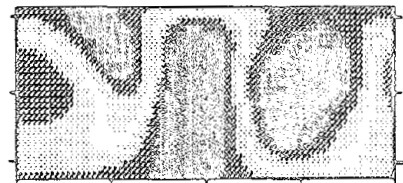
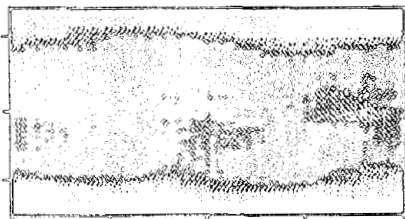
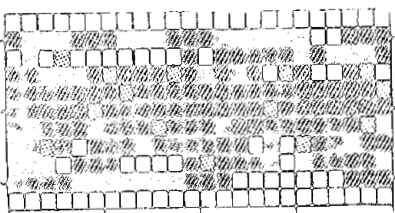
1974



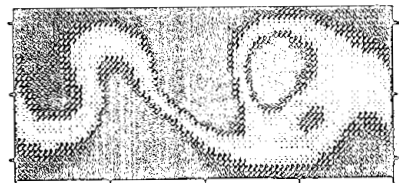
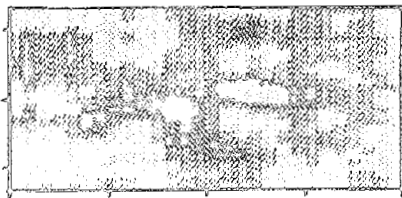
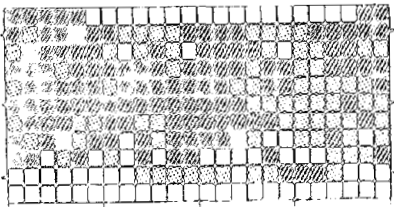
1976



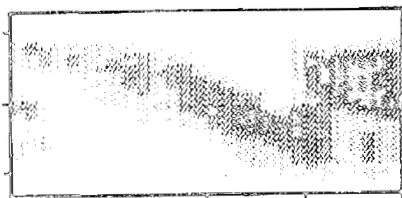
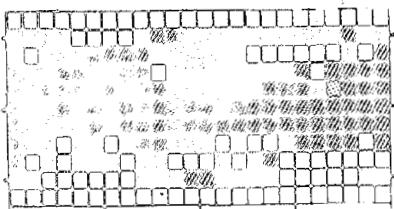
1978



1980



1982



more sharply defined patterns. Comparison with almost any of the source surface configurations calculated for 1982 shown in Figure 5-10 reveals a remarkably similarity. The structure in 1982 is beginning to resemble the that shown in 1974, though not quite as strongly, showing a relatively symmetric structure tilted with respect to the rotation axis. The structure reverts to a four sector structure during most of 1983.

These comparisons show that the structure in the most recent cycle is not unique. In each cycle near minimum a roughly equatorial current sheet with a significant quadrupole component would be expected. Early during the rising phase of the cycle the latitudinal extent of the sheet should increase until it reaches the polar regions for the year or so around solar maximum. The time near maximum will be a time of more rapid realignment of the fields, especially the shape of the current sheet. Even during this period one would expect large, strong field regions to be present and to persist for intervals as long as years. During the declining phase the polar coronal holes should reestablish themselves and bring more order to the heliospheric field. It appears that the lower latitude fields will also remain more stable. It will be interesting to see if the "monster streams" of 1974 are observed later in the declining phase of the present cycle.

#### *Solar Wind Velocity*

Reference was made in the previous section to the relationship between magnetic field strength and solar wind velocity. The following analysis will help to clarify the relation between the computed field and the solar wind velocity observed at 1 AU. One difficulty in such a study is isolating intervals when solar activity does not unduly influence the results. Near maximum the occurrence of flares, disappearing filaments and the like affect the solar wind velocity a substantial fraction of the time. Near minimum, however, the effects of solar activity are much less. For this reason that time period will be investigated first.

The first question to arise is what quantity derived from the source

surface field to relate to the solar wind velocity. There is an obvious minimum of solar wind velocity near the current sheet and a maximum above coronal holes. Possible correlations exist between velocity and the distance from the current sheet or the magnetic field strength, both of which are a minimum at the current sheet and increase over coronal holes. The distance from the current sheet is roughly equivalent to the idea of heliographic latitude dependence during intervals when the current sheet lies close to the equator, or to heliomagnetic latitude dependence if the field resembles a tilted dipole.

Zhao & Hundhausen (1981) inferred a relationship  $V(\text{km/s}) = 400 + 1000 \sin^2\lambda$  for the period in 1974 when the heliographic latitude of the current sheet varied sinusoidally with longitude (a tilted dipole configuration). Here  $\lambda$  is the latitudinal distance from the current sheet to the ecliptic. Since the current sheet was inclined  $30^\circ$  with respect to the equator, as determined from coronameter data, the Earth sampled a relatively large range in "heliomagnetic latitude". Recently this analysis has been extended to the period near minimum when the current sheet was more equatorial with a quadrupole warp away from the ecliptic (Zhao & Hundhausen, 1983). IPS measurements of the velocity at high latitudes were used to deduce the relationship:  $V(\text{km/s}) = 350 + 800 \sin^2\lambda$  for  $|\lambda| < 35^\circ$  and  $V = 600 \text{ km/s}$  for  $|\lambda| > 35^\circ$ . They again used the inferred current sheet position determined from coronal polarization brightness measurements from the Mauna Loa coronameter.

An immediate problem with using the latitudinal distance to the current sheet arises when one considers the more complex field configurations common at other times of the solar cycle. Through most of 1976 - 1983 the current sheet had a very strong four-sector structure. Hakamada & Munakata (1984) used the current sheets derived in the present analysis to compute the *angular distance*,  $\lambda$ , between the current sheet and the spacecraft which measure solar wind velocity during the interval from May 1976 through August 1977. During this interval the current extended to latitudes of up to about  $25^\circ$  which, when including the latitudinal excursion of the Earth, gave a range in latitude of  $\pm 30^\circ$  for the analysis. Hakamada & Munakata found a good correlation with the angular distance from the current sheet of the



form  $V(\text{km/s}) = 408 + 473 \sin^2 \lambda$ , but almost no correlation with the heliographic latitude.

Suess et al. (1977) modelled the acceleration of solar wind in the polar coronal hole described by Munro & Jackson (1977). Interesting results for the potential field analysis are an inferred polar field strength of 20 Gauss and the discovery that between  $2 R_o$ , where the field strength was substantially higher near the center of the coronal hole, and  $5 R_o$  the meridional gradient of the magnetic field had disappeared. According to the model, by 1 AU the field strength was higher near the boundaries of the hole than near the center. The important result for the present discussion is the direct relationship between the magnetic field strength at  $2 R_o$ , equivalent to the source surface, and the solar wind velocity. According to their coronal hole model a higher field strength corresponds to a higher solar wind velocity. This suggests the possibility of such a correlation over the whole source surface rather than just over coronal holes.

Figure 6-5 shows the relation between magnetic field strength and solar wind velocity for the same period as that studied by Hakamada & Munakata. Again there is a great deal of scatter, but the same sort of relation appears. Especially during this interval when the distance from the current sheet and the field strength are very closely related, one would expect to see little difference between the two correlations. The more interesting test will come near maximum when distance from the current sheet and field magnitude are not so closely related.

Because the period near solar maximum is so contaminated by activity related events, a decision was made to study a few rotations in detail rather than rely on statistics over a longer period to reduce the errors. Figure 6-6 from Suess et al. (1984) shows several solar and interplanetary quantities for

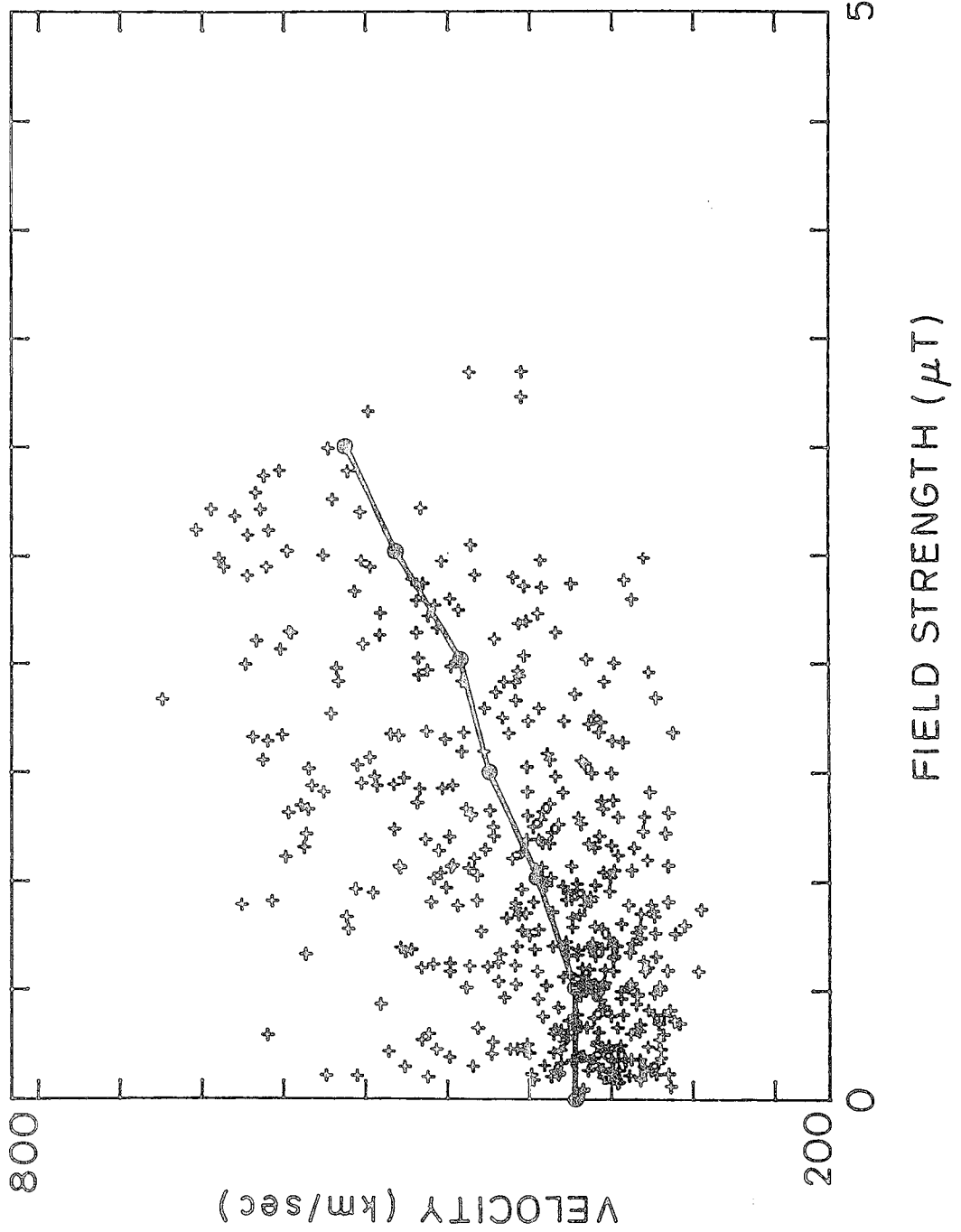
---

Figure 6-5: a) A scatter plot of daily solar wind velocity vs. source surface magnetic field strength for May 1976 through August 1977. The solid line shows the results averaged into bins of magnetic field strength. At least 4 values are required in each bin. b) The same for the interval May 1979 through August 1980. The dashed line skips a bin in which there were less than 4 observations. Note the change in the magnetic scale due to increase field strength near maximum.

Figure 6-5a

SOLAR WIND VELOCITY  
VS.  
SOURCE SURFACE FIELD STRENGTH

1976-1977



SOLAR WIND VELOCITY  
VS.  
SOURCE SURFACE FIELD STRENGTH

1979-1980

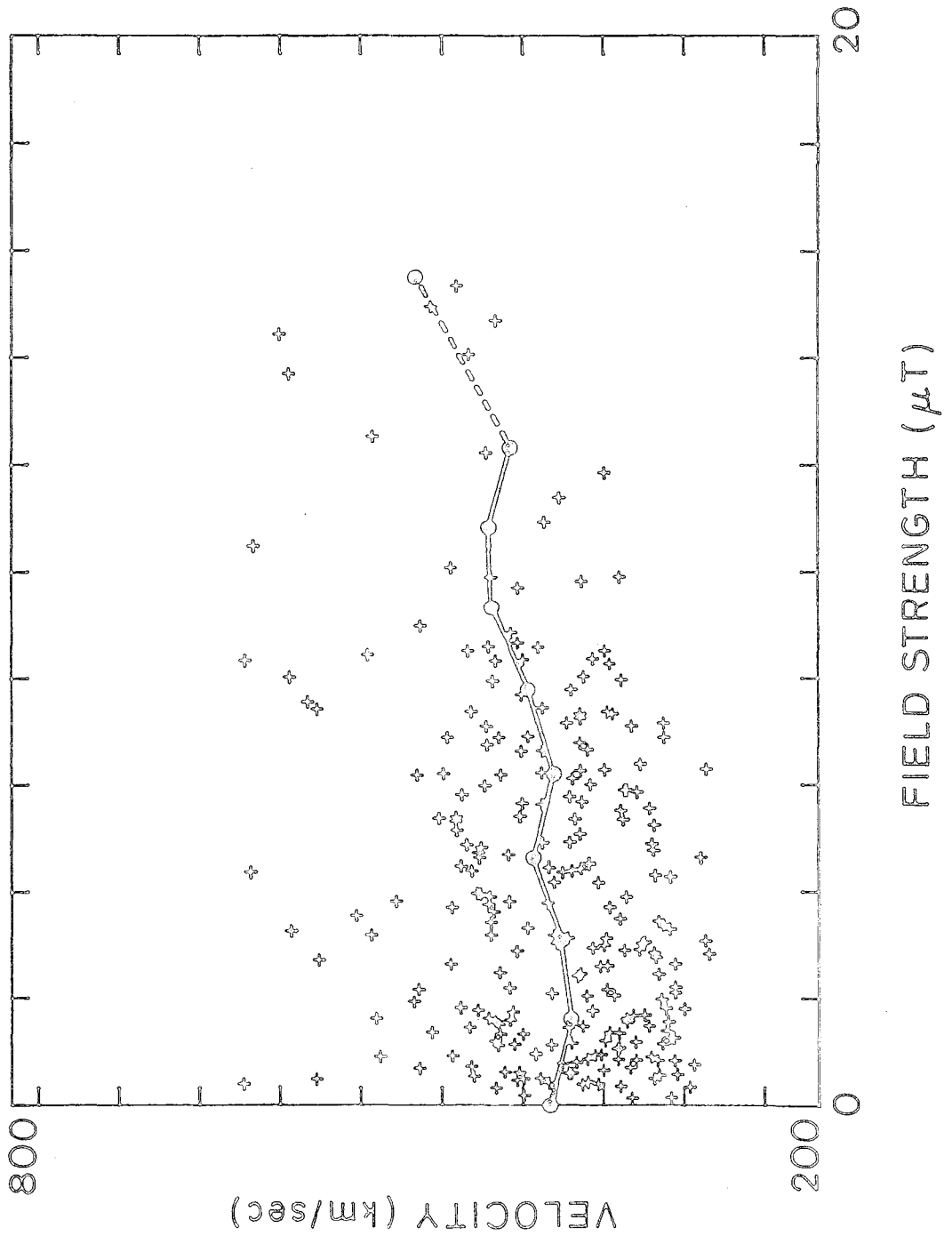


Figure 6-5b

CR 1683 - CR 1685. The top panel shows the direction of the IMF for each rotation. Regions corresponding to positive polarity are shaded. The second panel shows the IMF magnitude. The third panel shows the magnetic field strength computed on the source surface at the subterrestrial point. Again the positive polarity regions are shaded and show a very good correlation with the polarity observed at 1 AU. The fourth panel shows the solar wind velocity and the bottom panel shows the number density. All interplanetary quantities have been corotated back to the source surface using the observed solar wind velocity.

The problem of solar activity becomes apparent when one considers the IMF field magnitude, solar wind velocity, and density. Intervals which appear to be related to solar activity have been shaded in these panels. The determination has been made using the criteria of correlated density, field magnitude, and velocity changes in the observed solar wind and their location within a polarity sector. Each of these events can be traced to solar flares or filament eruptions, etc.

During CR 1683 a clear relation between field strength and velocity is visible. There are several coronal holes during this period which contribute to the high solar wind velocities. The source surface field and superposed coronal holes are shown in Figure 6-7. Each hole is located in a local maximum of field strength on the source surface. The coronal hole located near  $90^\circ$  decays rapidly between CR 1683 and CR 1684. However the configuration of the heliospheric current sheet does not change significantly. Thus the *distance* to the current sheet does not really change, though the *field strength* does. This is reflected in the decline of field strength on the source surface. The decrease in solar wind velocity is not apparent in CR 1684 unless you

---

Figure 6-6: Collected solar wind and source surface data for CR 1683, 1684, and 1685 mapped back to the sun. From top to bottom the panels show: IMF polarity, the IMF strength, the source surface field strength, the solar wind velocity, and the proton number density. The shaded intervals, A - E, indicate strong temporal variations.

Figure 6-7: The magnetic field on the source surface for CR 1683, 1684, and 1685. The contours are at 0,  $\pm 0.25$ , 3, 6, and  $9 \mu\text{T}$ . The locations of coronal holes deduced from He 10830 photographs are shown in hatched closed contours.

Figure 6-6

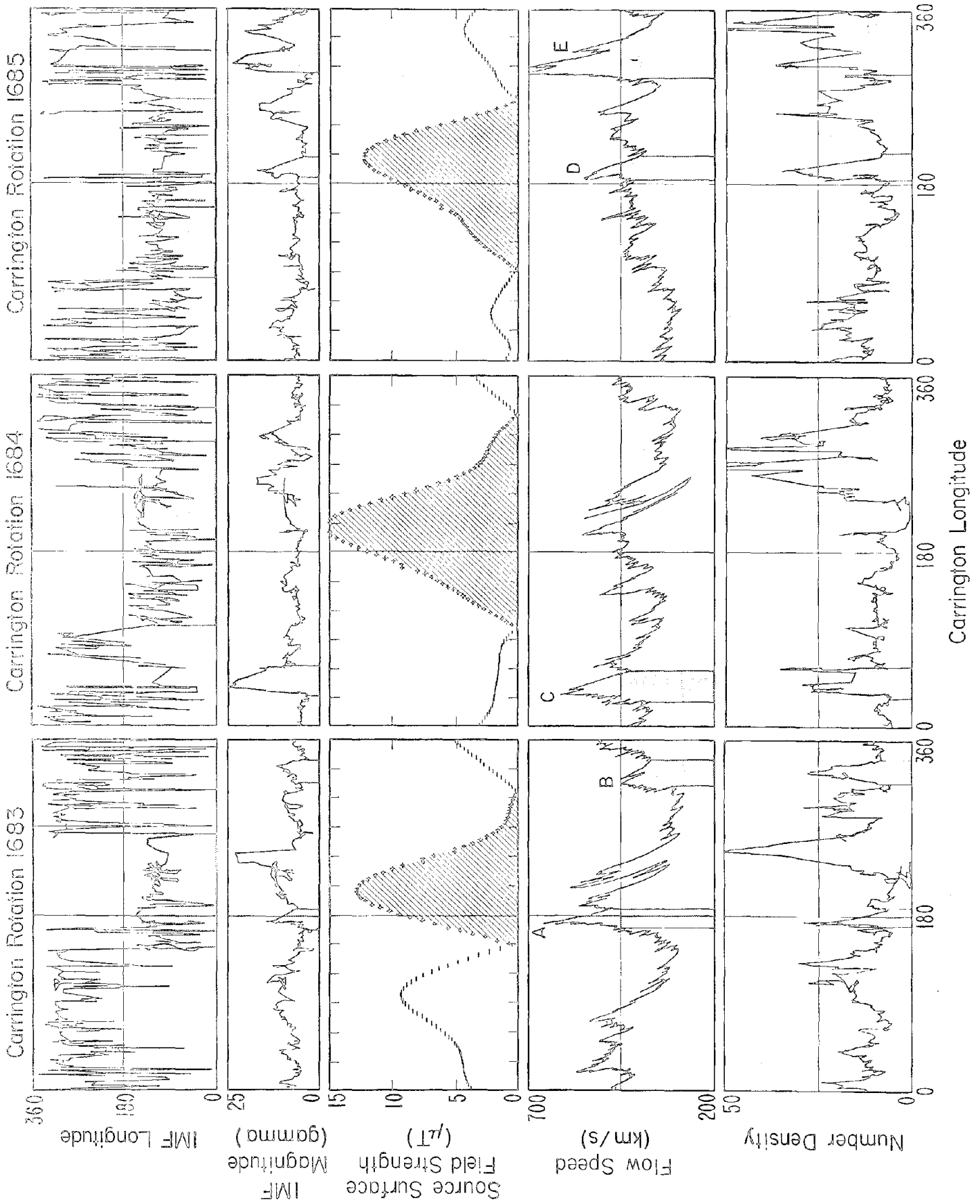
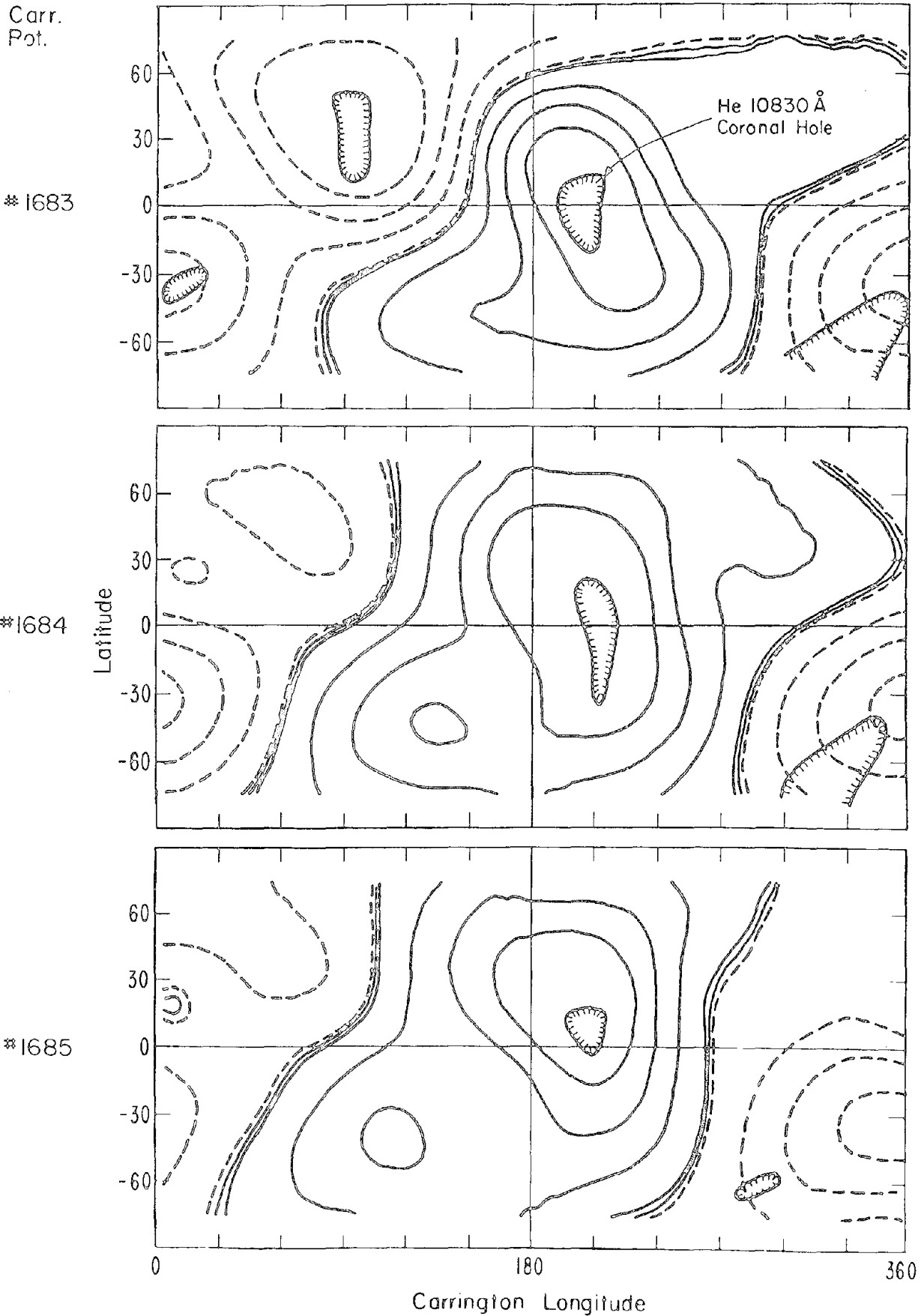


Figure 6-7

CONTOURS OF CONSTANT RADIAL MAGNETIC FIELD STRENGTH  
ON THE SOURCE SURFACE OF A POTENTIAL FIELD MODEL.  
THE SOURCE SURFACE RADIUS = 2.6 SOLAR RADII.



take into account the activity related event labelled C. The decrease in velocity is apparent at this longitude by CR 1685. See Suess et al. for a more complete discussion of this interval.

The conclusion is that probably there is too much activity during this time to draw any firm conclusions. The strongest result is that a minimum in source surface field strength (sector boundary) usually corresponds to a minimum in velocity. There is a suggestion of the relationship between maximum field strength and velocity demonstrated by the decline in velocity associated with the decrease in velocity near longitude  $90^\circ$  when activity is taken into account. Simply using the distance from the current sheet would not predict this decrease. However this relation remains questionable.

A further relation between the current sheet and solar wind velocity concerns the propagation of activity related disturbances in interplanetary space. Flare disturbances and coronal mass ejections generally propagate outward over a large solid angle. However, there is some suggestion that disturbances occurring across the current sheet from the Earth may be generally less geoeffective than those occurring within the same interplanetary sector. A confirmation of this has been found in the study of flare accelerated plasma. Lundstedt et al. (1981 and references therein) have related the direction of the large-scale flare site field to the effectiveness of flare acceleration. Specifically flares with a northward directed field direction are somewhat less likely to accelerate plasma toward the Earth. A further relationship is found when the location of the flare relative to the current sheet is considered. Flares across the current sheet from the Earth are less likely to have a detectable signature in the solar wind than those within the same sector (Merryfield & Hoeksema, private communication, 1983).

### *Coronal Holes and the Large Scale Field*

The relationship of coronal holes to the source surface fields has been alluded to in the previous sections. Here an attempt is made to describe the relationship in more detail. Coronal holes were first discovered by Waldmeier (1957), but were directly observed in X-ray measurements obtained during the Skylab experiments. Bohlin (1977a) provides a definition of coronal holes: "a fairly large-scale, cool, low-density area at low latitudes in the corona and at the polar caps, encompassing weak, predominantly unipolar magnetic fields which extend away from the sun in diverging open lines of force, that give rise to high-speed solar wind streams that cause geomagnetic storms." This definition should be expanded to include coronal holes which do not interact with the Earth, but is otherwise fairly accurate. Later investigations have shown that coronal holes can be observed from the ground using He 10830Å measurements.

During the declining phase of the cycle, corresponding to the Skylab period, coronal holes seem to dominate the structure of the corona and the solar wind. Near minimum the polar holes are very strong, but rarely extend to the equatorial regions and so have a smaller effect on the interplanetary medium. Near maximum the polar holes are absent, but smaller holes occur at all latitudes. These smaller holes do not last as long as the large holes during the declining phase which persisted for many months.

Several studies (e.g. Levine 1978, 1982) have used the potential field model to find the sources of open field regions by tracing the field lines back to the photosphere. They find that most of the open flux comes from coronal holes, active regions, and areas that will be or have been coronal holes or active regions. Coronal hole regions are the dominant contributor to the interplanetary flux. In the following discussion the relationship of coronal holes and the source surface field will be explored, specifically as it relates to the evolution of structures within which coronal holes evolve. Studies of the source regions of coronal holes are better done with higher resolution data and computations.

Harvey et al. (1982) published list of 63 coronal holes observed during



the interval 1975 - 1980 on which they made magnetic measurements. This is not a complete list of holes, but is representative of this time period and is not biased by our selection. Locations of coronal holes during CR 1663 and CR 1680 are shown in Figures 6-8 and 6-9 by circles containing an H. Holes with negative magnetic polarity are dashed. The size of the circle corresponds to the area measured by Harvey et al., but not to the shape of the hole. Most rotations during this interval contain less than two coronal holes. CR 1680 is unusual in this sense since it contains 10 identified holes. This may be due to some selection effect since it is unlikely that this rotation is really this different than neighboring rotations.

CR 1663 is typical of most of the interval. There is a single isolated coronal hole. This hole lies at relatively low latitudes and may be in some way connected to the polar hole. Using the source surface field alone the presence of a hole cannot be predicted; however, given that a low latitude, positive polarity hole exists during this rotation, the obvious choice is to locate the hole in the observed location because the field strength reaches a relative maximum near that longitude. This is generally true; if one knows that a hole exists in a given part of the sun, the approximate location of the hole can be predicted from local maximum in the field strength.

This is demonstrated more completely in CR 1680 where there are so many coronal holes that nearly every potential hole location contains a hole. Especially interesting is the positive, northern hemisphere hole at  $30^\circ$  longitude. As predicted from the potential field calculation, the associated solar wind stream does not manifest itself at the Earth even though the hole is located at only  $30^\circ$  North. In every case the coronal holes appear relatively far from the neutral line roughly located in the region of locally

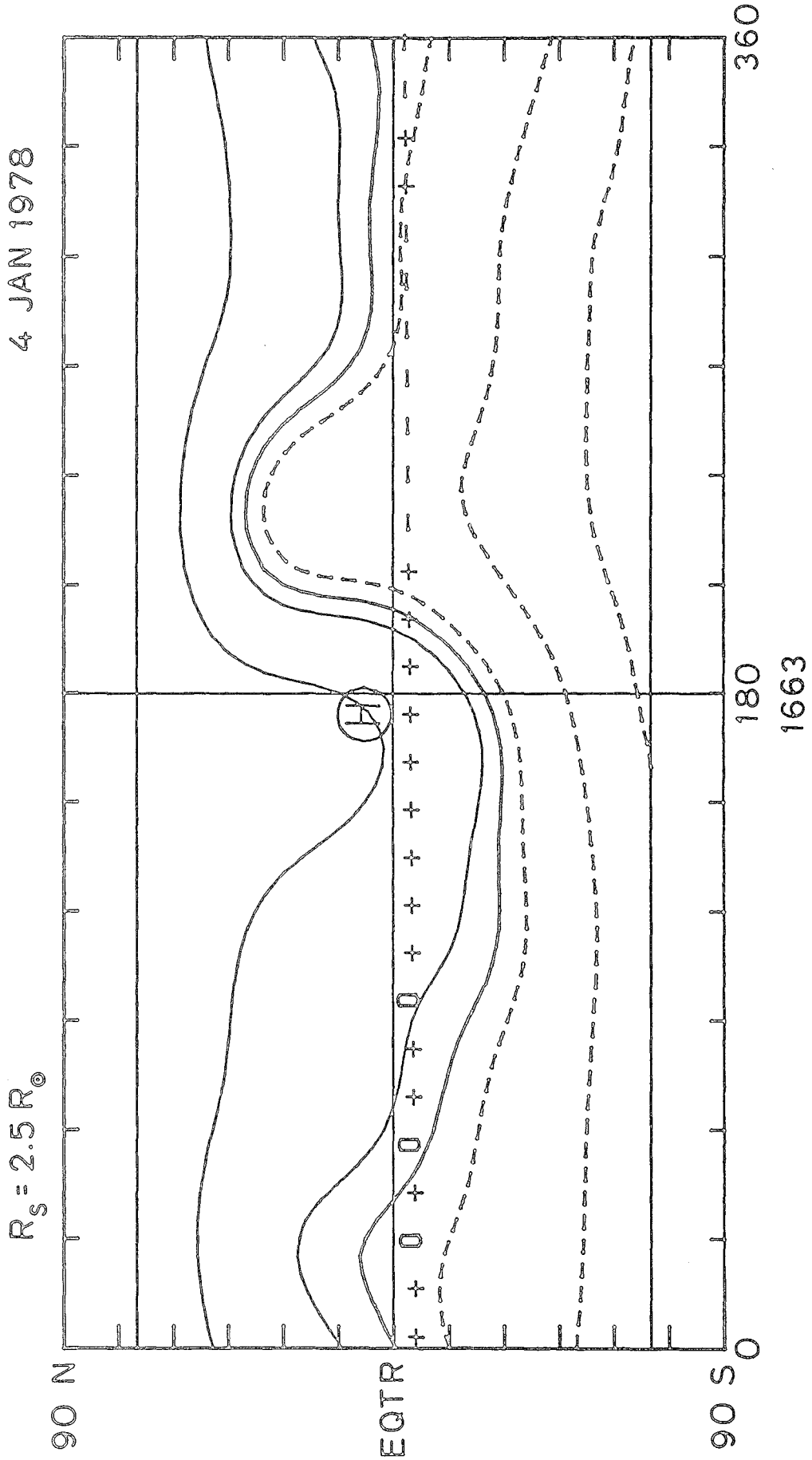
---

Figure 6-8: A contour map of the source surface field for CR 1663 with the location of a coronal hole from Harvey et al. (1982). Note that the hole occurs near a relative maximum in field strength at the given latitude.

Figure 6-9: A similar plot for CR 1680 with the location of several coronal holes from Harvey et al. (1982). Again the holes generally occur in relatively high field strength regions well away from the neutral line. The polarity of a hole always matches the polarity of the source surface field. Negative polarity holes are dashed. The size of the circle indicates the relative size but not the shape of the hole.

Figure 6-8

# SOURCE SURFACE FIELD AND CORONAL HOLE



# SOURCE SURFACE FIELD AND CORONAL HOLES

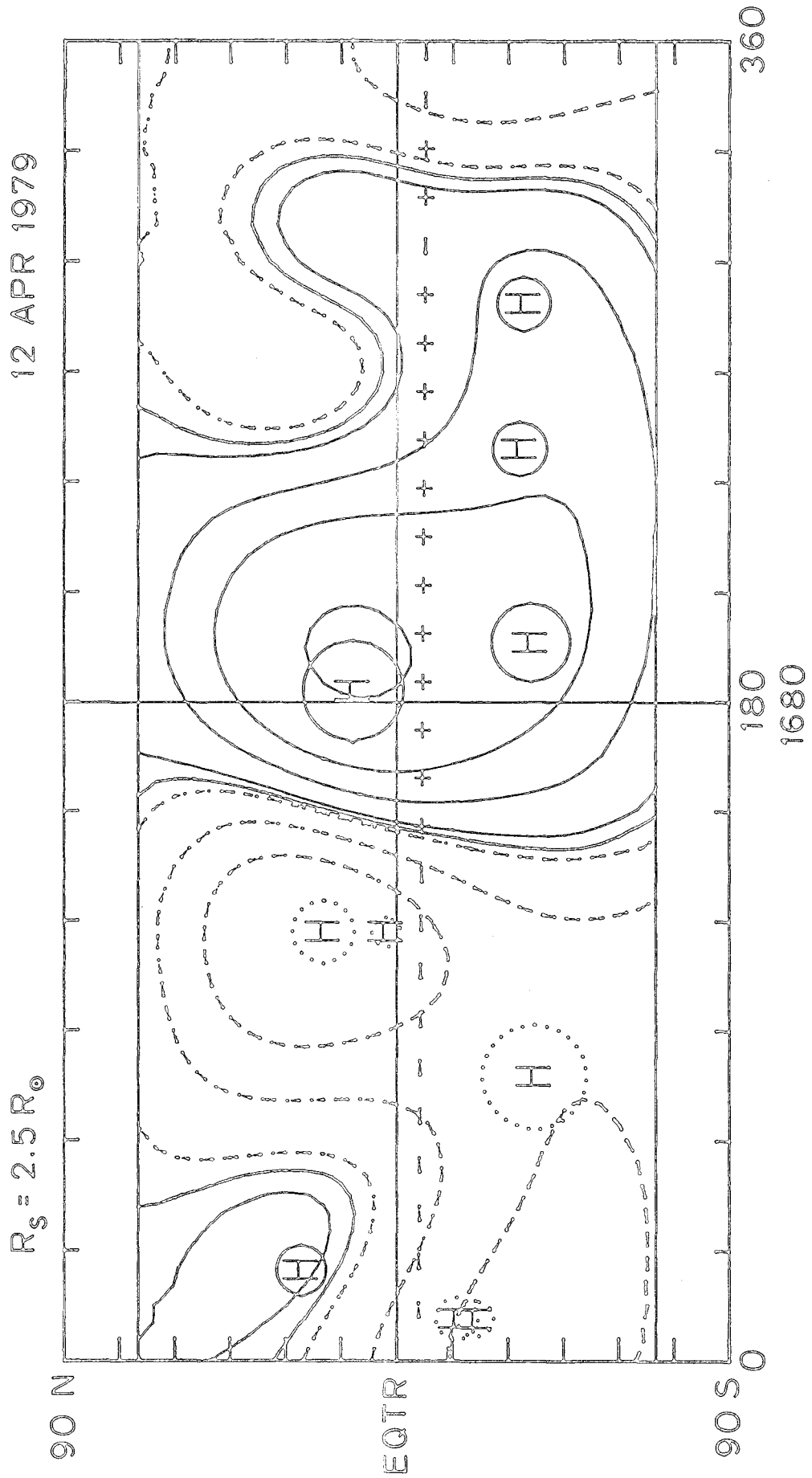


Figure 6-9

maximum field strength. The southern hole at  $75^\circ$  is a possible exception to the local maximum field strength condition, but lies far from the neutral line and on a saddle point of the field.

During this interval near maximum, most of the coronal holes listed in the study persisted for a few rotations before disappearing. One of the longest lived being the positive polarity hole shown at  $12^\circ\text{N}$  near  $180^\circ$  having an age of three rotations at this point. It lasted for a total of nine rotations, through CR 1686. Most other holes are identified on only a few rotations and attain a maximum age of 5 - 7 months. It is interesting to compare the structure observed for CR 1680 with the preceeding and following rotations as shown in Figure 5-9. The region containing the hole just mentioned can be traced forward and backward for many rotations if a drift in longitude is allowed. This hole is also shown in Figures 6-7 as are others. The large scale configuration of the field changes little over these rotations, though the field strength does. The high field strength regions develop before the identification of the coronal hole and persist long after the coronal hole dissipates.

Each coronal hole on the list appears within a polarity regions of the same polarity as the coronal hole. It would be disturbing if it did not. What then is the "average" environment into which a coronal hole fits? To answer this question the holes were divided into four groups: 1) Northern hemisphere, positive polarity holes; 2) Northern, negative holes; 3) Southern, positive holes; and 4) Southern, negative holes. During the time period covered by this study the polar field in the north was positive and the southern pole negative. Figures 6-10 a-d show the field environment into which coronal holes of each type appear. This is determined by taking the section of the source surface field map surrounding each appropriate hole, aligning the

---

Figure 6-10: Using the tabulated locations of coronal holes to determine the centers of regions, the fields surrounding the holes have been superposed to determine the average configuration of the source surface field near a coronal hole. a) The superposed source surface field about 24 northern hemisphere, positive polarity coronal holes. b) The average configuration about 10 positive polarity, southern hemisphere holes. c) The average about 7 negative polarity, northern hemisphere holes. d) The average about 8 negative polarity, southern hemisphere holes.

Figure 6-10a

# SUPERPOSITION ABOUT NORTHERN POSITIVE CORONAL HOLES

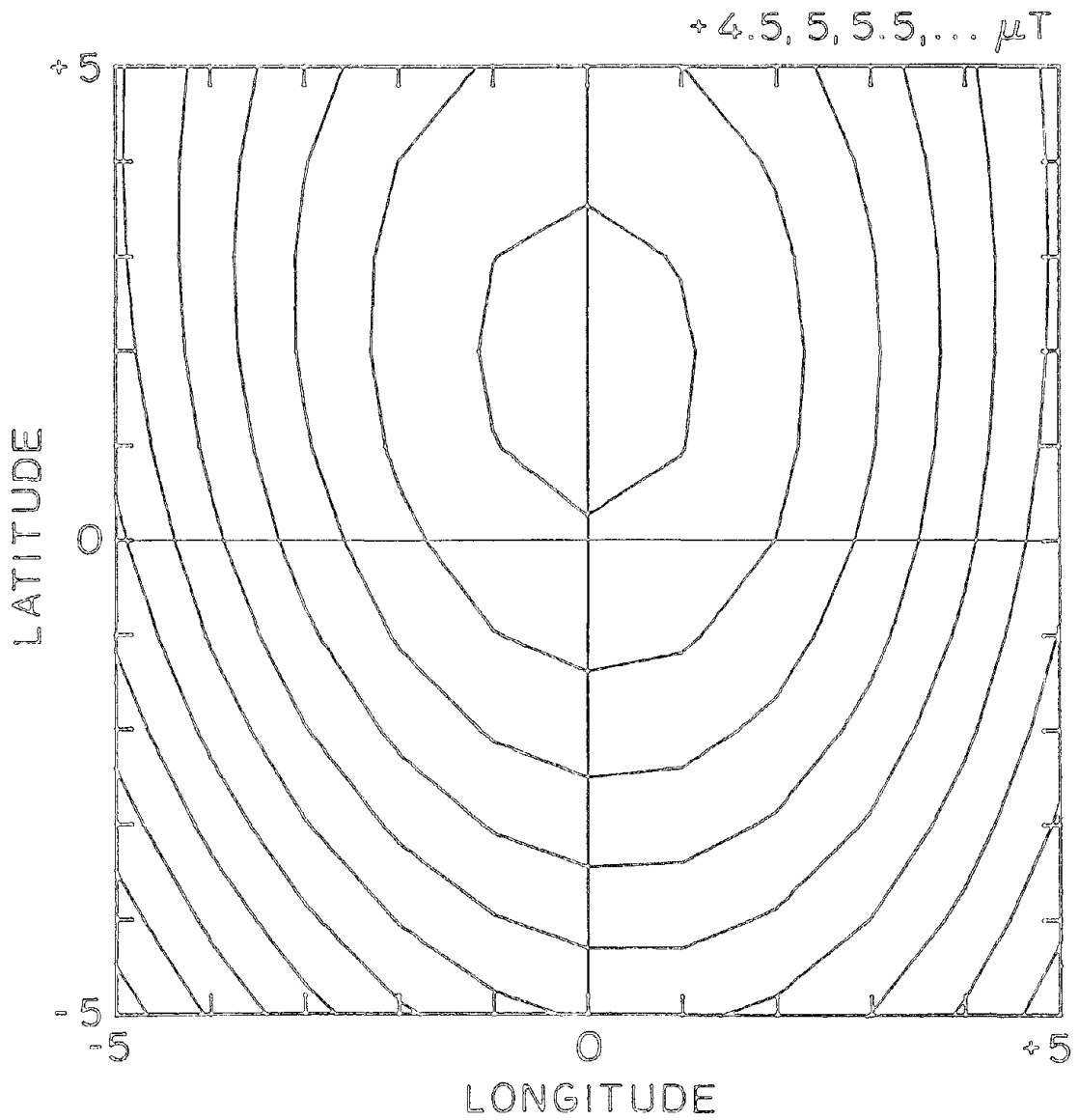


Figure 6-10b

# SUPERPOSITION ABOUT SOUTHERN POSITIVE CORONAL HOLES

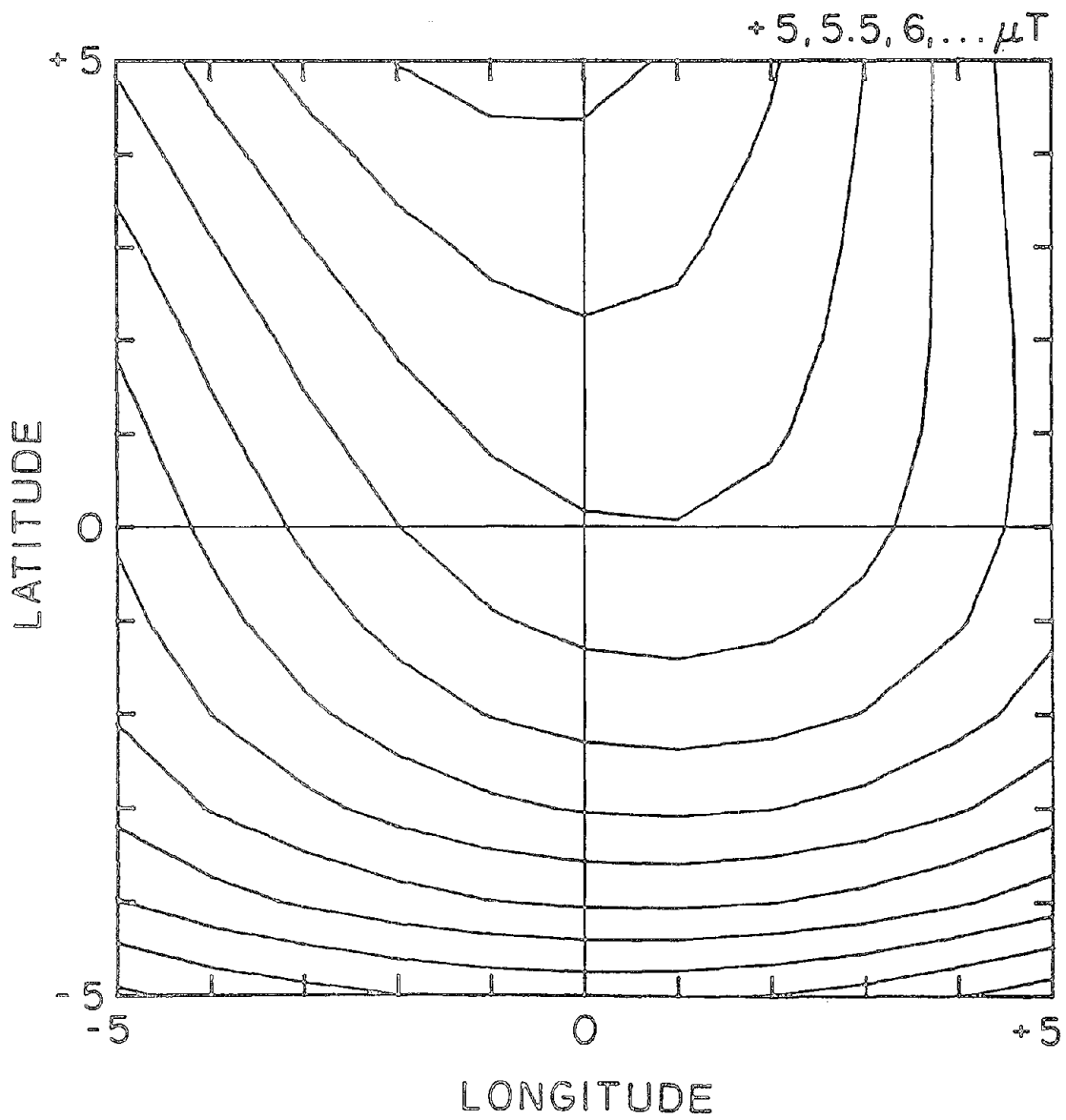


Figure 6-10c

# SUPERPOSITION ABOUT NORTHERN NEGATIVE CORONAL HOLES

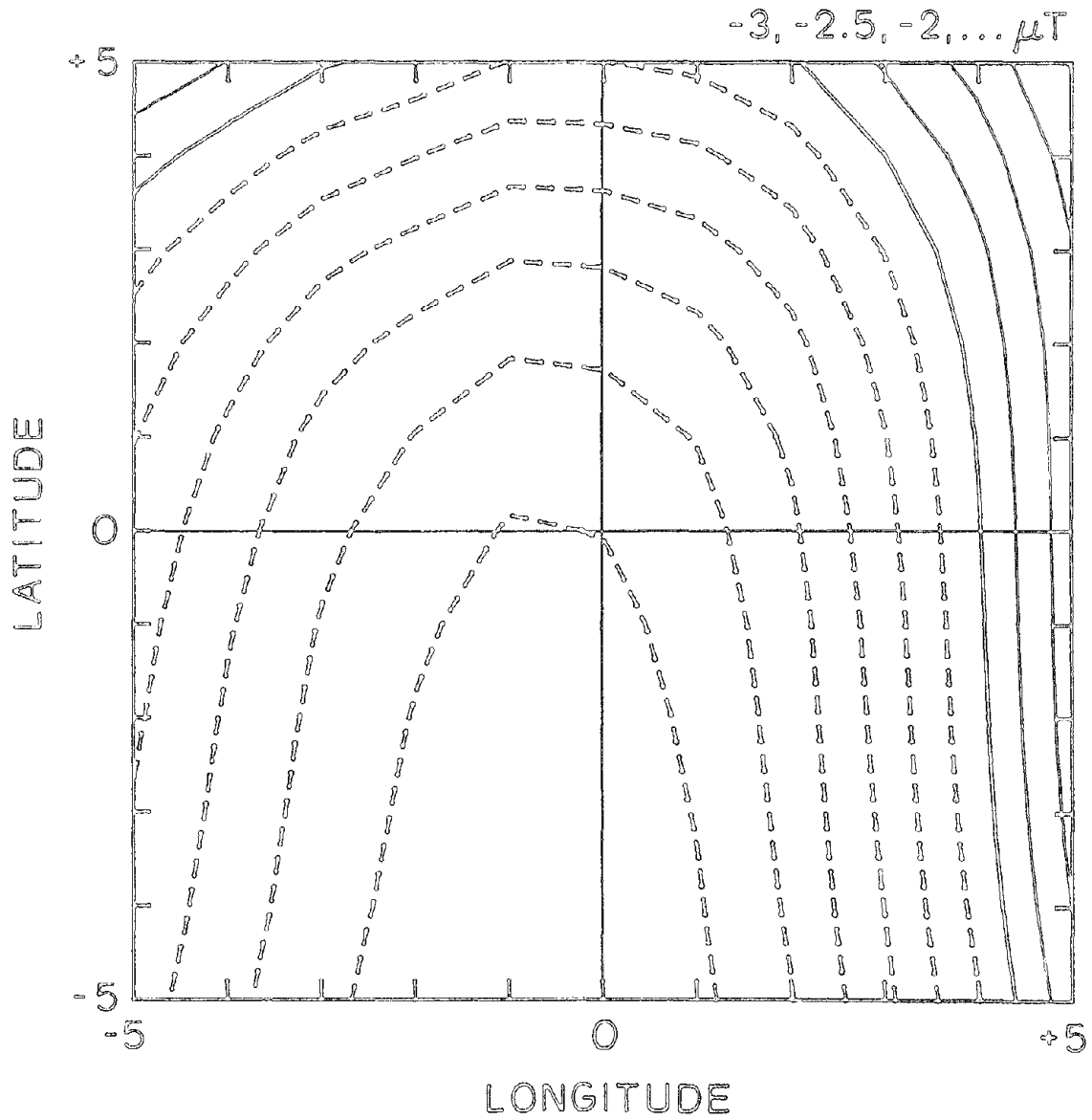
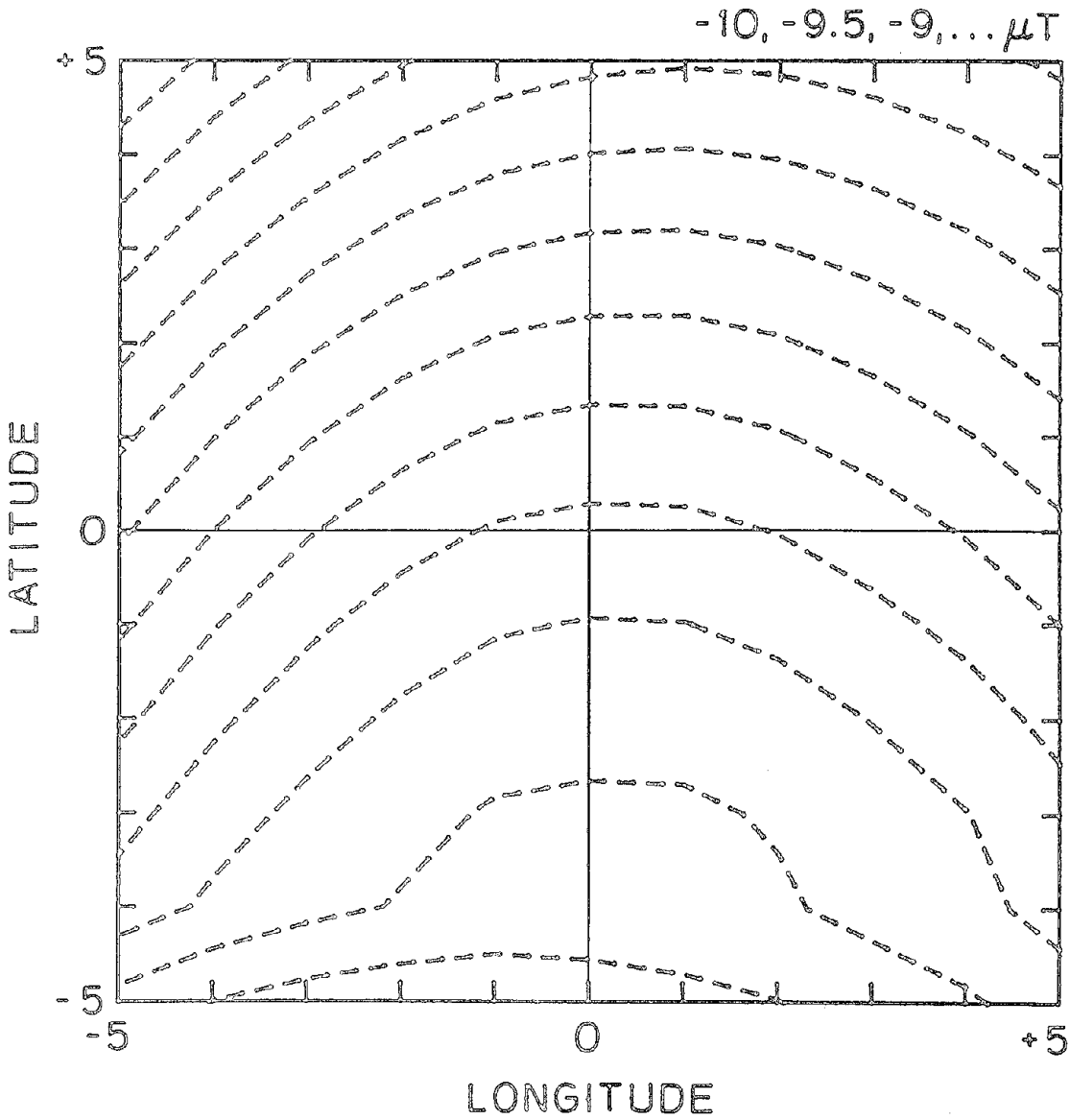


Figure 6-10d

# SUPERPOSITION ABOUT SOUTHERN NEGATIVE CORONAL HOLES





centers of the maps about the coronal hole position, and averaging the field values at each point of the map. This corresponds to a two-dimensional superposed map analysis with coronal hole locations providing the synchronization times.

The 24 northern hemisphere positive flares make up the largest group of holes in the list. There are 10 southern hemisphere positive holes, 7 northern negative, and 8 southern negative. It is unclear why there are so many more positive polarity holes. The location of the hole is centered at the center of the graph. Figure 6-10a shows that the locations of positive northern hemisphere holes coincide with or are a little south of the the maximum in field strength. During most of this interval the strongest fields were found at the poles. Since the list considered only low-latitude holes it is reasonable for the field strength maximum to be located north of the actual coronal hole position. Note that since Harvey et al. (1982) found that the average photospheric field corresponding to the coronal hole locations increase by about a factor of three from minimum to maximum, these averaged maps become weighted to emphasize the later holes.

The connection to the stronger polar regions becomes more obvious in Figures 6-10b, c, and d. Because there are fewer holes in each of these categories, the statistics are not quite as good, but the trend in each is obvious. The southern hemisphere positive holes appear to be parts of larger positive structures extending to the north. At the latitude of the holes, the field strength reaches a maximum though it generally increases northward. This confirms the impression gained from examining the general field structure that positive regions appear to "intrude" into the generally negative southern hemisphere and vice versa during this time period. Figure 6-10c demonstrates this even more clearly for the 8 northern hemisphere negative polarity holes. Again the holes seem to occur at maximum field strength for a certain latitude, but the general field strength increases to the south.

The map of superposed southern hemisphere, negative polarity holes shows a structure similar to the previous two cases, but much broader in longitude and the field strength is higher. This confirms the hypothesis that these holes are not "intruding" into a "hostile" polarity hemisphere. Unlike

the northern, positive holes, the southern, negative holes do not occur at a maximum field strength in the latitudinal direction; the field increases toward the corresponding pole much as it did for the intermediate cases. This may happen because of the smaller number of holes in this group, but it suggests that these holes have a firmer connection to the polar holes than to the northern holes. This question should be studied in more detail with a complete list of coronal holes.

What is the more fundamental quantity? Large scale structure or coronal holes? It appears that coronal holes arise within a pre-existing magnetic structure. A strong, large scale magnetic field will usually develop before a coronal hole appears and remain long after the coronal hole disappears. This suggests that the large scale field is the more fundamental quantity. This does not mean that coronal holes are not unique structures, it means that they arise within the context of the larger scale fields. One cannot yet say why a coronal hole will develop in a given location, in one high strength region and not in another, but the hole must be viewed as an evolutionary step in the development of a large scale region rather than as an isolated entity.

### *Cosmic Ray Modulation*

Cosmic ray intensity is modulated with an 11-year cycle which corresponds fairly well to the sunspot cycle. During activity maximum fewer cosmic rays reach the Earth; near minimum the largest cosmic ray flux is observed. Svalgaard & Wilcox (1976) suggested that the variation in the shape of the current sheet may be an important factor in determining the ease with which cosmic rays penetrate the heliosphere. They determined the solid angle of the polar field regions averaged over four cycles using the Rosenberg - Coleman effect (1969). This correlated fairly well with the variation in the flux of cosmic rays with rigidity  $> 0.5$  GV between 1961 and 1969. Jokipii & Thomas (1981) were able to model the effects of a simple tilted dipole configuration of the current sheet on the propagation of cosmic rays. They found that increasing the tilt of the sheet significantly decreases the

flux of cosmic rays at Earth. Hundhausen et al. (1980) showed a very good correlation between the area of the polar coronal holes and the Mt. Washington cosmic ray flux between 1966 and 1976.

Having computed the 3-dimensional structure of the current sheet for the interval 1976 - 1983, the solid angle of the polar field region can be found. Define the quantity  $A_1 = 4\pi$  minus the solid angle occupied by the area between the neutral line and the equator.  $A_1$  represents the solid angle of the polarity region connected to the solar poles within each hemisphere. It is closely related to the latitudinal extent of the current sheet. Three rotation averages of  $A_1$  are plotted in Figure 6-11 using a solid line. The obvious trend is a decrease from solar minimum to solar maximum followed by an increase thereafter. In addition to the trend, significant changes occur over short periods which are related to rapid, permanent changes in the latitudinal extent of the current sheet.

Cosmic ray intensity data from the Climax neutron monitor has also been plotted in Figure 6-11. These cosmic rays have rigidity  $> 3.03$  GV. This data has also been smoothed using a three rotation running average. The cosmic ray data has been lagged by three rotations relative to the source surface data.

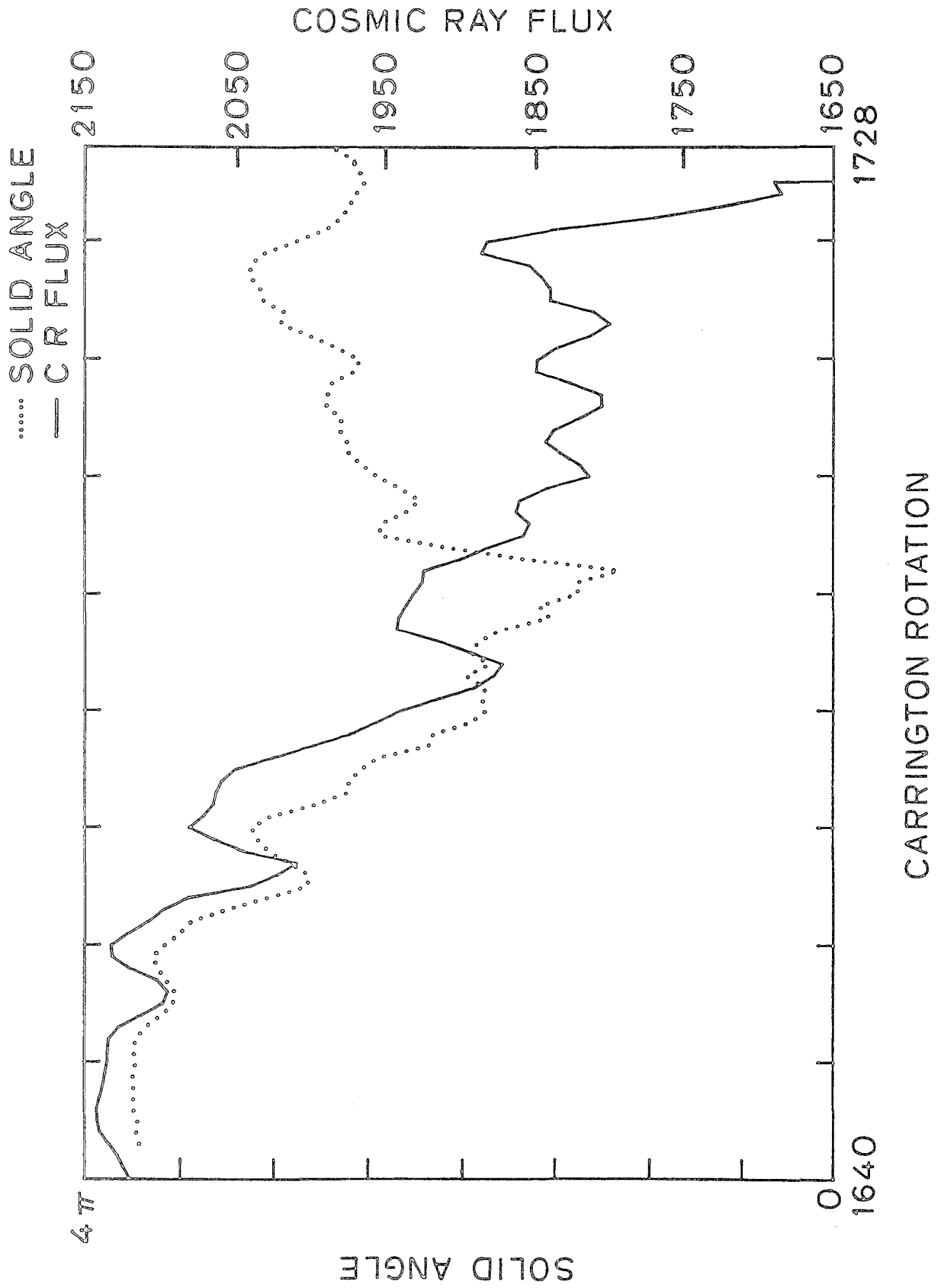
Before sunspot maximum in 1980, the two curves are very similar. Both the long term trend and the episodic events are reproduced quite well. After the polar field reversal at the end of 1979, the relation does not seem to hold. Both the long term trend and the shorter time scale characteristics show a poor correlation. One possibility is that the reversal of the polar field changed the dependence of the cosmic rays on the heliospheric configuration. Jokipii (1981) showed that if particle drift is considered, then perturbations in the equatorial IMF are more effective in modulating the

---

Figure 6-11: The cosmic ray flux and the solid angle of the polar field regions. For each Carrington Rotation the solid line represents the three rotation average of the cosmic ray flux measured by the Climax neutron monitor delayed three rotations. The dotted line shows for each rotation the three rotation average of  $4\pi$  minus the solid angle between the equator and the neutral line. This represents the solid angle of the polarity region connected to the pole in each hemisphere.

Figure 6-11

# COSMIC RAY FLUX AND CURRENT SHEET SOLID ANGLE vs. TIME



cosmic ray intensity during cycles when the field over the Sun's north polar region points inward rather than outward. Or perhaps both the cosmic ray intensity and the current sheet configuration are related to some more basic parameter of the solar cycle and the good agreement seen during the rising phase of the cycle is coincidental. This is somewhat hard to believe because of the close relationship found by Hundhausen et al. (1980) for most of the last cycle. In any case this will be an interesting area of further investigation when more of the cycle can be studied.

#### *Coronameter Data*

Coronameter measurements provide one of the few alternative methods for determining the current sheet configuration in the low corona. The correlation between coronal streamers and neutral sheet has been used by Newkirk (1972) and Pneuman et al. (1978). The observations of the current sheet in the low corona determined from bright coronal structures by Howard & Koomen (1974) using the techniques of Hansen et al. (1974) have already been described. Measurements from the Mauna Loa coronameter have been referred to several times and will be compared with the potential field model results over a short period in this section, as in the paper of Wilcox & Hundhausen (1983).

Photographs of the white light corona are taken each day at Mauna Loa using the K coronameter. The polarization brightness of the coronal is recorded at a height of  $1.5 R_{\odot}$ , somewhat lower than the optimum source surface used in the potential field computation. Polarization brightness is the intensity difference observed for tangentially and radially polarized light and a maximum in this quantity corresponds to a higher coronal density. From these photographs a synoptic chart of polarization brightness can be assembled for each of the two solar limbs. The method is described in Hansen et al. (1974). Hundhausen (1977) related the maximum contour to the neutral line.

Burlaga et al. (1981) used this relation to compare the neutral lines

determined using the potential field model (PFM) of Wilcox et al., (1980) with those found from the maximum brightness contour (MBC). Comparison of individual rotations using the coronameter data agreed better with the IMF measurements made by Helios I and II than did the potential field model calculation made from a 6-month average of the Mt. Wilson photospheric data. Besides the obvious problem with evolutionary effects over a six month interval, there was a general trend for the computed current sheets to lie at higher latitudes. In fact the PFM results were in conflict with the high latitude Pioneer 11 data which observed no current sheet above  $14^{\circ}$ N latitude. This was likely due to the fact that no polar field correction was made in the work of Wilcox et al., as pointed out by Burlaga et al.

PFM results for CR 1641 - CR 1658 were presented by Hoeksma et al. (1982). This analysis referred to individual rotations using Stanford data and included the polar field correction. The source surface radius was located at  $2.35 R_{\odot}$ . The monopole component has not been removed. Bruno et al. (1982) presented the the MBC determination of the current sheet for much of the same interval. Wilcox & Hundhausen (1983) compared the results which are shown in Figure 6-12. As stated by Wilcox & Hundhausen the figure "shows that the two methods lead to current sheets with very similar shapes and with similar amplitude displacements from the solar equator. For five of the six Carrington rotations to which both methods have been applied, the two methods are about equally successful in predicting the observed IMF polarity."

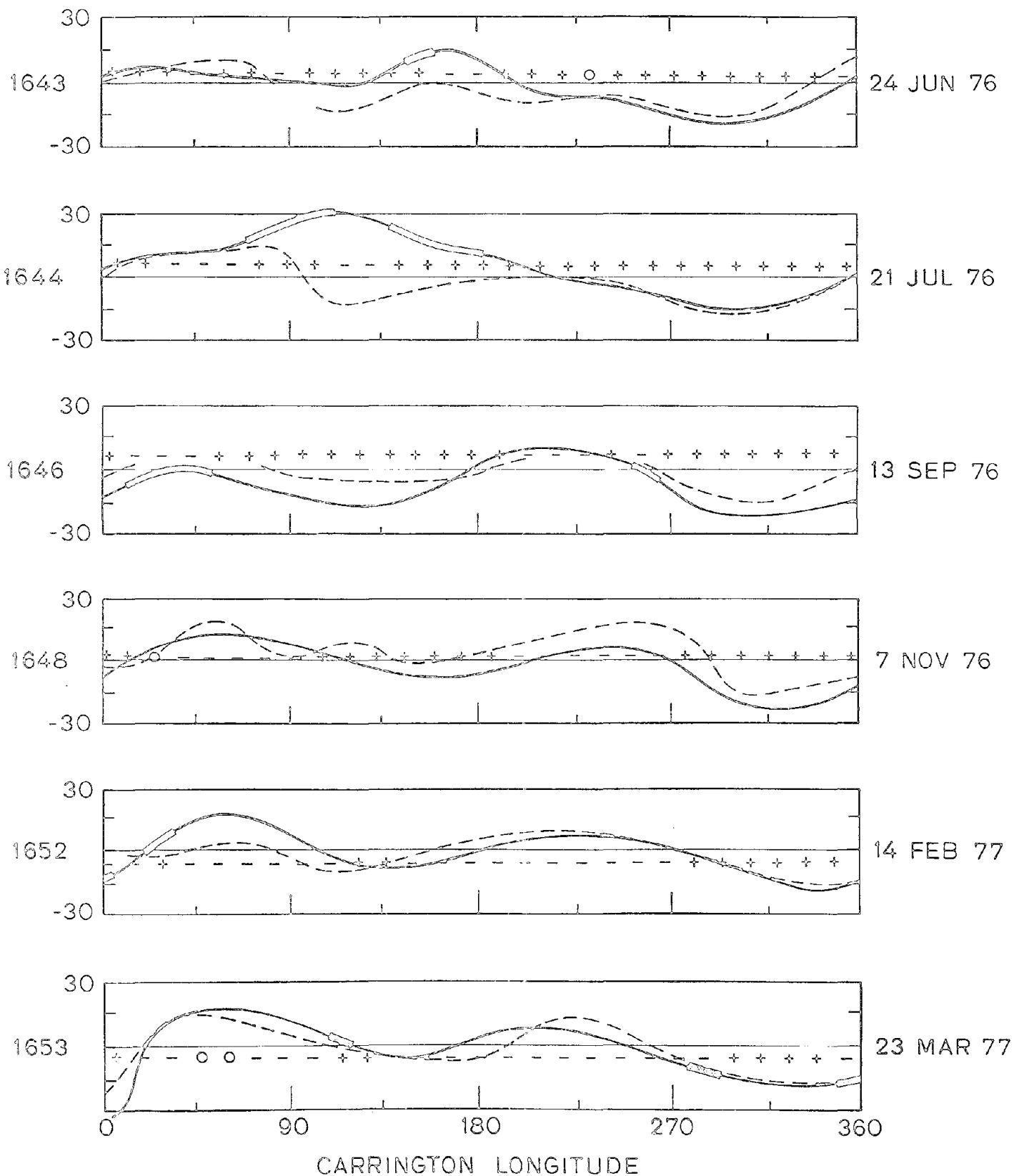
The major disagreement between the methods occurs in CR 1644 when the PFM near  $100^{\circ}$  extends substantially northward. This is unlike the structure computed for CR 1643 and CR 1645 and conflicts with the MBC result. The MBC sheet has better, though not perfect, agreement with the IMF

---

Figure 6-12: For each rotation for which coronameter data was available, the potential field model results from Figure 5-3 and 5-4 have been reproduced. The neutral line determined using the maximum brightness contour method is plotted as a dashed line. In all but CR 1644 the correspondence of the two methods is very good. (From Wilcox and Hundhausen, 1983). The plus and minus signs show the IMF polarity measured at Earth.

Figure 6-12

# HELIOSPHERIC CURRENT SHEETS



--- MAXIMUM BRIGHTNESS CONTOUR  
— POTENTIAL FIELD CALCULATION

polarity at that time. This large change in the field configuration was discussed by Hoeksema et al. (1982). Figures 6-13a, b, and c show the observed photospheric fields for CR 1643, CR 1644, and CR 1645. The change in the computed current sheet was caused by the appearance of an unusually strong magnetic region in the photosphere. A large bipolar magnetic region appeared in Rotation 1644 at longitude  $120^\circ$  with predominantly toward polarity field. The corresponding IMF polarity observed at Earth was away on several days during which the computed current sheet would lead to a prediction of toward polarity. There are more negative polarity days near  $120^\circ$  in the IMF during CR 1644 than during either CR 1643 or CR 1645 (see Figure 5-3).

The MBC neutral line, on the other hand, does not seem to change between CR 1643 and CR 1644. This suggests that the unbalanced photospheric flux region may be an artifact of the observing method. The agreement of the MBC surpasses that of the PFM for this rotation. However the MBC misses the negative polarity days near  $120^\circ$ . It seems possible that there may have been a region of toward magnetic field polarity in the heliosphere corresponding to this bipolar magnetic region as confirmed by the two days of negative polarity observed near  $120^\circ$ , but of a shape somewhat different than that suggested by either the PFM or the MBC.

A similar event occurred near  $140^\circ$  longitude in the southern hemisphere in Carrington Rotation 1651 (see Figure 5-4). Another rather rapid change in the computed current sheet near longitude zero from CR 1652 to CR 1653 was also caused by the appearance of a large bipolar magnetic region in the photosphere, but in this case the region remained in the photosphere for several rotations, and the corresponding effects on the computed current sheet also continued for several rotations. Both the MBC and the

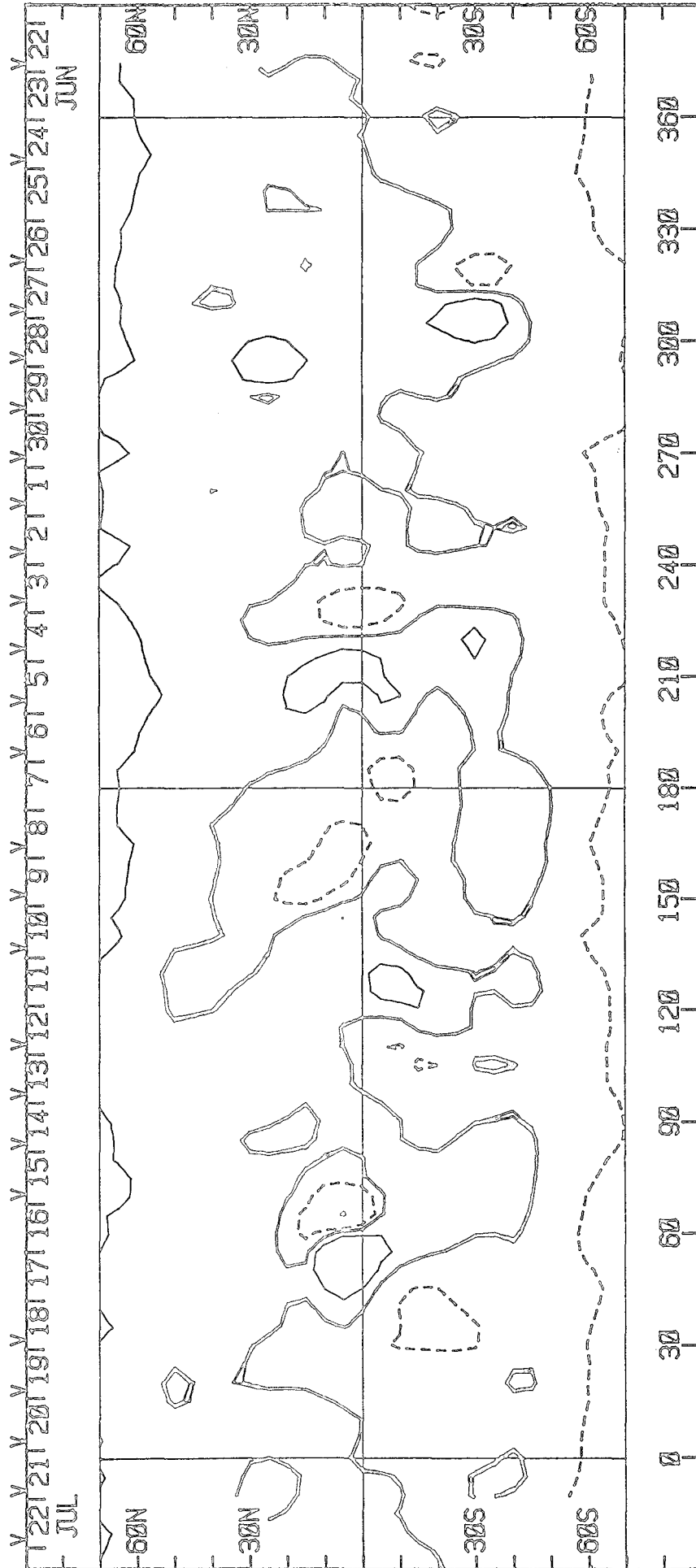
---

Figure 6-13a: A synoptic map of the line-of-sight photospheric magnetic field measurements observed at the Stanford Solar Observatory for Carrington Rotation 1643. Figure 6-13b: Carrington Rotation 1644. Notice the large active region that appeared in the northern hemisphere near longitude  $120^\circ$ . Figure 6-13c: Synoptic chart for Carrington Rotation 1645. The size and strength of the active region is greatly reduced.



# PHOTOSPHERIC MAGNETIC FIELD

$0, \pm 100, 500 \dots \mu T$



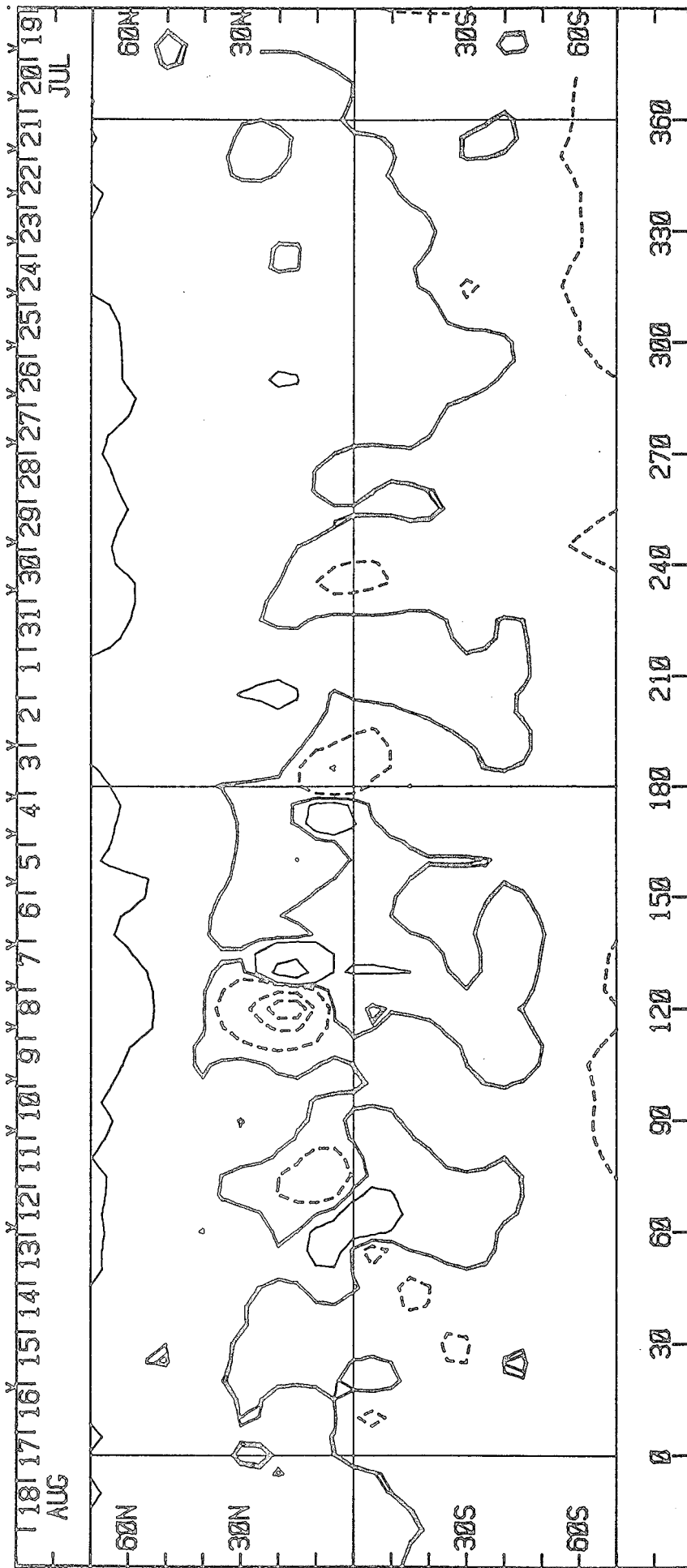
ROTATION 1643

Figure 6-13a

Figure 6-13b

# PHOTOSPHERIC MAGNETIC FIELD

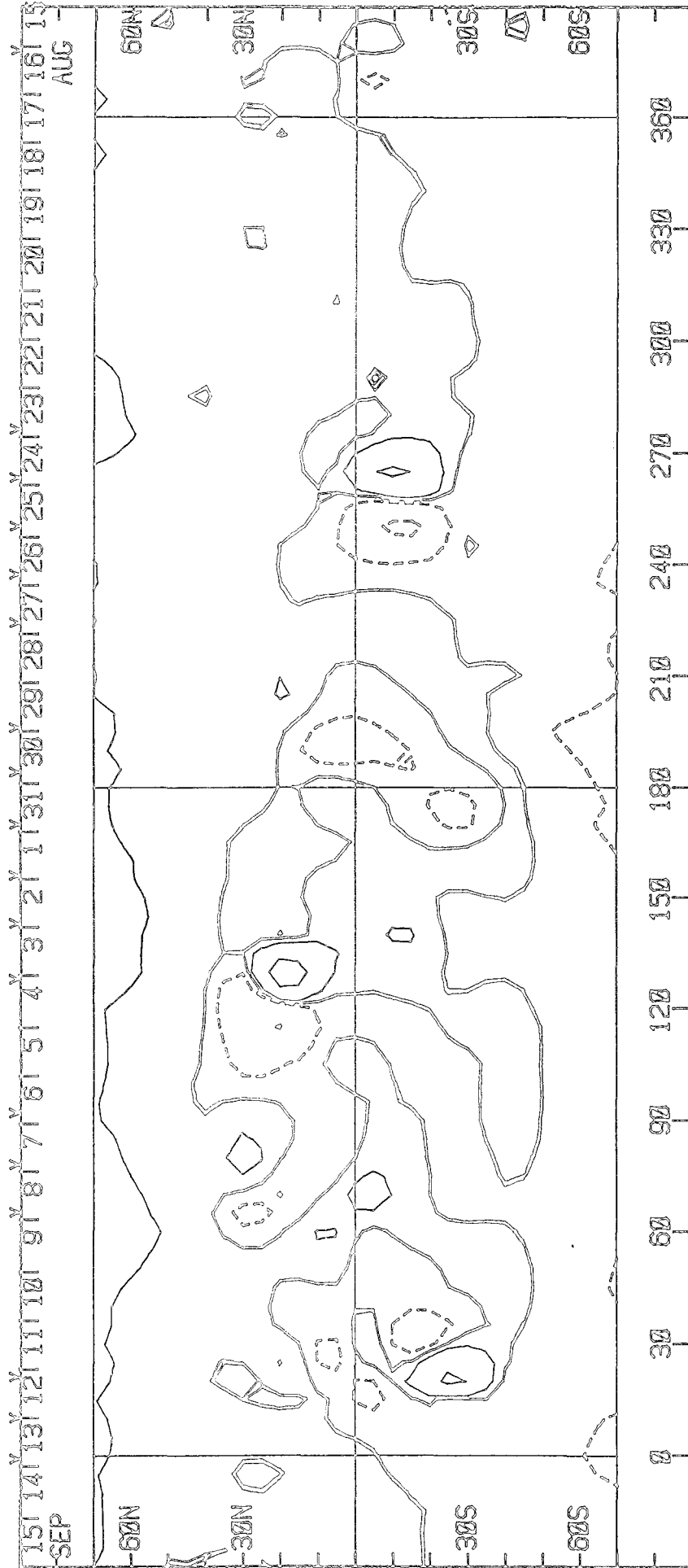
$0, \pm 100, 500 \dots \mu T$



ROTATION 1644

# PHOTOSPHERIC MAGNETIC FIELD

$0, \pm 100, 500 \dots \mu T$



ROTATION 1645

Figure. 6-13c

PFM responded to the presence of this region.

The difference in altitude between the MBC and PFM is not highly significant. Figures 6-14 and 6-15 show the direction of the computed field at  $1.5 R_0$  and  $2.49 R_0$ , at the level of the K coronameter observation and just below the source surface radius. Use caution when comparing these directly with the current sheets shown in Figure 6-12. These PFM calculations are plotted in a different projection where the y-axis is linear in sine latitude rather than latitude. Also these come from a single computation for the  $360^\circ$  interval, so the field near the edges may not be precisely the same as that in Figure 6-12. It is better to compare 6-14 and 6-15 directly since both are plotted in the same format. Each grid point is marked by a '+' symbol with a vector showing the direction of the field. The magnitude of the field is not represented. The contour line corresponds to the zero line of the radial field component.

The main difference between the two is that the lower altitude field extends to higher latitude than the source surface field. The structure at lower altitude is also somewhat more complex showing the increased influence of the higher order multipole fields. The locations where the current sheet crosses the equator do not change very much; the polarity predictions in the ecliptic will not be very different. Comparing the structure at  $1.5 R_0$  with the MBC neutral line shows only slightly less similarity than does the  $2.5 R_0$  result. The conclusion is that the structure seen at  $2.5 R_0$  is already evident at  $1.5 R_0$ . The K coronameter data agrees better with the PFM field at  $2.5 R_0$ . This may be because the assumption of a potential field and the assumption of radial field lines at the source surface tend to artificially increase the altitude at which the computed field lines become

---

Figure 6-14: The field direction at  $1.5 R_0$  for CR 1653 is shown in a format similar to Figure 3-6. The structure at this height is qualitatively similar to, but somewhat more complex than the field configuration at  $2.5 R_0$ . The coronameter measurements were made at this altitude.

Figure 6-15: The field direction just below the source surface at  $2.49 R_0$  for CR 1653. The structure extends to lower latitudes and is somewhat simpler than that shown in Figure 6-14. The field is almost entirely radial at this height.

DIRECTION OF  $\vec{B}$  AT  $R = 1.5R_0$

6 APR 1977

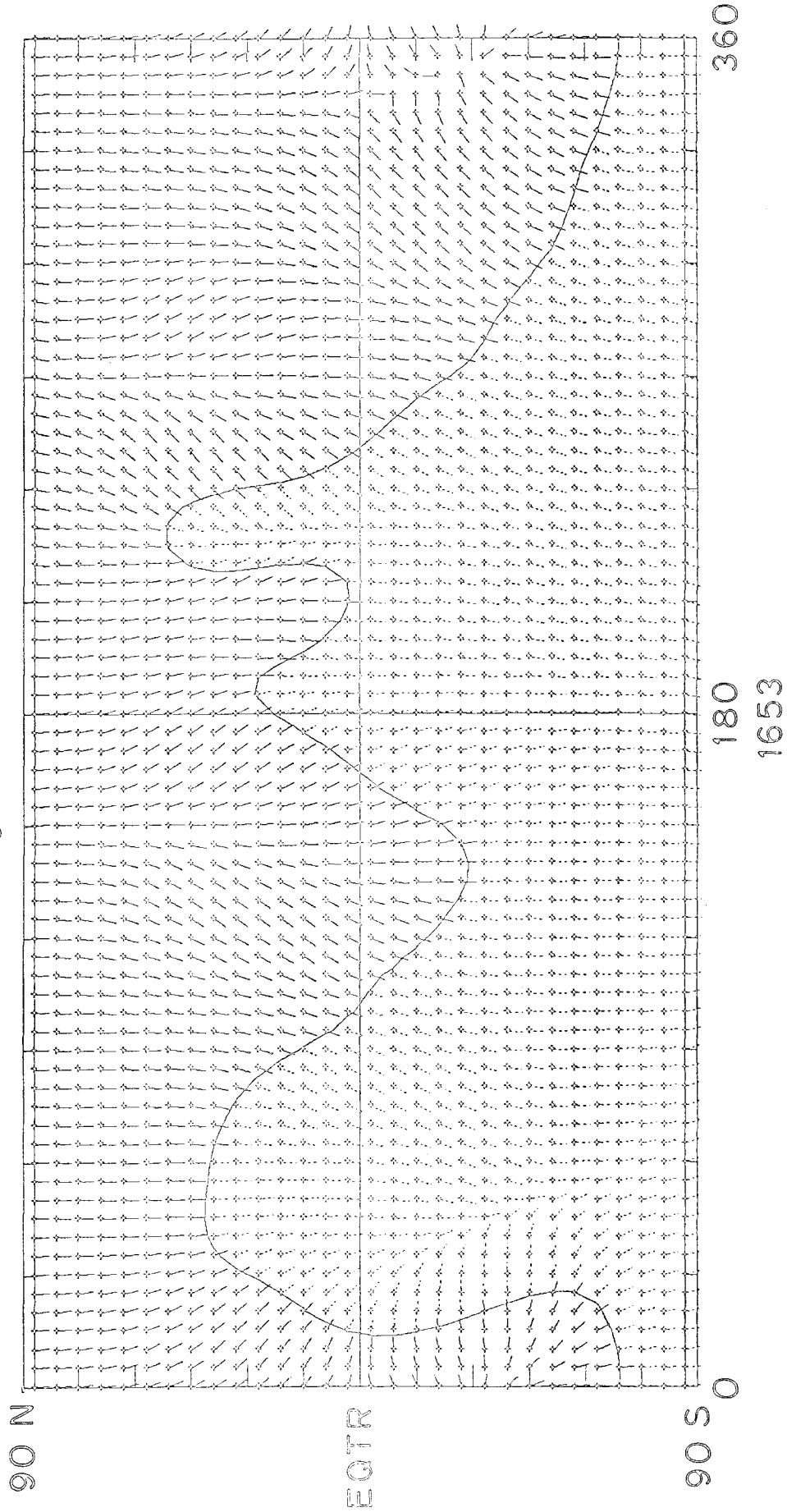
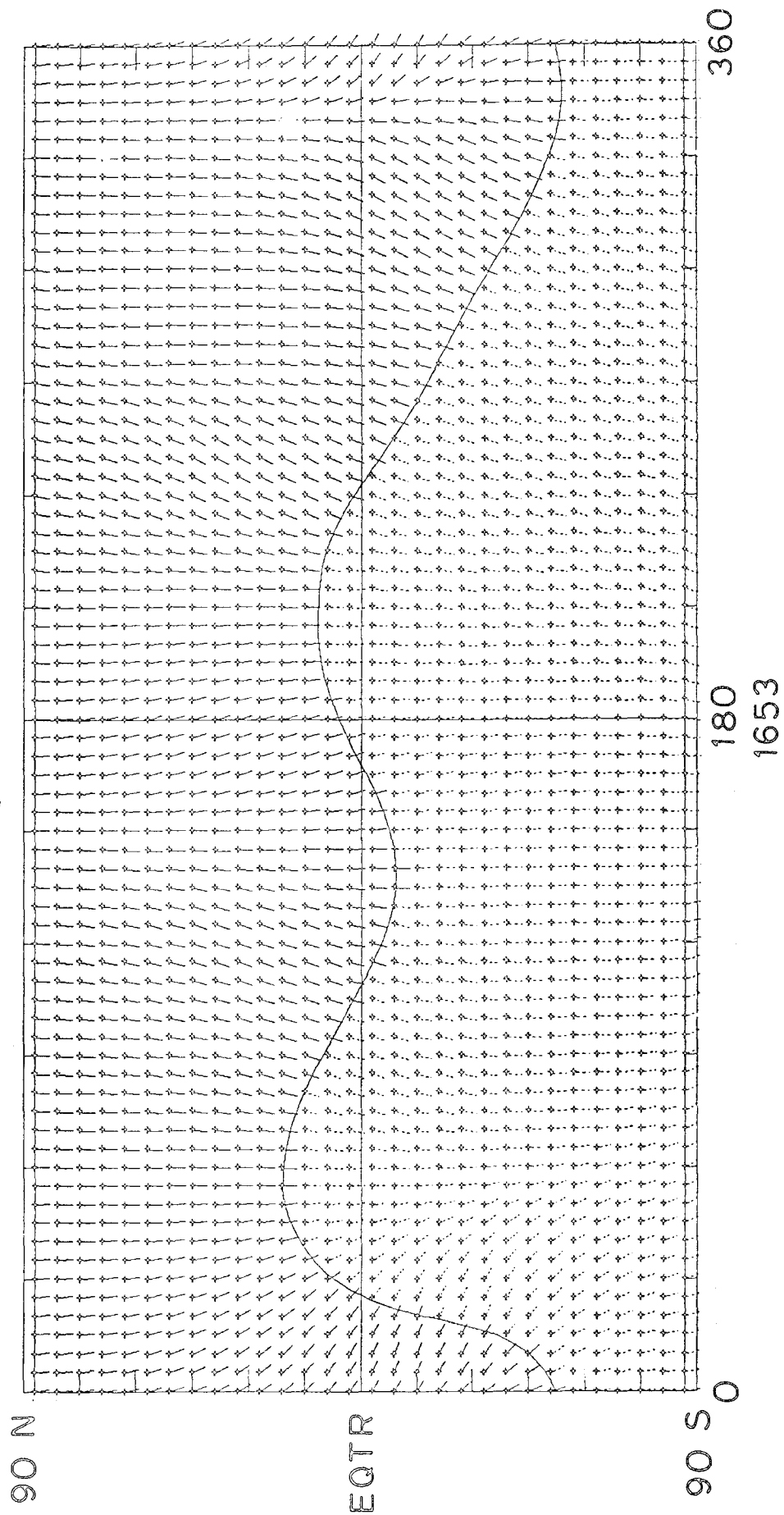


Figure 6-14

Figure 6-15

DIRECTION OF  $\vec{B}$  AT  $R = 2.49 R_0$

6 APR 1977



open to the interplanetary medium relative to the actual coronal field lines. This deserves study over a larger portion of the solar cycle.

For comparison Figure 6-16 shows the field computed at  $1.1 R_{\odot}$ , very near the photosphere. The structure at this altitude is extremely complex and it would be difficult to infer the simpler structure predicted by the MBC or the PFM at the source surface. Most of the field lines close and the structures simplify between the photosphere and  $1.5 R_{\odot}$ .

One hope for further study is the comparison of coronameter data with the PFM results during other parts of the cycle. Unfortunately, one of the problems with the coronameter data is that near maximum the structure becomes much more complex and the current sheet location is difficult or impossible to determine. This is true because of the increased level of activity. The occurrence of transient events makes the interpretation of coronameter data very difficult. Especially near maximum when the latitudinal extent of the current sheet is so high and the polar fields are weak, it would be good to have an independent measurement of the extent of the current sheet. We should also seek confirmation of the isolated current sheet regions found near maximum.

#### *Other Probes of the Heliosphere*

A few spacecraft have travelled to latitudes different from that of the Earth. Interesting comparisons can be made when several spacecraft measure the IMF at different latitudes simultaneously. Such a comparison will be described in the present section. Comets presently provide the only direct high latitude probe of the heliospheric field. Disconnection events (DEs) in comet tails can be related to the passage of sector boundaries (Niedner & Brandt, 1978, 1979, 1980). We will compare our results for the configuration

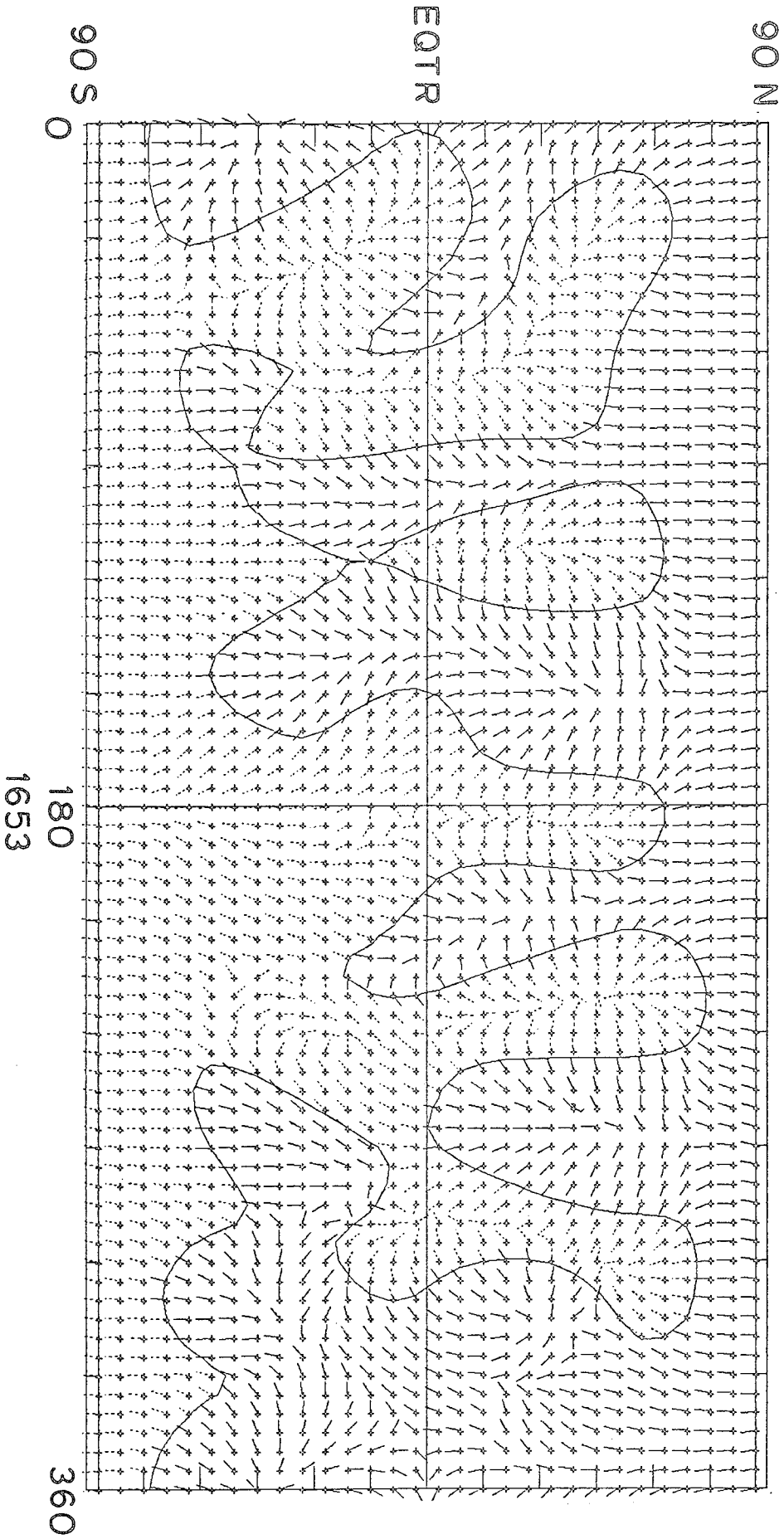
---

Figure 6-16: The structure at  $1.1 R_{\odot}$  is highly structured and the field direction varies greatly, reflecting the more of the complexity of the photospheric field.

Figure 6-16

DIRECTION OF  $\vec{B}$  AT  $R = 1.1R_0$

6 APR 1977





of the field with those of Niedner (1982) derived from DEs.

The two Helios spacecraft orbit the sun and often have latitudes different from each other and different from the Earth. This provides the opportunity to get a better determination of the heliospheric field configuration, even though we are still limited to a band  $\pm 7.25^\circ$  from the equator. Villante et al. (1979) published the Helios data for the interval January through May, 1976. Since Stanford data was unavailable for this period, Mt. Wilson data for the six rotations was averaged and the potential field was then computed. Figure 6-17 and 6-18 from Wicox et al. (1980) shows the result for these six rotations. The IMF polarity measurements from Helios have been corotated back to the source surface and plotted at the corresponding latitude and longitude. The latitude of Pioneer 11 which observed a single polarity at  $16^\circ$  N (Smith et al., 1978) is marked by the horizontal dashed line. As pointed out by Burlaga et al. (1981) who later made a comparison of the Helios data, the potential field model, and the coronameter results for this same interval, the extent in latitude is too great, probably due to the omission of the polar field correction. This would not substantially affect the field near the equator where the Helios spacecraft travel.

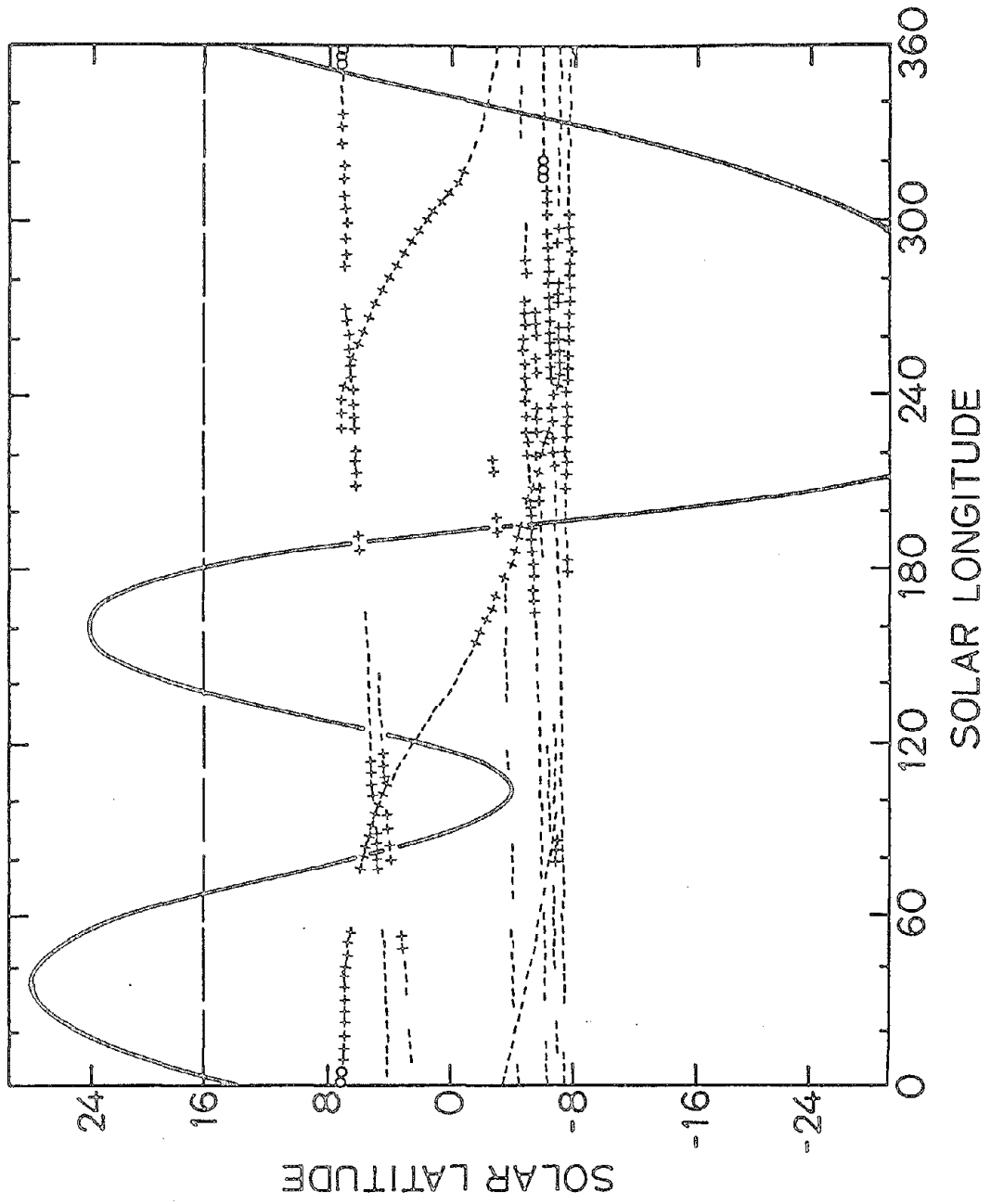
The quality of the agreement with the data with both the Helios and Earth data is quite good. These observations support the view that the large scale structure of the warped heliospheric current sheet can be computed from the observed photospheric magnetic field. This is in contrast to the "ballerina skirt" model current at that time which attributed the origin of the IMF structure to a simple plane which would then be slightly distorted by

---

Figure 6-17: The curved line represents the current sheet for five rotations from January 20 through May 23, 1976 calculated from Mt. Wilson photospheric data. The polar field correction was not made so the latitudinal extent of the sheet was too great. The dashed line at  $16^\circ$  N represents the approximate latitude of Pioneer 11 at 4 AU which observed only positive IMF polarity. The plus and minus signs represent the IMF polarity measured at Helios 1 and 2 projected back to the solar corona. The observed polarities agree well with the the computed field.

Figure 6-18: The same as for Figure 6-17 except that the plus and minus signs represent the inferred IMF polarity at the Earth mapped back to the source surface. The observed polarity changes occur near crossings of the computed current sheet.

Figure 6-17



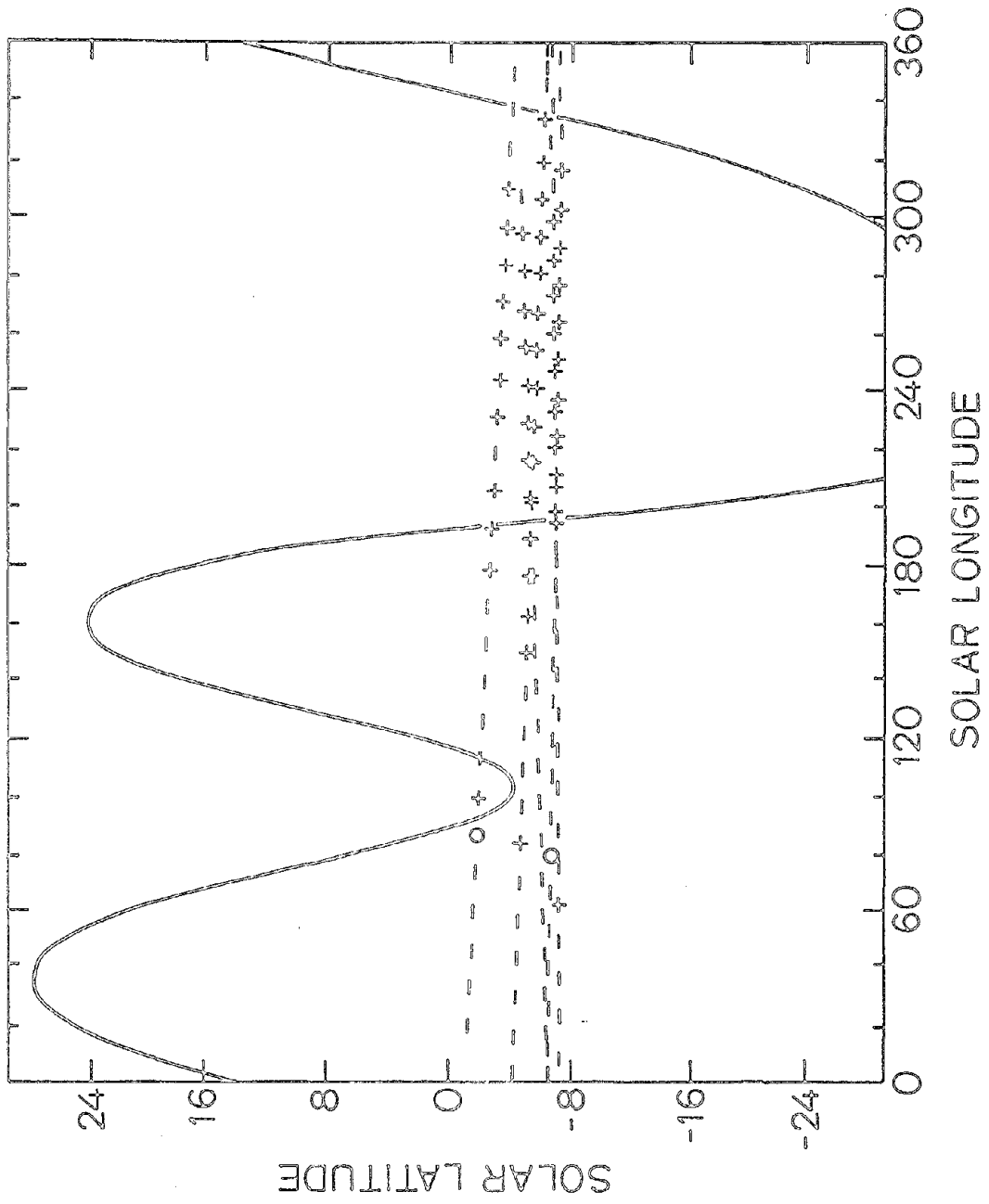


Figure 6-18

dynamic processes in the solar wind (e.g. Smith & Wolfe, 1979). Near minimum it was harder to distinguish between the two, since both models predicted a planar sheet with relatively small warps. However near maximum the distinction became clear.

Niedner (1982) used 72 disconnection events (DE) in comet tails observed since 1892 to investigate the latitudinal extent and the tilt properties of sector boundaries. He found a rough agreement with the latitudinal extent of the current sheet as extrapolated using the Rosenberg-Coleman effect (Svalgaard & Wilcox, 1976). However the sector boundary tilt angles (i.e. the inclination of the boundary with respect to the equator) was significantly more meridional and less ordered than would be expected for a simple sinusoidal current sheet configuration. In probing this question, it was found that two sorts of sectors exist, those which were extremely latitude dependant and those which were not. These would exist at the same time. This led Niedner to suggest that the simple sinusoidal, nearly equatorial current sheet was an oversimplification.

The computed current sheets presented in this study confirm this suspicion. Near minimum the current sheet is nearly equatorial and sinusoidal. During most of the cycle, however, the current sheet reached to much higher latitudes and is certainly not sinusoidal. At different longitudes during the same rotation the current sheet may be highly inclined to the equator and nearly parallel. Behannon et al. (1983) confirm this in a study of boundary inclinations using spacecraft magnetic field measurements.

The potential field model calculations presented in Chapter 5 help to interpret many other observations and lead to new insights. The discussions in this Chapter have shown the relationship of the current results to those for other solar cycles determined in a variety of methods. The structures observed during solar cycle 21 are much like those to be expected in any other cycle. The following chapter tries to use these results to come to a broader understanding of the relationship of the large scale field to the solar cycle.

## Chapter 7 -- Multipoles & Discussion

Often the heliospheric field can be characterized by its lowest order multipole terms. During 1973, for example, the field resembled a tilted dipole (Hundhausen, 1977). Near minimum the field could be characterized as a dipole field with a quadrupole distortion (Bruno et al. 1982). This suggests that an interesting alternative way of looking at the field is in terms of the multipole components derived in the potential field computation. That analysis will be described in this chapter and related to other discussions of the field in terms of its components. This is especially interesting when considering the reversal of the polar field near maximum. Later sections will consider the rotation of the coronal field and the large scale photospheric sources of the coronal field.

### *Multipole Components*

The  $g$  and  $h$  coefficients indicate the relative contributions of the various multipole moments to the field. The expression for the radial field strength,  $B_r$ , depends on the associated Legendre polynomials, the  $g$  and  $h$  coefficients and on a term which varies with radius (see Equation 3-1). In order to compare the importance of the various multipoles the  $g$ 's and  $h$ 's must be normalized by  $1/\sqrt{2l+1}$  and adjusted by the factor  $\frac{l+1}{r^{l+2}} + l \cdot \frac{r^{l-1}}{R_g^{2l+1}}$  where  $r$  and  $R_g$  must be expressed in units of solar radii. The normalization must be done in order to compensate for the form used for the associated Legendre polynomials. The radial term arises because the dependance on distance varies with  $l$ . The terms from outside the source surface give the dependance on positive powers of  $r$ ; the dependance on negative powers of  $r$  comes from the sources within the photosphere. The following table gives the factor by which each  $g$  and  $h$  coefficient must be multiplied for intercomparison at quarter  $R_g$  intervals between the photosphere and the source surface located at 2.5  $R_g$ . The comparison factor is independant of  $m$ , the order of the harmonic.

$l$	Radius						
	1.00	1.25	1.50	1.75	2.00	2.25	2.50
0	1.0000	0.6400	0.4444	0.3265	0.2500	0.1975	0.1600
1	1.1917	0.6282	0.3791	0.2524	0.1813	0.1383	0.1109
2	1.8508	0.5610	0.2788	0.1591	0.1022	0.0730	0.0572
3	1.5137	0.4983	0.2033	0.0978	0.0547	0.0356	0.0271
4	1.6670	0.4376	0.1475	0.0599	0.0288	0.0168	0.0123
5	1.8091	0.3795	0.1062	0.0366	0.0151	0.0078	0.0054
6	1.9415	0.3258	0.0758	0.0223	0.0079	0.0036	0.0024
7	2.0656	0.2772	0.0538	0.0135	0.0042	0.0016	0.0010
8	2.1828	0.2344	0.0379	0.0081	0.0022	0.0008	0.0004
9	2.2942	0.1971	0.0265	0.0049	0.0011	0.0003	0.0002

For example, to compare the field strength due to the dipole term and the quadrupole terms at the source surface, the dipole coefficients must be multiplied by 0.1109 and the quadrupole coefficients must be multiplied by 0.0572.

Most of the field comes from within the inner boundary at the photosphere. The photospheric fields determine the evolution of the coronal field as well. The structure at the source surface is observed through the outer heliosphere (subject to dynamic changes in the solar wind). The following discussion compares the multipole contributions at the source surface, since at that point the field configuration is frozen into the plasma and the relative contribution of the multipoles does not change with distance. However, it is important to realize that the physical source of the field lies within the sun where the relative magnitudes of the multipoles are rather different, especially for the higher order terms. This will be a matter for future study.

The relative contributions to the field strength at the source surface for the first three multipoles, the monopole, dipole, and quadrupole terms, are shown in Figure 7-1. These are scaled in microtesla and indicate the maximum field value which would be observed far from a node in each multipole. Each curve is plotted on a scale from 0 to 20  $\mu\text{T}$  and shows the total contribution for all values of  $m$ . For example, the dipole component,  $l=1$ , includes

the contribution from both the polar and equatorial dipoles. During most of the interval the polar dipole is the largest component.

Near minimum the dipole term dominates the other multipoles. The quadrupole has an amplitude of about  $1 \mu\text{T}$  compared with an amplitude of about  $6 \mu\text{T}$  for the dipole term. Thus the quadrupole field is about 17% the magnitude of the dipole. During this interval almost all of the dipole contribution comes from the polar component. The sectoral component is the largest quadrupole term during this period. This confirms the relation found from the Mauna Loa K coronameter data by Bruno et al. (1982) who determined that the sectoral quadrupole term was about 17% of the magnitude of the polar dipole. The relative contributions of the various dipole components will be discussed later.

Near the beginning of 1978 the strength of the dipole field begins to decrease and the other multipoles begin to increase. While the dipole is generally the strongest component, it does not really dominate the field configuration at the source surface during most of the several years around maximum. Occasionally during 1979 and 1980 the quadrupole component is somewhat larger. The dipole does dominate during much of 1982, but fades for much of 1983. This corresponds to the evolution from the strong two sector structure observed during most of 1982 to the four sector structure which began to develop near the end of 1982. The plots of the source surface field configurations for individual rotations in Figures 5-10 and 5-12 demonstrate this.

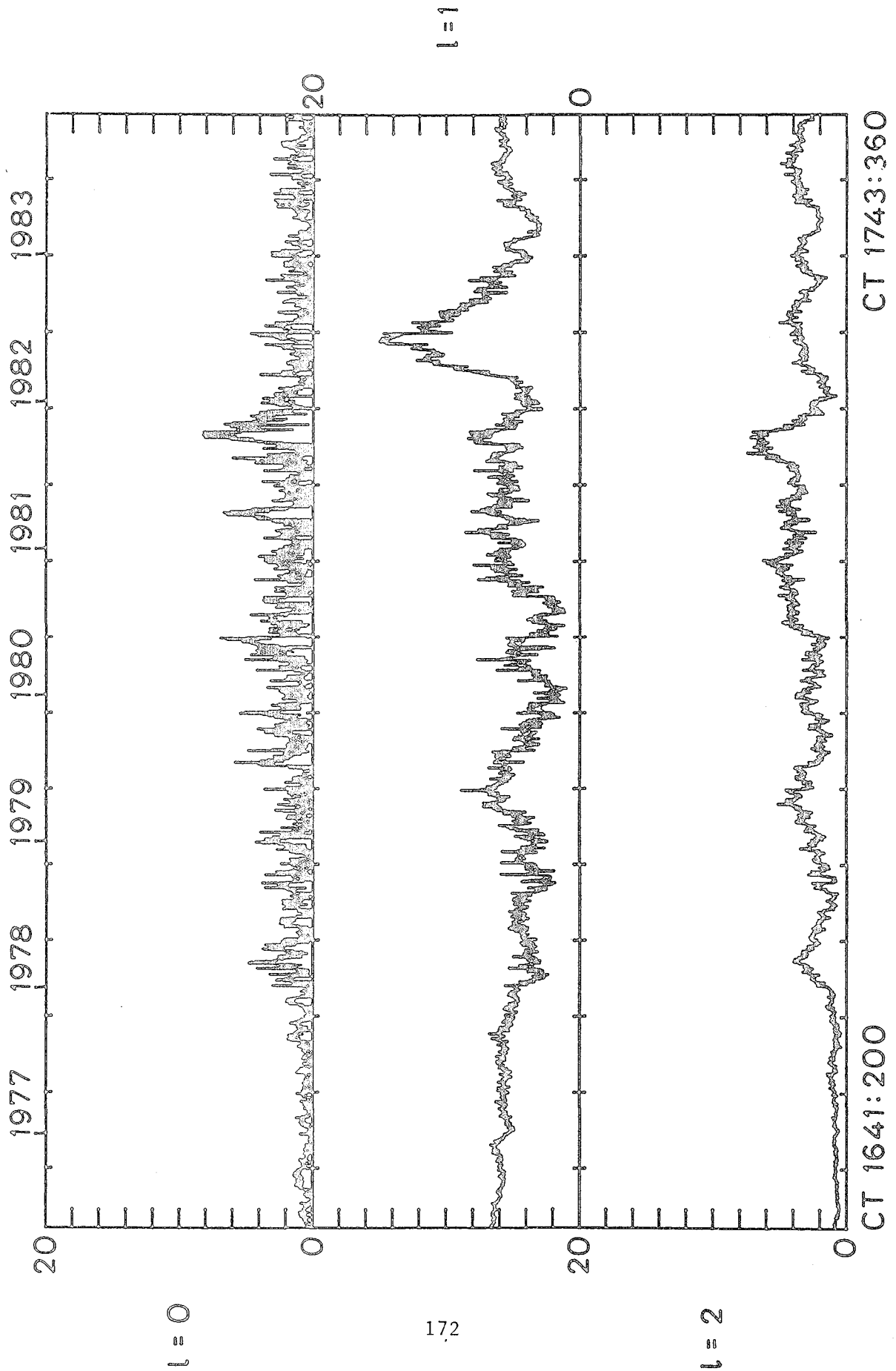
The origin of the monopole term has been discussed in some detail in Chapter 4. Except for brief periods attributable to rapid evolution of the photospheric field, the monopole is much smaller than the other strong terms.

---

Figure 7-1: The magnitudes of the  $l=0$  (monopole),  $l=1$  (dipole), and  $l=2$  (quadrupole), components of the magnetic field at the source surface. This shows the relative contribution of the multipoles to the heliospheric field configuration. The value is computed each ten Carrington degrees. Near minimum the dipole field dominates, but near maximum the quadrupole component has a comparable magnitude. The contribution of the monopole (zero offset) has been removed from the source surface field.

Figure 7-1

AMPLITUDE OF MODES:  $l = 0, 1, 2$





The octupole term, shown in Figure 7-2 cannot be neglected around maximum. In early 1979 its magnitude is comparable to the dipole and quadrupole terms. Each figure is plotted to a different scale, Figure 7-2 going from 0 to 5  $\mu\text{T}$ . The fields due to higher order multipoles, shown in Figures 7-2 and 7-3, contribute very little to the total field at the source surface. The panels in Figure 7-3 extend only from 0 to 0.2  $\mu\text{T}$ . Examination of the comparison factors in Table 7-1 reminds us that at the photosphere the contributions of the higher order terms will increase relative to the lower order terms by factors of several hundred, and so will be very strong at the solar surface.

Each term, with the exception of the dipole term, increases in magnitude from solar cycle minimum to maximum. Some time after maximum these terms begin to decrease slowly. The dipole component reaches a minimum in its average value in 1980, near maximum. This can be explained by the decrease and reversal of the polar field. The coefficients presented include the polar field correction which adds to the polar dipole component. The same dependence on solar cycle of the dipole term is seen if the polar field correction is not made, though not as strongly. The total flux at the source surface increases dramatically near maximum due to the increase in the higher order multipoles.

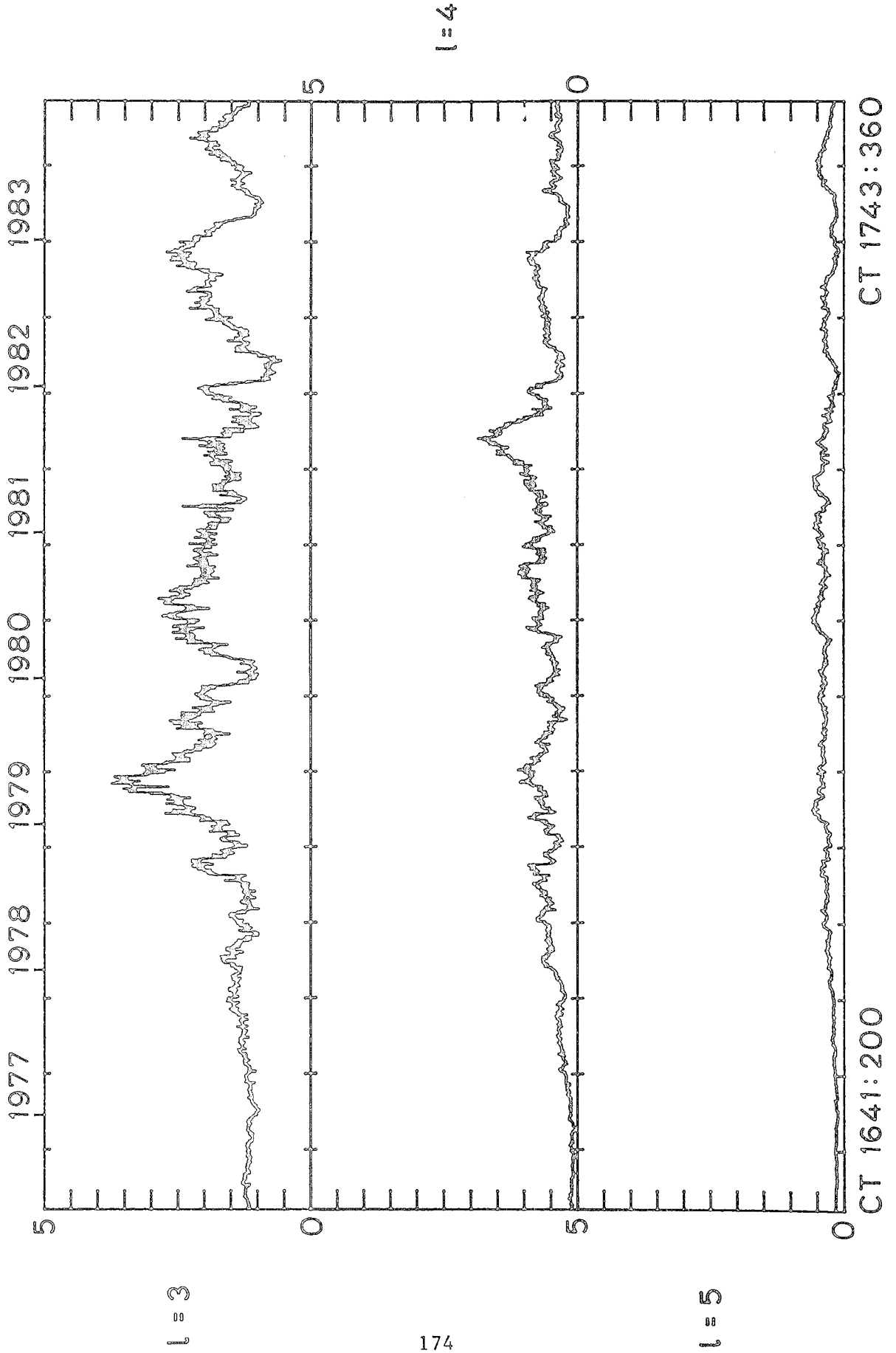
---

Figure 7-2: The relative contributions of the  $l=3$ , octupole,  $l=4$ , and  $l=5$ , multipole components at the source surface. Note the change in scale from Figure 7-1. Except for the octupole, these components contribute little to the large scale configuration of the heliospheric field.

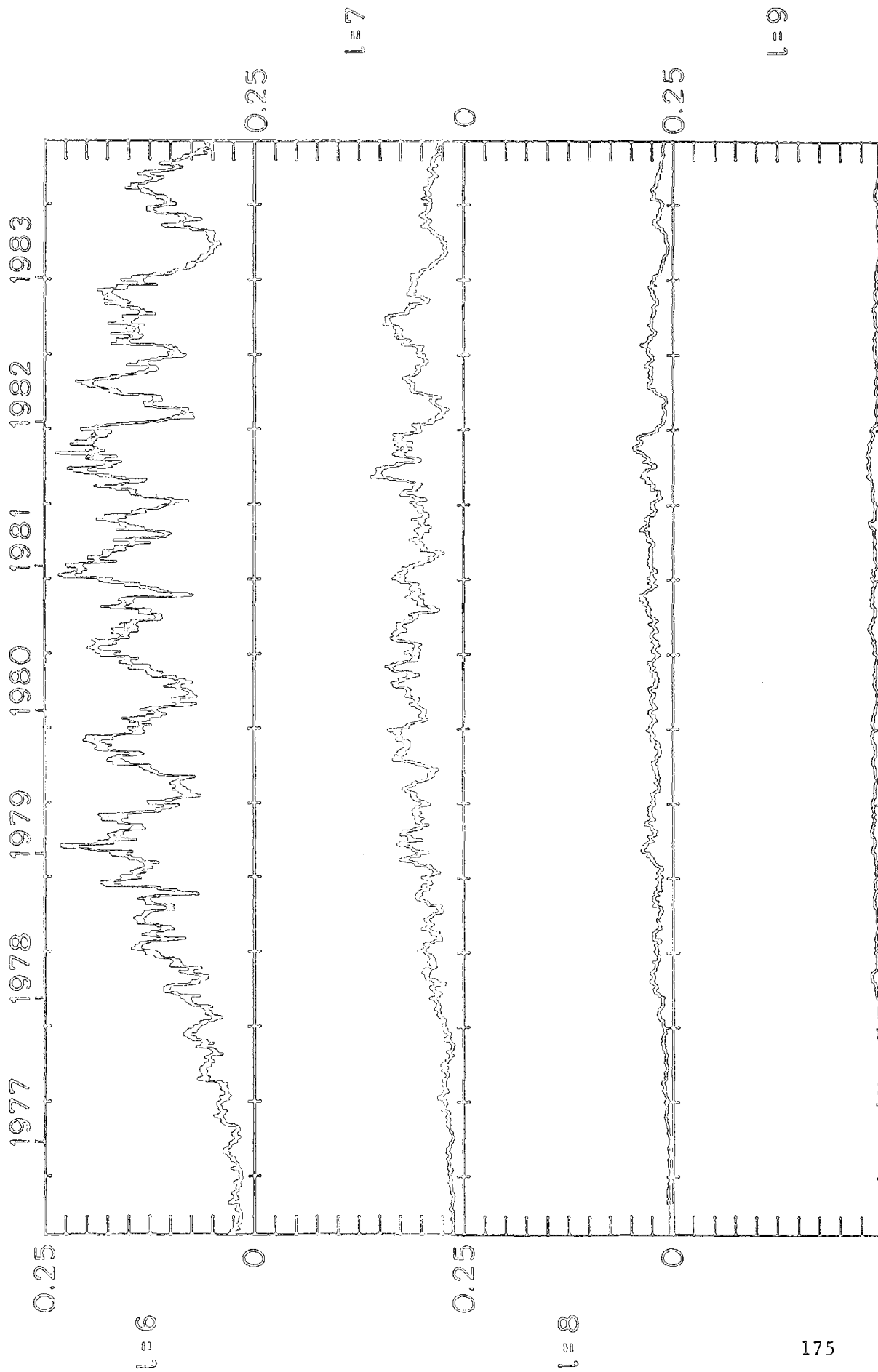
Figure 7-3: The contributions of the  $l=6, 7, 8,$  and  $9$  components. The scale here has again been expanded. Every component increases in magnitude near maximum. While these multipoles contribute little to the source surface fields, they are the dominant components of the photospheric field.

Figure 7-2

AMPLITUDE OF MODES:  $l = 3, 4, 5$



AMPLITUDE OF MODES:  $l = 6-9$



CT 1641:200

CT 1743:360

Figure 7-3

### *The Dipole Components*

Because the dipole has so often been used to characterize the heliospheric field, the following discussion deals with the individual dipole components. The analysis already presented demonstrates that during the several years around maximum an equivalent or greater share of the total flux comes from higher order multipoles. Even near minimum the higher order terms affect the Earth because it is so close to the equator. Near maximum the higher order field contributions would be evident at any latitude.

Figure 7-4 presents the values of the dipole components computed each 10° from 1976 through 1983. The top panel shows the polar dipole component. It shows a roughly constant magnitude for the year and a half after minimum followed by a gradual decline through 1978 and early 1979. For most of 1979 and 1980 the polar dipole remains essentially zero. The new polar fields (of opposite sign) regained strength gradually during 1981 and stayed roughly constant through 1982 and 1983 at a slightly lower strength than the minimum era field. If no polar field correction were made, the field strength near minimum and after 1981 would be somewhat lower and the polar component near maximum would be somewhat more erratic, but the general characteristics of the field would remain the same.

The equatorial dipole is sinusoidal in character. This is because only the  $h_{11}$  term has been plotted. The other equatorial dipole is identical except that it is out of phase by 90°. The  $g_{11}$  term is slightly more noisy because it has maximum amplitude at the point on the sphere where the "seam" occurs 180° from the center of the data window, therefore the h's are generally less noisy. With time the equatorial dipole points toward Earth, then perpendicular, then away, producing the sinusoidal shape. The envelope of the wave

---

Figure 7-4: The polar and equatorial dipole components of the heliospheric field. The polar dipole decays and reverses sign near solar maximum, growing in magnitude during the declining phase. The equatorial dipole shows modulation due to solar rotation. The envelope, corresponding to the magnitude of the equatorial dipole, apparently evolves independantly of the polar dipole. The equatorial dipole is the dominant component during most of 1982.

# SOLAR DIPOLE COMPONENTS

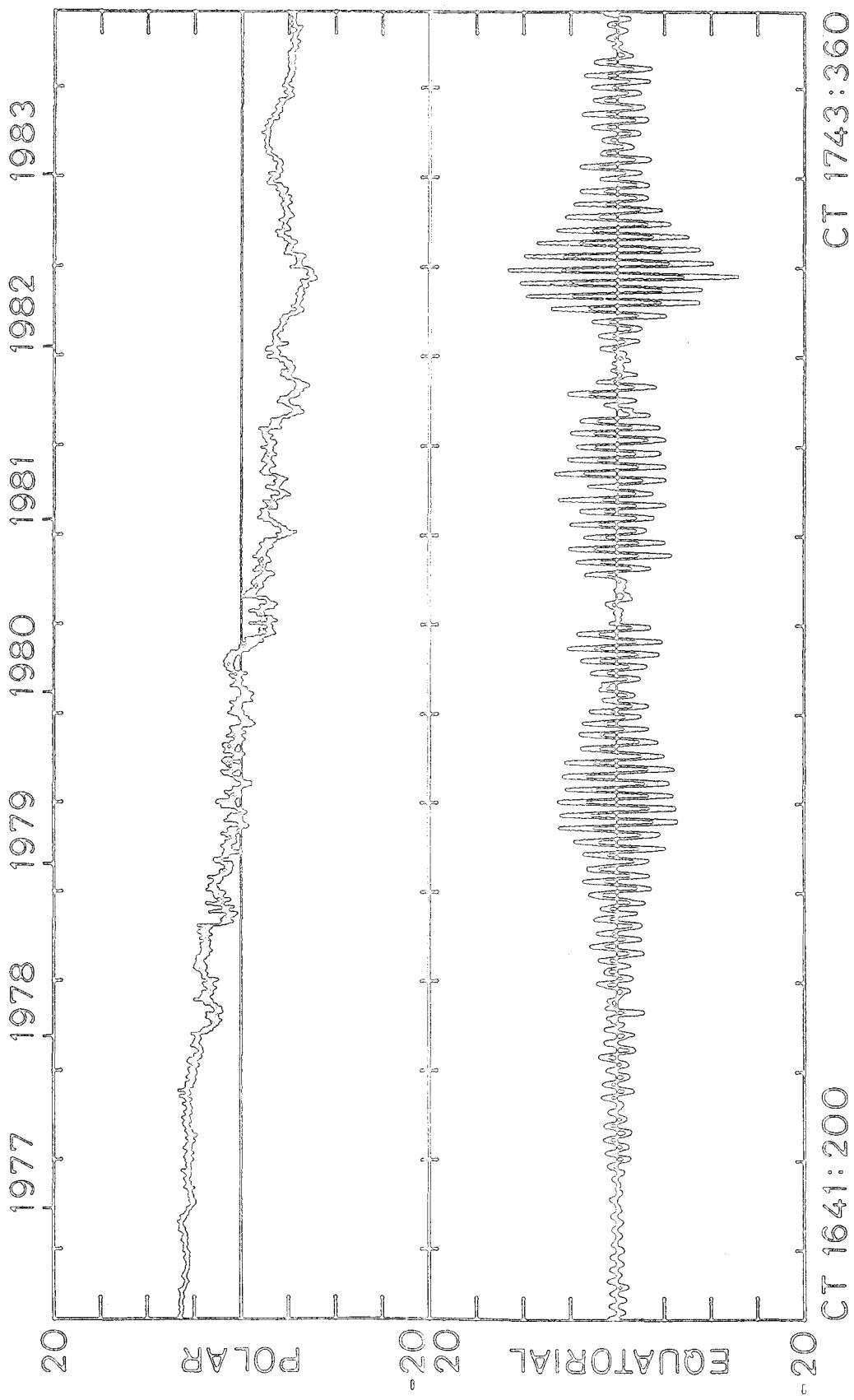


Figure 7-4

indicates the magnitude of the equatorial component.

Near minimum only a small equatorial component exists. The component first begins to grow in mid 1978. The amplitude of the component varies substantially from 1979 through 1983. The modulation does not appear extremely regular, though a periodicity of a little under 2 years may be present. This could correspond to a beating of two (or more) structures rotating at slightly different rates. The results of an FFT power spectrum analysis are shown in Figure 7-5. The peaks are labelled by the synodic periods corresponding to the frequencies obtained. The largest peaks occur at 27.0 days and 28.2 days. These are suggestive of the recurrence times found in geomagnetic activity and in the polarity structure of the IMF (Svalgaard & Wilcox, 1976). The significance of these rates is not clear. Are there two equatorial dipole structures rotating with different periods on the sun over a substantial fraction of the solar cycle? The discovery of these periods in the inferred IMF polarity over the last several sunspot cycles may support the reality of such a conjecture. Alternatively, active longitudes located at different latitudes having different rotation rates could also contribute to such a signal, although a 27 day period corresponds to the rotation of the photosphere only at the equator where there is little activity. The lifetimes of at least a year for the wiggles in Figure 7-4 preclude the correspondence of the equatorial dipole to individual active regions. Other modes show similar amplitude modulations, though with different periods. The location of the fields producing the patterns is unclear.

Schulz (1973), Antonucci (1974), Saito et al. (1978 and references therein), and others have characterized the reversal of the polar fields in terms of a rotating dipole. Near solar minimum the dipole is aligned with the rotation axis. Rotating slowly, the dipole becomes equatorial near maximum and finally approaches the rotation axis again near the following minimum, but pointing in the opposite direction. Having computed the field

---

Figure 7-5: The power spectrum of the equatorial dipole. The amplitude modulation of the equatorial dipole suggested beating between two periods. The FFT shows that power exists at 27.0 and 28.2 days and to a lesser degree at 27.5 days. No other peaks in the spectrum approach the magnitude of the peaks shown here.

POWER SPECTRUM  
OF EQUATORIAL DIPOLE

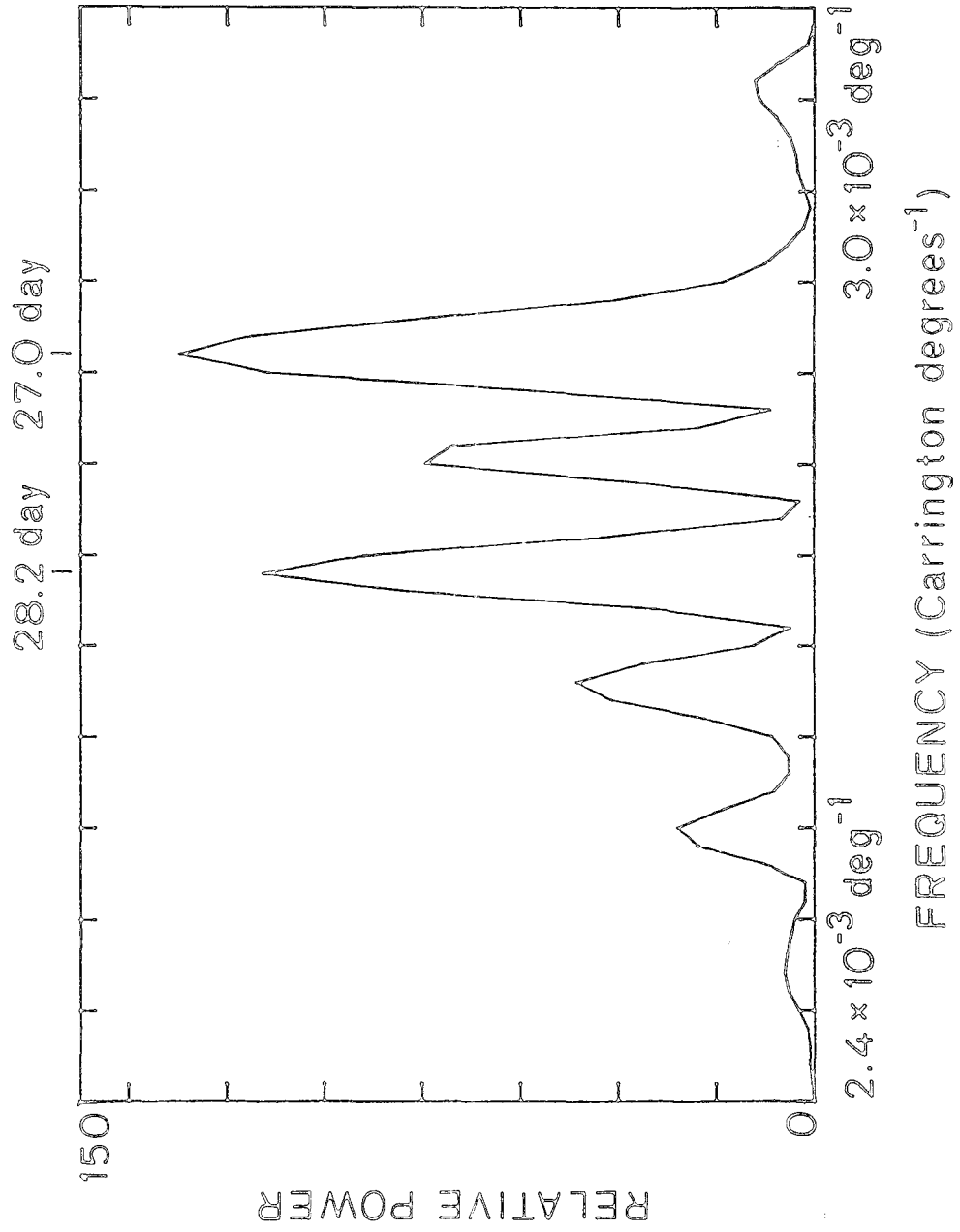


Figure 7-5

components from 1976 through 1983, the direction of the dipole field can be computed easily. Figure 7-6 shows the angle between the rotation axis and the dipole field, determined by finding the arctangent of the ratio between the magnitudes of the polar and equatorial dipole components. The angles shown in Figure 7-6 have been averaged over complete Carrington Rotations. The curve shows that the dipole angle remains near  $90^\circ$  through early 1978 and then decreases rapidly to  $0^\circ$ , remaining near  $0^\circ$  for a year beginning in early 1979. In mid 1980 the angle rapidly jumps to about  $60^\circ$  where it remains until near the end of 1983. The direction of the field varies substantially after 1980.

Does the dipole rotate? The behaviour of the dipole between 1976 and 1979 could support the rotating dipole concept (ignoring for the moment the other components of the field which have been shown to be roughly equivalent to the dipole near maximum). The polar dipole gradually decays and the equatorial dipole gradually gains in strength. The orientation of the dipole moves slowly from  $90^\circ$  to the equator. After 1980, however the orientation changes rather erratically, depending more on the apparently random fluctuations in magnitude of the equatorial dipole than on a regular relation between the two components. This is shown by the continual gradual increase of the polar dipole component and the varying magnitude of the equatorial component. The total power in the dipole varies too. This suggests that the two components are really unrelated. The equatorial dipole participates in the general increase of lower latitude fields taking place around maximum. The polar dipole simply decays between minimum and maximum and grows in the opposite direction after maximum.

This is certainly true of the photospheric fields which do not show the same large scale organization observed at the source surface. As will be

---

Figure 7-6: The direction of the dipole field with respect to the rotation axis computed from the polar and equatorial components. Near minimum the dipole is aligned with the rotation axis. During the rising phase the dipole appears to rotate since the equatorial component grows as the polar component decays. After maximum the direction of the dipole varies greatly suggesting that the two components are actually independent.



DIPOLE ANGLE vs. TIME

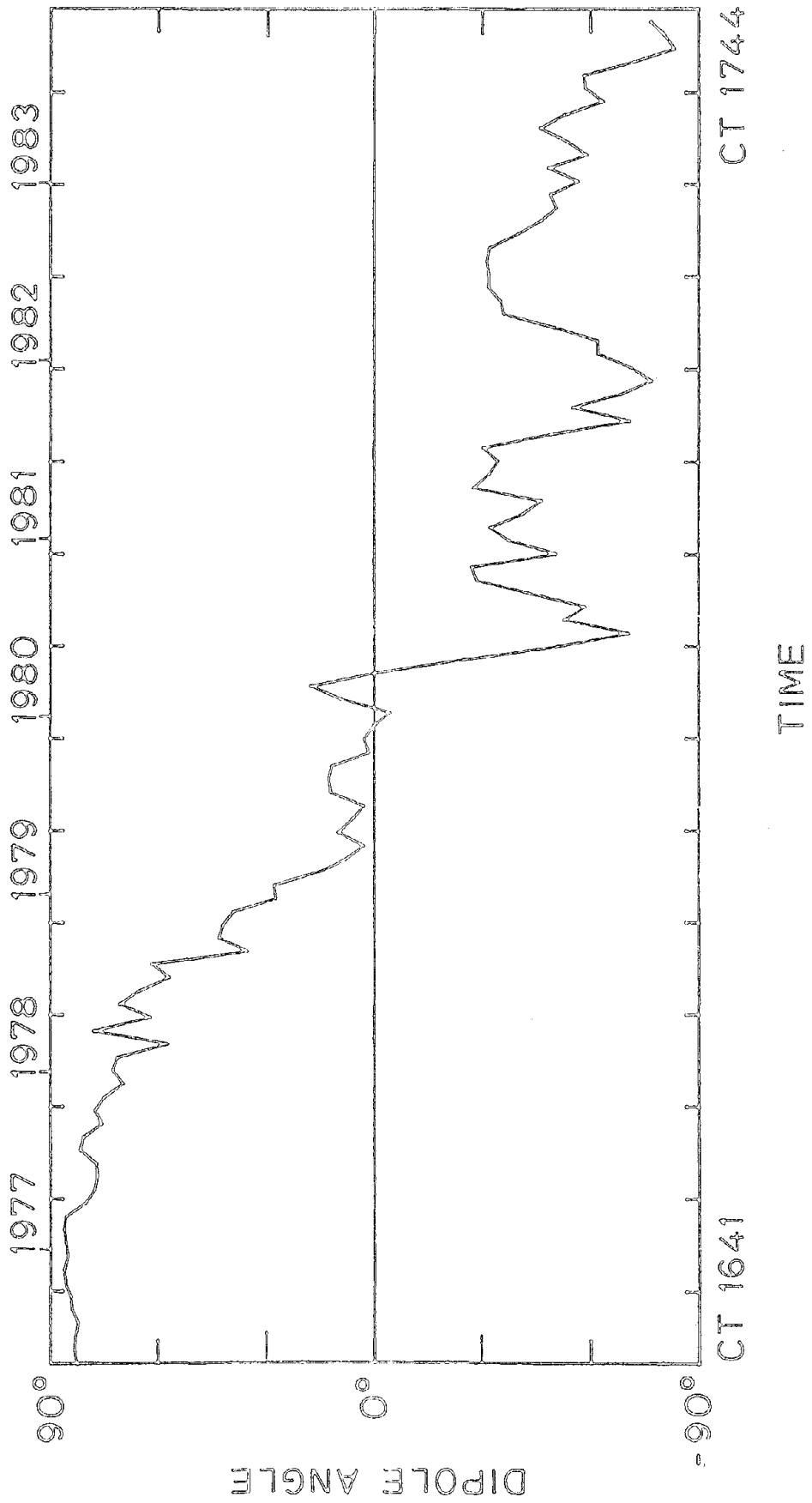


Figure 7-6

shown in a following section, the polar fields of the new cycle first appear at mid latitudes early in the cycle and gradually spread to the poles. One can still ask the question of whether the *heliospheric* field can be accurately *described* as a rotating dipole, independent of whether it is *truly* a rotating dipole. From Figure 7-6 alone the answer would be yes. The angle of the dipole component rotates from north to south during the cycle reversing at maximum. However, the real answer to this question depends on the magnitude of the other multipole components.

Reconsideration of Figure 7-1 shows that for much of the period around maximum the dipole term does not dominate the structure of the heliospheric field. Indeed during much of 1979 and 1980, when the dipole is reversing, the other components contribute more of the flux. Looking at the field configurations shown in Figure 5-9, the structure appears rather complex. There were rotations when the field resembled a dipole, e.g. CR 1682 or CR 1692, but during most rotations there was a great deal of structure at a wide range of latitudes, often forming four sectors in the equatorial plane. The north polar region became negative and south became positive at about the same time; by nature this tends to resemble a rotating dipole, but for most rotations that description is too simple. For this reason the heliospheric field can *not* be characterized as a rotating dipole, at least during the present solar cycle. Except near solar minimum, the dipole clearly dominated the structure of the field only during 1982 and that was due to the strength of the equatorial dipole which, if the dipole were actually slowly rotating from north to south, should have been decreasing during that interval.

Most of the observations used to infer the presence of a dipole have been taken during the declining phase of the sunspot cycle when a two sector structure in the IMF polarity is commonly observed at Earth. The observations have generally depended on low latitude measurements. During periods when the dipole component is strong, as in 1982, the tilt of the dipole cannot be reliably determined using low latitude measurements. It was near the end of the last cycle when a dipole tilted at  $30^\circ$  was observed in the coronameter data (Hundhausen, 1977). The situation observed in 1982 was very similar having a dominant dipolar field inclined  $50^\circ$  to  $60^\circ$  to the pole. While the tilted dipole description is appropriate during some parts of the cycle, the

fact remains that during most of the cycle the dipole description is not adequate in the ecliptic plane and during much of the cycle at higher latitudes.

#### *Multiple Current Sheets*

The higher multipole components contribute to the complexity of the heliospheric field structure. Second current sheets enclosing isolated polarity regions are not uncommon near maximum. Examples occur in CR 1674, CR 1679, CR 1686, and CR 1698. During some rotations, as in CR 1679, these structures do not interact with the Earth; on other occasions, as in CR 1698, they do. In the interplanetary medium these will produce smaller sectors limited to a narrow range in latitude as well as longitude. The inclination of boundaries observed near such sectors will depend sensitively on the location of the observer relative to the location of the sector. This has special significance with regard to using the effect of Rosenberg & Coleman (1969) to infer from the inclination of boundaries the latitudinal extent of the current sheet. The field configuration in a rotation such as CR 1698 (see Figure 5-8) would give misleading results.

The magnetic regions enclosed by separate current sheets do not appear randomly. In each case the strong field region at the center of the isolated region can be seen for several rotations before and after the second current sheet forms and disappears. A good example is again the large region in CR 1698. Easily visible in CR 1692 when it was connected to the positive south pole, the area south of the strong field region weakened during CR 1695 and CR 1696, causing the formation of a separate current sheet during CR 1697 - CR 1699. The region reconnected to the positive south polar region in CR 1700 (see Figure 5-10) and gradually weakened thereafter. The evolution of other separate regions may not last over such a long period, but in each case is due to a strong field region becoming isolated because of the disappearance of the weaker field region surrounding it.

This stability even for smaller regions surrounded by opposite polarity areas reinforces the impression that the large scale features evolve slowly.

Even during maximum when active regions seem to dominate the photospheric field configuration, the large scale features evident in the corona have life times from months to years.

### *The Reversal of the Polar Field*

It is difficult to conceptualize the reversal of the polar field, partly because of the format in which the fields are typically shown. Figure 7-7 shows a cartoon of the smooth evolution of the fields from minimum through maximum in two projections. The panels on the left show the field configuration in the standard format. The right hand panels show the same field configurations but projected as might be seen from the north pole. Actually the southern hemisphere is shown as well. The south pole is the outer circle, the inner circle represents the equator, and the north pole lies in the center. The perpendicular lines divide the sphere into the same quadrants shown in the left hand panels.

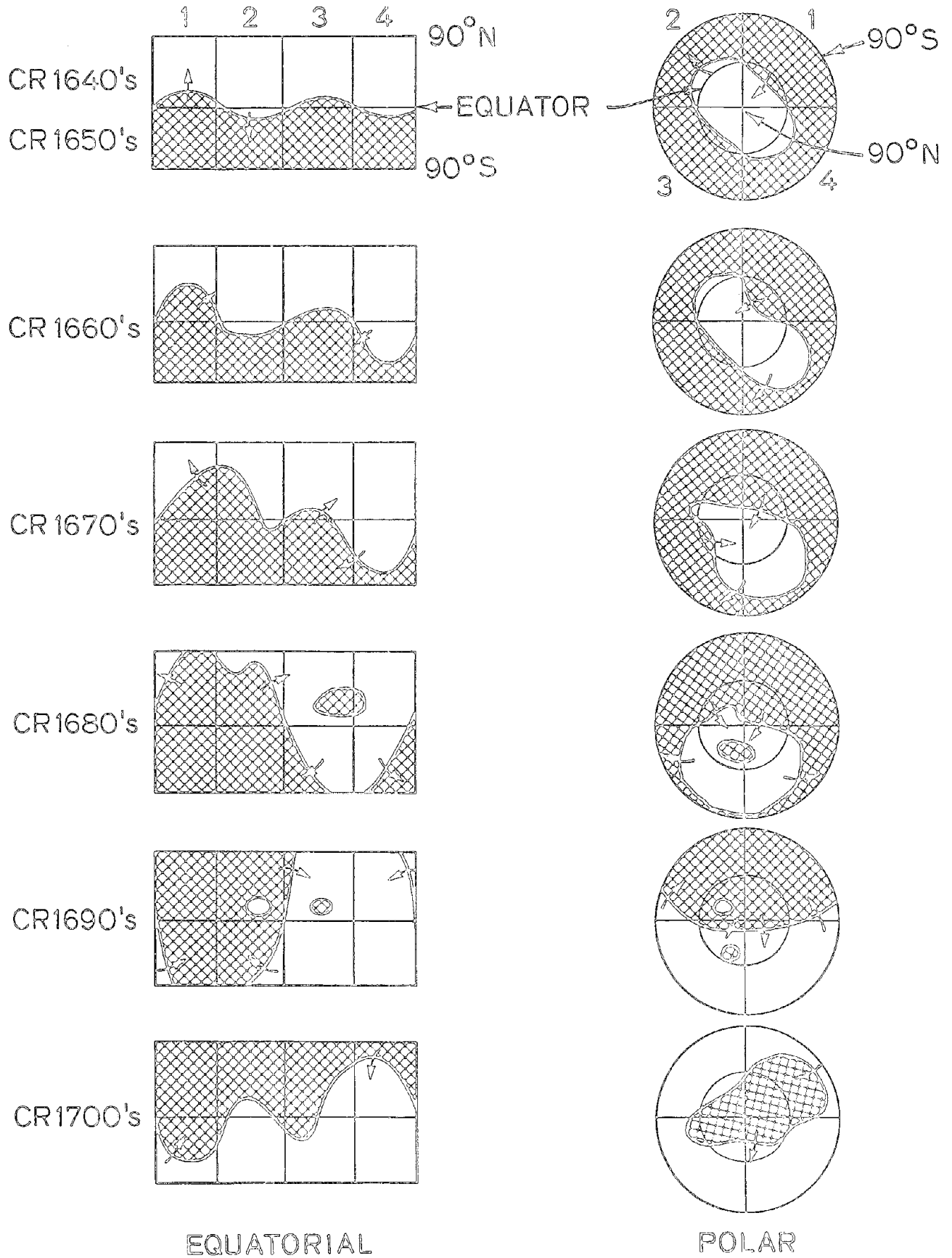
The evolution of the fields is shown from frame to frame as the current sheet progresses from a simple, low latitude four sector structure near minimum as through the CR 1660's, to a similar, non-symmetric high latitude structure observed in the CR 1670's. The fourth frame shows the high latitude, complex structure typical just before polar reversal during the CR 1680's. During the CR 1690's the current sheet extends from pole to pole and gradually sweeps across the polar regions as the polar fields change sign. The field settles down to a more simple structure as shown in the last frames which are representative of the CR 1700's and CR 1710's. Each frame has been drawn to be characteristic of the rotations during the indicated

---

Figure 7-7: The panels at the left show the evolution of the field configuration before and after maximum in the standard projection. Each frame typifies the field structure for the indicated rotations. The panels at the right show the polar azimuthal equidistant projection of the same field configuration. This illustrates the smooth evolution of the current sheet in the northern hemisphere from minimum through maximum and the beginning of the declining phase of the cycle. The arrows suggest the movement of the neutral line.

Figure 7-7

# MORPHOLOGY OF POLAR FIELD REVERSAL



interval. Compare these with the field structures displayed in Figures 5-6, 5-9, and 5-10. The details can be adjusted to match the actual patterns computed for this time period.

The polar projections show the evolution of the same fields from a different perspective. While the polar field reversal may seem sudden when viewed in the standard way, the polar projection reveals that the motion of the current sheet near the polar regions is smooth and predictable even near maximum.

### *Coronal Rotation*

The description of the field made in Chapter 5 emphasized the lack of observed differential rotation in the coronal structures. To investigate this more systematically, an autocorrelation has been made at each latitude. A maximum in the autocorrelation occurs for each latitude about one rotation later. The rotation rate found for each of the 30 latitude bins in degrees per day plotted in Figure 7-8 as plus symbols. The solid line is the best fit to the observed data. Also plotted are the rotation rates observed for coronal holes (dot-dashed, Bohlin, 1977b); solar features (dotted, Bohlin, 1977b) such as prominences, coronameter enhancements, magnetic field patterns, white light and 5303 enhancements (PCMF); and the recurrence rates for long-lived sunspots (long-dashed, Newton & Nunn, 1951). There is a smooth curve of rotation rate vs. latitude for the coronal structures, but the coronal differential rotation is much smaller than that of the sunspots or magnetic features. Fitting these data to a function of the usual form, the relationship  $\text{Rotation (degrees/day)} = 13.2 - 0.5 \sin^2\phi$  is found. This is very similar to the

---

Figure 7-8: The differential rotation curves for various solar features. The long dashed line shows the Newton and Nunn (1951) curve for recurrent sunspots; the dotted line shows the synodic rotation rate for photospheric features (Bohlin, 1977b); the dash-dot line shows the rotation of coronal holes (Bohlin, 1977b); and the solid line the best fit rate of the coronal fields determined in this study. The plus symbols show the actual rates determined from the autocorrelation analysis. Each curve has an error of approximately 0.1 degree/day.

# DIFFERENTIAL ROTATION

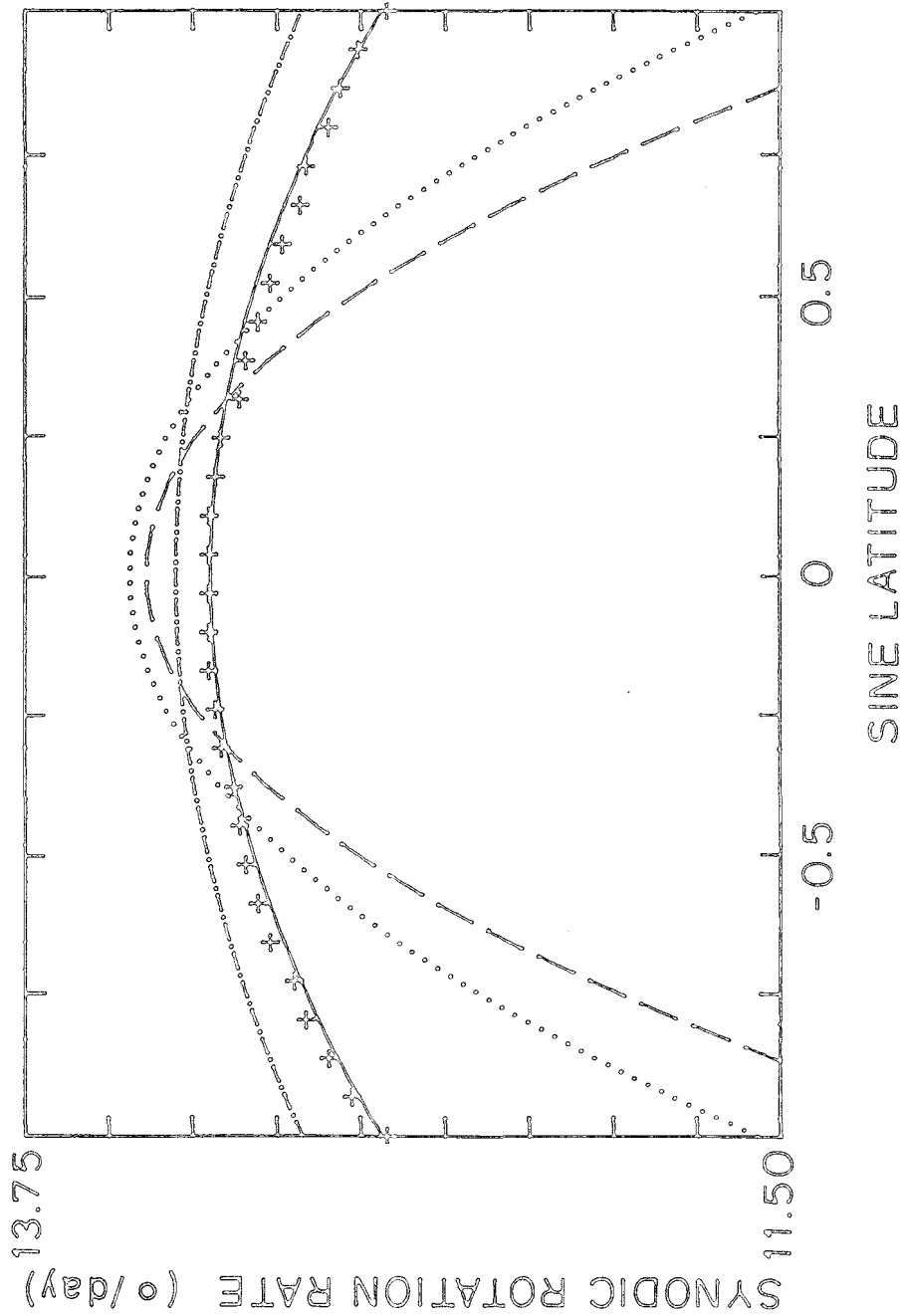


Figure 7-8

rotation rate of coronal holes (Timothy, 1975; Bohlin, 1977b) or the coronal green line structures (Antonucci & Svalgaard, 1974). The field at the source surface rotates less differentially than the large scale photospheric field.

Fisher (1982) studied the rotation rate of coronal features observed with the Mauna Loa K coronameter during 1980 and 1981. During this interval he found that the polar region and equatorial region fields rotated with a period of about 28.0 days. The active region latitude fields rotated with a period near 27.6 days. These results are not confirmed in the present study. This may occur because of the different time intervals of the two studies. The present analysis includes the entire interval from 1976 through 1983. The rotation rates may vary during the cycle as different latitudes contribute varying fractions of the flux making up the coronal field. If the altitude difference of the two methods is significant, the coronameter data will tend to be more sensitive to the smaller scale field which would tend to participate more in the differential rotation of the photospheric field. Sheeley & Harvey (1981) found a rotation rate of 28.0 days for high latitude coronal holes observed before 1979. This is in better agreement with the present data. In the next section the photospheric sources of the coronal fields are sought.

#### *Photospheric Sources of the IMF*

The life times of the large scale structures are much too large to be related to individual active regions. Yet the photospheric fields are the source of the long lasting coronal features. In this section two methods for finding the sources of the coronal structure will be used. The first attempts to find the latitudinal distribution of the photospheric field by computing the longitudinal average of the field at each latitude for each Carrington rotation and making a contour plot of the resulting map which shows the evolution in time of the latitude structure of the field. Similar analysis has been done for the Mt. Wilson data (Yoshimura, 1976a, b, Howard & LaBonte, 1981) and for the early Stanford data (Hoeksema et al., 1980). The second method tries to determine where a sector boundary observed at Earth originates in the



photosphere. This is accomplished by superposing several synoptic charts about days on which a polarity change is detected at Earth.

Figure 7-9 shows the zonal averages of the magnetic field from 1976 through 1983. For each rotation, all the data at a given latitude is averaged. The polar fields have not been corrected. The results for each rotation are put into the columns of an array, each column corresponding to a rotation. No averaging over solar rotations has been performed. A contour map is drawn from these data showing the latitudinal distribution of the field as it changes through the solar cycle. Rotations having missing data have been filled in using the same method developed for the potential field model: the average of the data from the preceeding and following rotations at the same longitude is used to replace the missing values. Since at the photosphere the monopole component is insignificant it has been ignored.

Near minimum there is very little flux on the surface. The dominant structure is the positive north pole and the negative south pole. The neutral line lies near the equator. Nowhere does the net flux at a given latitude get very large. In mid 1977 regions of flux opposite in sign to the dominant polarity in that hemisphere appear in both the north and the south. It is interesting that following polarity is seen before leading polarity in each hemisphere and that it appears so early in the cycle. These mid latitude bands are maintained until 1980 or 1981, by which time they have expanded and become the new polar field. Through 1980 the equatorward boundary of these bands remains roughly constant. This is contrary to expectation if the feature were simply due to the diffusion of following polarity regions toward the poles.

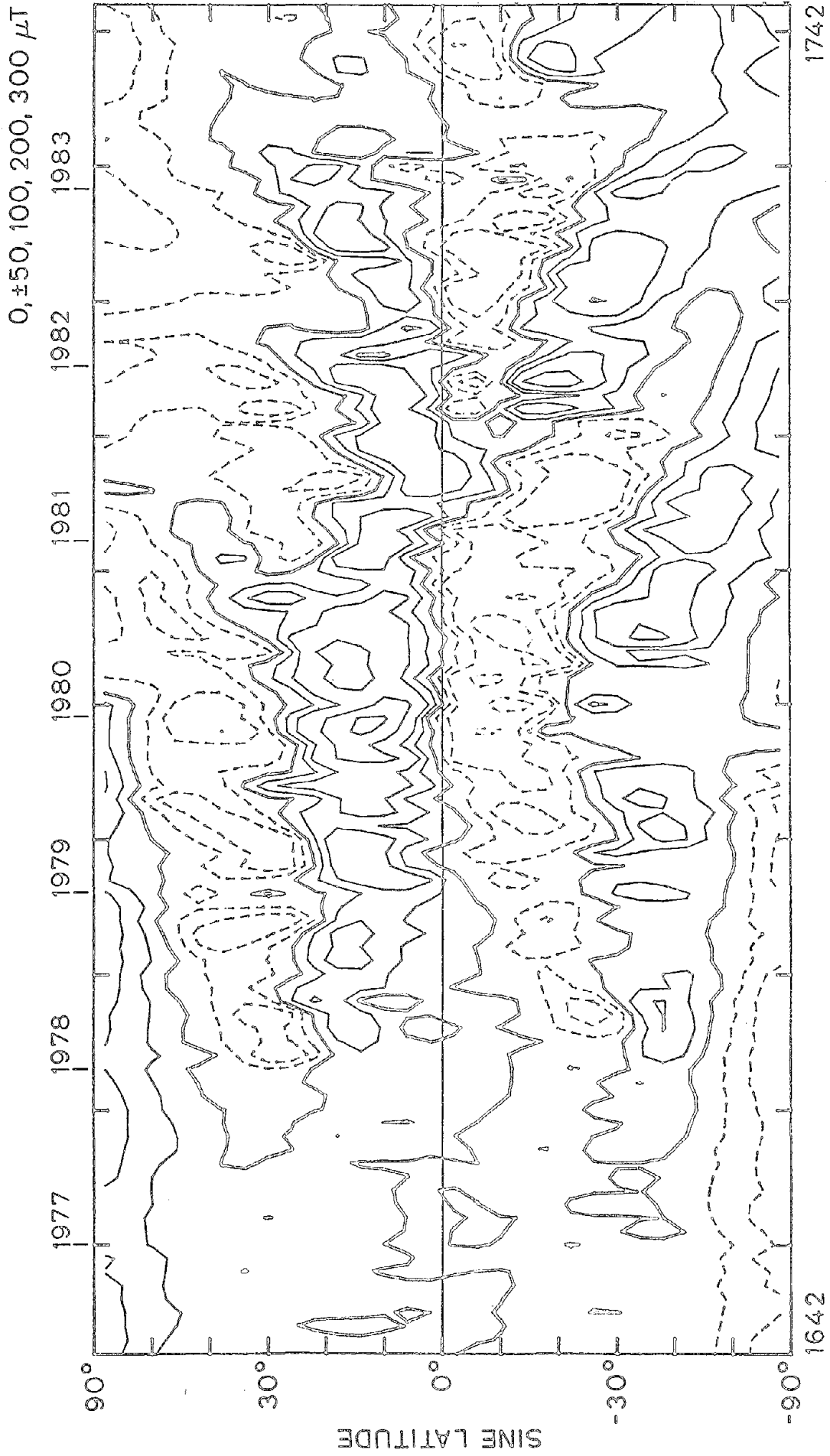
The fields at lower latitudes attain their largest values near sunspot maximum in 1979 and 1980. During 1980 the mid latitude feature reached

---

Figure 7-9: Zonal averages of the photospheric field. The field at all longitudes for each rotation has been averaged showing the net flux at each latitude vs. time. The new polar fields emerge at mid latitudes in 1977 in each hemisphere and gradually move toward the poles. The equatorward boundary of these regions remain the same for several years. Interesting episodes of rapid flux migration toward the south pole occur in 1981 and 1982.

Figure 7-9

ZONAL AVERAGE FIELD



the north pole. The southern feature reached the south pole in 1981. It should be emphasized that because of the large aperture at the Stanford Observatory, measurements taken near the poles are not as accurate as those taken with higher resolution. Two interesting events occur in the southern hemisphere in 1981 and 1982. In 1981 a negative polarity region migrates rapidly toward the south pole, apparently reaching it in 1982. This is followed about 8 months later by a positive region which reaches the south pole late in 1982. A smaller but similar event can be seen in the northern hemisphere beginning late in 1980. The strong negative surge toward the south pole may be related to the strong negative feature extending far into the southern hemisphere observed near 180° on the source surface plots in Figure 5-10. Because there is no longitudinal information it is difficult to relate these structures directly to the source surface features.

Except for these episodes of field migration toward the poles, the years after maximum show little exciting behaviour. The activity bands seem to meet at the equator and gradually fade away. During 1983 the polar fields are strengthening and the zero contour separating the new polar fields from lower latitude opposite polarity approaches the equator.

It is interesting to note that the field during most of this period is divided into four bands, unlike a dipole field. This quadrupole nature of the field has been predicted by numerical dynamo models. (Yoshimura, 1976b). The new solar polar field appears long before it actually becomes the *polar* field. This new feature contributes to the large latitudinal extent of the current sheet observed through much of the cycle; the poleward migration of the feature can be followed on the source surface charts in Figure 5-9 in the maximum latitudinal extent of the current sheet.

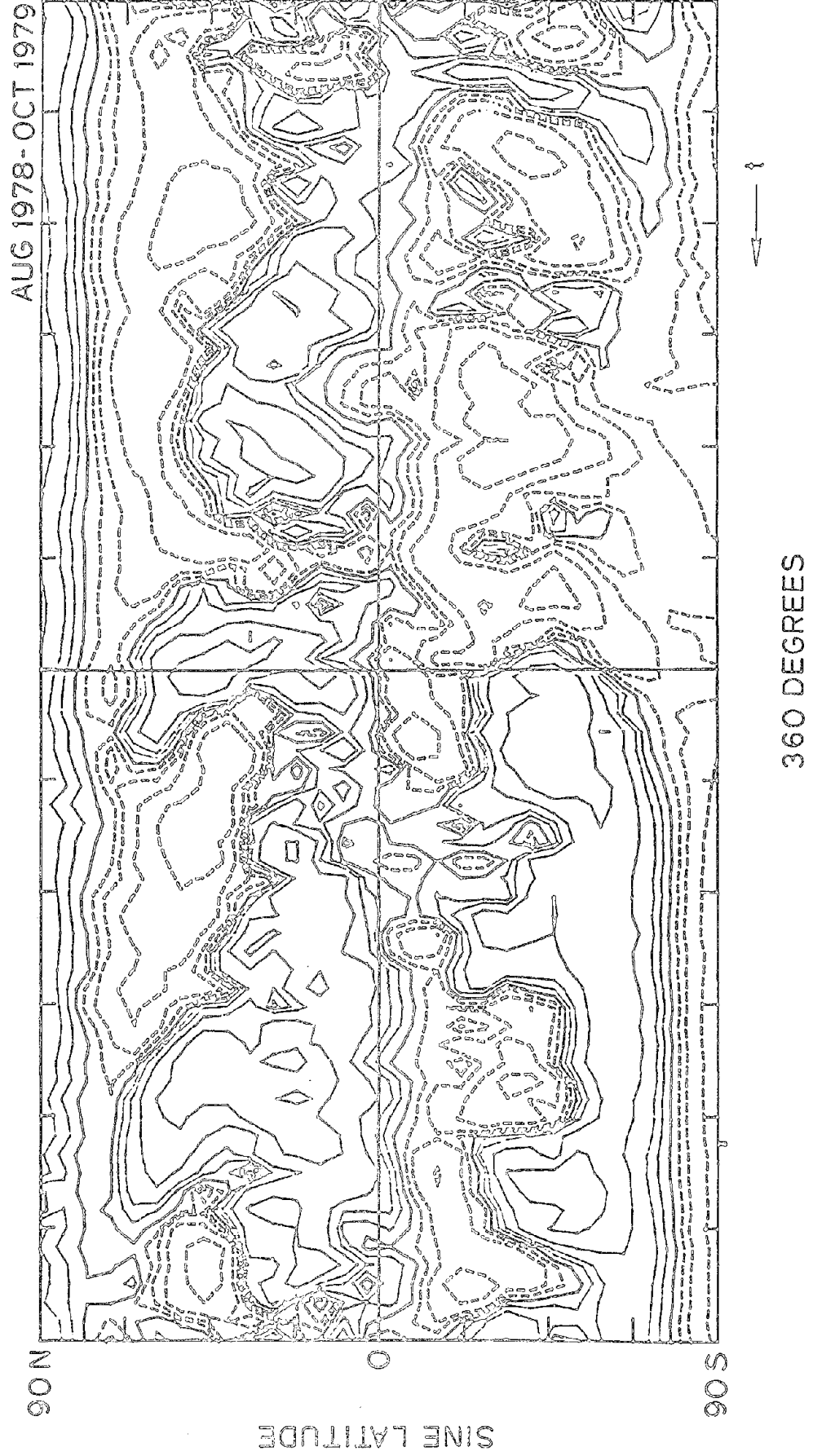
Because the photospheric fields are so much more complex than the

---

Figure 7-10: A -, + sector boundary which recurred with a period of about 28 days beginning August 20, 1978 for the following 14 rotations was used to determine key times about which to superpose photospheric synoptic charts. The average field shows organization at only a few latitudes. A strong organization in the mid-latitude southern hemisphere field can be observed with the correct polarity change suggesting that the IMF sector was influenced by the southern hemisphere field.

Figure 7-10

SYNOPTIC CHARTS SUPERPOSED ABOUT -, + IMF BOUNDARY



source surface fields and because the photospheric fields, at least at small scales, do not last as long as the coronal structures, identification of coronal structures in the photosphere is difficult. One way around these problems is to look at the photospheric structures averaged over a longer period of time. Of interest to the Earth are those structures which contribute to the IMF sector structure. Presented here is a superposition of synoptic charts of the photospheric field corresponding to a sector boundary observed at Earth for 15 months with a recurrence period of just over 28 days. This is the negative to positive boundary first observed at Earth on August 20, 1978 and each 28.07 days thereafter for 14 more rotations. The southern hemisphere structure near 180° degrees in Figure 7-10 corresponds to a change in polarity from negative to positive. This is just where such a boundary would be expected to occur given the recurrence period. This is the only feature which shows a great deal of organization using this recurrence frequency. There is a predominance of positive structure to the left of the boundary in each hemisphere. This is the correct polarity to contribute to the positive sector being entered at each boundary. We have examined several IMF boundaries with recurrence periods of 27 days to 28.5 days using this technique. In each case there is some organization of the photospheric field, though not always as clear as in this case. Generally the fields at the latitudes having a differential rotation rate close to that of the sector show the most organization. Comparison to the source surface fields in Figure 5-9 do not show any clear relationship to the surface fields shown above. With the exception of coronal holes, the relationship of photospheric, coronal, and interplanetary fields is very difficult to sort out.

## Chapter 8 -- Conclusions

The original goal of this study, to learn about the evolution of the three dimensional structure of the large scale solar and heliospheric magnetic fields as they evolve through the solar cycle, has been accomplished. Specifically, the intent was to learn about the latitudinal extent of the current sheet, the importance of the dipole field, the morphology of the field when the polar field reverses, and the relation of the coronal structures to those seen in the photosphere and observed in the neighborhood of the Earth. In this chapter the methods used and the results obtained will be summarized and several new questions which have arisen during the course of this analysis requiring further work will be described.

### *Summary of Methods*

The photospheric field has been observed almost every day at Stanford, providing a record of the magnetic structures visible on the sun's surface spanning a substantial portion of the sunspot cycle. The large aperture, high resolution, low noise spectrograph provides ideal data for studying the large scale structure of the solar field. The quality of the data during the interval 1976 - 1983 is uniformly excellent with the exception of occasional gaps due to weather and equipment. Because the large scale field evolves slowly, data gaps can be eliminated by interpolation of the data from the preceeding and following rotations.

The polarity structure of the solar wind is simple, having four or two sectors each solar rotation. The photospheric field is much more complex. To explain the simplification of the magnetic structure, the potential field model has been developed to relate the photospheric, coronal, and interplanetary structures. The assumption of a potential field leads to the simplification of the fields with height above the photosphere. Currents must actually flow in the corona, but fortunately their flow does not greatly alter the configuration

of the magnetic field. To match the observed coronal structure and for ease of computation the field is constrained to become radial at a certain altitude. This assumption can be justified because coronal structures above a few solar radii are observed to be radial and because the energy density of the transverse magnetic field dominates the plasma out to approximately the same height. Between this surface and the photosphere the magnetic field is described by a potential.

The assumptions described above may be relaxed, but have been found to contribute little to the accuracy of the large scale features while greatly increasing the complexity of the computation. To answer the questions posed in the present analysis, the large scale configuration of the field is of greatest interest, so the simplest model has been used. To eliminate the insensitivity of the model to rapid changes in the field and the problem of computing a global field model from data collected during a month long interval two steps have been taken: 1) the model has been calculated many times each rotation to minimize the effect of the data window; and 2) the zero offset, or monopole, field has been removed from the data.

To determine the accuracy of the model and to set the height of the source surface, the predicted IMF polarity and the measured IMF polarity at Earth were compared. Locating the source surface near  $2.5 R_{\odot}$  produced the best agreement. Comparison with coronameter and high latitude spacecraft data indicated that the computed current sheet extended too far from the equator when the photospheric observations were not corrected for the strong, sharply peaked polar fields. With these parameters and corrections the model predicts the correct IMF polarity at Earth about 80% of the time and agrees quite well with determinations of the current sheet from coronameter data. Comparisons made with data from spacecraft orbiting the sun show similar levels of agreement.

### *Summary of Results*

Since the observations confirm the predictions of the model to such a high degree, the structures computed can be viewed with a fairly high level of confidence. The importance of the three dimensional nature of the current sheet has been established beyond doubt. Through most of the solar cycle observed in this study the current sheet extended at least  $50^\circ$  from the equator. Generally the large scale structure included four sectors at the latitude of the Earth.

Near minimum the current sheet was nearly equatorial with two warps north and two warps south of the equator, predicting the observed four sector structure at Earth. In 1976 the sheet extended less than  $15^\circ$  north of the equator and occasionally a little farther south. This pattern lasted for at least two years. The observed changes related mostly to the increasing contribution of the sectoral quadrupole to the field configuration. The shape of the structure stayed the same, but the latitudinal extent of the warps increased throughout 1977 and 1978. During this entire period the structure observed in the IMF at Earth changed very little, exhibiting four sectors per solar rotation.

Near maximum the structures became more complex, though strong field regions could still be observed for periods longer than a year. The configuration of the current sheet seemed somewhat less stable, apparently being more subject to the rapid evolution of the weaker field regions. The strong regions seemed just as stable during this interval as near minimum. The actual reversal of the polar fields took place between CR 1688 and CR 1692, judging from the source surface fields. In the years around maximum, isolated polarity regions bounded by a second current sheet were not uncommon. The polarity pattern in the ecliptic remained rather simple even during this period, showing two or four sectors per rotation as it did near minimum. By mid 1980 the new polar fields were firmly established, at least in the interplanetary medium as represented by the source surface fields.

During 1980 and 1981 the structure strongly resembled the structure observed in 1978, only having the opposite polarity and extending to slightly



higher latitudes. During 1982 a very stable, strong pattern developed consisting of just two sectors at nearly every latitude less than  $60^\circ$ , reminiscent of the structure in 1974. This interval corresponds to the strong equatorial dipole described in Chapter 7. From the end of 1982 through 1983 a stable four sector pattern develops, again like that of 1978. If the present cycle follows the pattern of the last cycle, a structure reminiscent of the Skylab era should form in the next year or so, having large polar coronal holes extending down to the equator. It will be interesting to see if this occurs.

During all phases of the cycle the large, strong magnetic field regions on the source surface persist for as long as two years. With some imagination, some regions can be followed for even longer periods. Even the smallest regions, those contained in isolated, separate current sheets, are visible for several rotations before, during, and after the formation of the separate sheet. These sheets behave just like the normal, primary current sheet when they interact with the Earth.

The "tilted dipole" description describes the heliospheric field only during certain times during the solar cycle. During most of the cycle the higher order multipoles distort the structure substantially from a dipole-like configuration. Even near minimum when the field is most like a polar dipole, the structure in the equatorial region where the Earth orbits depends on the smaller quadrupole field. For most of the period near maximum the current sheet is highly warped and extends to high latitudes. Therefore one must be careful in using the tilted dipole terminology.

A "rotating dipole" has been used to describe the change in heliospheric field configuration as it passes from minimum to maximum to minimum. If the other multipole contributions to the structure are ignored, there is some merit to this description, although the equatorial dipole seems to be largely independent of the polar dipole. In this context it can be seen that there is no *real* dipole rotating from north to south during the cycle, though the dipole component of the field can be very roughly described in that way. However, the other multipoles can not be ignored during the years preceding and following maximum, so the "rotating dipole" description does not really work. Examination of the source surface fields during that interval

shows this clearly.

The morphology of the polar field reversal was shown in Chapter 7. The actual reversal of the field takes place over a rather short interval, though the field evolves toward the reversal gradually. The reversal has been shown to be a smooth progression of the location of the strong field regions on the source surface. The transition in the photosphere is not quite so clear. Flux of the new solar polarity emerges at mid latitudes near the beginning of the cycle and moves gradually toward the poles. In the photosphere the change is a relatively smooth one.

The solar wind parameters other than the polarity are harder to predict from the model, largely because of dynamic effects in the solar wind. A problem still exists with the magnitude of the field being too small by a factor of about five. The solar wind velocity can be related to the magnetic field strength at the source surface. Near minimum this is roughly equivalent to the distance from the current sheet and the predictions of both methods show a good correlation with the observed velocity. Near maximum the test is much more difficult because of the effects of activity related events. Nevertheless, if activity related intervals are excluded, a fairly good relation is shown between  $|B|$  and solar wind speed, better than would be found from the distance to the current sheet. The most significant relationship connects the minimum solar wind speed with the minimum magnetic field strength (i.e. the current sheet).

A coronal hole at a given latitude lies in the region of strongest field strength at that latitude. The polarity of the hole and the open field regions always agree. From the source surface data the locations where coronal holes can *not* occur can be found with great accuracy.

The relationship of cosmic ray flux to the field configuration cannot be explained at this time. There seems to be an inverse relationship between the extent in latitude of the current sheet and the cosmic ray flux during the last solar cycle and the first half of the present cycle. After the reversal of the polar fields the relationship deteriorates. Perhaps a longer time period is needed over which to study the problem.

The structures in the corona do not fully participate in the differential rotation observed for the photospheric fields and plasma. This has been observed for the large scale photospheric fields and for coronal holes as well. The lifetimes of the structures suggest that something organizes the emergence of new flux at the photosphere such that the large scale features are reinforced over a large range in latitude.

This may be related to the results of the study of the individual multipole components comprising the heliospheric field. The equatorial dipole had power at frequencies corresponding to 27.0 day and 28.2 day rotation periods. Perhaps there is some large scale organization of the field rotating at these periods which tends to lock the coronal fields and the emerging photospheric flux into the observed patterns. The evolution of the dipole field revealed that the equatorial and polar components were evolve independently, not as if a relatively constant magnitude dipole were rotating during the cycle.

A close relationship exists between the photospheric sources of coronal holes and the source surface fields overlying them, but other sources of the coronal structures are difficult to find. Tracing field lines requires higher resolution data and computations. Looking at the latitudinal distribution of field over the last 8 years shows that the polar flux emerges first at mid latitudes early in the cycle. These regions grow toward the poles and envelop them near maximum. No obvious direct relation exists between these regions seen in longitudinal averages of the field and structures on the source surface. Looking at synoptic charts superposed about the times of sector boundary passages observed at Earth reveals organization in the photospheric field. The differential rotation rate at the latitude of the organized field corresponds to the observed recurrence rate in the IMF for the limited number of samples checked. No obvious structure at the source surface corresponded to the photospheric feature, even though the sector boundaries were predicted by the model. With the exception of coronal holes, identification of coronal and photospheric structures is difficult.

### *Suggestions for Further Study*

At least two areas for further study present themselves. One area involves continuation of the basic analysis techniques presented in this investigation. Because the solar cycle has not yet been completed, interesting questions still remain about the structure of the heliospheric field during the latter part of the declining phase. Similarities and differences between solar cycles will also be interesting to observe.

Further refinements of the modelling technique have already been completed by others, but comparison of the results of the model with other methods of determining the coronal structure would be fruitful. Specifically, a study of the latitudinal extent of the sheet observed with coronagraphs near maximum would give helpful information for determining the accuracy of the polar field correction during that period. Another area for further comparison currently available is the measurement of solar wind velocity at higher latitudes using interplanetary scintillation techniques.

The real answer of what happens over the higher latitude regions will come when a spacecraft goes to observe. An important limitation to our understanding of the heliospheric field will be eliminated when a spacecraft either confirms or refutes our ideas regarding the polar regions. The potential field model should be able to predict the IMF structure observed by such a spacecraft. Even the use of multiple spacecraft measurements near the ecliptic has helped to clarify the differences between the predictions of the potential field model and the coronameter.

Extensions of the current methods could profitably try to improve the prediction of other solar wind quantities. Development of a model which could use the computed field quantities at the source surface and model the propagation of the solar wind out to the Earth might provide valuable information for predicting terrestrial effects. Conceivably the solar wind velocity, field strength and density could be modelled in addition to just the field polarity.

The other area for further study involves using the data presented here to learn more about the sun employing different analysis techniques. The

relationship of differential rotation in the photosphere and more rigid rotation for the large scale and coronal fields must be of fundamental importance for understanding the origin of the field. The large scale fields seem to reflect more organization than the surface fields alone exhibit. The relative strengths of the multipole components during different parts of the cycle should be predictable by dynamo models which try to explain the solar magnetic cycle. The relationship of these fields to the internal structure of the sun should be fertile ground for further investigation.

## Appendix -- Model Implementation

This Appendix presents the amply commented text of the potential field model program and a short description of how it works and is meant to complement the discussion in Chapter 3. The original program was written in Algol by Leif Svalgaard who should be credited with the fast algorithms and tricky ways of calculating the spherical harmonics. It has since been modified extensively and translated to the C programming language.

To compute the source surface each 10 Carrington degrees from May 1976 through December 1983 requires 36 computations per rotation on each of over 100 rotations, or about 3600 potential field calculations. Using the following program this takes approximately 650 minutes of VAX 11/780 cpu time and would typically finish overnight on an unloaded system. It is interesting to note that for this project the model was computed over nearly the entire interval at eight different source surface radii. At each source surface radius the computation was made with each of four values of the polar magnetic field. Each run generated 0.8 megabytes of data to analyze and plot for the just the radial field values.

The mathematics of the problem has been described in Chapter 3 and the description here will simply outline the computer program in terms of that discussion. For a single calculation the steps in the main program are 1) to read the data, in *readrot*; 2) to determine the coefficients of the Legendre polynomials, in *get\_lgh*; 3) to generate the field components at the radius of interest, in *get\_br*; and 4) to save the data, in *saveBr*. The additional step of merging the data is inserted when several calculations are made for each rotation in *putbr\_inc*.

The data is read in the standard dataset format developed for our computer system and the results are stored in the same form. The specified line-of-sight component of the polar field is added to the data in *readrot*. In the *get\_lgh* routine, for each value of the index,  $m$ , the corresponding coefficients, or  $g$ 's and  $h$ 's, are found by first determining the  $a$  and  $b$  coefficients from the line-of-sight measured magnetic field data in *get\_ab*.

Then the  $K$  matrix described in Chapter 3 is determined in *get\_K* and solved for the  $g$ 's and  $h$ 's in *solve*. The harmonic expansion is truncated at order 9 because higher orders contribute nothing significant to the fields at the source surface.

From the harmonic coefficients the field values anywhere between the photosphere and the source surface can be calculated using

$$B_r = -\frac{\partial \Psi}{\partial r} = \sum_{lm} P_l^m(\cos \vartheta) (g_{lm} \cos m \varphi + h_{lm} \sin m \varphi) \left[ (l+1) \left( \frac{R_o}{r} \right)^{l+2} - l \left( \frac{r}{R_s} \right)^{l-1} c_l \right]$$

and

$$B_\vartheta = -\frac{1}{r} \frac{\partial \Psi}{\partial \vartheta} = \sum_{lm} \left[ \left( \frac{R_o}{r} \right)^{l+2} + c_l \left( \frac{r}{R_s} \right)^{l+1} \right] (g_{lm} \cos m \varphi + h_{lm} \sin m \varphi) \frac{\partial P_l^m(\cos \vartheta)}{\partial \vartheta}$$

and

$$B_\varphi = -\frac{1}{r \sin \vartheta} \frac{\partial \Psi}{\partial \varphi} = \sum_{lm} \left[ \left( \frac{R_o}{r} \right)^{l+2} + c_l \left( \frac{r}{R_s} \right)^{l-1} \right] m \cdot P_l^m(\cos \vartheta) \cdot (g_{lm} \sin m \varphi - h_{lm} \cos m \varphi).$$

This is done in *get\_br* for the radial fields at the source surface or in *get\_b* for all three components at other radii. The  $g$  and  $h$  coefficients are printed out and may be stored in a standard dataset at a later time. For a single calculation the field values are simply stored directly in a dataset by *saveBr*. When the fields are calculated at intervals of  $10^\circ$ , the central  $30^\circ$  of each computation are retained and a weighted average is stored on the dataset as described in Chapter 3. The averaging and storage is accomplished in the *putbr\_inc* procedure.

A word is in order to describe the form of the Associated Legendre functions used in this program. The Neumann form of the functions is:

$$P_{l,m}(\vartheta) = \frac{(2l)!}{2^l l! (l-m)!} \sin^m \vartheta \left\{ \cos^{l-m} \vartheta - \frac{(l-m)(l-m-1)}{2(2l-1)} \cos^{l-m-2} \vartheta \right. \\ \left. + \frac{(l-m)(l-m-1)(l-m-2)(l-m-3)}{2 \cdot 4 \cdot (2l-1)(2l-3)} \cos^{l-m-4} \vartheta - \dots \right\}$$

which have widely varying mean values depending on  $m$ . We use a different normalization,  $P_l^m(\vartheta) \left\{ \frac{\cos}{\sin} \right\}^m \vartheta$  which have the same order of magnitude for the various degrees,  $m$ , and can be compared directly (see the discussion in Chapman and Bartels, 1940). The mean square value of these functions over the sphere is  $\frac{1}{(2l+1)}$ . They are related to the above Neumann form by:

$$P_l^m(\vartheta) = \left\{ g_m \frac{(l-m)!}{(l+m)!} \right\}^{\frac{1}{2}} P_{l,m}(\vartheta)$$

where  $g_m = 2$  for  $m > 0$  and  $1$  for  $m = 0$ . If we introduce the matrix  $W$  which is calculated in the procedure `get_W`:

$$W_l^m = \left\{ \frac{g_m [(2l-1)!!]^2}{(l-m)!(l+m)!} \right\}^{\frac{1}{2}}$$

and  $U_i^{l,m}$  defined by the recursion relation:

$$U_0^{l,m} = 1; \quad U_i^{l,m} = U_{i-2}^{l,m} \frac{(l-m-i+1)(i-2-l+m)}{i(2l-i+1)} \quad \text{for } i > 0.$$

Then our associated Legendre Polynomials can be expressed as follows:

$$P_l^m(\vartheta) = W_l^m \sin^m \vartheta \sum_{i=0,2,4,\dots}^{l-m} U_i^{l,m} \cos^{l-m-i} \vartheta$$

which is computed by `get_pp` using  $W$  and the function `p`. Note that when the derivatives of the Legendre polynomials are required for determining the three dimensional field below the source surface they can be determined in terms of the previously calculated functions using the recursion relation:

$$\sin(\vartheta) \frac{\partial P_l^m}{\partial \vartheta} = \frac{1}{2l+1} \left\{ l \left[ (l+1)^2 - m^2 \right]^{\frac{1}{2}} P_{l+1}^m - (l+1) (l^2 - m^2)^{\frac{1}{2}} P_{l-1}^m \right\}$$

which are computed in `get_pda`.

The text of the program follows.



```

#define aat 10 /* order of expansion + 1 */
#define aii 31 /* NS dimension of Data Grid + 1 */
#define AII 32 /* Number of Saved Items /Longitude Strip */
#define ajj 73 /* EW dimension of data grid + 1 */
#define AJJ 74 /* EW dimension of data grid + 2 */

```

```

#include <stp.h>

```

```

/* Parameters

```

```

    ii=30          ; ii = zones of cos(theta)
    jj=72          ; jj = strips in longitude
    order=9        ; principal order of expansion
    in=synoptic    ; source of bls-data (synoptic charts)
    out=ssdata     ; where to put the output dataset.
    frot=1642      ; first rotation
    lrot=rot       ; last rotation number. If not specified only the
                    ; rotation specified above will be processed.
    addpolar=0     ; Fraction of Standard Polar Field to Add
    monopole=1    ; if 0 the monopole component is included in
                    ; the computation of the field.
    rs=2.5         ; source surface radius (in solar radii).
    clong.355      ; start longitude
    inc=10         ; increment for multiple source surface calculations

```

```

*/

```

```

float w[aat][aat],g[aat][aat],h[aat][aat],cth[aii],sth[aii];
float bls[ajj][aii],br[ajj][aii],bt[ajj][aii],bp[ajj][aii],da[ajj][aii];
float pp[aat][aat][aii],pd[aat][aat][aii];
float r,rs;
int t,ii,jj,mp,firstlong;

```

```

float p(), dot_product();
double pavb();

```

```

main()

```

```

{
dataset °dsin,°ds;
dataset °get_ds();
int inc;
int i,j,rot,lrot;
TIME ct;

```

```

mp= is_param("monopole") ? 0.0 : 1.0; /* Initialize parameters */
ii= parameter("ii",30.0); /* dflt: no mp; mp=first n value */
jj= parameter("jj",72.0); /* 30 points North-South */
t = parameter("order",9.0); /* 72 points East-West */
rs= parameter("rs",2.5); /* Use Legendre Poly. Orders 0-9 */
r = parameter("r",rs); /* Source Surface Radius */
/* Radius to Compute the Field */

```

```

initialize(); /* Init arrays & find harmonics */

```

```

if((inc=parameter("inc",0.0)) != 0.0)                               /* Incremental Procedure */
{
    rot=parameter("frot",1642.0);                                  /* Determine time bounds */
    lrot=parameter("lrot",(double)rot);
    firstlong=parameter("clong",355.0);

    dsin=dsopen("in=<","r");                                       /* Open datasets */
    ds = get_ds(0);

    for(ct=360*rot-firstlong; ct<=360*lrot-firstlong; ct+=inc)
    {
        /* At Each Incremental Time .... */
        int xrot,xlong;
        for(j=0;j<ajj;j++)                                         /* Zero data array */
            for(i=0;i<aii;i++)
                bls[j][i] = 0.0;
        readrot(dsin,ct,bls);                                       /* Read in Data */
        get_lgh(bls,rs,g,h);                                         /* Solve for g's & h's */
        get_br(r,rs,g,h,br);                                        /* Determine Radial field */
        putbr_inc(ds,ct,br,inc);                                    /* Average & save data */

        xlong=360 - (long)ct % 360; xrot = (ct+xlong)/360;
        fprintf(stderr,"Rot %4d:%3d0,xrot,xlong);
        printit(g); printit(h);                                    /* Print out coefficients */
    }
    dsclose(dsin);
    dsclose(ds);
}

else                                                                /* Single Calculation */
{
    rot = parameter("frot",1642.0);                                /* Set the Carrington time */
    firstlong = parameter("clong",355.0);
    ct = 360 * rot - firstlong;

    dsin=dsopen("in=<","r");                                       /* Open datasets */

    readrot(dsin,ct,bls);                                          /* Read data */
    get_lgh(bls,rs,g,h);                                           /* Solve for g's & h's */

    fprintf(stderr,"Oot: %4d SSRadius: %4.2f0,rot,rs);
    printit(g); printit(h);                                       /* Print out coefficients */

    if(r==rs)                                                      /* If field at source surface... */
    {
        get_br(r,rs,g,h,br);                                       /* Get radial field at rs */
        ds = get_ds(0);                                           /* Get a Dataset */
        for(i=0;i<ajj;i++)                                         /* and save on dataset. */
            saveBr(ds,ct+i*5,&(br[i][0]));
    }

    else                                                            /* Otherwise find all components */

```

```

    {
        get_b(r,rs,g,h,br,bt,bp);           /* Get all components */
        ds = get_ds("r");                   /* Get a dataset... */
        for(i=0;i<ajj;i++)                 /* ...save br on dataset. */
            saveBr(ds,ct+i*5,&(br[i][0]));
        ds = get_ds("t");                   /* Get a dataset... */
        for(i=0;i<ajj;i++)                 /* ...save bt on dataset. */
            saveBr(ds,ct+i*5,&(bt[i][0]));
        ds = get_ds("p");                   /* Get a dataset... */
        for(i=0;i<ajj;i++)                 /* ...save bp on dataset. */
            saveBr(ds,ct+i*5,&(bp[i][0]));
    }
}

* ----- END ----- OF ----- MAIN ----- */

initialize() /* Called from main -- sets up w,cth,sth,pp, & pd */
{
    register int i,j;
    for(j=0;j<ajj;j++) /* Fill data arrays with zero */
        for(i=0;i<aii;i++)
            bls[j][i] = da[j][i] = 0.0;
    for(i=0;i<aat;i++) /* Fill coef. + weight array with zero */
        for(j=0;j<ajj;j++)
            g[i][j] = h[i][j] = w[i][j] = MISSING;
    get_w(w); /* Used in Calculating Plm's */
    get_theta(cth,sth); /* Gets sines and cosines for grid points */
    get_pp(pp); /* Finds values of Poly. at grid points */
    if(parameter("pd",1.0) >= 0.0)
        get_pd(pd); /* Get Derivatives of Poly. if necessary */
}

get_w(w) /* Called from initialize to set up w[][] */
float w[][aat]; /* used in calculating legendre polynomials */
{int n,m,k,p,q,r,s; double u;
  for(n = 0; n <= t; n++)
    for(m = 0; m <= n; m++)
        {r = 2*n-1; p = n+m; q = n-m; s = 0;
          u = m == 0 ? 1 : 2;
          for(k = 2*n;k>=1;k--)
              {u = u*r; r = r-s; s = 2-s;
                if(p>1) { u = u/p; p--;}
                else if(q>1) { u = u/q; q--;}
              }
          w[n][m] = sqrt(u);
        }
}

get_theta(cth,sth) /* Called by initialize to find sin,cos for each i */
float cth[],sth[];

```

```

{float th; int i;
 for(i = 1; i<=ii; i++)
  {th = 1.57079633-asin(((double)((ii+1.0-i-i)/(double)ii));
   cth[i] = cos(th); sth[i] = sin(th);
  }
}

get_pp(pp)          /* Calculates legendre polynomials for n,m at i */
float pp[][][aat][aai]; /* Called by initialize */
{int n,m,i;
 for(n = 0; n<=t; n++)
 for(m = 0; m<=n; m++)
 for(i = 1; i<=ii; i++)
  pp[n][m][i] = p(n,m,i);
}

float p(n,m,th)     /* Called from get_pp - evaluates Pn,m at th */
int n,m,th;
{int i,nm; float s,u,c,c2;
 c = cth[th]; c2 = c*c; nm = n-m; s = u = 1;
 for(i = 2; i<=nm; i+=2)
  {u=u*(i-nm-2)*(double)(nm-i+1)/(double)(n+n-i+1)/(double)i; s = s*c2+u;}
 if(nm % 2 == 1) s = s*c;
 return(s*w[n][m]*pow((double)sth[th],(double)m));
}

get_pd(pd)         /* Called by initialize if pd is set - needed if */
float pd[][][aat][aai]; /* if r != rs to find derivatives of Leg. poly. */
{int n,m,i;
 for(n = 0; n<=t; n++)
 for(m = 0; m<=n; m++)
 for(i = 1; i<=ii; i++)
  pd[n][m][i] = m==0 ? -sqrt(n*(n+1)/2.0)*(n==m ? 0.0 : pp[n][1][i])
  : 0.5*(sqrt((m>1 ? 1.0 : 2.0)*(n+m)*(n-m+1))*pp[n][m-1][i] -
  (n==m ? 0.0 : sqrt((double)((n+m+1)*(n-m))*pp[n][m+1][i]));
}

printit(a)         /* Called from main - prints g's and h's */
float a[][aat];
{if(parameter("print",1.0)>=0.0)
 {int i,n; fprintf(stderr," ");
  for(i = 0; i<=t; i++) fprintf(stderr,"%5d ",i);
  fprintf(stderr,"0");
  for(n = 0; n<=t; n++)
   {fprintf(stderr,"%2d",n);
    for(i = 0; i<=t; i++)
     if(a[n][i] != MISSING) fprintf(stderr,"%7.3f ",a[n][i]);
    fprintf(stderr,"0");
   }
  fprintf(stderr,"0");
}
}

```

```

get_b(r,rs,g,h,br,bt,bp)          /* Called from main find magnetic fields, */
float r,rs;                        /* from g's & h's br,bp,bt if r!=rs */
float g[][aat],h[][aat],br[][aai],bt[][aai],bp[][aai];
{int n,m,i,j; float c,kr,ka,gh;gp,gg,hh,kgh;
float cmphi[ajj], smphi[ajj], p[aai], d[aai], s[aai];
for(i=0;i<aai;i++)
for(j=0;j<ajj;j++)
    br[j][i] = bt[j][i] = bp[j][i] = 0.0;
for(n = mp; n<=t; n++)
    {c = -1.0/pow((double)rs,(double)(n+2)) * pow((double)(r/rs),(double)(n-1));
    kr = (n+1)/pow((double)r,(double)(n+2)) - n*c;
    ka = 1.0/pow((double)r,(double)(n+2)) + c;
    for(m = 0; m<=n; m++)
        {gg = g[n][m]; hh = h[n][m];
        if(gg != 0 || hh != 0)
            {get_mphi(m,cmphi,smphi);
            for(i = 1; i<=ii; i++)
                {p[i] = pp[n][m][i]; d[i] = pd[n][m][i]; s[i] = p[i]/sth[i];}
            for(j = 1; j<=jj; j++)
                {gh = gg*cmphi[j] + hh*smphi[j];
                gp = (gg*smphi[j] - hh*cmphi[j])*m;
                kgh = kr*gh; gh = ka*gh; gp = ka*gp;
                for(i = 1; i<=ii; i++)
                    {br[j][i] += p[i]*kgh;
                    bt[j][i] -= d[i]*gh;
                    bp[j][i] += s[i]*gp;
                    }
                }
            }
        }
}

```

```

get_br(r,rs,g,h,br)                /* Called by main to get br */
float r,rs; float g[][aat],h[][aat],br[][aai]; /* from g's & h's if r=Rs */
{int n,m,i,j; float gg,hh,c,kr,gh;
float cmphi[ajj], smphi[ajj], p[aai];
for(i=0;i<aai;i++)
for(j=0;j<ajj;j++)
    br[j][i] = 0.0;
for(n = mp; n<=t; n++)
    {c = -1.0/pow((double)rs,(double)(n+2))*pow((double)(r/rs),(double)(n-1));
    kr = (n+1)/pow((double)r,(double)(n+2)) - n*c;
    for(m = 0; m<=n; m++)
        {gg = g[n][m]; hh = h[n][m];
        if((gg != 0) || (hh != 0))
            {get_mphi(m,cmphi,smphi);
            for(i = 1; i<=ii; i++)          p[i] = pp[n][m][i];
            for(j = 1; j<=jj; j++)
                {gh = (gg*cmphi[j] + hh*smphi[j])*kr;
                for(i = 1; i<=ii; i++)
                    br[j][i] += p[i]*gh;
                }
            }
        }
}

```

```

get_lgh(bls,rs,g,h)                /* Called from main to get g's & h's */
float bls[][aai],g[][aat],h[][aat]; float rs;

```

```

{int m; get_blssth(bls);
for(m = 0; m<=t; m++)
    {int n; float a[aa], b[aa], k[aa][aa];
    get_ab(bls, m, a, b); get_K(k, m, rs); solve(k, m, a, b);
    for(n = m; n<=t; n++)
        {g[n][m] = a[n]; h[n][m] = b[n];}
    }
}

get_blssth(bls)                /* Called by get_Lgh to get bls(j,i)*sin(i) */
float bls[][aai];
{register j,i;
for(j = 1; j<=jj; j++)
for(i = 1; i<=ii; i++)
    bls[j][i] = bls[j][i]*sth[i];
}

get_ab(bb, m, a, b)            /* Called from get_Lgh - finds a's and b's, */
float bb[][aai], a[], b[]; int m; /* the harmonic coefficients for the photo- */
{int i, j, n; float sa, sb, si; /* spheric fields, for a given m. */
float x[aai], c[ajj], s[ajj];
get_mphi(m, c, s);
for(n = m; n<=t; n++)
    {sa = sb = 0;
    for(i = 1; i<=ii; ++i)
        x[i] = pp[n][m][i];
    for(j = 1; j<=jj; ++j)
        {si = dot_product(x, bb, j);
        sa = sa + c[j]*si;
        sb = sb + s[j]*si;
        }
    a[n] = sa*(2.0*n+1.0)/(double)(ii*jj);
    b[n] = sb*(2.0*n+1.0)/(double)(ii*jj);
    }
}

float dot_product(x, bb, j)    /* Takes the dot product of x and bb[j] */
float x[], bb[][aai]; int j; /* Called from get_ab */
{float si=0.0; register i;
for(i=1; i<=ii; i++) si += x[i]*bb[j][i];
return(si);
}

get_K(k, m, rs)                /* Called from get_Lgh to setup k matrix */
float k[][aat]; int m; float rs; /* needed to relate a's & b's to g's & h's */
{int i, n; float m2;
m2 = m*m;
for(n = m; n <= t; ++n)
    {for(i = m; i <= t; i++)
    k[i][n] = 0;
    k[n][n] = ((n+1.0)*(n+2.0)+m2)/(2.0*n+3.0) + ((n-1.0)*n+m2)/(2.0*n-1.0) /
    pow((double)rs, (double)(2*n+1));
    }
}

```

```

    }
    for(n = m+2; n <= t; n++)
        k[n][n-2] = -sqrt((double)((n-1.0)*(n-1.0)-m2)*(double)(n*n-m2))/(2.0*n-1.0);
    for(n = t-2; n >= m; --n)
        k[n][n+2] = -sqrt((double)((n+1.0)*(n+1.0)-m2)*((n+2.0)*(n+2.0)-m2))/
(2.0*n+3.0)/pow((double)rs,(double)(2*n+5));
}

solve(k,m,a,b)          /* Called from get_lgh; Given K matrix, solves */
float k[][aat],a[],b[]; int m; /* for g's and h's for a given m value given */
{                          /* the a's and b's. */
float div,ratio; int i,j,h;
for(i = m; i <= t; i++)
    { div = k[i][i];
      for(j=m; j<=t; j++) k[i][j] = k[i][j]/div;
      a[i] = a[i]/div;
      b[i] = b[i]/div;
      for(j=m; j<=t; j++)
          if(i != j)
              {ratio = k[j][i];
                if(ratio != 0)
                    {for(h = m; h <= t; h++) k[j][h] -= ratio*k[i][h];
                      a[j] -= ratio*a[i]; b[j] -= ratio*b[i];
                    }
              }
    }
}

get_mphi(m,cmphi,smphi) /* Called by get_ab,b,br to get sin,cos(m phi) */
int m; float cmphi[],smphi[];
{float s,mphi; int j;
s = 2*3.14159265*m/jj;
for(j = 1; j<=jj; j++)
    {mphi = (jj-j+0.5)*s;
      cmphi[j] = cos(mphi); smphi[j] = sin(mphi);
    }
}

readrot(dsin,ct,bls) /* Called in main to fill bls with synoptic */
dataset *dsin; TIME ct; /* chart data. Doesn't initialize bls. */
float bls[][aai]; /* Adds polar field correction. */
{TIME ctime=ct;
double v,tmp,tmq,plr; double pf[aai];
double cut=parameter("cut",0.0);
int i,j,mct;

double addpolar=parameter("addpolar",0.0); /* Determines the polar */
plr = addpolar * 640 * pavb(ct)/92.0; /* field to include */
if(addpolar != 0.0)
    for(i=1; i<aai; i++)
        pf[i] = plr * pow((double)cth[i],8.0) * ((i+i)<aai?1:-1) * sth[i];

dsseek(dsin,ctime); /* Reads data; fills in for Missing */
for(j = 1; j<ajj; j++) /* with ave. of previous & next rotation */
    {dsgrp(dsin);

```

```

mct=0;
for(i = 1; i<alii; i++)
  {v = dget(dsin,0,i-1,0);
  if(fabs(v) > 4000.0) /* Unreasonably high field rejected*/
    {dsseek(dsin,ctime-360.0); dsgrp(dsin); tmp=dget(dsin,0,i-1,0);
    dsseek(dsin,ctime+360.0); dsgrp(dsin); tmq=dget(dsin,0,i-1,0);
    if(fabs(tmp) > 4000.0) tmp=MISSING;
    if(fabs(tmq) > 4000.0) tmq=MISSING;
    v = tmp==MISSING ? tmq : tmp;
    v = tmq==MISSING ? tmp : (v+tmq)/2.0;
    if(v==MISSING)
      fprintf(stderr,"MISSING VALUE");
    dsseek(dsin,ctime);
    dsgrp(dsin);
    mct++;
    }
  if(cut != 0.0)
    v = v>cut ? cut : v< -cut ? -cut : v;
  bls[j][i] += v;
  }
if(addpolar != 0.0) for(i=1;i<alii;i++) bls[j][i] += pf[i];
bls[j][0] = mct>10 ? -mct : 0.0;
ctime += 5;
}
}

```

```

double pavb(ctim) /* Calculates the Average Polar B-field. Called from */
TIME ctim; /* readrot to determine time dependant polar magnetic */
/* field strength ratio */
TIME stant,BC1,BC2;
int i,n;
BC1 =ymdtime(1978,6,10,0,0,0); /* Returns 92 before June 10, 1978 */
BC2 =ymdtime(1980,12,16,0,0,0); /* Returns 53 after Dec. 16, 1980 */
caritime(&ctim,&i,&n); /* Interpolates between these dates */
stant = curtime._time;
if (stant<BC1) return (92.0);
else if (stant<BC2) return (92.0-145.0*(stant-BC1)/(BC2-BC1));
else return (-53.0);
}

```

```

putbr_inc(ds,ct,br,inc)
dataset °ds;
int inc; float br[][alii]; double ct;

```

```

/* Called from main if increment is set : stores computed source
surface data through ct+180+inc/2 on ds. Brings ds up to date
through that point. If possible, averages 3 computations of each
position to form a smooth mapping. */

```

```

{int i, j, det, hinc, dinc;
float °zs, zbuf[AII], mbuf[AII], t1, t2, t3, t4, center;

```



```

static int no=1;
static TIME timelast=0.0;
double time0;
j=0;
for(i=0;i<All;i++) mbuf[i]=zbuf[i]=MISSING;
dct = 360.0/jj;
center=ct+180; dinc=inc/dct; hinc=inc/2;
t1=center-inc-hinc-dct;
t2=center-hinc;
t3=center+hinc;
t4=center+inc+hinc;
time0 = timelast != 0.0 ? timelast + dct : ds->ds_last>t2 ? t2 : ds->ds_last;
while(time0 < t1)
{if(time0 == ct+dct*(j-1))
{zs=zbuf+1;
for(i = 1; i<=ii; i++) *zs++ = br[j][i];
if(bls[j][0]<0.0) *zs++ = bls[j][0];
else *zs = ct;
saveBr(ds,time0,zbuf); timelast = time0;
j++; time0 += dct;
}
else if(time0 > ct+dct*(j-1))
j++;
else if(time0 < ct+dct*(j-1))
time0 += dct;
}
while(time0 >= t1 && time0 < t2)
{if(time0 == ct+dct*(j-1))
{zs=zbuf+1;
for(i = 1; i<=ii; i++) *zs++ = (br[j][i]+da[j]+dinc)[i]/no;
if(bls[j][0]<0.0) *zs++ = bls[j][0];
else *zs = ct-inc;
saveBr(ds,time0,zbuf); timelast = time0;
j++; time0 += dct;
}
else j++;
}
while(time0 >= t2 && time0 < t3)
{for(i = 1; i<=ii; i++) da[j][i] = 2*br[j][i] + da[j+dinc][i];
time0 += dct; j++;
}
no += 2;
while(time0 >= t3 && time0 < t4)
{for(i = 1; i<=ii; i++) da[j][i] = br[j][i];
time0 += dct; j++;
}
if(no >= 4) no = 4;
}
saveBr(ds,ct,br) /* Called from putbr_inc or main to save of Br strip.
dataset *ds; TIME ct; float *br;
*/

```

```

{
int i;
dsseek(ds,ct);
dsgrp(ds);
for(i=0;i<All;i++)
    dput(ds,0,i,0,(double)(*(br+i+1)));
}

dataset *get_ds(a)    /* Returns to main an opened dataset suitable for      */
char *a;              /* storing B maps as specified by out={}a . Makes                    */
{                    /* new dataset if necessary.                                           */
char name[32];
dataset *dsx,*ds;
strcat(name,nameparam("out=","ssdata"));
if((int)a != 0) strcat(name,a);
if(access(name,0)==0)
    return(dsopen(name,"c+"));
else
{
ds = dsdup( dsx = dsopen("/data/source/ss2.50ds","r"));
fprintf(stderr,"making dataset0);
dsadditem(ds,dsx->ds_item[0]);
dsadditem(ds,dsx->ds_item[1]);
dsset(ds,"DATASET=ss;FIRST=590560;LAST=-MISSING;SEL=0;X=30");
ds->ds_first = 360*parameter("frot",1641.0) - parameter("long",360.0);
head(ds->ds_txtfp,"sph ",0);
dsnew(ds,name,"w+");
return(ds);
}
}

```

## Bibliography

- Adams, J., and G.W. Pneuman, A new technique for the determination of coronal magnetic fields: a fixed mesh solution to Laplace's equation using line-of-sight boundary crossings, *Solar Phys.*, *46*, 185, 1976.
- Altschuler, M.D. and G. Newkirk, Jr., Magnetic fields and the structure of the solar corona, *Solar Phys.*, *9*, 131, 1969.
- Altschuler, M.D., D.E. Trotter, G. Newkirk, Jr., and R. Howard, The Large-Scale Solar Magnetic Field, *Solar Phys.*, *39*, 3, 1974.
- Altschuler, M.D., D.E. Trotter, G. Newkirk, Jr., and R. Howard, Tabulation of the Harmonic Coefficients of the Solar Magnetic Field, *Solar Phys.*, *41*, 225, 1975.
- Altschuler, M.D., R.H. Levine, M. Stix, and J.W. Harvey, High resolution mapping of the magnetic field of the solar corona, *Solar Phys.*, *51*, 345, 1977.
- Antonucci, E., Solar rotating magnetic dipole?, *Stanford University Institute for Plasma Research Report No. 570*, 1974.
- Antonucci, E. and L. Svalgaard, Rigid and differential rotation of the solar corona, *Solar Phys.*, *34*, 3, 1974.
- Armstrong, J.W., and W.A. Coles, Analysis of three station interplanetary scintillation, *J. Geophys. Res.*, *77*, 4602, 1972.
- Behannon, K.W. L.F. Burlaga, and A.J. Hundhausen, A comparison of coronal and interplanetary current sheet inclinations, *J. Geophys. Res.*, *88*, 7837, 1983.
- Bohlin, J.D., An observational definition of coronal holes, in J.B. Zirker (ed.), *Coronal Holes and High Speed solar Wind Streams*, Colo. Assoc. Univ. Press, Boulder, 27, 1977a.
- Bohlin, J.D., Extreme-ultraviolet observations of coronal holes, *Solar Phys.*, *51*, 377, 1977b.
- Bruno, R., L.F. Burlaga, A.J. Hundhausen, Quadrupole distortion of the heliospheric current sheet in 1976 and 1977, *J. Geophys. Res.*, *87*, 10337, 1982.
- Burlaga, L.F., K.W. Behannon, S.F. Hansen, G.W. Pneuman, and W.C. Feldman, Sources of magnetic fields in recurrent interplanetary streams, *J. Geophys. Res.*, *83*, 4177, 1978.
- Burlaga, L.F., A.J. Hundhausen, and X-P. Zhao, The coronal and interplanetary current sheet in early 1976, *J. Geophys. Res.*, *86*, 8893, 1981.
- Chapman, S. and J. Bartels, *Geomagnetism, Vol. II.*, Oxford University Press,

London, 1940.

Dittmer, P.H., Large-scale periodic solar velocities: an observational study, Ph.D. Thesis, *Stanford University Institute for Plasma Research Rep. No. 686*, 1977.

Duvall, T.L. Jr., A study of large-scale solar magnetic and velocity fields, Ph.D. Thesis, Stanford University Institute for Plasma Research Report No. 724, 1977.

Fisher, R.R., On the nature of the solar corona near the maximum of cycle 21, *Astrophys. J.*, *259*, 431, 1982.

Frazier, E.N. and J.O. Stenflo, On the small scale structure of solar magnetic fields, *Solar Phys.*, *27*, 330, 1972.

Hakamada, K. and S.-I. Akasofu, A cause of solar wind speed variations observed at 1 A.U., *J. Geophys. Res.*, *86*, 1290, 1981.

Hakamada, K. and Y. Munakata, A cause of the solar wind speed variations: an update, *J. Geophys. Res.*, *89*, 357, 1984.

Hansen, S.F., C. Sawyer, and R.T. Hansen, K-corona and magnetic sector boundaries, *Geophys. Res. Lett.*, *1*, 13, 1974.

Harvey, J.W., W. Livingston, and C. Slaughter, *Proc. Conference on Line Formation in a Magnetic Field, Boulder, Colorado, September, 1971*, 1972.

Harvey, K.L., N.R. Sheeley, Jr., and J.W. Harvey, Magnetic measurements of coronal holes during 1975 - 1980, *Solar Phys.*, *79*, 149, 1982.

Hoeksema, J.T., P.H. Scherrer, and J.M. Wilcox, A two-sector solar magnetic structure with 29 day rotation *Bull. Am. Astron. Soc.*, *12*, 474, 1980.

Hoeksema, J.T., J.M. Wilcox, and P.H. Scherrer, Structure of the heliospheric current sheet in the early portion of sunspot cycle 21, *J. Geophys. Res.*, *87*, 10331, 1982.

Hoeksema, J.T., J.M. Wilcox, and P.H. Scherrer, The structure of the heliospheric current sheet: 1978 - 1982, *J. Geophys. Res.*, *88*, 9910, 1983.

Howard, R., Studies of solar magnetic fields, *Solar Phys.*, *52*, 243, 1977.

Howard, R., and J. Harvey, Spectroscopic determinations of solar rotation, *Solar Phys.*, *12*, 23, 1970.

Howard, R.A. and M.J. Koomen, Observation of sectorized structure in the outer solar corona: correlation with interplanetary magnetic field, *Solar Phys.*, *37*, 469, 1974.

Howard, R., and B. Labonte, Surface magnetic fields during the solar activity

cycle, *Solar Phys.*, 74, 131, 1981.

Howard, R. and J.O. Stenflo, On the filamentary nature of solar magnetic fields, *Solar Phys.*, 22, 402, 1972.

Hundhausen, A.J., An interplanetary view of coronal holes, in J.B. Zirker (ed.), *Coronal holes and high speed wind streams*, Colo. Assoc. Univ. Press, Boulder, pp. 225, 1977.

Hundhausen, A.J., Solar wind spatial structure: the meaning of latitude gradients in observations averaged over solar longitude, *J. Geophys. Res.*, 83, 4186, 1978.

Hundhausen, A.J., R.T. Hansen, and S.F. Hansen, Coronal evolution during the sunspot cycle: coronal holes observed with the Mauna Loa K-coronameters, *J. Geophys. Res.*, 86, 2079, 1981.

Hundhausen, A.J., D.G. Sime, R.T. Hansen, S.F. Hansen, Polar coronal holes and cosmic ray modulation, *Science*, 207, 761, 1980.

Jackson, B.V. and R.H. Levine, A comparison of type III metric radio bursts and global solar potential field models, *Solar Phys.*, 73, 183, 1981.

Jokipii, J.R., Correlation of the cosmic ray intensity with solar terrestrial parameters, *Geophys. Res. Lett.*, 8, 837, 1981.

Jokipii, J.R., and B. Thomas, Effects of drift on the transport of cosmic rays IV: Modulation by a wavy interplanetary current sheet, *Ap. J.*, 243, 1115, 1981.

King, J.H., *Interplanetary Medium Data Book (Supplement 1)*, Rep. NSSDC 7908, NASA Goddard Space Flight Center, Greenbelt, Md. 1979.

King, J.H., Solar cycle variations in IMF intensity, *J. Geophys. Res.*, 84, 5938, 1979.

Levine, R.H., Open magnetic structure on the Sun: the Skylab period, *Ap. J.*, 218, 291, 1977a.

Levine, R.H., Large-scale solar magnetic fields and coronal holes, in J.B. Zirker, *Coronal Holes and High Speed Solar Wind Streams*, Colo. Assoc. Univ. Press, Boulder, 1977b.

Levine, R.H., The relation of open magnetic structures to solar wind flow, *J. Geophys. Res.*, 83, 4193, 1978.

Levine, R.H., Open magnetic fields and the solar cycle, I, *Solar Phys.*, 79, 203, 1982.

Levine, R.H. and M.D. Altschuler, Representations of coronal magnetic fields including currents, *Solar Phys.*, 36, 345, 1974.

Levine, R.H., M. Schultz, and E.N. Frazier, Simulation of the magnetic structure of the inner heliosphere by means of a non-spherical source surface, *Solar Phys.*, 77, 363, 1982.

Lundstedt, H., J.M. Wilcox, and P.H. Scherrer, Solar flare acceleration of solar wind: influence of active region magnetic field, *Science*, 212, 1501, 1981.

Marubashi, K. and S. Watanabe, Synoptic maps of open magnetic fields in the solar corona from August 1959 to January 1974, *Radio Research Laboratories, Report 12*, Tokyo, Japan, 1983.

Munro, R.H. and B.V. Jackson, Physical properties of a polar coronal hole from 2 to 5  $R_{\odot}$ , *Astrophys. J.* 213, 874, 1977.

Newkirk, G.A., Coronal magnetic fields and the solar wind, in *Solar Wind*, C.P. Sonett, P.J. Coleman, Jr. and J.M. Wilcox, (eds.) NASA SP-308, Washington, 1972.

Newkirk, G. Jr., D.E. Trotter, M.D. Altschuler, and R. Howard, A microfilm atlas of magnetic fields in the solar corona, *NCAR-TN/STR-85*, 1973.

Newton, J.W., and M.L. Nunn, *M.N.R.A.S.*, 111 413, 1951.

Niedner, M.B., Jr., Interplanetary Gas XXVIII: A study of the three-dimensional properties of interplanetary sector boundaries using disconnection events in cometary plasma tails, *Astrophys. J. Supp.*, 48, 1, 1982.

Niedner, M.B., Jr., and J.C. Brandt, Interplanetary Gas XXIII: plasma tail disconnection events in comets: evidence for magnetic field line reconnection at interplanetary sector boundaries?, *Astrophys. J.*, 223, 655, 1978.

Niedner, M.B., Jr., and J.C. Brandt, Interplanetary Gas XXIV: are cometary plasma tail disconnections caused by sector boundary crossings or by encounters with high speed streams?, *Astrophys. J.*, 234, 723, 1979.

Niedner, M.B., Jr., and J.C. Brandt, *Icarus*, 42, 257, 1980.

Pneuman, G.W. and R.A. Kopp, Coronal streamers III: energy transport in streamer and interstreamer regions, *Solar Phys.* 13, 176, 1970.

Pneuman, G.W., and R.A. Kopp, Gas-magnetic field interactions in the solar corona, *Solar Physics*, 18, 258, 1971.

Pneuman, G.W., S.F. Hansen and R.T. Hansen, On the reality of potential magnetic fields in the solar corona, *Solar Phys.*, 59, 313, 1978.

Poletto, G., G.S. Vaiana, M.V. Zombeck, A.S. Krieger, and A.F. Timothy, A comparison of coronal X-ray structures of active regions with magnetic fields computed from photospheric observations, *Solar Phys.*, 44, 83, 1975.

Rickett, B.J. and W.A. Coles, Solar cycle evolution of the solar wind in three

- dimensions, in *Solar Wind Five*, Marcia Neugebauer, ed., NASA Conference Publication 2280, 323, 1983.
- Riesebieter, W. and F.M. Neubauer, Direct solution of Laplace's equation for coronal magnetic fields using line-of-sight boundary conditions, *Solar Phys.*, *63*, 127, 1979.
- Rosenberg, R.L., and P.J. Coleman, Helio-graphic latitude dependence of the dominant polarity of the interplanetary magnetic field, *J. Geophys. Res.*, *74* 5611, 1969.
- Saito, T., T Sakurai, and K. Yumoto, The Earth's paleomagnetic sphere as the third type of planetary magnetosphere, *Planet. Space Sci.*, *26*, 431, 1978.
- Schatten, K.H., Large scale configuration of the coronal and interplanetary magnetic field, Ph. D. Thesis, University of California, 1968a.
- Schatten, K.H., Prediction of the coronal structure of the solar eclipse of September 22, 1968, *Nature*, *220*, 1211, 1968b.
- Schatten, K.H., Coronal structure at the solar eclipse of September 22, 1968, *Nature* *223*, 652, 1969.
- Schatten, K.H., The magnetic field structure in the active solar corona, in R. Howard (ed.), *Solar Magnetic Fields, IAU Sump.* *43*, 595, 1971a.
- Schatten, K.H., Current sheet magnetic model for the solar corona, *Cosmic Electrodynamics*, *2*, 232, 1971b.
- Schatten, K.H., J.M. Wilcox and N.F. Ness, A model of interplanetary and coronal magnetic fields, *Solar Phys.*, *6*, 442, 1969.
- Scherrer, P. H., J. M. Wilcox, L. Svalgaard, T.L. Duvall, Jr., P.H. Dittmer and E.K. Gustafson, The mean magnetic field of the sun: observations at Stanford, *Solar Phys.*, *54*, 353, 1977.
- Scherrer, P.H., J.M. Wilcox, and L Svalgaard, The rotation of the sun: observations at Stanford, *Astrophys. J.*, *241*, 811, 1980.
- Schulz, M., Interplanetary sector structure and the heliomagnetic equator, *Astrophys. and Space Sci.*, *24*, 371, 1973.
- Schulz, M., E.N. Frazier, and D.J. Boucher, Jr., Coronal magnetic field model with non-spherical source surface, *Solar Phys.*, *60*, 83, 1978.
- Sheeley, N.R., Jr. and J.W. Harvey, Coronal holes, solar wind streams, and geomagnetic disturbances during 1978 and 1979, *Solar Phys.*, *70*, 237, 1981.
- Sime, D.G. and B.J. Rickett, The latitude and longitude structure of the solar wind speed from IPS observations, *J. Geophys. Res.*, *83*, 5757, 1978.

Slavin, J.A. and E.J. Smith, Solar cycle variations in the interplanetary magnetic field, in *Solar Wind Five*, Marcia Neugebauer, ed., NASA Conference Publication 2280, 323, 1983.

Smith, E.J., and K.H. Schatten, *Nature*, 226, 1130, 1970.

Smith, E.J., B.T. Tsurutani, and R.L. Rosenberg, Observations of the interplanetary sector structure up to heliographic latitudes of  $16^\circ$ : Pioneer 11, *J. Geophys. Res.*, 83, 717, 1978.

Smith, E.J. and J.H. Wolfe, Fields and plasmas in the outer solar system, *Space Sci. Rev.*, 23, 217, 1979.

Stelzried, T.T., G.S. Levey, T. Sato, W.V.T. Rusch, J.E. Ohlson, K.H. Schatten, and J.M. Wilcox, The quasi-stationary coronal magnetic field and electron density as determined from a faraday rotation experiment, *Solar Phys.*, 14, 440, 1970.

Stenflo, J.O., Observations of the polar magnetic fields, *I.A.U. Symposium No. 43, Solar Magnetic Fields*, 714, 1971.

Stenflo, J.O., Evolution of solar magnetic fields over an 11-year period, *Solar Phys.*, 23, 307, 1972.

Stenflo, J.O., Magnetic field structure of the photospheric network, *Solar Phys.*, 32, 41, 1973.

Suess, S.T., A.K. Richter, C.R. Winge, S.F. Nerney, Solar polar coronal hole -- a mathematical simulation, *Ap. J.*, 217, 296, 1977.

Suess, S.T., J.M. Wilcox, J.T. Hoeksema, H. Henning, and M. Dryer, Relationships between a potential field -- source surface model of the coronal magnetic field and properties of the solar wind at 1 AU, *J. Geophys. Res.*, in Press, 1984.

Svalgaard, L., Polar cap magnetic variations and their relationship with the interplanetary magnetic sector structure, *J. Geophys. Res.*, 78, 2064, 1973.

Svalgaard, L., An Atlas of interplanetary sector structure 1957 - 1974, *Stanford University Institute for Plasma Research Report No. 629*, 1975.

Svalgaard, L., Interplanetary sector structure 1947 - 1975, *Stanford University Institute for Plasma Research Report No. 648*, Stanford, California, 1976.

Svalgaard, L., T.L. Duvall, Jr., and P.H. Scherrer, The strength of the Sun's polar fields, *Solar Phys.*, 58, 225, 1978.

Svalgaard, L. and J.M. Wilcox, Long term evolution of solar sector structure, *Solar Phys.*, 41, 461, 1975.

Svalgaard, L. and J.M. Wilcox, Structure of the extended solar magnetic field



- and the sunspot cycle variation in cosmic ray intensity, *Nature*, 262, 766, 1976.
- Svalgaard, L. and J.M. Wilcox A view of solar magnetic fields, the solar corona, and the solar wind in three dimensions, *Ann. Rev. Astron. Astrophys.*, 16, 429, 1978.
- Timothy, A.F., A.S. Krieger, and G.S. Viana, The structure and evolution of coronal holes, *Solar Phys.*, 42, 135, 1975.
- Villante, U., R. Bruno, F. Mariani, L.F. Burlaga, and N.F. Ness, The shape and location of the sector boundary surface in the inner solar system, *J. Geophys. Res.*, 84, 6641, 1979.
- Villante, U., F. Mariani, and P. Francia, The IMF sector pattern through the solar minimum: two spacecraft observations during 1974 - 1978, *J. Geophys. Res.*, 87, 249, 1982.
- Wagner, W.J., Solar rotation as marked by extreme-ultraviolet coronal holes, *Astrophys. J. Lett.*, 198, 141, 1975.
- Waldmeier, M., *Die Sonnenkorona, Vol.2, Verlag Birkhauser, Basel, 1957.*
- Wilcox, J. M., Why does the Sun sometimes look like a magnetic monopole?, *Comments on Astrophys. and Space Phys.*, 4, 141, 1972.
- Wilcox, J. M., J.T. Hoeksema, and P.H. Scherrer, Origin of the warped heliospheric current sheet, *Science*, 209, 603, 1980.
- Wilcox, J.M. and R. Howard, Differential rotation of the photospheric magnetic field, *Solar Phys.*, 13, 251, 1970.
- Wilcox, J.M. and A.J. Hundhausen, Comparison of heliospheric current sheet structure obtained from potential magnetic field computations and from observed maximum coronal brightness, *J. Geophys. Res.*, 88, 8095, 1983.
- Wilcox, J. M. and N.F. Ness, Quasi-stationary corotating structure in the interplanetary medium, *J. Geophys. Res.*, 70, 5793, 1965.
- Wilcox, J.M., K.H. Schatten, and A.S. Tanenbaum, Photospheric magnetic field rotation: rigid and differential, *Solar Phys.*, 14, 255, 1970.
- H. Yoshimura, Solar cycle evolution of the general magnetic field, eds. Bumba & Keiczek, *Basic Mechanism of Solar Activity*, 137, 1976.
- H. Yoshimura, Solar cycle general magnetic fields of 1959 - 1974 and dynamical structure of the convection zone, *Solar Physics*, 47, 581, 1976 b.
- Zhao, Xue-pu and A.J. Hundhausen, Organization of solar wind plasma properties in a tilted, heliomagnetic coordinate system, *J. Geophys. Res.*, 86, 5423, 1981.

Zhao, Xue-pu and A.J. Hundhausen, Spatial structure of the solar wind in 1976, *J. Geophys. Res.*, *88*, 451, 1983.

Zirker, J.B. (ed.), *Coronal Holes and High Speed Wind Streams*, Colorado Assoc. Univ. Press, Boulder, Colorado, 1977.